

UC Santa Barbara

UC Santa Barbara Electronic Theses and Dissertations

Title

Group III-V Nanowire Growth and Characterization

Permalink

<https://escholarship.org/uc/item/1jx2h6q9>

Author

Wang, Mingjin

Publication Date

2016

Peer reviewed|Thesis/dissertation

UNIVERSITY OF CALIFORNIA

Santa Barbara

Group III-V Nanowire Growth and Characterization

A thesis submitted in partial satisfaction of the
requirements for the degree Master of Science
in Electrical and Computer Engineering

by

Mingjin Wang

Committee in charge:

Professor John Bowers, Chair

Professor James S. Speck

Professor Jon Schuller

March 2016

The thesis of Mingjin Wang is approved.

James S. Speck

Jon Schuller

John Bowers, Committee Chair

March 2016

Group III-V Nanowire Growth and Characterization

Copyright © 2016

by

Mingjin Wang

ACKNOWLEDGEMENTS

This thesis would never have seen the light of day if there were not advisor's encouragement and advice and, above all, his infinite patience and precious time. I am deeply grateful for my advisor, Professor John Bowers, for all his guidance, supervising my master thesis, and revising the script.

I am thankful to my supervisory committee members, Professor James S. Speck and Professor Jon Schuller. I thank them for their precious time and the enthusiasm with which they have approached this commitment. I especially like to thank Professor James S. Speck for teaching me the analysis for crystallography. UC Santa Barbara provides a broad support base for semiconductor material study and research, and a dense intellectual atmosphere stimulates me to pursue a further scientific career.

Here I would like to thank all the people who supported me. A special thank goes to my parents, who have always given me their encouragement and support for my interest no matter how impractical.

ABSTRACT

Group III-V Nanowire Growth and Characterization

by

Mingjin Wang

Electronic and optical devices typically use bulk or quantum wells today, but nanowires (NW) are promising building blocks for future devices, due to their structural characterizations of larger aspect ratio and smaller volume. *In situ* growth of semiconductor devices is extremely attractive, as it doesn't require expensive lithography treatment. Over the past ten years, a great deal of work has been done to explore NW, incorporation of group III-V materials and band engineering for the electronic and optoelectronic devices. Because pseudo one-dimensional (1D) heterostructures may be grown without involving lattice mismatch defects, NWs may give rise to superior electronic, photonic, and magnetic performances as compared to conventional bulk or planar structures.

TABLE OF CONTENTS

| | |
|--|-----|
| I. Introduction | 1 |
| II. Thermodynamics (Statistical Mechanics) and Kinetics of Nanowire Growth | 4 |
| A. Free Energy | 4 |
| B. Phase Transformation | 21 |
| C. Kinetic Models..... | 36 |
| D. Diffusion..... | 47 |
| E. Nucleation..... | 53 |
| F. Summary..... | 56 |
| III. Growth Technology of Nanowire..... | 58 |
| A. Top-Down Lithography | 58 |
| B. Vapor-Liquid-Solid (VLS)..... | 65 |
| C. The Catalysts in Nanowire..... | 76 |
| D. Nanowire Induced by Foreign Catalysts..... | 87 |
| E. Self-Catalyst Group III-V Nanowire..... | 103 |
| F. Template-Assisted & Selected-Area Nanowire Growth..... | 114 |
| G. Summary..... | 119 |
| IV. Controllable Physical, Chemical, Electronic, and Photonic Properties of Nanowire..... | 120 |
| A. Physical and Chemical Processes | 121 |
| B. Surface Structure, Morphology, Crystallography, and Strain Effect of Nanowire | 148 |

| | |
|---|-----|
| C. Defects, Dopants, and Bandgap Engineering of Nanowire..... | 183 |
| D. Summary..... | 213 |
| V. Conclusion and Outlook..... | 215 |
| References..... | 227 |

LIST OF FIGURES

| | |
|---|-----|
| Figure 1. The NW model with driving forces..... | 36 |
| Figure 2. The dependence of transition energy on the transition distance..... | 124 |
| Figure 3. The NW model with capillary forces | 145 |
| Figure 4. The crystallographic directions of (a) WZ; (b) ZB | 149 |
| Figure 5. The crystal structures of (a) WZ(2H);(b) ZB(3C);(c) 4H;(d) 6H..... | 151 |
| Figure 6. The crystallographic directions of NW | 153 |
| Figure 7. The side view of $\{110\}$ surfaces..... | 156 |
| Figure 8. The side view of (a) and (b) $\{001\}$ surfaces; (c) and (d) $\{113\}$ surfaces..... | 160 |
| Figure 9. The side view of $\{111\}$ surfaces..... | 164 |
| Figure 10. The side view of $\{112\}$ surfaces | 166 |
| Figure 11. The side view of $\{10\bar{1}0\}$ surfaces..... | 167 |
| Figure 12. The side view of $\{1\bar{1}20\}$ surfaces..... | 168 |
| Figure 13. The top view of (100)B-c(2×8) surfaces..... | 171 |
| Figure 14. The top view of (001)A-(2×4) with mixed dimers..... | 173 |
| Figure 15. The top view of (100)A -c(8×2) surfaces..... | 174 |
| Figure 16. The top view of (100)B-c(4×4) surfaces | 175 |
| Figure 17. The top view of (111)A-(2×2) surfaces..... | 178 |
| Figure 18. The top view of (111)B- $\sqrt{19}\times\sqrt{19}$ R23.4° surfaces | 179 |
| Figure 19. The cross-sections of NW (a) ZB $\{1\bar{1}0\}$; (b)ZB $\{1\bar{1}2\}$; (c)WZ $\{1\bar{1}00\}$; (d)WZ $\{1\bar{1}20\}$ | 182 |
| Figure 20. Principles of operation of an n-type TFET..... | 217 |

| | |
|---|-----|
| Figure 21. Illustration of a simplified axial NW laser..... | 219 |
| Figure 22. Illustration of a simplified radial NW laser..... | 220 |
| Figure 23. Illustration of a general qubit as a Bloch sphere..... | 222 |
| Figure 24. Schematic structure of a radial NW solar cell..... | 225 |

I. Introduction

In 1959, R. P. Feynman gave a notable talk entitled “There’s plenty of room at the bottom” at Caltech [1]. In the talk, he introduced a new field about manipulating and controlling things on the atomic scale. He imagined that humans can rearrange the atoms to realize miniaturization in the future. Inspired by this bold and brash revolutionary idea, nanotechnology’s contribution to human beings can stand shoulder to shoulder with the household Feynman Lectures on Physics and quantum electrodynamics from the perspectives of present and future.

Modern semiconductor devices and condensed matter physics have advanced since the important theoretical considerations were proposed by H. Kroemer [2,3], and the double heterostructure laser was formulated independently by H. Kroemer [4], and Zh. I. Alferov with R. F. Kazarinov [5]. Since then, the development of micro- and optoelectronics towards miniaturization to the nanoscale has been proved by Moore’s law. Over the past decades, the scalability of semiconductor devices has been reduced to the nanometer range. For further meeting the industrial demands, the trend of novel structure towards lower dimension has to be provided. During the last half century, incalculable techniques have been applied for the realization of miniaturization. Only those technologies that can be integrated and scaled up for large hierarchical systems will survive and have impact [6].

In 1969, superlattice in monocrystalline semiconductors was initiated with a proposal for 1D periodic variation of dopants or of alloy composition by L. Esaki and R. Tsu [7,8]. The advantages of heterostructure originate essentially from modification of the density of states produced by the confinement of charge carriers. Thus this has been widely used to

improve the electrical, optical, and magnetic properties of semiconductor devices. However, the quality of heterostructure is deteriorated by the presence of lattice mismatched defects.

The first NW, called whisker, can be traced back to 1964. Whiskers are grown with Au-assisted in Vapor-Liquid-Solid (VLS) mechanism by R. S. Wagner et al. [9]. Till now, an enormous amount of work has been carried out to explore and analyze NW in experiments and simulations. One of its most attractive properties is accommodating huge lattice mismatch between different materials, allowing very flexible design for bandgap engineering. In 1995, W. E. Buhro et al. developed Solution-Liquid-Solid (SLS) growth mechanism analogous to VLS growth [10]. The unique properties of SLS originate from transformation in a cocktail of surface ligands, which systematic control of NW growth, surface passivation, solubility, and large scale production. Likewise, some similar routes involving different growth mechanisms are used to improve the deposition process. The controlling of atomically sharp interface makes human being realize rearranging atoms today. In 2002, the synthesis of radial and axial heterostructure NWs was explored by C. M. Lieber et al. [11,12]. The formation of low defect density heterostructure with huge lattice mismatch materials promises a better building block for semiconductor devices. With the semiconductor industry developing, the size of future frontier can be reduced to the magnitude of the carrier coherence length.

Heterostructure NW combines with the semiconductor spintronics [13-16] will be a promising mean to develop quantum bits in quantum computing. The optoelectronic transitions dependence on size will be beneficial to low dimensional optoelectronics devices.

In summary, the research on NW is a relative young and growing field. However, the applicability of past theories has not been always guaranteed. Fortunately, some mechanics, theories and techniques of NW can still inherit from the existings in planar and bulk

structures. There is still a tremendous amount of work to do for a better understanding and a complete control of NW.

II. Thermodynamics (Statistical Mechanics) and Kinetics of Nanowire

Growth

The technology of NW growth depends on the thermodynamics and kinetics, with controlled phase transformation from evaporated material or solution to a crystalline solid and reaction proceeded to equilibrium by reaction paths at the corresponding kinetic rates. In statistical thermodynamics, the phenomena are explained as the resulting from the mechanics of all the atoms present in NW model. Equations of state can be derived directly from the statistical mechanics to describe of phase equilibrium. First principles calculations, quantum and non-quantum mechanical Monte Carlo, and molecular-dynamics atomistic calculations can be used to compute thermodynamic properties. Thermodynamics and kinetics are compatible and interrelated in the processes of NW growth.

II. A. Free Energy

The theoretical prediction of NW structures based on first-principles total energy calculation is very useful for exploring, analyzing and exploiting the properties of NW. For the local equilibrium structure, where the system exchanges materials and entropy with its environment, the free energy of system is the key to understand the phase transformation. As a NW grows, with a composition determined by the incorporation fluxes, the top and surface of NW will adjust its composition by exchanging atoms with the new layer to minimize the total free energy. The thermodynamic properties undergoing the transition are determined by the equations of state.

Consider the growth system at constant temperature and constant pressure, and assume the natural variables of the characteristic potential are entropy and volume without being controlled experimentally. The Legendre transforms generate the Gibbs free energy,

$$\begin{aligned} G^\alpha(P, T, N_a) &= H^\alpha(P, T, N_a) - TS^\alpha(P, T, N_a) \\ &= U^\alpha(P, T, N_a) - TS^\alpha(P, T, N_a) + PV^\alpha(P, T, N_a) \end{aligned} \quad (1)$$

where H^α is the enthalpy of phase α , T is the absolute temperature, S^α is the entropy, U is the characteristic potential (the internal energy), P is the pressure, V^α is the volume, and N_a is the number of moles of a single component a .

In the case of group III-V alloy growth, compositions of materials should be taken into consideration. The Gibbs free energy of the component A_xB_{1-x} is given by the sum of each composition,

$$G_m = x_A G_A^0 + x_B G_B^0 = x G_A^0 + (1-x) G_B^0 \quad (2)$$

where G_m is the molar free energy of the component AB , and G^0 is the molar free energy for pure element. For α phase, the molar Gibbs free energy is derived [17],

$$G_m^\alpha(P, T, x^\alpha) = \frac{G^\alpha(P, T, N_A^\alpha, N_B^\alpha)}{N_A^\alpha + N_B^\alpha} \quad (3)$$

And the chemical potentials of A and B components in the phase α can therefore be written as,

$$\mu_A^\alpha(P, T, x^\alpha) = \left[\frac{\partial G^\alpha(P, T, N_A^\alpha, N_B^\alpha)}{\partial N_A^\alpha} \right]_{N_B^\alpha} = G_m^\alpha(P, T, x^\alpha) - x^\alpha \frac{\partial G_m^\alpha(P, T, x^\alpha)}{\partial x^\alpha} \quad (4)$$

$$\mu_B^\alpha(P, T, x^\alpha) = \left[\frac{\partial G^\alpha(P, T, N_A^\alpha, N_B^\alpha)}{\partial N_B^\alpha} \right]_{N_A^\alpha} = G_m^\alpha(P, T, x^\alpha) - (1-x^\alpha) \frac{\partial G_m^\alpha(P, T, x^\alpha)}{\partial x^\alpha} \quad (5)$$

where x is the atomic fraction.

In the theoretical NW growth mechanism, at least two phases with two and more components are mentioned. Thus, the total Gibbs free energy becomes the equilibrium condition, which is the sum of all Gibbs free energy of different phases. In the situation of two phases, the equilibrium compositions x_0 of phase α and β can be derived in below functions from the molar Gibbs free energy for two phases, and fraction of the system can be obtained based on the lever rule.

$$\left[\frac{\partial G_m^\alpha(P, T, x^\alpha)}{\partial x^\alpha} \right]_{x_0^\alpha} = \frac{G_m^\beta(P, T, x_0^\beta) - G_m^\alpha(P, T, x_0^\alpha)}{x_0^\beta - x_0^\alpha} \quad (6)$$

$$\left[\frac{\partial G_m^\beta(P, T, x^\beta)}{\partial x^\beta} \right]_{x_0^\beta} = \frac{G_m^\beta(P, T, x_0^\beta) - G_m^\alpha(P, T, x_0^\alpha)}{x_0^\beta - x_0^\alpha} \quad (7)$$

The impact of different composition influences on the Gibbs free energy of various phases, which can be analyzed based on first-principles density-functional calculations. Some concrete semi-empirical models are summarized [17-19] to deduce the chemical potentials of different components in various situations. The real situation may be much more complicated than the models, because more detailed quantities should be taken into consideration.

In group III-V NW growth, the cluster variation method (CVM) built by statistical mechanics may be used to introduce the macroscopic systems, such as enthalpies and entropies, from the microscopical constituents [20-23]. The statistical mechanical models are used to describe and evaluate thermodynamics [23-26]. The CVM provides an approximate technique for the treatment of cooperative phenomena in the periodic systems and the numerical minimization of free energy. The CVM can provide a relatively precise value for free energy, but the minimization of many variable functions is required near stoichiometric phases. The Monte Carlo (MC) simulation agrees within the description of an

exact numerical procedure for solving lattice problems. The first-principles calculations mapped onto the Ising model are used in connection with either the CVM or the MC to treat the statistical mechanics.

The initial Ising model which is a model of a magnet has been widely used in the CVM and MC simulations to compute thermodynamic properties of alloys and lattice properties [27-32]. The analysis on the group III-V semiconductors or transition metal-group III-V semiconductor phase transitions depends on their phase diagrams, which is computed by mapping the alloy problems onto the lattice models. The detailed phase boundaries and reactions between them can be determined through the frequent free energy evaluations of the lattice Hamiltonian. In the group III-V NW model, gas beam, catalyst droplet, substrate, and NW act as traditional 3D phases, meanwhile, the interfaces of gas-catalyst, droplet-NW, and NW facets-gas are treated as the 2D phases. The significance of these 2D phases has played up due to high aspect ratio in NW. For the magnetic materials or magnetically doped semiconductors [33], the Ising model gives expression to the collective contribution of dipole moments of atomic spins where the Hamiltonian \mathcal{H} is proportional to the spin s_i [29],

$$\mathcal{H} \approx -J \sum_{\langle ij \rangle} s_i s_j - B \sum_i s_i \quad (8)$$

and the general form for the partition function which contains all of the essential information in the system,

$$Z = \sum_{\{s_i\}} e^{-\frac{\mathcal{H}}{k_B T}} \quad (9)$$

where J is the interactions of nearest neighbours and B is external magnetic field. In the extended Ising model, the truncated Hamiltonian \mathcal{H} consists of the nearest neighbor spin interactions through coupling constants [30],

$$\mathcal{H} \approx \sum_{\alpha} J_{\alpha} \prod_{\alpha \supset i, j, \dots l} \sigma_i \quad (10)$$

where J_{α} is the effective interaction for cluster α . The actual interactions and clusters depend on the lattice type. The ground state energy for cluster α can be obtained by the generalized Ising Hamiltonian,

$$\varepsilon = \sum_{\alpha} J_{\alpha} \langle \sigma_{\alpha} \rangle \quad (11)$$

In the self-consistent mean field (Bragg-Williams) equations, the energy is expressed in terms of the concentrations, which instead of the magnetisation [34],

$$\varepsilon = \sum_{\alpha} J_{\alpha} \langle \sigma_{\alpha} \rangle = \sum_{\alpha} J_{\alpha} \tanh \left[\ln \left(\frac{c_{\alpha}}{1-c_{\alpha}} \right) \right] \quad (12)$$

and

$$\bar{G}(c) = 2 \sum_{n, m \subset \alpha} J_{nm} c_n c_m + k_B T \sum_{n \subset \alpha} \left[c_n \ln c_n + (1-c_n) \ln (1-c_n) \right] \quad (13)$$

A similar compressible Ising model can be applied to group III-V semiconductors. For compound AB, one can assume $S=+1$ for A atom, $S=-1$ for B atom, and $S=0$ for vacancy. The corresponding Hamiltonian \mathcal{H} can be written as [31],

$$\begin{aligned} \mathcal{H} &= \mathcal{H}_{ext} + \mathcal{H}_{chem} + \mathcal{H}_{bond} + \mathcal{H}_{angle} \\ &= -\mu_A \sum_i \delta_{S_{i+1}} - \mu_B \sum_i \delta_{S_{i-1}} + \sum_{i-j} \varepsilon_{(S_i, S_j)} + \sum_{i-j} e_{(S_i, S_j)} \left[r_{ij}^2 - R_{(S_i, S_j)}^2 \right]^2 + \sum_{i-j-k} A_{(S_i, S_j, S_k)} \left[r_{ij} r_{kj} + R_{(S_i, S_j)} R_{(S_k, S_j)} / 3 \right]^2 \end{aligned} \quad (14)$$

where the subscript ext stands for the affection of nuclei, $\varepsilon_{(S_i, S_j)}$ is the chemical binding energies of nearest neighbor covalent bonds, $R_{(S_i, S_j)}$ is the nearest neighbor bond lengths $\sim 3a^2/16$, $e_{(S_i, S_j)}$ bond stiffness for nearest bonds, and $A_{(S_i, S_j)}$ is the angular stiffness for nearest neighbor bonds. The free energy of the system in the periodic boundary $\Lambda_{x,y,z}$ can be obtained with statistics,

$$F = -k_B T \ln \left\{ \sum_{\{S_i\}} \int d\Lambda_x \int d\Lambda_y \int d\Lambda_z \int d^3 r_1 \dots \int d^3 r_N \exp \left(-\mathcal{H} / k_B T \right) \right\} \quad (15)$$

In the CVM simulations, a number of 2D and 3D Ising lattices with pairs and many-body interactions are applied in the model. The simulation attempts to reflect the correct topology in crystal. The approximate expressions for the number of configurations Ω ($F = E - k_B T \ln \Omega$) having definite distribution of a set of cluster variables and the numerical minimization of free energy are calculated via the Ising lattices with points, pairs, and multibody interactions. In the simplified approximation for counting ensemble configurations, only the number of clusters per unit cell should be taken into considerations [35,36]. The number of configuration is given by [23],

$$\Omega = \frac{\prod_{-N(r,t)/N > 0} \left\{ \prod_i [N! x_i(r,t)]^{\alpha_i(r,t)} \right\}}{\prod_{-N(r,t)/N < 0} \left\{ \prod_i [N! x_i(r,t)]^{\alpha_i(r,t)} \right\}} \quad (16)$$

where N is the total number of lattice points and $x_i(r,t)$ is the concentration of the (r,t) cluster in the i configuration, $N(r,t)$ is the total number of (r,t) clusters in the system, and α_i is the geometrical constants. In principal, one can choose arbitrarily large clusters. The larger a cluster of N sites, the more important the intracluster interactions are relative to that of intercluster interactions. However, there is a tradeoff between the accuracy of simulation and the time consuming, because the computational cost increases with the size of cluster exponentially. Different cluster approximate expressions for FCC, BCC, and HCP were investigated in [23,37-40].

In the simplest 1D linear lattice for point approximation, point itself is the cluster. For the ensemble composed of A atoms (i.e. group-III) with fraction x_1 and B atoms (i.e. group-V) with fraction $x_2 (=1-x_1)$, the number of distinguishable configuration is

$$\Omega_{1D-point} = \frac{N!}{\prod_i (x_i N)!} \quad (17)$$

For pair approximation, in which pair is the cluster, the configurations will transform into A-A pair with fraction y_1 , A-B pair with fraction y_2 ($=x_1-y_1$), B-A pair with fraction y_2 , and B-B pair with fraction y_3 ($=x_2-y_2$). The number of distinguishable configuration with pair cluster can be written,

$$\Omega_{1D-pair} = \frac{\prod_i (x_i N)!}{\prod_i [(y_i N)!]^{\beta_i}} \quad (18)$$

where β_i are the degeneracies for configurations A-A ($\beta_i=1$), A-B/B-A ($\beta_i=2$), and B-B ($\beta_i=1$). For triangular lattice with triangle cluster, the ensemble of triangles composed of A_3 with fraction z_1 , A_2B with fraction z_2 ($=y_1-z_1$), AB_2 with fraction z_3 ($=y_2-z_2$), and B_3 with fraction z_4 ($=y_3-z_3$). So the number of configuration with triangle cluster is given,

$$\Omega_{triangle} = \frac{\left\{ \prod_i [(y_i N)!]^{\beta_i} \right\}^3}{\prod_i (x_i N)! \left\{ \prod_i [(z_i N)!]^{\gamma_i} \right\}^2} \quad (19)$$

where γ_i are the degeneracies for configurations A_3 ($\gamma_i=1$), A_2B ($\gamma_i=3$), AB_2 ($\gamma_i=3$), and B_3 ($\gamma_i=1$). For the common ZB lattice in group III-V semiconductors, consists of cation FCC sublattice and allocated anion one. For the triangular cluster, the configuration is different with that in triangular lattice,

$$\Omega_{triangle}^{ZB} = \frac{\left\{ \prod_i (x_i N)! \right\}^2 \left\{ \prod_i [(y_i N)!]^{\beta_i} \right\}^3}{(N!)^2 \left\{ \prod_i [(z_i N)!]^{\gamma_i} \right\}^3} \quad (20)$$

For the tetrahedral cluster in ZB lattice, the ensemble of tetrahedra composed of A_4 with fraction w_1 , A_3B with fraction w_2 ($=z_1-w_1$), A_2B_2 with fraction w_3 ($=z_2-w_2$), AB_3 with

fraction $w_4 (=z_3-w_3)$, and B_4 with fraction $w_5 (=z_4-w_4)$. So the number of configuration with tetrahedra cluster can be derived,

$$\Omega_{tetrahedra}^{ZB} = \frac{\left\{ \prod_i (x_i N)! \right\}^3}{(N!)^2 \prod_i [(w_i N)!]^{\delta_i}} \quad (21)$$

where δ_i are the degeneracies for configurations A_4 ($\delta_i=1$), A_3B ($\delta_i=4$), A_2B_2 ($\delta_i=6$), AB_3 ($\delta_i=4$), and B_4 ($\delta_i=1$). Likewise in the ZB structure, the WZ structure can also be represented as a set of tetrahedrons with cations (anions) in their corners, half of such tetrahedrons have anions (cations) in their centers, and the others of the tetrahedrons are empty.

The general configuration entropy in the CVM can be written by,

$$S = k_B \ln \Omega = Nk_B \sum_{(r,t)} \frac{-N(r,t)}{N} \sum_i g_i(r,t) x_i(r,t) \ln x_i(r,t) \quad (22)$$

or

$$S = Nk_B \sum_{(r,t)} \left[\frac{-N(r,t)}{N} + \sum_{r \leq r' \leq r_{\max}} M(r,r') \frac{N(r',t)}{N} \right] \sum_i g_i(r,t) x_i(r,t) \ln x_i(r,t) \quad (23)$$

where g_i is the general degeneracy constants, indicating the number of configurations of type i generated by the symmetry operations of clusters. If r stands for the largest cluster, the entropy is the first equation. If r clusters is contained in r' cluster, the entropy is written as the bottom one. An intuitively ideal tetrahedron configurational entropy in terms of five constituents can be written as [41],

$$\begin{aligned} S_{tetra} = & -2k_B \sum_i w_i \ln w_i - 2k_B (w_2 \ln 4 + w_3 \ln 6 + w_4 \ln 4) \\ & + 6k_B \left[\left(w_1 + \frac{w_2}{2} + \frac{w_3}{6} \right) \ln \left(w_1 + \frac{w_2}{2} + \frac{w_3}{6} \right) + 2 \left(\frac{w_2}{4} + \frac{w_3}{3} + \frac{w_4}{4} \right) \ln \left(\frac{w_2}{4} + \frac{w_3}{3} + \frac{w_4}{4} \right) + \left(\frac{w_3}{6} + \frac{w_4}{2} + w_5 \right) \ln \left(\frac{w_3}{6} + \frac{w_4}{2} + w_5 \right) \right] \\ & - 5k_B \left[\left(w_1 + \frac{3w_2}{4} + \frac{w_3}{2} + \frac{w_4}{4} \right) \ln \left(w_1 + \frac{3w_2}{4} + \frac{w_3}{2} + \frac{w_4}{4} \right) + \left(\frac{w_2}{4} + \frac{w_3}{2} + \frac{3w_4}{4} + w_5 \right) \ln \left(\frac{w_2}{4} + \frac{w_3}{2} + \frac{3w_4}{4} + w_5 \right) \right] \end{aligned} \quad (24)$$

From the above statistical explanation of entropy, the CVM method expresses the exact variational principle of the equilibrium statistical mechanics. Under the CVM calculations, the Gibbs free energy can be expressed as the polynomial expansions in the regular solution model [40],

$$G(x, T) = x_1 G_1(T) + x_2 G_2(T) + RT(x_1 \ln x_1 + x_2 \ln x_2) + \sum_{i=0}^n x_1 x_2 P_i(x_1 - x_2) A_i(T) \quad (25)$$

In the MC simulations, a smaller number of representative configurations are selected. The equilibrium is based upon the partition function containing all of the essential information about the system. Thermodynamic quantities and characteristics of an ensemble can be calculated from their partition functions. The MC simulations provide a direct evaluation of the ensemble average. The ensemble is a set of the same macroscopic systems being in all possible states under the given conditions. When the temperature is held fixed, the most common canonical ensemble is a set of the closed macroscopic systems which have thermal contact with their surroundings. In this situation for semiconductor alloys, the changes of the volume and the numbers of particles are prohibited, and the alloys are treated as a closed system for a given temperature. The general partition function of the canonical ensemble (fixed composition) is,

$$Z(T, V, N_i) = \sum_j g_j(V, N_i) \exp(-U_i/k_B T) \quad (26)$$

where g_j is the degeneracy factor, which equals to the number of states. Then the configurational partition function for binary AB compound can be written as,

$$Z = \sum_{N_{ab}} g(N_a, N_b, N_{ab}) \exp\left(-\frac{\Omega_{ab} N_{ab}}{k_B T}\right) = \frac{\exp\left[\left(\sum_i^n \mu_a^i\right) - E_j\right]}{\sum_j^{2^n} \exp\left[\left(\sum_i^n \mu_a^i\right) - E_j\right]} \quad (27)$$

where Ω is the interaction parameter, and the term in bracket is the relative energy. In the MC simulation, the density matrix with a specific possible configuration α is written

$$\rho_\alpha = Z^{-1} \exp(-E_\alpha/k_B T) = Z^{-1} \exp[-U(r^N)/k_B T] \quad (28)$$

The corresponding partition function Z for system in the canonical ensemble is,

$$Z_{\text{canonical-ensemble}} = \sum_{\alpha} e^{-E_\alpha/k_B T} = \int e^{-U(r^N)/k_B T} d\mathbf{r}^N \quad (29)$$

where the pseudopotential approximation was described in the pseudopotential code Siesta simulation [42], k_B is Boltzmann's constant, E_α is the energy of state α , and \mathbf{r}^N is N -dimensional configuration vectors. The canonical ensemble is very appropriate to describe the alloys for the regular solution model. The free energy of the crystalline solid associated with the canonical ensemble is represented,

$$F = U - TS = -k_B T \ln Z = -k_B T \ln \left\{ Z_{\text{int-A}}^{N_A} Z_{\text{int-B}}^{N_B} \left[\exp\left(-\frac{u_{AA}}{k_B T}\right) \right]^{N_{AA}} \left[\exp\left(-\frac{u_{AB}}{k_B T}\right) \right]^{N_{AB}} \left[\exp\left(-\frac{u_{BB}}{k_B T}\right) \right]^{N_{BB}} \right\} \quad (30)$$

where the subscript int stands for the contributions of the internal degrees of freedom. In group III-V semiconductor system, the more realistical Gibbs free energy (G) and the Helmholtz free energy (F) are similar because of the contribution of volume term being negligible. The free energy of the entire system is expressed in terms of the distribution variables. The free energy is minimized with respect to the variational parameters (the upper bounds for free energy).

The overall canonical-ensemble partition function is the sum over the several degrees of freedom of the system, including the electronic, vibrational and configurational contributions [43-48],

$$Z_{\text{canon}} = \sum_{\sigma} \exp\left(\frac{-E_{\text{configuration}}(\sigma) - E_{\text{relaxation}}(\sigma)}{k_B T}\right) \times \sum_{\text{vibration}-\sigma_v} \exp\left(\frac{-E_{\text{vibration}}(\sigma)}{k_B T}\right) \times \sum_{\text{electronic}-\sigma_e} \exp\left(\frac{-E_{\text{electronic}}(\sigma)}{k_B T}\right) \quad (31)$$

where the configuration variables σ are appropriate for the Ising model. The corresponding density function or matrix can be written by,

$$\rho(\sigma) = \frac{\exp\left[\frac{-E_{\text{configuration}}(\sigma) - E_{\text{relaxation}}(\sigma) - E_{\text{vibration}}(\sigma) - E_{\text{electronic}}(\sigma)}{k_B T}\right]}{Z_{\text{canon}}} \quad (32)$$

and the expectation value of the total energy,

$$U = \langle E \rangle = \sum_{\{\sigma\}} \rho(\sigma) [E_{\text{configuration}}(\sigma) + E_{\text{relaxation}}(\sigma) + E_{\text{vibration}}(\sigma) + E_{\text{electronic}}(\sigma)] \quad (33)$$

One can extend the canonical ensemble to the isobaric-isothermal or the variation of the number of atoms situations. The ensemble is a set of the closed macroscopic systems having mechanical and thermal contacts with the surroundings. In the open systems of group III-V materials growth (MBE or MOCVD), the systems have fixed volume, but can freely exchange energy and matters with their environment. When the number of particles is allowed to fluctuate, the relevant thermodynamic potential can be written by the work function $U - TS - \sum \mu_i N_i = -k_B T \ln \Xi$. The ensemble is changed to the grand-canonical ensemble, where T , V , μ_i are the independent variables and are represented as a set of open macroscopic systems, with fixed walls permeable for heat and particles. The partition function for the general grand-canonical ensemble,

$$\Xi(T, V, \mu_i) = \sum_{j, i, N_i} g_{j, i, N_i}(V) \exp\left(-\frac{U_j - \mu_i N_i}{k_B T}\right) \quad (34)$$

In the MC simulations, the corresponding partition functions (isothermal-isobaric ensemble and grand-canonical ensemble) are obtained separately,

$$Z_{\text{iso}} = \int \exp(-P_e V / k_B T) \int \exp[-U(r^N) / k_B T] dr^N dV \quad (35)$$

and

$$Z_{grand} = \sum_{N=0}^{\infty} e^{(\mu N/k_B T)} \int \frac{V^N}{N! \left(h / \sqrt{2\pi m k_B T} \right)^{3N}} e^{-U(r^N)/k_B T} d\mathbf{r}^N \quad (36)$$

where P_e is the external pressure, h is the Planck constant, and m is atom mass. The corresponding grand potential for species i in configuration $\{\sigma\}$ is [28],

$$\Phi_{grand} = -\frac{k_B T}{N} \ln \left\{ \sum_{\{\sigma\}} \exp \left[-\frac{E(\sigma) + \mu N_i(\sigma)}{k_B T} \right] \right\} \quad (37)$$

The free energy depends on the number of component bonds and the bond energies between adjacent atoms. Thus the degrees of ordering or clustering have an influence on the free energy. Using the MC simulation in the CVM approximation [49,50], the grand potential can be written in terms of probabilities,

$$\Phi_{grand} = \omega_{co} N \sum_{ij} E_{ij} p_{ij} - \sum k_B T \left[(2\omega_{co} - 1) \sum_i (x_i \ln x_i - x_i) - \omega_{co} \sum_{ij} (p_{ij} \ln p_{ij} - p_{ij}) + (\omega_{co} - 1) \right] - \sum_i N \mu_i x_i \quad (38)$$

where ω_{co} is one half the coordination number, N is the total number of lattice points, and p_{ij} is the probability of configuration with energy E_{ij} .

For microcanonical ensemble the partition function $Z(U, V, N_i)$ equals to the degeneracy factor $g(U, V, N_i)$, where the degeneracy factor is the number of arrangements of atoms over the lattice sites. And then the entropy is just the configurational entropy. The entropy dependence on the microcanonical partition function for N_d -dimensional integrals over the components of coordinates and momenta of the particles,

$$S = k_B \ln Z_{micro-canon} = \frac{1}{h^{dN} N!} \int \int \Theta [E - \mathcal{H}(x_i, p_i, V)] dx dp \quad (39)$$

where Θ is the Heaviside's step function.

Algorithms enable the automated calculation of thermodynamic quantities in the MC simulations. The MC schemes rely on the Markov processes [29]. Define a set of N variables via an array which can take the values ± 1 . The simulation processes start with all spins up (Fully ordered as the initial state for convenient. In semiconductors, assume A atoms with $s_i=+1$ for spin up, and $s_i=-1$ for B atoms). \rightarrow Ensure all spins have the same number of neighbours and local geometry. \rightarrow Select the temperature to perform the simulation (The easiest initial temperature is zero, and the Ising model stays at its ground state) and choose a spin s_i at random (Random points in that region are chosen via a random number generator) at a slightly altered position ($r \rightarrow r'$) and flip this spin. \rightarrow Compute the energy change $\Delta \mathcal{H}$

$$\Delta \mathcal{H} = E_\nu - E_\mu = -J \sum_{\langle ij \rangle} s_i^\nu s_j^\nu + J \sum_{\langle ij \rangle} s_i^\mu s_j^\mu \quad (40)$$

(where the energy difference origins from the new ν state to the old μ state) resulting from the configurational change, $\exp(-\Delta \mathcal{H}/T)$ (If $\exp(-\Delta \mathcal{H}/T)/[1 + \exp(-\Delta \mathcal{H}/T)] > r$, where $r \in [0,1]$ is a random number, then accept the new state and the transition is performed, otherwise, keep the old state for the averaging). In a MC simulation with Ising model, the average spin having all possible configurations has the form,

$$\langle M \rangle = \frac{Tr \sum_i s_i \exp(-\mathcal{H}/T)}{Tr \exp(-\mathcal{H}/T)} \quad (41)$$

where s_i is the spin of the corresponding state, and the trace over all states of systems is an integral over phase space or a cumulant in classical systems,

$$Tr \equiv \frac{1}{N!} \prod_\alpha \int \frac{dp dx}{h^{dN}} \quad \text{or} \quad Tr \equiv \sum_{\sigma_1} \dots \sum_{\sigma_N} \quad (42)$$

The integrated function is the fraction of the points that fall below the curve multiplied by the area of the sample region. → Advance MC time from t to $t+\Delta t$. Run the simulation for a long period of time until the system has come to equilibrium at the temperature. In the grand-canonical ensemble, the transition $\alpha \rightarrow \alpha'$ is taken to be the flip $s_i \rightarrow -s_i$ of a randomly chosen spin. In the canonical ensemble, a nearest neighbor AB pair is chosen at random and interchanged. The probability can be obtained by iterating the initial probability $p(0)$ [29],

$$p(t) = p^t p(0) = p^t \sum_i a_i v_i = \sum_i a_i \lambda_i^t v_i \quad (43)$$

where λ_i is the eigenvalue of the Markov matrix p corresponding to the eigenvector v_i , and the quantities a_i are coefficients. When the system at equilibrium, the probability of a configuration α is

$$p_{eq}(\alpha) = \frac{\exp[-\mathcal{H}(\alpha)/k_B T]}{\sum_{\alpha} \exp[-\mathcal{H}(\alpha)/k_B T]} \quad (44)$$

where the Hamiltonian consists of the chemical potential term and the multibody interaction terms [51],

$$\mathcal{H} = -\frac{1}{2}(\mu_A - \mu_B) \sum_i s_i + \mathcal{H}_{multi-interactions} \quad (45)$$

For the metropolis algorithm of the Ising model, the MC simulation processes work by repeatedly choosing a new state and then accepting or rejecting it at random with an acceptance probability. The simulations start from the configuration i having energy E_i at random. Likewise the process above, a trial is made to change the spin (If $s_i=1$ then change it to -1 and vice versa, find new energy E_{i+1}). Find a new configuration $i+1$ having a new energy E_{i+1} . The judgement of whether to add the new configuration to the trajectory is based upon the ratio of the probabilities $\rho_{i+1}/\rho_i = \exp[(E_{i+1}-E_i)/k_B T]$ (If the ratio is larger than a random number $\in (0,1)$, the new state is accepted; if the ratio is smaller than the ratio, the

new state is rejected, and the site i has the old spin and energy E_i . And then accumulate averages). For the Ising model phase diagram in the MC simulations, the equilibrium concentrations are obtained by sweeping through the chemical potential $\mu_A - \mu_B$ at fixed temperature. Sweeping starts from pure A phase and decreases the chemical difference down to the pure B phase.

For the simulations of the high temperature phase boundaries in a semi-grand-canonical ensemble, the thermodynamic potential is given by [52],

$$\phi = -\frac{k_B T}{N} \ln \left\{ \sum_{\{\sigma\}} \exp \left[-\frac{E(\sigma) + \mu x(\sigma)}{k_B T} \right] \right\} = F - \mu x \quad (46)$$

When the initial state is defined as the low temperature state, the dependence of the potential on the ground energy is written [52],

$$\phi = \varepsilon_{\text{ground}}(x_{\text{ground}}) - \mu x_{\text{ground}} - \frac{k_B T}{N} \sum_i \exp \left(-\frac{\Delta \varepsilon_{i,\text{ground}} - \mu \Delta \eta_{i,\text{ground}}}{k_B T} \right) \quad (47)$$

where $\varepsilon_{\text{ground}}$ is the ground state energy with the composition x_{ground} , $\Delta \varepsilon_{i,\text{ground}}$ is the variation in the total energy associated with changing the identity of the atom sitting at site i in ground state, and $\Delta \eta_{i,\text{ground}}$ is the variation in (Nx) associated with the same change. For potential variation for the disordered phase at high temperature,

$$\frac{\phi(T_1, \mu_1)}{k_B T_1} = \frac{\phi(T_0, \mu_0)}{k_B T_0} + \int_{T_0, \mu_0}^{T_1, \mu_1} \left(E - \mu x, -\frac{x}{k_B T} \right) d(T, \mu) \quad (48)$$

For the high temperature expansion, the potential is written in terms of high order terms,

$$\phi(T, \mu) = -N k_B T \ln 2 - \frac{1}{2^N k_B T} \sum_{\sigma} [E(\sigma) - \mu x(\sigma)]^2 + o \left[\left(\frac{E(\sigma) - \mu x(\sigma)}{k_B T} \right)^3 \right] \quad (49)$$

where the cluster expansion is

$$E(\sigma) = \sum_{\langle i,j \rangle} V \sigma_i \sigma_j \quad (50)$$

The entire phase boundary of (α - β first order transition) can be determined by the equilibrium of the derivations of the potentials,

$$\left. \frac{\partial(\phi_\alpha/k_B T)}{\partial(1/k_B T)} \right|_\mu d\left(\frac{1}{k_B T}\right) + \left. \frac{\partial(\phi_\alpha/k_B T)}{\partial\mu} \right|_{1/k_B T} d\mu = \left. \frac{\partial(\phi_\beta/k_B T)}{\partial(1/k_B T)} \right|_\mu d\left(\frac{1}{k_B T}\right) + \left. \frac{\partial(\phi_\beta/k_B T)}{\partial\mu} \right|_{1/k_B T} d\mu \quad (51)$$

The equilibrium can be simplified as

$$\frac{d\mu}{d(1/k_B T)} = \frac{E_\beta - E_\alpha}{(x_\beta - x_\alpha)/k_B T} - \frac{\mu}{1/k_B T} \quad (52)$$

Run the algorithm for both phases at the chemical potential μ . The above equation with energies and compositions for each phase is integrated. In simulation, the perturbation caused by noise is

$$\frac{d\Delta\mu}{d(1/k_B T)} = -\Delta\mu \frac{d \ln(x_\beta - x_\alpha)}{d(1/k_B T)} \quad (53)$$

The calculated Gibbs free energy can be recognized as the sum of the thermodynamic potential and the corresponding chemical potential,

$$G(T, x) = \phi(T, \mu) + \mu(T, x) x \quad (54)$$

The spinodal decomposition is commonly in semiconductor growth, nucleation, and annealing, which involves cluster, order-disorder, and phase separation. The assumption of free energy or chemical potential depends only on local concentration, which is valid as long as concentration gradient is not too large. Ignore the attractive interactions between atoms, and the simplified statistical sum can be obtained

$$Z = \left[1 + \exp\left(\frac{\mu + xV}{k_B T}\right) \right]^N \quad (55)$$

where the sublattice concentration $x = k_B T (\partial \ln Z / \partial \mu) / N$, and V is the corresponding volume. Differentiation of the above equation with respect to x can derive to the maximum and minimum concentrations, which are the boundaries of spinodal decomposition region. Inside the spinodal region, the higher order derivation of free energy should be taken into consideration due to the large gradient in concentration with uphill diffusion. For the uphill diffusion, the amplitude of fluctuation induced by small density oscillations will further increase with time. The detailed equilibrium of multicomponent system can be derived in Cahn & Hilliard method [53-55]. To solve the local equilibrium incorrect, the total free energy is written with higher order derivation with respect to coordinate,

$$G = \int_V g \left(x(r), \frac{\partial x}{\partial r_{\lambda_1}}, \frac{\partial^2 x}{\partial r_{\lambda_1} \partial r_{\lambda_2}}, \dots \right) \frac{dr}{V_\Omega} \quad (56)$$

where $g(x)$ stands for the molar free energy, the subscript λ_i indicates coordinate and there are six independent in three-dimension, and V_Ω is volume. If the crystal has inversion symmetry, apply the Taylor expansion. Then

$$\begin{aligned} G &= \int_V \left\{ g(x) + \frac{1}{2} \sum_{\lambda_1} \sum_{\lambda_2} m_{\lambda_1, \lambda_2}(x) \frac{\partial x}{\partial r_{\lambda_1}} \frac{\partial x}{\partial r_{\lambda_2}} + \frac{1}{2} \sum_{\lambda_1} \sum_{\lambda_2} n_{\lambda_1, \lambda_2}(x) \frac{\partial^2 x}{\partial \lambda_1 \partial \lambda_2} \right\} \frac{dr}{V_\Omega} \\ &= \int_V \left\{ g(x) + \frac{1}{2} \sum_{\lambda_1} \sum_{\lambda_2} \kappa_{\lambda_1, \lambda_2}(x) \frac{\partial x}{\partial r_{\lambda_1}} \frac{\partial x}{\partial r_{\lambda_2}} \right\} \frac{dr}{V_\Omega} \end{aligned} \quad (57)$$

where the gradient energy coefficient κ is written

$$\kappa_{\lambda_1, \lambda_2}(x) = m_{\lambda_1, \lambda_2}(x) - n_{\lambda_1, \lambda_2}(x) \quad (58)$$

The equilibrium chemical potential μ_{equ} can be obtained through variational minimize G . So the equilibrium chemical potential can be obtained from order parameter (η difference of sublattice concentrations) gradients arise and the additional energy associated with gradient

energy term. The chemical potential can be written as sum of the interstitial diffusion and extra energy term,

$$\mu_{equ} = \frac{\partial g(x)}{\partial x} - 2\kappa_{\lambda_i}(x) \frac{\partial^2 x}{\partial^2 r} \quad (59)$$

In the Ising model, the variable η can represent the coarse grained field of spins or magnetization. Based on the known experiments, the free energy and pressure can be written in terms of the Taylor expansion in η . The Ising model theory of Landau raised the order parameter into a conventional form [31,51],

$$\eta = \tanh\left(\frac{B}{2} + \frac{\eta}{T_r}\right) \quad (60)$$

where B is the external magnetic field, and $T_r = T/T_c$. T_c is the critical point derived from the van der Waals equation based on the mean field theory.

II. B. Phase Transformation

The materials in the systems of NW growth try to reach their equilibrium state, which is equivalent to a minimization of the energy of system in a closed system or a minimization of one of free energies. In the irreversible transformation of an open system, entropy increases with the Gibbs free energy. The relationship between the change of the irreversible entropy and the variation of the Gibbs free energy can be written [17]

$$dS_{irr}^{sys} = (dS_{irr}^{sys} + dS_{rev}^{sys}) - (dS_{rev}^{sys}) = (dS^{sys}) - \left(\frac{dU^{sys} - PdV^{sys}}{T} \right) = -\frac{dG^{sys}}{T} \quad (61)$$

where the subscript *irr* indicates irreversible part and *rev* means reversible part of the entropy change. Therefore, the equilibrium transformation occurs when dG^{sys} is approximately zero. Thus this induces that the change of irreversible entropy is also

approximately zero and entropy is conserved. In the case of group III-V NW growth, the equilibrium is described by minimizing the Gibbs free energy under given pressure, temperature and composition.

Traditional thermodynamics gives a clear definition of entropy, but the physical nature of entropy should be gained from statistical thermodynamics discussed in the previous section. The entropy of system can be derived from the variation principle [56],

$$S = -k_B \sum_{\{\sigma\}} \rho(\sigma) \ln \rho(\sigma) \quad (62)$$

The corresponding free energy can be derived from the first-principles calculations. The detailed probability distributions and graphical models in some common structures, such as FCC, BCC, wurtzite (WZ), zincblende (ZB), and binary lattices, have been summarized [17,20-26,57,58]. Considering the cluster interactions, the free energy becomes [44,23]

$$\begin{aligned} F = U - TS &= \sum_{i'} m_{i'} E_{i'} \xi_{i'} - k_B T \sum_{i=1} \alpha_i \sum_{\sigma_i} \rho(\sigma_i) \ln \rho(\sigma_i) \\ &= \sum_{i'} m_{i'} E_{i'} \langle \sigma_{p1} \sigma_{p2} \dots \sigma_{pn} \rangle - k_B T \sum_{i=1} \alpha_i \sum_{\sigma_i} \rho(\sigma_i) \ln \rho(\sigma_i) \end{aligned} \quad (63)$$

This cluster expansion provides a method of treating configurational disorder on lattices.

In group III-V NW growth system, ideal solid solution behavior might occur rarely in semiconductor NW alloys, but might in the metal segments, where the components do not interact chemically with each other and distribute randomly in the condensed phase. For the solid solution with more than one component, its free energy ($F=U-TS$) is determined by the internal energy and the configurational entropy that arises from the many different ways in which atoms are arranged over the lattice sites. In the Bragg-Williams model, its internal energy of the random binary solid solution equals to the binding energy,

$$U = \frac{Nz}{2} [x_A E_{AA} + x_B E_{BB} + x_A x_B (2E_{AB} - E_{AA} - E_{BB})] \quad (64)$$

where there are 2^N possible arrangements (configurations or microstates) of atom A and atom B on a fixed lattice of N points. For the random binary solid solution, its configurational entropy of the mixture system is given via the Stirling's approximation $N! \approx N^N e^{-N} \sqrt{2\pi N}$,

$$\begin{aligned} S_{conf} &= k_B \ln \frac{(N_A + N_B)!}{N_A! N_B!} \\ &= -k_B N_A \ln \frac{N_A}{N_A + N_B} - k_B N_B \ln \frac{N_B}{N_A + N_B} + k_B \ln \sqrt{2\pi(N_A + N_B)} - k_B \ln \sqrt{2\pi N_A} - k_B \ln \sqrt{2\pi N_B} \end{aligned} \quad (65)$$

For perfect group III-V semiconductors in NW system, the configurational entropy contribution vanishes in the ordered state. The energy of perfect crystal consists of the net binding energy at zero temperature, the vibrational energy (the motion of atoms), and the electronic energy (the thermal excitations of the electrons). Electronic entropy is evaluated in the independent electron approximation through the electron state occupation $f(\varepsilon, T)$,

$$S_{ele}(T) = -k_B \sum_k \left\{ f(\varepsilon, T) \ln f(\varepsilon, T) + [1 - f(\varepsilon, T)] \ln [1 - f(\varepsilon, T)] \right\} \quad (66)$$

The vibrational entropy is the integral of the vibrational density of states, $g(\omega)$,

$$S_{vib} = k_B \int g(\omega) \left[1 + \ln \left(\frac{k_B T}{\hbar \omega} \right) + \dots \right] d\omega \quad (67)$$

However, the actual semiconductors are not in perfect structures. The configurational entropy of the semiconductors with defects, such as vacancy, has to be taken into consideration. Likewise in the solid solution, the entropy of formation of vacancies is primarily determined by the configurational entropy. The disordered configurational entropy for a small number ($N_v \ll N$) of vacancies,

$$S_{conf} = k_B \ln \Omega = k_B \ln \left[\frac{N!}{(N - N_v)! N_v!} \right] \approx k_B \left[N \ln N - (N - N_v) \ln (N - N_v) - N_v \ln N_v \right] \quad (68)$$

Besides the configurational contributions, the lattice vibrations in substitutional alloys have also a significant influence on the entropy. The vibrational entropy is caused by the thermal oscillations of atoms. The vibrational entropy change can be attributed to the changes in bond stiffness associated with the changes in bond-length [43]. The effect of ordered alloy on its vibrational entropy has been attributed to the fact that bonds between different chemical species have a different stiffness than the bonds between identical species. The disordered state reduces the number of bonds between unlike atoms and thus has larger vibrational entropy. In NW system, the vibrational contributions play a more important role due to the enhanced degeneracies caused by a high aspect ratio.

At low temperature, chemical species segregate apart or ordered compounds are formed due to the existence of finite interactions between atom A and B [56]. In the ordered state, all bonds are A-B bond, and then the configurational entropy contribution is negligible. So the free energy becomes $F \approx U = 4NE_{AB}$. At high temperature, ordered or phase-separated species transform into a homogeneous disordered structure, and then the configurational entropy dominates. For the disordered state, the internal energy becomes $U = 2NE_{AB} + N(E_{AA} + E_{BB})$, the configurational entropy increases to $S_{\text{conf}} = Nk_B \ln 2$, and the temperature dependence of vibrational entropy becomes large. So the free energy becomes $F \approx 2NE_{AB} + N(E_{AA} + E_{BB}) - Nk_B T \ln 2 - TS_{\text{vib}}$. Most group III-V semiconductor alloys exhibit spontaneous long-range order in the epitaxy growth [59,60], while short-range order is present in liquid phases.

For the liquid alloys with random distribution of atoms (liquid mixtures in a catalyst or liquid semiconductors), their entropies are the sum of the entropies of the constituents and configurational entropy,

$$S = \sum_i x_i S_i + S_{conf} = x_A S_A + x_B S_B + S_{conf} = x_A S_A + x_B S_B + R[x_A \ln x_A + x_B \ln x_B] \quad (69)$$

The phase diagrams of binary, ternary, and quaternary group III-V systems were calculated from the thermodynamic data using the quasi-equilibrium approach [61-64]. There are three kinds of bonds connecting the nearest neighbouring atoms. The interaction parameter Ω_{AB} is written [65]

$$\Omega_{AB} = N_{nearest} [E_{AB} - (E_{AA} + E_{BB})/2] \quad (70)$$

where E_{ij} represents the interaction energy of the nearest neighbor pair, and $N_{nearest}$ is the number of the nearest neighbors. The detailed Ω_{AB} and $N_{nearest}$ depend on the materials. The bond energy between two unlike atoms may be either more negative than the bond energy between equal atoms (for compound formation or ordering) or more positive (for a miscibility gap). For the first nearest neighbors, the negative resultant of Eq.70 indicates that the phase is stable. For the second nearest neighbors, the right hand side of the equation equals zero, and thus indicates the ordered phase is composed of two simple cubic sublattices (B_2). When the right hand side is negative, new ordered phase DO_3 are formed, in which the lattice is decomposed into four FCC sublattices.

The general chemical potential μ of component a , and the general Gibbs free energy (for gas, liquid or solid) in a binary compound $a-b$ system consisting of two constituent species a and b can be written

$$\mu_a = G_a^0 - S_a (T - T_0) + RT \ln v_a x_a + (P - P_0) V_{molar} \quad (71)$$

$$G^{OV} = \sum_{i=1}^n x_i \left[G_i - \sum_j h_{ij} H_j^{SER} + RT \ln(x_i) \right] + RT \ln \left(\frac{P}{P_0} \right) \quad (72)$$

$$\begin{aligned} G^{0L} &= x_a G_a + x_b G_b + \Delta G_{mix} + G_{ex} \\ &= x_a G_a + x_b G_b + \Omega_{ab} x_a x_b + RT(x_a \ln x_a + x_b \ln x_b) - T \Delta S_{non-conf} \end{aligned} \quad (73)$$

$$\begin{aligned}
G^{0S} &= x_a G_a + x_b G_b + \Delta G_{mix} + G_{ex} \\
&= x_a G_a + x_b G_b + RT(x_a \ln x_a + x_b \ln x_b) - T\Delta S_{non-conf} + x_a x_b \sum L_{ab}^i (x_a - x_b)^i \quad (74) \\
&\approx \sum_{i=1}^n x_i G_i + RT \sum_{i=1}^n x_i \ln(x_i) + \sum_i \sum_{j>i} x_i x_j \frac{z[E_{ij} - (E_{ii} + E_{jj})/2]}{2}
\end{aligned}$$

where v_i are the activity coefficients for different atoms and P_0 is the standard pressure ($\sim 10^5$ Pa). The superscripts V, L, and S represent vapor, liquid, and solid phase separately. The mixing free energy ΔG_{mix} is the excess free energy associated with the formation of a solution (liquid or solid) from the pure elements. The excess mixing Gibbs free energy is affected by not only the purely configurational entropy but also the interaction term (the mixing enthalpy) as well as the non-configurational contributions,

$$\Delta G_{mix}^L = \Delta H_{mix} - T\Delta S_{mix}^{conf} - T\Delta S_{non-conf} \approx -T\Delta S_{mix}^{conf} + \Omega_{ab}^L x_a x_b - T\Delta S_{non-conf} \quad (75)$$

where the entropy of mixing is the increase in the total entropy when several initially separate systems of different composition each in a thermodynamic state of internal equilibrium are mixed without chemical reactions. According to the discussion in the section of calculations of entropy, the random configurational entropy of the system is given via the Stirling's approximation,

$$\Delta G_{mix}^L \approx -T\Delta S_{mix}^{conf} + \Omega_{ab}^L x_a x_b - T\Delta S_{non-conf} \approx -RT \left\{ x_a \ln[\gamma_a(x) x_a] + x_b \ln[\gamma_b(x) x_b] \right\} + \Omega_{ab}^L x_a x_b - T\Delta S_{non-conf} \quad (76)$$

where $\gamma_i(x)$ is the composition dependent activity coefficient, which is nearly unity for liquid and solid phase. For an ideal solution, the configuration entropy is zero. The solution enthalpy is the sum of all products of pairs by their binding energies. The non-configurational entropy term consists of the vibrational and electronic contributions. In the liquid of binary system, the excess mixing Gibbs free energy can be obtained in terms of the composition terms,

$$\Delta G_{mix}^L = RT \left[(1-x^L) \ln(1-x^L) + x^L \ln x^L \right] + \Delta G_b^L x^L (1-x^L) \quad (77)$$

Likewise, the excess mixing Gibbs free energy in the solid binary system can be written by,

$$\Delta G_{mix}^S = RT \left\{ (1-x^S) \ln(1-x^S) + x^S \ln x^S + (1-x^S) L_1 \left[(T/T_1) - 1 \right] + x^S L_2 \left[(T/T_2) - 1 \right] \right\} + \Delta G_b^S x^L (1-x^L) \quad (78)$$

where L_i are the free energies of fusion apportioned between the two components. ΔG_b has a relationship with the lattice mismatch, and increases with the enhancement of the lattice mismatch. Thus it implies there is miscibility gap as the lattice mismatch is large [66]. For a ternary system, the sum of binary excess Gibbs energies in extrapolation and the ternary excess Gibbs energy in assessment are calculated as the total excess Gibbs energy.

For a regular solution, the enthalpic term $x_a x_b \Omega_{ab}$ dominates, while the non-configurational entropy terms are negligible. The phase diagrams can be tuned through the progressive changes of the interaction coefficients of liquid or solid phases of semiconductor materials. The effects of strain and lattice mismatch also play an important role in group III-V NW,

$$\Delta G_{surf}^{L-S} = \frac{2}{R} \left[\left(\gamma_a^L V_a^{0L} - \gamma_a^S V_a^{0S} \right) x_a + \left(\gamma_b^L V_b^{0L} - \gamma_b^S V_b^{0S} \right) x_b \right] \quad (79)$$

where γ is the surface tension, and V_i^0 is molar volume for liquid and solid phases.

The excess molar Gibbs free energy caused by the lattice elastic energy dominantly. The binary excess Gibbs energy can be derived in the Redlich-Kister equation,

$$G_{ex} = x_a x_b \sum L_{ab}^S (x_a - x_b)^i \quad (80)$$

where L_{ab}^S is the binary excess Gibbs free energy parameter. In Eq.80, the non-regular terms are taken into account. There are many extensions for the excess Gibbs energy model. The interaction coefficient L_{ij} (\sim J/mol) in the above equation gives a single interaction parameter for the phase in the binary i-j system but it is not enough to describe the experiments. The

interaction parameter may be extended into the Redlich-Kister power series, which is reasonable as the excess enthalpy in a smooth function.

$$L_{ij} = \sum_{m=0}^k (x_i - x_j)^m L_{ij}^m = \sum_{m=0}^k (x_i - x_j)^m (H_{ij}^m + TS_{ij}^m) \quad (81)$$

The excess Gibbs energy for a high order system also behaves as a composition-dependent,

$$G_{ext} = G_{bin} + G_{tern} + G_{higher-order} = \sum_{i=1}^{n-1} \sum_{j=i+1}^n L_{ij} x_i x_j + \sum_{i=1}^{n-2} \sum_{j=i+1}^{n-1} \sum_{k=j+1}^n L_{ijk} x_i x_j x_k + \dots \quad (82)$$

The enthalpy of mixing will be obtained by summing of the bond energies of adjacent atoms.

$$H_{mix} = N_{tot} z x_a x_b \Omega_{ab} = N_{tot} N_{nearest} z x_a x_b [E_{ab} - (E_{aa} + E_{bb})/2] \quad (83)$$

where N_{tot} is the number of atoms in solution. The heat of formation of a binary compound can be applied directly to the substitutional alloys:

$$\Delta H_{mix} = \Delta H^{A_x B_{1-x} C} - x \Delta H^{AC} - (1-x) \Delta H^{BC} = \alpha^S x (1-x) \quad (84)$$

Hillert extended the ternary excess coefficient [67],

$$L_{ijk} = \frac{1}{3} \left[(2x_i - x_j - x_k + 1) L_{ijk}^i + (2x_j - x_i - x_k + 1) L_{ijk}^j + (2x_k - x_i - x_j + 1) L_{ijk}^k \right] \quad (85)$$

Considering the influences of the magnetic term, the general molar Gibbs free energy for phase ϕ (=FCC or HCP) can be obtained [68],

$$G_m^\phi = x_A^\phi G_A^\phi + x_B^\phi G_B^\phi + RT (x_A^\phi \ln x_A^\phi + x_B^\phi \ln x_B^\phi) + G_{ex-mix}^\phi + G_{mag-mix}^\phi \quad (86)$$

$$G_{ex-mix}^\phi = x_A^\phi x_B^\phi \sum_{i=0}^z L_{A,B}^\phi (x_A^\phi - x_B^\phi)^i = x_A^\phi x_B^\phi \sum_{i=0}^z (a^\phi + b^\phi T + c^\phi T \ln T) (x_A^\phi - x_B^\phi)^i \quad (87)$$

where a, b, and c are parameters to be determined during optimization.

$$G_{mag-mix}^\phi = RT \ln(M^\phi + 1) g(T/T_c^\phi) = RT \ln(M^\phi + 1) g \left\{ T / [T_{c-A}^\phi (1 - x_B) + T_{c-A,B-ex}^\phi x_B (1 - x_B)] \right\} \quad (88)$$

The excess Gibbs free energy of mixing can be written in the terms which are influenced by temperature [69,70],

$$\Delta G_{ex-mix} = \alpha(T, P)x(1-x) = H_m - \Delta S_{ex-mix}T = \left(\alpha - T \frac{\partial \alpha}{\partial T} \right) x(1-x) - \left[-\frac{\partial \alpha}{\partial T} x(1-x) \right] T \quad (89)$$

In vapor phase boundaries, $RT \ln \gamma_v = \alpha^v (1 - x_v)^2$, where the vapor α^v can be obtained from vapor pressure. The liquid α^L can be obtained from liquidus data. For the liquidus interaction, $\alpha = a - bT + cT^2$. For a group III-V binary solution, the temperature coefficient can be changed into

$$\alpha = a - bT = 2(\Delta H_f + \Delta H^F) - 2(\Delta S_f + \Delta S^F - R \ln 4)T \quad (90)$$

The Newton-Raphson method can be used for expressing the derivatives of the partial Gibbs energies [41],

$$-x^\alpha \left(\frac{\partial^2 G_m^\alpha}{\partial x^{\alpha 2}} \right) \frac{dx^\alpha}{dT} + x^\beta \left(\frac{\partial^2 G_m^\beta}{\partial x^{\beta 2}} \right) \frac{dx^\beta}{dT} = S_1^\alpha - S_1^\beta \quad (91)$$

$$(1 - x^\alpha) \left(\frac{\partial^2 G_m^\alpha}{\partial x^{\alpha 2}} \right) \frac{dx^\alpha}{dT} - (1 - x^\beta) \left(\frac{\partial^2 G_m^\beta}{\partial x^{\beta 2}} \right) \frac{dx^\beta}{dT} = S_2^\alpha - S_2^\beta \quad (92)$$

The relationship of x-T can be obtained by solving this set of equations,

$$\frac{dx^\alpha}{dT} = \frac{(S_1^\alpha - S_1^\beta)(1 - x^\beta) + (S_2^\alpha - S_2^\beta)x^\beta}{(x^\alpha - x^\beta)(\partial^2 G_m^\alpha / \partial x^{\alpha 2})} \quad (93)$$

In the treatment of binary and ternary phase boundaries, the group III-V systems are dominated by the presence of a near stoichiometric, congruently melting solid phase with a high melting point. Through the input parameters α , ΔS^F , and T^F based on the liquidus data, the activity coefficient γ can be obtained in a binary system based upon the Henry's law,

$$RT \ln \gamma_A = \alpha_{AB}^L x_B^2 \quad (94)$$

$$RT \ln \gamma_B = \alpha_{AB}^L x_A^2 \quad (95)$$

In a dilute range, all phases have the property that the activity of the corresponding constituent varies inversely with the constituent. The input data α , ΔS^F , and T^F yield the binary solution equation in the computer program,

$$\alpha_{AB}^L = -\frac{RT \ln[4x_A(1-x_A)] + \Delta S_{AB}^F(T_{AB}^F - T) - \Delta C_p[T_{AB}^F - T - T \ln(T_{AB}^F/T)]}{2(0.5 - x_A)^2} \quad (96)$$

The entropy of fusion can be expressed as a sum of the entropy of fusion of the solid phase, the entropy of dissociation that occurs when the semiconductor transforms to a metallic liquid, and the entropy of mixing of the liquid phase, as well as the entropy which increases between 0K and the melting point [70],

$$\Delta S = \Delta S_m^F + \Delta S_{dis}^F + R \ln 4 + \partial \Delta U / \partial T \quad (97)$$

For ternary liquid or solid systems, G_{ex} is the sum of all binary excess Gibbs free energies for all binary phases in the system. Simple solution can be extended to ternary systems in a similar expression,

$$RT \ln \gamma_A^L = \alpha_{AC}^L x_C^2 + \alpha_{AB}^L x_B^2 + (\alpha_{AC}^L + \alpha_{AB}^L - \alpha_{BC}^L) x_B x_C \quad (98)$$

To analyze the interface equilibrium of NW and its drop in VLS mechanism, the T-x phase diagram should be calculated in the solid-liquid equilibrium [71]

$$\ln \left[\frac{1}{4x(1-x)} \right] + \ln \left(\frac{\nu_A^{S,L} \nu_B^{S,L}}{\nu_{A(1-x)} \nu_{B(x)}} \right) \approx \frac{2\Delta S^F}{R} \left(\frac{T^F}{T} - 1 \right) \quad (99)$$

where ΔS^F is the entropy of fusion, T^F is the melt temperature, R is the gas constant, and ν_i are the activity coefficients of different atoms:

$$\nu_A = \left\{ \frac{[1 + 4x(1-x)(\exp(2\Omega_{AB}/N_{nearest}RT) - 1)]^{1/2} - 1 + 2x}{x[1 + 4x(1-x)(\exp(2\Omega_{AB}/N_{nearest}RT) - 1)]^{1/2} + 1} \right\}^{N_{nearest}/2} \quad (100)$$

$$v_B = \left\{ \frac{\left[1 + 4x(1-x)\left(\exp\left(2\Omega_{AB}/N_{nearest}RT\right) - 1\right)\right]^{1/2} + 1 - 2x}{(1-x)\left[\left[1 + 4x(1-x)\left(\exp\left(2\Omega_{AB}/N_{nearest}RT\right) - 1\right)\right]^{1/2} + 1\right]} \right\}^{N_{nearest}/2} \quad (101)$$

The calculation of phase diagram is carried out numerically through Eq.38,71,73,80 and 99, as well as the introduce of the interaction energies of different material structures. The equilibrium conditions for ternary and quaternary systems were described by G.B. Stringfellow [62-64]. Several numerical methods, such as Kohler model, Colinet model, Muggianu model, Hillert model, and Chou model, were summarized to simulate the Gibbs free energy of binary, ternary, and higher-order systems [72-75]. The detailed phase transformations in the NW growth processes can be analyzed in the phase diagram calculation software packages [76-82].

The liquidus and solidus curves can be calculated by the known fusion entropy and temperature. In binary AB compound, the equilibrium equation for the liquidus line on the T-x phase diagram is given by [61,62,69,70],

$$\frac{\gamma_A^{L-sto} \gamma_B^{L-sto}}{\gamma_A^L \gamma_B^L} = 4x^L (1-x^L) \exp \left[\frac{\Delta S^F (T^F - T)}{RT} \right] \quad (102)$$

This equation can be simplified into,

$$\frac{1}{\gamma_A x_A} = \exp \left[\frac{\Delta S_A^F (T_A^F - T)}{RT} \right] \quad (103)$$

In the binary system, the corresponding activity parameters γ_i can be written as

$$\gamma_A = \left[\frac{\Upsilon - 1 + 2x}{x(\Upsilon + 1)} \right]^{\frac{z}{2}} \quad (104)$$

$$\gamma_B = \left[\frac{\Upsilon + 1 - 2x}{(1-x)(\Upsilon + 1)} \right]^{\frac{z}{2}} \quad (105)$$

$$\Upsilon = \left\{ 1 - 4x(1-x) \left[\exp^2 \left(\frac{2E_{AB} - E_{AA} - E_{BB}}{2k_B T} \right) - 1 \right] \right\}^{\frac{1}{2}} \quad (106)$$

The binary liquidus for group III-V can be plotted as,

$$RT \ln(4x_A x_B) = -(\Delta H_{AB}^F - T \Delta S_{AB}^F) - 2\alpha_{AB}^L (0.5 - x_A)^2 \quad (107)$$

The equilibrium conditions for the solid solution $A_{1-x}B_xC$ can be treated as species A and C in the ternary liquid and compound AC in the solid [69],

$$\gamma_{AC}^S (1 - x^S) = \frac{4\gamma_A^L \gamma_C^L}{\gamma_B^{L-sto} \gamma_C^{L-sto}} x_A^L x_C^L \exp \left[\frac{\Delta S_{AC}^F (T_{AC}^F - T)}{RT} \right] \quad (108)$$

This T-x equilibrium equation provides the liquidus curve $x_A^L(T)$ in the binary AC system. Meanwhile, a similar separate equilibrium condition describes species B and C in the liquid and compound BC in the solid,

$$\gamma_{BC}^S x^S = \frac{4\gamma_B^L \gamma_C^L}{\gamma_B^{L-sto} \gamma_C^{L-sto}} x_B^L x_C^L \exp \left[\frac{\Delta S_{BC}^F (T_{BC}^F - T)}{RT} \right] \quad (109)$$

where γ is the activity coefficient of the compound, x is the mole fraction, the superscript sto stands for the stoichiometric liquid, and F stands for the fusion. The activity coefficients can be estimated through the interaction equation,

$$RT \ln \gamma_i = \sum_{j=1, i \neq j}^n J_{ij} x_j - \sum_{j=1}^n \sum_{k=j+1}^n J_{jk} x_j x_k \quad (110)$$

Through appropriate input parameters, the melting points T^F and entropies of fusion of the end compounds ΔS^F , approximate expressions for the activity coefficients γ based on fitting the binary data, and the interaction parameters J in regular solutions, which can be obtained

from the published thermodynamic data, the full liquidus-solidus phase diagram can be solved based upon the above three equations. The detailed activity coefficients in the regular solution model can be written [62],

$$RT \ln \gamma_A = N_B^2 J_{AB} + N_C^2 J_{AC} + N_B N_C (J_{AB} - J_{BC} + J_{AC}) \quad (111)$$

$$RT \ln \gamma_B = N_C^2 J_{BC} + N_A^2 J_{AB} + N_A N_C (J_{BC} - J_{AC} + J_{AB}) \quad (112)$$

$$RT \ln \gamma_C = N_A^2 J_{AC} + N_B^2 J_{BC} + N_A N_B (J_{AC} - J_{AB} + J_{BC}) \quad (113)$$

$$J_{\alpha\beta} = \frac{V_\alpha V_\beta}{N_\alpha V_\alpha + N_\beta V_\beta} \left[(c_{s-\alpha} - c_{s-\beta})^2 - \frac{C_J (\chi_\alpha - \chi_\beta)^2}{\sqrt{V_\alpha V_\beta}} \right] \quad (114)$$

where C_J is the constant, V is molar volume, χ is the electronegativity, and c_s is the solubility.

The binary excess parameter can also be used to estimate the solubility in semiconductor (such as, defect H in group III-V semiconductor materials) [83]

$$x_H = \frac{1}{K \gamma_H} \sum_i x_i \left(\ln \frac{\gamma_{III-V-H}}{\gamma_{H,i} \gamma_{III-V,i}} \right) = \frac{\gamma_{III-V-H}^L}{\gamma_H \gamma_{III-V-H}^S} \exp \left(\frac{\mu_{III-V-H}^S - \mu_{III-V-H}^L}{RT} \right) \sum_i x_i \left(\ln \frac{\gamma_{III-V-H}}{\gamma_{H,i} \gamma_{III-V,i}} \right) \quad (115)$$

where K is the equilibrium segregation constant, and γ_i is the composition dependent activity coefficient. The actual segregation constant can also be affected by the size of NW or the diffusion processes. When the defect concentration reaches the limit, the excess Gibbs free energy is under supersaturation.

To enable the growth of NW, some inequilibrium is intentionally created and thus drives the system to produce the desired structure. To induce a transition from a stable phase to another, the pressure and temperature will be controlled to actuate the free energy of the target phase to be smaller than that of initial phase. Thus, the chemical potential of vapor phase has to be larger than the chemical potential of liquid phase of catalysts or solid phase

of adatoms on the substrate, otherwise the evaporation can occur. The chemical potential of adatoms has to be larger than that of a catalyst otherwise the adatoms will induce the substrate growth. Particles from the initial phase cross the boundary toward the target one to allow the system to approach the equilibrium via supercooling or supersaturation. The difference of the chemical potential induces the driving force for phase transformation dependence on the supersaturation ζ [84],

$$\Delta\mu = k_B T \ln(\zeta + 1) = \mu_{III}^L + \mu_V^L - 2\mu_{III-V} \quad (116)$$

where μ_{III-V} is the half chemical potential of group III-V semiconductor crystal nucleation. The relationship between the chemical potential of species and their pure chemical potential is,

$$\mu_i^L = \mu_i^{L-pure} + RT \ln(a_i^L) \quad (117)$$

where a_i is the activity. So the driving force for group III-V NW phase transform can be derived [85-87],

$$\Delta\mu = RT \left(\ln a_{III}^L + \ln a_V^L \right) + \left(\mu_{III}^L - H_{III}^{S-pure} + \mu_V^{L-pure} - H_V^{S-pure} \right) - \left(2\mu_{III-V} - H_{III}^{S-pure} - H_V^{S-pure} \right) \quad (118)$$

The second and third terms in Eq.118 are the differences between the chemical potential and enthalpy for the pure III/V droplet and the NW crystal separately. The first term is concerned with interactions in the alloy, which is denoted by the atomic concentration c ,

$$RT \ln a_A^L = RT \ln c_A + c_A^2 \omega_{A,B} = RT \ln c_A + \frac{c_B^2 V_A^0 V_B^0}{c_A V_A^0 + c_B V_B^0} \left[\left(h_{Hs-A} - h_{Hs-B} \right)^2 - \frac{C'(\chi_A - \chi_B)}{\sqrt{V_A^0 V_B^0}} \right] \quad (119)$$

where V_i^0 is the molar volume in the liquid phase, χ is the Pauling electronegativity, C' is the constant ($\sim 1.256 \times 10^5$ for GaAs if all quantities are in SI units [85]), the energy coefficients ω is

$$\omega_{AB} = \frac{1}{N_A} \frac{V_A V_B}{c_A V_A + c_B V_B} \left[(h_{Hs-A} - h_{Hs-B})^2 - \frac{C'(\chi_A - \chi_B)^2}{\sqrt{V_A V_B}} \right] \quad (120)$$

and the Hildebrand solubility parameter h_{Hs} is

$$h_{Hs} = \sqrt{(\Delta Q - RT)/V} \quad (121)$$

where ΔQ is the molar heat (in unit~kJ/mol).

The driving force can be expanded into a Taylor series at equilibrium temperature or pressure. So the expanding function can be derived [88]

$$\Delta\mu(\Delta T = T - T_e) \approx \frac{1}{N} \left[-\frac{\Delta H_{latent}}{T_e} \Delta T - \frac{\Delta C_p}{2T_e} (\Delta T)^2 \right] \quad (122)$$

or

$$\Delta\mu(\Delta P = P - P_e) \approx \frac{1}{N} \left[\Delta V_e \Delta P - \frac{V_{e\beta} \kappa_{e\beta} - V_{e\alpha} \kappa_{e\alpha}}{2} (\Delta P)^2 \right] \approx \left(\frac{RT}{P_a + P_b} \right) \left[P_a \ln \left(\frac{P_a}{P_{ea}} \right) + P_b \ln \left(\frac{P_b}{P_{eb}} \right) \right] \quad (123)$$

where subscript e indicates equilibrium, ΔH_{latent} is the latent heat exchanged during phase transition, ΔC_p is the difference of specific heat, κ is the compressibility, P_a and P_b are the partial pressures of a and b atoms, respectively.

For the equilibrium systems which contain defects (ions, or electrons) in group III-V semiconductors, the electrochemical potential equilibrium needs to be satisfied to reach the phase equilibrium,

$$\overline{\mu}_i^\alpha = \mu_i^\alpha + ze\varphi^\alpha = \overline{\mu}_i^\beta = \mu_i^\beta + ze\varphi^\beta \quad (124)$$

where φ is the internal potential of the phase, and ze is the valence charges of species i.

II. C. Kinetic Models

The driving force has the sense of describing the phase transformation, not the transformation rates which depend on the kinetics of materials. We introduce kinetics to describe out of equilibrium of systems and lead to predict the morphology of NWs. The variation of supersaturation, which is determined by the deposition process, has an influence on the phase formation, the nucleation energy barrier, the critical nucleus radius, and some other characteristics [89]. So the NW formation depends on the growth kinetics. Kinetics exhibits dependence of the growth rate on the kinetic factors, chemical reaction, the balance between adsorption and desorption, diffusion processes, and nucleation.

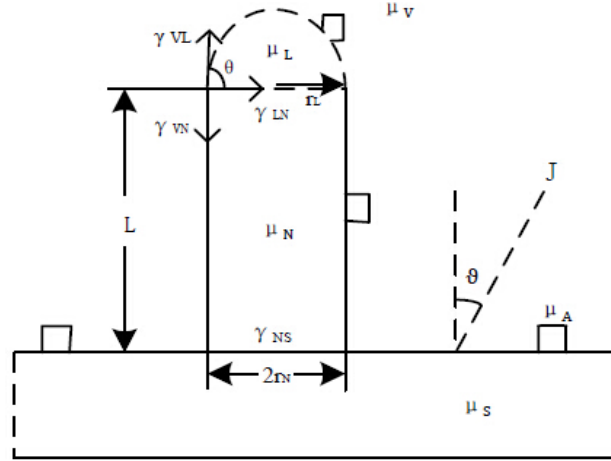


Figure 1. The NW model with interface energies and chemical potentials.

In the case of NW growth, a catalyst is widely used to dictate the morphology of NW, such as composition, and geometry. Fig. 1 shows the NW model with different parts of interfacial boundaries that can be described by macroscopic chemical potentials and the interface energies: μ indicates the chemical potential of vapor (V), liquid (L), NW (N),

adatom (A), and substrate (S), and γ_i stands for the interfacial free energy. The surface energy depends on the dangling bonds of different chemical composition, and the crystallographic orientation of the corresponding planes. The interface equilibrium characterized by the existence of surface energy, is extremely important in the early stages of phase transformation of growth, separating the particle and the matrix. Relatively high catalyst surface energy is required for the stability of NW growth. The spherical surface equilibrium dependence on the thermodynamic quantities can be described by the Young-Laplace equation,

$$\Delta P = 2\gamma/r \quad (125)$$

where ΔP is the internal pressure relative to the environment pressure. For a spherical cap on NW, ΔP transforms into $2\gamma\sin\theta/r$. The equilibrium pressure difference is inversely proportional to the radius, thus the internal pressure will be large in the case of low-dimensional NW. The small particle in NW will be not stable due to a tremendous increase of pressure, and the corresponding elevation of its chemical potential. For no matter a relative internal pressure influence or the effects of surface tension and coarsening driven by capillarity, the limitations of these phenomena will be beneficial to the synthesis of nanostructures.

The free energies of surfaces or interfaces are more important in group III-V NW, due to a larger aspect ratio in system. The interface free energy γ depends on the surface tension [90] because of the presence of separating two heterogeneous and coexisting phases at equilibrium. The particle free energy relative to the substrate pressure equals to the relative pressure on the molar volume, so the interface free energy γ can be written,

$$\gamma = \frac{\Delta G_r r}{2V_{molar}} = \frac{\left(-N\Delta\mu + \sum_i S_i \gamma_i\right) r}{2V_{molar}} = \frac{\left(-Nk_B T \ln(P_V / P_{partial-saturated}) + \sum_i S_i \gamma_i\right) r}{2V_{molar}} \quad (126)$$

where r is the radius of interface. The relative free energy can be written in the format of chemical potential difference. In Fig. 1, the dependence of growth of NW on the equilibrium of interfacial free energies and surface tension forces can be described by

$$\gamma_{VN} = \gamma_{LN} + \gamma_{VL} \cos \theta \quad (127)$$

The contact angle will therefore be given by

$$\cos \theta = \frac{\gamma_{VN} - \gamma_{LN}}{\gamma_{VL}} \quad (128)$$

When $(\gamma_{VL} + \gamma_{LN})/\gamma_{VN}$ is greater than unity, a catalyst cannot wet the NW because the drop is unstable, otherwise the catalyst will wet the NW as the Young's equation cannot be satisfied.

When a catalyst wets the substrate, the Volmer-Weber islands are energetically preferred to thin film growth. A smaller contact angle means a lower nucleation barrier. When three phase junction reaches the equilibrium at the junction-line in Fig. 1, the tension equilibrium can be written,

$$\sigma_{VL} + \sigma_{LN} + \sigma_{VN} = 0 \quad (129)$$

In a group III-V NW system, the liquid sorption current is sum of sorption from the triple line and the droplet surface [91],

$$\begin{aligned} I_{sorp} &= \int \Delta\Gamma_{AL,i} dl + \int \Delta\Gamma_{VL,i} dS \\ &= l_{tr} J_{AL} \left[\rho_i - \rho_i^{ERS} \frac{x_i}{x_i^{ERS}} \exp\left(\frac{\Delta\mu_{L-ERS,i}}{k_B T}\right) \right] + A_{VL} \left[J_V - \frac{x_i}{x_i^{ERS}} \frac{P_i^{ERS}}{\sqrt{2\pi m_i k_B T}} \exp\left(\frac{\Delta\mu_{L-ERS,i}}{k_B T}\right) \right] + A_{VL} J_{Incident} \end{aligned} \quad (130)$$

where l_{tri} is the triple line length, S is surface area of droplet, and J_{AL} is the single atom transition flux. The ERS chemical potential of group III/V equals to the liquid chemical potential when liquid and solid are in equilibrium,

$$\mu_{\text{III}}^{\text{ERS}} = \mu_{\text{III}}^{L-\infty} = \mu_{\text{III}}^{S-\infty} + \mu_{\text{V}}^{S-\infty} - \mu_{\text{V}}^{L-\infty} \quad (131)$$

The dissolution of semiconductor atoms from vapor sources into a liquid catalyst is very fast and the liquid surface always maintains equilibrium with the vapor phase. In NW systems, the atoms in a droplet are so rapid that the liquid has a uniform composition. In general, the droplet is regarded as a pseudo-binary alloy with the metal being the solvent, while semiconductor as the solute materials. The fraction concentrations of different species in droplet and NW are given by [92],

$$c_{\text{III}}^L = \frac{n_{\text{III}}^L}{n_{\text{III}0}^L} = (1 - I_{\text{vapor}}) + I_{\text{vapor}} \exp\left(-\frac{v\pi r_N^2 t}{n_{\text{III}0}^L \Omega}\right) \quad (132)$$

$$c_{\text{V}}^L = \frac{n_{\text{V}}^L}{n_{\text{V}0}^L} = (1 - c_{\text{III}}^L) + I_{\text{vapor}} \left[1 - \exp\left(-\frac{v\pi r_N^2 t}{n_{\text{III}0}^L \Omega}\right) \right] \quad (133)$$

where $n_{\text{III}0} = \beta_L \pi r_L^3 n_L / 3$, n_L is the concentration of semiconductor in liquid and β_L is size factor of droplet~2-4. In a liquid droplet, the percentage of group-III atoms in the droplet is of several tens of percent, while no significant amount of group-V atoms is ever detected in the droplet, especially for As and P elements. And the fraction concentrations in solid phase are,

$$c_{\text{III}}^S = (1 - I_{\text{vapor}}) + I_{\text{vapor}} \exp\left(-\frac{3vtr_N^2}{\beta_L n_L r_L^3}\right) \quad (134)$$

$$c_{\text{V}}^S = I_{\text{vapor}} \left[1 - \exp\left(-\frac{3vtr_N^2}{\beta_L n_L r_L^3}\right) \right] \quad (135)$$

The NW formation is strongly affected by the Gibbs-Thomson effect. The driving force caused by a difference of chemical potential leads to out of equilibrium in the NW growth processes. The difference in chemical potential between the vapor and the substrate can be written,

$$\Delta\mu_{VS} = \mu_V - \mu_S = k_B T \ln(v_{dep}/v_{dep}^{eq}) \quad (136)$$

where v_{dep} is the deposition rate, and v_{dep}^{eq} is the equilibrium deposition rate at which the deposition equalizes the desorption from the substrate [93]. The difference in chemical potential between the adatoms and the substrate can be written as

$$\Delta\mu_{AS} = \mu_A^\infty - \mu_S = \Delta\mu_{VS} - 2k_B T \ln(\lambda_0/\lambda) \approx k_B T \ln(n/n_{eq}) \quad (137)$$

where λ is the effective diffusion length when the growth occurs, λ_0 is the diffusion length of adatom at the equilibrium, n is the concentration of adatoms, and n_{eq} is the equilibrium concentration on the substrate and depends on the mean lifetime of atoms. At the high vapor saturation, $\Delta\mu_{AS}$ is lower than $\Delta\mu_{VS}$, because the effective diffusion is limited by the surface nucleation. Otherwise, $\Delta\mu_{AS}$ matches $\Delta\mu_{VS}$, because of the surface growth rate reducing to zero.

The chemical potential in the drop is modified by the Gibbs-Thomson effect, which gives the dependence of the surface curvature of the droplet on its chemical potential. Therefore,

$$\mu_L = \mu_L^\infty + 2V_L\gamma_{VL}/r_L \quad (138)$$

Consider the diffusion growth occurs only at $\mu_A^\infty > \mu_L$. So the diffusion-induced growth has to satisfy the condition

$$\Delta\mu_{LS}^\infty = \mu_L^\infty - \mu_S < \Delta\mu_{VS} - 2k_B T \ln(\lambda/\lambda_0) - 2V_L\gamma_{VL}/r_L \quad (139)$$

The equilibrium conditions between the vapor phase and the condensed state (liquid or solid) in NW system can be reached,

$$\mu_i^L = \mu_i^{V,0} + RT \ln \frac{P_i}{P_i^0} \quad (140)$$

and

$$\mu_{i'}^{NW} = \mu_{i'}^{V,0} + RT \ln \frac{P_{i'}}{P_{i'}^0} \quad (141)$$

The driving force in the droplet with respect to the stoichiometric ZB solid is given by [86,94]

$$\Delta\mu = \mu_{III}^L + \mu_V^L - \mu_{III-V}^S = \mu_{III}^L + \frac{k_B T}{4} \ln \left[\frac{v_V}{v_V^0} - \frac{1 + \cos \theta}{2v_V^0} \frac{dL}{dt} \right] - \mu_{III-V}^S \quad (142)$$

where $v_V = J_V \Omega$ and $v_V^0 = \Omega' P_V / \sqrt{(2\pi m k_B T)}$. The first term on the right side should be controlled primarily by the surface temperature T and the group-III atom concentration due to a low solubility of group-V atoms in the common catalytic metals. The driving force associated with the stoichiometric WZ structure can be realized when

$$\Delta\mu > \max \{ \Delta\mu_{triple-point}, \Delta\mu_{center} \} \quad (143)$$

where the driving forces on the triple-line and the center are written separately,

$$\Delta\mu_{triple-point} = \frac{G_{WZ-ZB}}{1 - \left[\frac{x(\gamma_{N-WZ} - \gamma_{LV} \sin \theta) + (1-x)\gamma_{SL}}{x(\gamma_{N-ZB} - \gamma_{LV} \sin \theta) + (1-x)\gamma_{SL}} \right]^2} \quad (144)$$

$$\Delta\mu_{center} = \frac{G_{WZ-ZB}}{1 - \left[\frac{x(\gamma_{N-WZ} - \gamma_{LV} \sin \theta) + (1-x)\gamma_{SL}}{\gamma_{SL}} \right]^2} \quad (145)$$

According to the calculations, $\Delta\mu_{\text{center}}$ is very large at a high group-III concentration, so pure ZB can exhibit with a high group-III concentration. The exhibition of $\Delta\mu_{\text{center}} < \Delta\mu_{\text{triple-point}}$ occurs at a low group-III concentration.

The axial grow rate of NW depends on the lateral size of droplet, and there is proof of the existence of a certain minimum diameter of drop under which the whiskers would not grow [95]. The minimum radius of the catalyst and its dependence on the degree of supersaturation is given by [96]

$$r_{\min} = \frac{2\gamma_{VL}V_{\text{molar}}}{RT \ln \gamma_{VL}} \quad (146)$$

However, some experimentally mismatch exhibits the dependence of diameter independent [97] or an opposite result [98] on the growth rate, due to the different growth mechanics. Meanwhile, it demonstrates the growth of NW is a non-monotonic dependence of the growth rate on the lateral size. Analyzing the thermodynamics equilibrium enables one to determine the morphology of NW during growth. The total free energy is the sum of one bulk part and another surface part

$$G = G_{\text{bulk}} + G_{\text{surf}} = \pi r_N^2 L \mu_N + \pi r_L^3 f(\theta) \mu_L + V_{\text{adatom}} \mu_A + \pi r_N^2 \gamma_{NS} + 2\pi r_N L \gamma_{VN} \\ + \pi r_L^2 g(\theta) \gamma_{VL} + \pi r_L^2 h(\theta) \gamma_{LN} \quad (147)$$

where $f(\theta)$, $g(\theta)$, and $h(\theta)$ are the functions of contact angle θ . When $h(\theta)$ is unity, the drop covers all the top of NW. If $h(\theta)$ is smaller than unity, the uncovered area has the interfacial free energy of $\gamma_{VN\text{-top}}$. Another situation is a NW incorporating a droplet, and the incorporating length l will affect the catalyst volume, the contact interface between catalyst and NW side-wall, and the catalyst surface. Taking the differential of contact angle θ , the surface energy will decrease for the wetting case and increase otherwise. Just considering the first ideal situation with the same periphery for catalyst bottom and NW top, the

equilibrium will be reached when the free energy is minimized. The NW systematic equilibrium with vapor phase for the interface of vapor and catalyst,

$$G = -\Delta P \pi r_L^3 f(\theta) \mu_L + \pi r_L^2 g(\theta) \gamma_{VL} \quad (148)$$

Taking the differential of both sides, the environment pressure can be obtained in the expression of the equilibrium pressure P_e for two phases separated by the interface,

$$P_{environ} = P_e \exp\left(\frac{V_{molar} \gamma_{VL} dS_{VL}}{k_B T dV_L}\right) \quad (149)$$

where $S_{VL} = \pi r_L^2 g(\theta)$, and $V_L = \pi r_L^3 f(\theta)$. In the NW system, the transformation pressure increases with the decrease in the size of the wire.

There are no continuous kinetics pathways for the decomposition processes, because the supersaturated solid is a metastable state. There is an incubation period occurring before the quasi-steady state nucleation. Then a nucleation process depends on the number of the critical nuclei and the rate with atoms attached to the critical nucleus. A nucleation mechanism derived by S. A. Kukushkin et al. [99] is applied, the nucleation rate I caused by condensation from vapor, and the growth rate v caused by the nucleation from the supersaturation can be obtained in the following two equations,

$$I = \frac{\pi n^2 r_c l_{diff} v_{des}}{4} \sqrt{\frac{(\gamma_{LN}/k_B T)^2 \pi V_0/h_0}{2\pi}} \exp\left(-\frac{E_d}{k_B T} - \frac{(\gamma_{LN}/k_B T)^2 \pi V_0/h}{\ln(1+\zeta) - r_0/r_L}\right) \quad (150)$$

where $\zeta = n/n_{eq} - 1$ is the supersaturation of alloy, n_{eq} is the equilibrium concentration in the eutectic alloy and depends on the mean lifetime of atoms, r_c is the linear boundary radius of a critical nucleus, $r_0 = 2\Omega_{sy} V_N/k_B T$ is the characteristic size, l_{diff} is the length of diffusion jumping of adatoms, v_{des} is the frequency of desorption, V_0 is the particle volume, h_0 is the height of monolayer, and E_d is the activation energy. The growth rate can be derived from

the combination of the Fick's second law, the random variable related to the injection flow, and the nucleation rate. The growth rate is given by

$$v = \frac{n - n_{eq}}{\left(\sqrt{\tau v} / l_{diff} \pi r_L\right) \exp(E_d / 2k_B T) + k(1/2\pi r_L + 1/S)} \quad (151)$$

where τ is the time for desorption, k is the kinetic coefficient, S is the surface for incorporation of atoms. Several kinds of geometrical situations for the transformed areas were summarized by [100]

$$S = \begin{cases} \pi r_L^2, & r_L \leq r_N - \rho \\ r_N^2 (\theta/2 - \sin \theta/2) + r_L^2 (\varphi/2 - \sin \varphi/2), & r_N - \rho \leq r_L \leq r_N + \rho \\ \pi r_N^2, & r_L \geq r_N + \rho \end{cases} \quad (152)$$

The growth rate decreases after the diameter reaches the critical level, because of the supersaturation decreasing. The dependence of the growth rate on supersaturation can be written [101]

$$v = b_{prob} \left(\frac{\Delta\mu_0 - 2V_0\alpha_{free}/r_N}{k_B T} \right)^n \quad (153)$$

where b_{prob} is a proportional coefficient, $\Delta\mu_0$ is the same difference of chemical potential at the boundary, and α_{free} is the specific free energy of NW surface. When the supersaturation in gas phase reduces to zero, the growth process will stop. Therefore the nucleus of critical radius of NW is derived

$$r_c = 2V_0\alpha_{free}/\Delta\mu_0 \quad (154)$$

The material growth rate is influenced by the adsorption and desorption processes on the surface, directly impinged by the vapor phase or molecular beams. However, the growth of NW may be not only attributed to the differences of supersaturation between the gaseous phase, the liquid alloy, and the solid surface on the NW, but also influenced by the adatom

diffusion. Especially in the molecular beam epitaxy (MBE) growth, the diffusion length of adatom is approximately 1~10 μm , which is compared with the lengths of NW. V. G. Dubrovskii et al. introduced the diffusion flux of adatoms J_L into the growth rate [93,102]

$$\frac{\pi r_N^2}{V_0} \frac{dL}{dt} = \left(\frac{\nu - \nu_s}{V_0} - \frac{2nl_L}{\tau_L} \right) \pi r_N^2 + J_L \quad (155)$$

where ν_s is the growth rate of nonactivated surface, l_L is the interatomic distance in the liquid phase, and τ_l is the mean lifetime of atoms in the liquid. So the NW growth induced by diffusion can be simplified

$$\frac{dL}{dt} \approx -\frac{2V_{0S}}{r_N} D \nabla n \approx 2V_{0S} r_N \left(1 + \frac{\lambda}{r_N} \right) \quad (156)$$

When adsorption, desorption, and diffusion processes are introduced into the growth, the NW growth rate is therefore written as [103,104]

$$\frac{dL}{dH} = \frac{\varepsilon_S - \varepsilon_L}{\varepsilon_V} + \left(\frac{dL}{dH_{dep}} \right)_{diffusion-induced} \quad (157)$$

where ε_i is the activity coefficient and proportional to $\exp(\mu_i/k_B T)$, and H_{dep} is the deposition thickness. The detailed dependence of diffusion dL/dH on the structure of NW was analyzed through the simulations and experiments in [104].

For the analysis of the diffusion and nucleation processes in NW system, kinetic factors are taken into consideration to control NW growth operating far from equilibrium. The kinetics of adsorption and thermal desorption play an important role in the dynamic equilibrium. The rate of adsorption is proportional to the pressure and the vacant adsorption sites [105]

$$d\delta/dt = k_{ads} P N_{ava} (1 - \delta) \quad (158)$$

where δ is the fractional coverage, k_{ads} is the adsorption rate constant, and N_{ava} is the total number of available adsorption sites. The adsorption is made up of physisorption and chemisorption, and the adhesive energy is $E_{ad} = (1+\cos\theta)\gamma_{VL}$. In the case of NW growth, the kinetics is controlled by the adsorption of group-V elements, and the growth rate is determined only by the group-III element flux. On the other hand, desorption consists of the dissociation from the compounds and incident atoms which are not chemisorbed. The desorption rate is given

$$-d\delta/dt = k_{des}N_{ava}\delta \quad (159)$$

The distribution of the impinging atoms with corresponding energies on the surface satisfies the Boltzmann distribution. In the case of NW growth, the thermal accommodation coefficient reflects the processes of absorption, desorption, and reevaporation appropriate to the temperatures,

$$\gamma_{accommodation} = (T_i - T_e)/(T_i - T_s) \quad (160)$$

where T_i is the temperature of the incoming atoms, T_e is the temperature of arrival atoms, and T_s is the temperature reflecting the evaporation energy of atoms from the substrate. The sticking coefficients in epitaxy can be defined as the proportion of the incident flux which reaches the special state. The sticking coefficient is affected by the temperature and incident fluxes. When there is no desorption, the sticking coefficient is unity. Actually, the growth rate is considerably slower than the real calculated rate. The growth and nucleation rates are limited by the convection and diffusion occurred in the system, meanwhile, the surface adsorption and desorption also affect the NW growth rate.

II. D. Diffusion

In the kinetic studies of NW growth, the crystal growth rate is measured as a function of driving forces, which are caused by not only the thermodynamic driving force, but also the kinetic mechanisms. These driving forces lead to phase transformations and NW growth. At the mention of kinetics of materials, phase equilibrium equalizes the uniformity of the diffusion potential. As mentioned above, phase transformation occurs when free energy is reduced by changing the quantities which have relationship with the phase of NW. The detailed diffusion growth can be separated into distinct steps: nucleation including incubation, precipitation and growth, and coarsening. The diffusion process in the NW is described as an empirical relation, the Fick's first law. The relation expresses the dependence of the flux of chemical components J_i on its concentration gradient ∇n_i ,

$$\vec{J}_i = -D\nabla n_i \quad (161)$$

where D is the diffusion coefficient. The diffusivity in droplet can be calculated in statistics,

$$D_L = \lim_{t \rightarrow \infty} \frac{1}{6Nt} \sum_{i=1}^N \left| \vec{r}_i(t) - \vec{r}_i(0) \right|^2 \quad (162)$$

The flux arises from the different sources of driving forces, and thus leads to an introduction of correct term into the diffusion equation [106]. The extra diffusion is induced by the driving forces, such as the gradient in electrostatic potential, a thermal gradient, the stress, and capillarity. If the added source is taken into consideration, the Fick' second law gives the time and spatial dependence on the concentration.

$$\frac{\partial n}{\partial t} = \dot{n} - \nabla \cdot \vec{J} = \dot{n} + D\nabla^2 n \quad (163)$$

The equilibrium of concentration will not stop the diffusion process described in the Fick's law, because the free energy is not equilibrium in practice. An alternative way to

describe the flux is to consider the drift velocity. Based on the difference of chemical potentials, flux of atoms is driven to the top of NW in the model.

$$\vec{J} = \vec{v}_{dr} n = -D_\mu n \frac{\partial \mu}{\partial r} = -L \nabla \mu \quad (164)$$

Comparison with Eq.161,

$$D = D_\mu RT \left(1 + \frac{d \ln v_i}{d \ln (n_i/n)} \right) \quad (165)$$

In the model provided by V. G. Dubrovskii [93,103,104,107], the formation of NW was attributed to the combination of the diffusions of substrate and side wall surface. In the steady state, the concentrations obey

$$D_s \Delta n_s + \vec{J} \cos \vartheta - n_s / \tau_s = 0 \quad (166)$$

$$D_{Nf} \left(\frac{d^2 n_{Nf}}{dr^2} \right) + \vec{J} \sin \vartheta - n_{Nf} / \tau_{Nf} = 0 \quad (167)$$

where the subscript Nf indicates the NW surface, and ϑ is the angle between the flux to the substrate normal. Actually, the diffusivities in group III-V crystalline materials are extremely slow owing to the strongly directed bonds. The general solutions are given by

$$n_s \approx J \tau_s \cos \vartheta + C_1 \frac{D_{Nf} \lambda_s G(r/\lambda_s)}{D_s \lambda_{Nf} G'(r/\lambda_s)} \approx J \tau_s \cos \vartheta + A_1 J_0 \left(\frac{r}{\lambda_s} \right) + A_2 K_0 \left(\frac{r}{\lambda_s} \right) \quad (168)$$

$$n_{Nf} = J \tau_{Nf} \sin \vartheta + C_1 \sinh(r/\lambda_{Nf}) + C_2 \cosh(r/\lambda_{Nf}) \quad (169)$$

where the effective diffusion length λ is defined as $\lambda = \sqrt{(D\tau)}$, and G is the radius independent function. J_n and K_n denote the modified Bessel functions of the order of n, A_1 and A_2 are the Bessel function coefficients, and the coefficients C_1 and C_2 can be written

$$G(r/\lambda_s) = K_1 \left(1/2 \lambda_s \sqrt{D_{Nf}} \right) I_0(r/\lambda_s) + I_1 \left(1/2 \lambda_s \sqrt{D_{Nf}} \right) K_0(r/\lambda_s) \quad (170)$$

$$G'(r/\lambda_s) = K_1(1/2\lambda_s\sqrt{D_N})I_1(r/\lambda_s) + I_1(1/2\lambda_s\sqrt{D_N})K_1(r/\lambda_s) \quad (171)$$

$$C_1 = - \frac{J(\varepsilon\tau_s \cos \vartheta - \tau_{Nf} \sin \vartheta) \left[\Gamma_D \sinh\left(\frac{L}{\lambda_{Nf}}\right) + \cosh\left(\frac{L}{\lambda_{Nf}}\right) \right]}{\sinh\left(\frac{L}{\lambda_{Nf}}\right) + \Gamma_D \cosh\left(\frac{L}{\lambda_{Nf}}\right) + \Gamma_{Nf} \left(1 - \frac{G}{\Gamma_s G'}\right) \left[\Gamma_D \sinh\left(\frac{L}{\lambda_{Nf}}\right) + \cosh\left(\frac{L}{\lambda_{Nf}}\right) \right]} - \frac{J\tau_{Nf} \sin \vartheta - \frac{\exp\left(\frac{\mu_L^\infty r_N + 2V_{0L}\gamma_{VL} \sin \theta}{r_N k_B T}\right)}{S_L}}{\sinh\left(\frac{L}{\lambda_{Nf}}\right) + \Gamma_D \cosh\left(\frac{L}{\lambda_{Nf}}\right) + \Gamma_{Nf} \left(1 - \frac{G}{\Gamma_s G'}\right) \left[\Gamma_D \sinh\left(\frac{L}{\lambda_{Nf}}\right) + \cosh\left(\frac{L}{\lambda_{Nf}}\right) \right]} \quad (172)$$

$$C_2 = \frac{J(\varepsilon\tau_s \cos \vartheta - \tau_{Nf} \sin \vartheta) \left[\Gamma_D \cosh\left(\frac{L}{\lambda_{Nf}}\right) + \sinh\left(\frac{L}{\lambda_{Nf}}\right) \right]}{\sinh\left(\frac{L}{\lambda_{Nf}}\right) + \Gamma_D \cosh\left(\frac{L}{\lambda_{Nf}}\right) + \Gamma_{Nf} \left(1 - \frac{G}{\Gamma_s G'}\right) \left[\Gamma_D \sinh\left(\frac{L}{\lambda_{Nf}}\right) + \cosh\left(\frac{L}{\lambda_{Nf}}\right) \right]} + \frac{\frac{\Gamma_{Nf}(\Gamma_s G' - G)}{\Gamma_s G'} \left[J\tau_{Nf} \sin \vartheta - \frac{\exp\left(\frac{\mu_L^\infty r_N + 2V_{0L}\gamma_{VL} \sin \theta}{r_N k_B T}\right)}{S_L} \right]}{\sinh\left(\frac{L}{\lambda_{Nf}}\right) + \Gamma_D \cosh\left(\frac{L}{\lambda_{Nf}}\right) + \Gamma_{Nf} \left(1 - \frac{G}{\Gamma_s G'}\right) \left[\Gamma_D \sinh\left(\frac{L}{\lambda_{Nf}}\right) + \cosh\left(\frac{L}{\lambda_{Nf}}\right) \right]} \quad (173)$$

where K_i and I_i are the i order modified Bessel functions, D_N is the density of nanowire, S_L is the surface area of drop, ε is the transition coefficient corresponding to the difference of activation energies between the substrate and NW surface, and ε is proportional to $\exp(\Delta E_{S-Nf}/k_B T)$. The quantity $\Gamma = D/\lambda k_i$, where k_i is the corresponding velocity of the adatom transition. The solution of non-steady state diffusion involving the error function, are summarized by R. W. Balluffi et al [106]. When one combines the results of Eq.155, 166, and 167, the NW growth rate is derived

$$\frac{dL}{dt} = \frac{2V_{0S}D_{Nf}}{r_N\lambda_{Nf}} \left\{ \frac{J(\varepsilon\tau_s \cos \vartheta - \tau_{Nf} \sin \vartheta)}{\sinh\left(\frac{L}{\lambda_{Nf}}\right) + \Gamma_D \cosh\left(\frac{L}{\lambda_{Nf}}\right) + \Gamma_{Nf} \left(1 - \frac{G}{\Gamma_S G'}\right) \left[\Gamma_D \sinh\left(\frac{L}{\lambda_{Nf}}\right) + \cosh\left(\frac{L}{\lambda_{Nf}}\right) \right]} \right. \\ \left. + \frac{\left[\cosh\left(\frac{L}{\lambda_{Nf}}\right) + \frac{\Gamma_{Nf}(\Gamma_S G' - G)}{\Gamma_S G'} \right] \sinh\left(\frac{L}{\lambda_{Nf}}\right) \left[J\tau_{Nf} \sin \vartheta - \frac{\exp\left(\frac{\mu_L^\infty r_N + 2V_{0L}\gamma_{VL} \sin \theta}{r_N k_B T}\right)}{S_L} \right]}{\sinh\left(\frac{L}{\lambda_{Nf}}\right) + \Gamma_D \cosh\left(\frac{L}{\lambda_{Nf}}\right) + \Gamma_{Nf} \left(1 - \frac{G}{\Gamma_S G'}\right) \left[\Gamma_D \sinh\left(\frac{L}{\lambda_{Nf}}\right) + \cosh\left(\frac{L}{\lambda_{Nf}}\right) \right]} \right\} \quad (174)$$

This equation enables controlling NW growth rate from selected conditions. The NW growth rate is inversely proportional to the radius of NW, so the derived minimum radius equation is similar to Eq.146.

$$r_{\min} = \frac{2\gamma_{VL}V_{0L} \sin \theta}{\Delta\mu_{AS} - \Delta\mu_{LS}^\infty} \quad (175)$$

In NW growth, continuous phase transformation begins with an infinitesimal variation initiating the transformation by reducing the free energy. Take into consideration the local diffusion potential for the phase transformation based on Eq.59 and 163,

$$\vec{J} = -L_D \frac{\partial^2 g}{\partial x^2} \cdot \nabla x + 2\kappa_{\lambda_i}(x) L_D \nabla^3 x \quad (176)$$

Take Eq.176 into Eq.161 and 163, so the conserved order kinetic equation for the concentration can be obtained

$$\frac{\partial n}{\partial t} = \Omega_{inter} L_D \frac{\partial^2 g}{\partial x^2} \frac{\partial^2 n}{\partial r^2} - 2\Omega_{inter} L_D \kappa_{\lambda_i} \frac{\partial^4 n}{\partial r^4} \quad (177)$$

This is equivalent to using the difference quantities compared with the average concentration in Cahn-Hilliard method. The variation of concentration in the continuous phase transformation is solved in the Fourier transformation method,

$$\Delta n(r,t) = \frac{1}{\sqrt{2\pi}} \int_0^\infty [2A(q)\cos(qr) - 2B(q)\sin(qr)] e^{\left(-q^2\Omega_{inter}L_D\frac{\partial^2 g}{\partial x^2} - q^4 2\Omega_{inter}L_D\kappa_{\tilde{q}}\right)t} dq \quad (178)$$

where $q = 2\pi/\lambda$, where λ is the wavelength which depends on the crystal structure and orientation. The superposition of cosine and sine terms each having different wavelengths in the parenthesis can be written in the exponential form, which is the position dependence. The exponential term is the time dependence on the decay or amplification factor. The typical decay or amplification factor dependence of the wavelength has a maximum at a fastest growing wavelength. As a wavelength is larger than the fastest growing wavelength, the factor decreases gradually, approaching zero as wavelength infinity. When a wavelength is smaller than the fastest growing wavelength, the factor decreases very rapidly, tending to infinity at wavelength near zero. In the solution of the above equation, coefficients $A(q)$ and $B(q)$ are written

$$A(q) = \frac{1}{\sqrt{2\pi}} \int_{-\infty}^\infty \Delta c \cos(qr) dr \quad (179)$$

$$B(q) = -\frac{1}{\sqrt{2\pi}} \int_{-\infty}^\infty \Delta c \sin(qr) dr \quad (180)$$

This is a generic form for a linear perturbation analysis, but the analysis only predicts the short time. Time decay of long wavelength is slower than that of short wavelength, because of the longer diffusion distance redistributing atoms to phase separating. Periodicity arises from wavelengths, and the longest wavelength should dominate the morphology. The longer the wavelength, the faster the wave should develop. The periodic length increases because of the microstructural coarsening. The fluctuations can be generalized by introducing the wave vector q in a Fourier representation.

If the order parameter η (difference of sublattice concentrations) is not conserved, there is no equation expressed similar to Eq.161. For some structural transition, i.e., order-disorder transition, second order phase transition occurs. Introduce the phenomenological kinetic coefficient α_η into the evolution function,

$$\frac{\partial \eta}{\partial t} = -\alpha_\eta \left[\frac{\partial \Delta g_0}{\partial \eta} - 2\kappa_{\lambda_i} \left(\frac{\partial^2 \eta}{\partial r^2} - \frac{1}{r_N} \frac{\partial \eta}{\partial r} \right) \right] \quad (181)$$

The above equation describes the behavior of highly metastable systems near the spinodal boundary. The diffusion potential kinetic equations derived from the variational principles enable one to draw some conclusions to analyze the microstructural phenomena in NW, and thus are capable to describe the stationary configuration of the critical nucleus. Equilibrium corresponds to the phase composition and fractions can be predicted by minimizing free energy.

In the case of epitaxy with controllable pressure and temperature above the substrate, the nucleation rate is also controlled by the arrival rate onto the surface and the kinetics of adatoms diffusing on the surface to the nucleation sites. The impinging vapor flux depends on the pressure P_V , and temperature T_V ,

$$I_{Vi} = P_V / \sqrt{2\pi m k_B T_V} \quad (182)$$

Inversely, there are atoms desorbing from the surface, in which the process depends on the surface temperature. Under the equilibrium, the desorption rate is equal to the deposition rate. Based on the Henry's law, the fraction coverage is proportional to the impinging vapor flux. The rates of adsorption and desorption are given in Eq.158 and 159 separately. The growth rate can be described by the difference of fluxes of atoms, which is equivalent to the difference between the gas pressure and the equilibrium pressure based on the earlier

equation. The desorption time relies on the thermal oscillation frequency of the crystal ν_{thermal} and the activation energy for desorption E_{des} ,

$$\tau_{\text{des}} = \frac{1}{\nu_{\text{des}}} = \frac{1}{\nu_{\text{thermal}}} \exp\left(\frac{E_{\text{des}}}{k_B T}\right) \quad (183)$$

The adatoms without reevaporation from the surface diffuse on the substrate, side-wall and catalyst surface. The surface diffusion process is affected by the surface diffusion frequency and the activation energy for surface diffusion,

$$\tau_{\text{diff-surface}} = \frac{1}{\nu_{\text{diff}}} \exp\left(\frac{E_d}{k_B T}\right) \quad (184)$$

The surface diffusion coefficient can be defined as

$$D_{\text{sur}} = \frac{l_{\text{diff}}^2}{2\omega_{\text{co}} \tau_{\text{diff-surface}}} \quad (185)$$

So the diffusion length of adatom λ_0 can be obtained,

$$\lambda = \sqrt{D_{\text{sur}} \tau_{\text{des}}} = \sqrt{\frac{l_{\text{diff}}^2 \exp(E_{\text{des}}/k_B T)}{2\omega_{\text{thermal}} \tau_{\text{diff-surface}}}} \quad (186)$$

II. E. Nucleation

Nucleation process at the NW top is determined by the growth kinetics, which acts as discontinuous phase transformation. The transformation of solidification of compositional alloys is thought to occur as a sequence of nucleation and its subsequent growth [108]. The solidification front velocity v_{solid} dependence on the temperature gradient can be written in the expression for the energy conservation,

$$\frac{v_{solid}\Delta H_m}{V_{molar}} = -k_N \nabla T_N + k_L \nabla T_L \quad (187)$$

where k_N and k_L are the thermal conductivities of solid and liquid separately. In a regular solution model, ΔH_m is the sum of bond energies of adjacent atoms, which reflects endothermic or exothermic processes in nucleation. Nucleation is accomplished by the thermodynamic driving force in the solidification of undercooled alloys. The nucleation rate therefore has an important influence on the NW growth rate. Heterogeneous and homogeneous nucleations are treated for different growth situations. In the case of nucleation, the formation of a certain critical nucleus is caused by thermal fluctuation afterwards the nucleus spreads out laterally to form a new layer on the top of NW. The dependence of nucleation on the free energy determines the critical size and the growth rate.

In the NW system, interfacial properties are affected by structural and chemical contributions caused by misfit of crystal lattice and total interfacial bonding energies. It is energetically favorable to maintain coherent in NW, as the surface energy domains in the contribution of energy. This mechanism can reduce the dislocation density in NW structure.

The homogenous nucleation can occur in uniform regions of a system with large supercoolings taking place, and need the supercooling to overcome the nucleation barrier. The energy change with supercooling ΔT inducing the formation of nucleus can be written by

$$\Delta G_{\text{homo}} = -\pi r_L^3 f(\theta) \left(\frac{L_{\text{fusion}} \Delta T}{T_m} - \Delta g_{\text{strain}} \right) + \pi r_L^2 h(\theta) \gamma_{LN} \quad (188)$$

where L_{fusion} is the latent heat of fusion per unit volume, and the strain energy Δg_{strain} needs to be overcome to nucleate. The critical size can be derived by differentiation of Eq.188,

$$r_{L\text{homo}}^* = \frac{2h(\theta)\gamma_{LN}T_m}{3f(\theta)(L_{\text{fusion}}\Delta T - \Delta g_{\text{strain}}T_m)} \quad (189)$$

The crystal that is smaller than the critical size will be unstable solid particles and disappear, otherwise the crystal will grow from the nucleus. From Eq.189, increasing the supercooling leads to the reduction of critical size and its energy change, and this phenomenon was verified in experiment [109]. In the process of particle growth, once the size of particles reach the critical size and pass the critical barrier of ΔG^* , further growth will have a negative barrier for the solidification. Therefore limiting the NW radius or increasing the critical size is necessary in NW growth, to avoid the semiconductor growth in the favored tendency for formation of bulk phase.

The equilibrium distribution of clusters for a stable solid nucleus formation is given by,

$$n_{\text{neq}} = n \exp\left(-\frac{\Delta G_{\text{homo}}^*}{k_B T}\right) \quad (190)$$

where ΔG_{homo}^* is the energy change with the critical size. The rate of formation of stable nucleus can be accounted for the rate of added atoms which advance through cluster space [106].

$$I_{\text{homo}} = -I_s \left[\frac{\partial n_c}{\partial n} + \frac{1}{k_B T} n_c \frac{\partial \Delta G_{\text{homo}}^*}{\partial n} \right] \approx I_s n \sqrt{\frac{\Delta G_{\text{homo}}^*}{3\pi n_{\text{crit}}^2 k_B T}} \exp\left(-\frac{\Delta G_{\text{homo}}^*}{k_B T}\right) \quad (191)$$

where I_s is a constant describing the rate of single atom phase transformation, n_c is the number of clusters having size c in the system, and n_{crit} is the number of clusters in the critical size. In general, the nucleation rate exhibits a similar expression with Eq.150.

In practice, heterogeneous nucleation occurs more often in the interface between catalyst and NW. The nucleation barrier can be reduced through heterogeneous nucleation. The ratio between the homogenous nucleation barrier and the heterogeneous one is a

structural factor caused by the NW geometry in an ideal model. The equilibrium condition of the embryo wetting the NW is described in Eq.33 and 34. The energy change in the embryo is given by

$$\Delta G_{hetero} = -\pi r_L^3 f(\theta)(\mu_L - \Delta g_{strain}) - 2\pi r_N L \gamma_{VN} + \pi r_L^2 g(\theta) \gamma_{VL} + \pi r_L^2 h(\theta) \gamma_{LN} \quad (192)$$

The real nucleation barrier will be reduced further, and this is caused by the preexisting defects, or because of the nucleation occurring at grain edges and corners. The critical size can be derived by the differentiation of Eq.192,

$$r_{Lhetero}^* = \frac{g(\theta) \gamma_{VL} + h(\theta) \gamma_{LN}}{\sqrt{3f(\theta)(\mu_L - \Delta g_{strain})}} + \sqrt{\frac{[g(\theta) \gamma_{VL} + h(\theta) \gamma_{LN}]^2}{3f(\theta)(\mu_L - \Delta g_{strain})} - 2\pi L \gamma_{VN}} \quad (193)$$

The rate of heterogeneous nucleation is proportional to the probability of stable solid nucleus formation,

$$I_{hetero} \propto \exp\left(-\Delta G_{hetero}^*/k_B T\right) \quad (194)$$

Although some theoretical models have been provided to describe the growth mechanics of NW, a tremendous amount of work devoted to the problem needs to be done. More accurate models are required to assist the analysis of experimental results.

II. F. Summary

This chapter makes contributions to the understanding of fundamental principles for group III-V NW growth mechanisms. A systematic introduction to thermodynamic and statistic functions based on the CVM or the MC method in the Ising model is presented. The calculations from first-principles data show correct trends and topology, meanwhile, can give theoretical predictions for phase transformations. However, the theoretical calculations

are often far from the accuracy needed by scientific and industrial applications. Phase equilibrium calculations are analyzed in the equilibrium systems, while kinetics of materials is explored out of the equilibrium of systems. The kinetics provides an appropriate tool for NW growth modeling. For NW growth, the model is not a monotonic dependence of any single growth parameter. The kinetic processes on the surfaces and interfaces as well as in the catalyst and NW bulk are relatively complex because of involving the control of diffusion, driving forces, reactions and supersaturation in the droplet leading to nucleation. The morphology of NW varies accompanied with any minor changes of experimental parameters, due to the changes of driving force caused by the difference of chemical potential and supersaturation.

III. Growth Technology of Nanowire

In past thin film epitaxy scientists tried to propose different countermeasures to prevent whisker formation and growth. In contrast, NW formation requires the preferential growth of whisker, and the inhibition of substrate film. The existing growth mechanisms generally fall into two categories: top-down and bottom-up.

III. A. Top-Down Lithography

Lithography approach is easily applied to the top-down NW fabrication, where the dimensions of NW are limited to what is lithography achievable. The attainable minimum features depend on different lithography techniques, such as optical lithography, electron beam lithography (E-beam), extreme-ultraviolet (EUV), X-ray lithography, nanoimprint lithography, and directed self-assembly [110-112]. In lithography, the minimum feature size is restricted by the wavelength of the light, the refractive index of the lens, the lattice constant of the substrate, and some systematic parameters.

In lithographic processes, the optical polarization and pupil shape of light are modulated through the mask (or reticle). For optical projection printers, the resolution of the projection system is referred to as and beyond the Rayleigh's criterion [113],

$$W_{res} = \frac{k_{pho} \lambda_{opt}}{NA} \quad (195)$$

where k_{pho} is a constant which is determined by the optical system and material. It ranges from 0.05 to 0.8 and depends on the ability of the photoresist to distinguish variations in intensity. λ_{opt} is the emission wavelength, and NA is the numerical aperture. For optical lithography, the corresponding depth of focus is given by [110],

$$D_{focus} = \frac{k'_{pho} \lambda_{opt}}{NA^2} \quad (196)$$

where k'_{pho} is also a constant depending on the specific photoresist material. The depth of focus is a parameter which can be used to measure the focusing efficiency. The decrease of the depth of focus is determined by the enhancement of NA number, and therefore the exposure becomes the more sensitive to the variation of vertical distances. Monochromatic light in the system is necessary to ensure the prevention of aberrations. The illumination wavelengths are varied in the range from long-wavelength UV 365 nm, to 248 or 193 nm, to short-wavelength EUV 13.5 nm. Through choosing an appropriate wavelength, the half of the resolution can be reduced to the same order of magnitude as the radii of NW. Taking into consideration of effects of the diffraction, the intensity of dose on the pattern is given by [114],

$$I(x_{pa}) = I_0 + \frac{2}{\pi} \sum_i \frac{I_0}{2i+1} \sin \left[\frac{2\pi x_{pa} (2i+1)}{W_{res}} \right] \quad (197)$$

where x is the position on the pattern. The average error of the image caused by the position error should be controlled under a low-frequency measurement $err_{low-freq}$,

$$err_{low-freq} = \frac{1}{t_e} \int_{-t_e/2}^{t_e/2} e_p(t) dt \quad (198)$$

where t_e is the exposure time, and $e_p(t)$ is the error caused by the position as a function of time.

In Eq.195, the resolution scales linearly with the wavelength, so the improvement of resolution can be obtain via decreasing the wavelength to EUV [115-118] or X-ray [119-123], reducing k_{pho} [124], and increasing NA (such as enhancing the NA by an index of refraction of 1.44-water in the immersion lithography [125,126]). From Eq.195, reducing the

wavelength allows the minimum feature size down to sub-50 nm [127], sub-20 nm in manufacturing industry [128], even approaching- or sub-10 nm for non-vertical NW (By the size-reduction structure approach, the resolution of pattern is beyond the limitation of photolithography [129]). For regular scanned optical-beam, sub-10 nm is hard to be realized directly. From the view of engineering, the resolution enhancement can be realized through applying the phase-shift mask or off-axis illumination source [130]. For the future generation of lithography, such as E-beam [131-135], ion beam [136-138], nanoimprint [139,140], scanning probe [141-143] and self-assembly [144-146] techniques, acceptable approaching- or sub-10 nm image can be obtained fairly. All the future generation lithographic technologies are expected to have a better performance and lower costs meanwhile they have to face their own challenges. The pursuing of the most promising and commercial methods is the aims of industrial manufacturing and academic research.

Although up to now commercially and experimentally available systems have not been applied to grow NW widely, a variety of systems still provide a lot of methods worth learning and applying for NW growth. Patterned line-space nanostructures (e.g. 1D photoresist film) can be used to make the non-vertical NW directly or dot arrays (e.g. 2D photoresist film). Patterned dot or hole arrays are efficient ways to prepare the substrates for vertical NW growth.

EUV lithography has been the most promising candidate in the international technology roadmap for semiconductors [147]. The modern EUV lithography is application of 13.5 nm radiation and using X-ray optics to reduce the mask image. The extremely short wavelength reduces the resolution limit to approximately 3.5 nm and greatly improves the pattern distortions due to light diffraction caused by the surface roughness of the optical components. The NA for commercially available EUV has been increased from 0.25 to 0.33

and above [115,148]. The enhancement of NA makes contribution to the increased angles on the mask, accompanied by side effects of a lower reflection of the light and a reduced image contrast. The situation can be improved by the increase of the magnification. The challenges for EUV include the development of photoresists, the design of systems and masks, as well as the improvement of processes of exposing, developing and etching in engineering.

The photoresist of EUV is required to satisfy the rigorous conditions of high resolution, high sensitivity, low outgassing and low line edge roughness. However, high absorptivity of EUV for most materials is a huge problem. The normal properties of lens can reduce the image size of mask by a lens factor, but lens-based refractive optics cannot be used in EUV lithographic system due to the high absorptivity.

One of the most common organic photoresist for EUV is PMMA [149,150]. In EUV lithography, the photoresist polymer and ~100 eV photons interact and generate electrons and cations. The sensitivity of PMMA is related to the rate of chain scission on the interaction with the high energy photon. Another kind of organic photoresist is Poly(1-butene sulfone) [151], which is a copolymer of sulfur dioxide and a vinyl monomer. The sensitivity of polysulfones is greater than that of PMMA. For organic photoresists, acid diffusion, blurring and latent image can deteriorate the resolution. There is a tradeoff for the decrease of the photoresist film between the improvement of the pattern collapse and the image degradation.

In X-ray lithography, the resolution is less of an issue with printing, because of the wavelength of X-rays being much shorter than EUV. Unfortunately, X-ray (~1 nm) lithography has not fitted for the contemporary industrial requirements now, because the corresponding researches had not kept up with the times of EUV, and some problems have not been solved, such as photoelectron scattering in the materials, X-ray mask, the distortion

of the pattern, and the radiation damage. However, the current situation for X-ray lithography cannot be the final outcome in the future. The soft X-ray (~several nanometers) lithography technology will emerge to improve the on-going resolution limitation reduction of EUV lithography. Meanwhile, X-ray has a better transparency for materials than that of EUV. Further, X-ray lithography can be considered for the specific purposes. No matter soft X-rays or hard X-rays offer a sufficient penetration depth in materials. Thus it is an appropriate lithographic technique with respect to the penetration depth in photoresists and high aspect ratios patterns. For hard X-rays (~0.1 nm), lithography might be the unique technique for nanodot or specific dopants controlling under the mature X-rays infrastructure in the future. Direct-write lithography via hard X-rays avoids the influences of masks and patterns [123].

E-beam (or ion-beam) lithography is a sequential pattern producing technology, whose resolution can be reduced to several nanometers. Based upon the scanning of a focused electron beam, the high intensity, high uniformity, high stability, and high resolution patterns have abilities to achieve a 2 nm isolated feature size [135]. By scanning focused electron beams, layout patterns on the wafers are drawn directly with an extremely short wavelength and a large depth of focus under a maskless exposure [138]. At a time only one pixel can be written, so E-beam lithography is a time-cost technology. For NW arrays growth, the formation of patterning periodic arrays is a process of the construction of the written circles. In E-beam lithography, the resolution is limited by electron scattering, secondary-electron range, and photoresist. The fine controlling electron beam doses to the deposited film is necessary in lithography.

Some organic photoresists for E-beam lithography, e.g. PMMA [132], 3,3'-dimethoxy-4,4'-diazidobiphenyl (DMDA) [152], hexaacetate p-methnlycalix[6]arene (MC6AOAc)

[153], and 4-methyl-1-acetoxycalix[6]arene (MAC) [154], have been studied intensively. The non-chemically-amplified organic photoresists provide small resist surface roughness due to the avoidance of acid-catalyzed reactions. Different photoresist materials need different doses of exposure. One common inorganic hydrogen silsesquioxane (HSQ) material [134,135,155] is also used to act as photoresist. In the lithography process, HSQ has an interaction with high energy electrons and photons. HSQ molecules are monomers in a cage of $(\text{HSiO}_{3/2})_{2n}$ with different sizes. During the exposure for Si-H bonds, Si-H bonds are broken and form silanol groups. Then the silanol groups break the cage and form a linear network which is insoluble in alkaline solution. Another kind of resist ZrO_2 as the mask was also used in group III-V compound semiconductors [156]. No matter organic or inorganic photoresists exploited, the resolutions of E-beam lithography have been reduced below 10 nm. The resolution of E-beam is not limited by diffraction due to the short wavelength of electrons. But the short wavelength accompanied with high energy (~ 100 keV) beam could cause pattern distortions. To improve the resolution of E- or ion-beam for 1D structure growth, the beam size, focus, exposure dose, and developing factors need to be controlled and coordinated reasonably.

Unlike the above mentioned lithographic techniques, there is no any energetic beams exploited in nanoimprint lithography. Nanoimprint lithography is not a traditional lithography technique, but rather a technique exploiting a resist relief pattern by deforming the resist mechanically. The technique is low cost and high throughput, because the mold is repeatable. The resolution for nanoimprint technique can be reduced below 10 nm where the resolution is not limited by effects of diffraction, scattering, and interference. Therefore nanoimprint can be a viable contender with EUV.

In nanoimprint lithography processes, a durable mold is pressed into the resist and the pattern with images of lines or dots is duplicated on the resist film. The polymer is fixed by UV radiation or crosslinking polymer via a thermal cure. Then the residual resist in the compressed region is removed via reactive ion etching and the pattern is left on the substrate. Mold release agents are used to reduce the resist adhesion to the mold, and the appropriate resist material is used to maintain the mechanical stability for pattern. When the mold is pressed into or removed from the resist, there is nanometer variation on the mold, which can be transferred into the side walls. Thermal expansion, defects, contamination and overlay can intimidate the features on the resist.

The resolution of nanoimprint based on hard molds can be enhanced by a directed self-assembly technique by the block copolymer composed of highly incompatible polymers. A controlled position and orientation patterns defined by lithography are exploited to produce NW. The material can achieve self-assembly because of applying a local chemical energy minimum of a system, in which patterns can form themselves. In the processes of self-assembly lithography, block copolymer is coated on the mold and treated with organic vapor, e.g. acetone or toluene for self-assembly. The organic vapor swells the polymer chains to make them flexible enough to reorganize and form ordered nanostructures. The certain types of polymers can separate into different phases as annealing. The sizes of the different phase regions are determined by the size of the block copolymer. Then the self-assembled block copolymer is transferred onto the substrate. The self-assembled block copolymer is pressed and it adheres to the substrate when the mold is removed. After plasma oxidation and reactive ion etching treatment, planar NW arrays or dot arrays are formed on substrate. The common block copolymers, such as poly(styrene-*b*-dimethylsiloxane) (PS-PDMS) or poly(styrene)-block-poly(methylmethacrylate) (PS-*b*-PMMA), induce the formation of

ordered hexagonal, cylindrical or spherical arrays based on the volumetric composition of the individual component. Likewise in nanoimprint approach, self-assembly technique can reduce the lithography cost. Low cost processing and simple fabrication methods based on self-assembly for the fabrication of non-vertical NW arrays were studied [157-160]. With advances in lithography, the integration density of NW keeps on increasing.

The advantage of top-down lithography originates from the compatible with the existing fabrication technology. Top-down lithography and anisotropic etching were exploited by D. L. Kwong et al. to fabricate gate-all-around transistor for pushing scaling beyond the semiconductor roadmap [161,162]. NW is more convenient to fabricate the gate-all-around structure than the planar structure, and thus leads to a better control over charge carriers and reducing short channel effects. However, top-down approaches exhibit more complicated, and have to suffer from even more hostages to the resolution of lithography and etching.

III. B. Vapor-Liquid-Solid (VLS)

Very fine whisker growth by vapor-solid deposition and diffusion control was analyzed by G. W. Sears et al. [163-165], J. M. Blakely et al. [166], and V. Ruth et al. [167]. However, the problem for early whisker is the existence of obvious imperfection. An axial screw dislocation appears in the whisker, because of the original nucleus containing a screw dislocation or an introduction of screw dislocation in the growth process. In whisker growth, most of semiconductor materials have high melting temperatures and the actual growth circumstance where the vapour pressure of precursors has to be sufficiently low at rigour temperatures. In the case of vapor-solid whisker growth, the supersaturation is insufficient for 3D nucleation by the effects of dislocation. Thus whisker growth is caused by the low

supersaturation only enough for 2D nucleation (pseudo-1D NW growth) in each NW layer. A lower supersaturation of tip and a lower activation energy barrier are required to improve the whisker growth. A half century ago, R. G. Wagner et al. introduced a liquid phase by a so-called catalyst to reduce the barrier for reaction on the vapor-liquid interface, and to low the activation energy of nucleation at liquid-whisker interface at the same time [9]. Now the VLS mechanism has been the most commonly used to produce NW. In the VLS mechanism, the promotion of precursors depositing and dissolving on the catalyst, as well as the improvement of diffusion and nucleation processes are exhibited. Meanwhile, the supersaturation of the vapor is controlled at a low level to make sure the chemical potential difference between vapour and substrate is greater than the difference between the catalyst and substrate. Furthermore, the deposition of particles on the substrate is suppressed to reduce the thin film growth.

The VLS mechanism relies on the atomic sources from vapor phase precursors and adatoms on the surface. These atoms impinge on liquid phase catalyst globule, and cause the droplet to become supersaturated relative to the NW materials. Then precipitation of the materials from the droplet leads to the nucleation on the top of NW. At last, the nucleus spreads out laterally to form a new layer and indicates the NW growth. Impingement, adsorption, diffusion controlled and reevaporation of atoms act as the general mechanisms for predictions of whisker growth. The incubation time and nucleation processes can seriously affect the overall growth rate. In general, the VLS mechanism as a representative of the bottom-up approaches is less complicated than top-down approaches and provides higher quality materials.

The NW growth is the reconciliation of contributions from desorption, condensation and solidification. In the VLS mechanism, the condensation coefficient is much larger than

the coefficients in direct desorption growth. This means precursors stick preferentially to the surface of a liquid particle and decompose there. The probability of decomposition at the deposition location is high, thus it leads to a local increase in the amount of precursors around the droplet. Then the precursors dissolve into the eutectic mixture until the composition reaches the liquidus line. The adsorption driving force is caused by the free energy difference at vapor-liquid interface and the solidification of alloy at the liquid-nanowire interface. The crystallization of eutectic alloy on the top of NW is possible only when the alloy is supersaturated. The supersaturation has a determination on the nucleation and the dimension of critical radius for NW growth given in Eq.154. The material concentration, orientation and surface tension all exhibit influences on the degree of supersaturation for phase transformation. When an appropriate supersaturation is achieved, nucleation occurs at the liquid-NW interface. The mechanism of nucleation based upon the critical size effects. The homogeneous and heterogeneous nucleations were discussed by D. Turnbull [108,168], and the nucleation rates have been discussed in accordance with Eq.191 and 194.

There are 2D thermodynamic interfaces dividing the separated phases, such as vapor-droplet, vapor-NW, and droplet-NW. The phases located at both sides of the interfaces perturb the interface over a distance, the effective range of the atomic interactions. For the interfaces with condensed phases and high-vacuum, the surface bonds are distorted and the surface reconstruction is caused by the strain. For the interfaces with two condensed phases, the interfacial structures are affected by the crystal structures. The work function of the interface is

$$\Omega = U - TS - \sum_i \mu_i N_i = \sigma A \quad (199)$$

For a droplet in the open system, the change in the radius of droplet induces the variation of the work function,

$$d\Omega = -4\pi r_L^2 \left[P^L - P^V - \frac{2\sigma}{r_L} \right] dr_L \quad (200)$$

For NW in the system, the third term in the bracket transforms into $-\sigma/r_{NW}$. The equilibrium in the droplet is maintained by $P^L - P^V \approx 2\sigma/r_L$. Very narrow radius in VLS growth leads to a high laplacian pressure with an enormous promotion of chemical potential.

The great advantage of VLS synthetic method for generating NW is the combination of control over low-dimensional anisotropic structure, morphology and uniformity simultaneously. The low-dimensional anisotropic structure exhibits a high aspect ratio in NW system. The radius of NW is fundamentally determined by the size of nanoparticle catalyst and the detailed experimental conditions. Nanoparticles can be transformed through annealing the deposition catalyst thin film on the substrate, where the sizes of catalysts can be controlled by the thickness of deposition thin firm [169]. Templated assisted method was exploited to control the radius too, in which the diameter of NW was close to the pore size distribution of the templated material [170]. Furthermore, a size selected particle method was developed by L. Samuelson et al. [171,172]. In addition, a laser ablation method was used to define the size of NW by C. M. Lieber et al. [172-175].

Laser ablation approach overcomes the limitation of equilibrium nanoparticle sizes in determining the minimum NW diameters [173]. The group III-V NW, whose diameters were lower than 10 nm, had been grown by exploiting monodisperse catalysts in experiments [174-176]. The diameters of NW are generally larger than the catalysts, because of the precursors dissolving into and reacting with the eutectic mixture. The monodispersity of NW is limited by the dispersity of the colloids. The formation of monodispersed colloids

and their nucleation mechanism caused by the condensation from supersaturated solutions were studied in [108,177]. Some tools, such as scanning tunnelling microscope and atomic force microscope have also been studied. Besides of controlling catalytic nanoparticles, the wetting angle, pressure, temperature, and precursors are also modulated to determine the low dimensional growth.

Another advantage of low dimensional growth is that 1D structure can reduce the effects of materials mismatch. The critical radius of NW can be simulated as the critical thickness of systems derived by J. H. van der Merwe [178,179] and J. W. Matthews et al. [180-184]. The critical radius depends on the stresses and energies of interfaces. The interface energy can be written as the sum over strain energy and misfit energy

$$E_{\text{interface}} = -\frac{\mu_{\text{in}} a_{\text{ref}} M}{4\pi^2} \ln \left[2M \left(1 + M^2 \right)^{\frac{1}{2}} - 2M^2 \right] + \frac{\mu_{\text{in}} a_{\text{ref}}}{4\pi^2} \left[1 + M - \left(1 + M^2 \right)^{\frac{1}{2}} \right] \quad (201)$$

where μ_{in} is the interfacial rigidity modulus, the reciprocal of the reference lattice constant a_{ref} is the sum of the reciprocals of the individual lattice constant located at both interfacial sides. The parameter M is given by

$$M = 2\pi \frac{a_{\text{ref}}}{d_{\text{dis}}} \frac{\mu_{+}}{\mu_{\text{in}} (1 - \nu_{+})} \quad (202)$$

where d_{dis} is the dislocation spacing, μ_{+} and ν_{+} are the rigidity modulus and Poisson's ratios of crystal at the interface, respectively. The subscript “-” means the other side crystal at the interface. The minimum interface energy occurs at a homogeneous strain ε_{min} ,

$$\varepsilon_{\text{min}} = \frac{(1 - 2\nu) a_{-} \mu_{0} (2 - \varepsilon_{\text{het}}) (1 + \varepsilon_{\text{het}})}{8\pi^2 (1 - \nu) d \mu_{-} \varepsilon_{\text{het}} (2 + \varepsilon_{\text{het}})} N \ln \left[2N \left(1 + N^2 \right)^{\frac{1}{2}} - 2N^2 \right] \quad (203)$$

where ε_{het} is the heterogeneous strain, d is the thickness, and the parameter N is given by

$$N = \frac{8\pi\mu_- \varepsilon_{het}}{(1-\nu)(1+\mu_-/\mu_+)\mu_0(2+\varepsilon_{het})^2} \quad (204)$$

The critical thickness occurs when the maximum force exerted by the misfit strain equals two times the force exerted by the dislocation line tension. The critical thickness can be written as [180]

$$d_c = \frac{a_+}{4\pi\varepsilon_{\max}} \frac{(1-\nu \cos^2 \theta_{dis})}{(1+\nu) \cos \theta_{slip}} \left(\ln \frac{d_c}{I_{dis}} + 1 \right) \quad (205)$$

where ε_{\max} is the maximum value of the misfit strain, θ_{dis} is the angle between dislocation line and its Burger's vector b , θ_{slip} is the angle between the slip direction and the direction which is perpendicular to line of intersection of the slip plane and the interface, and I_{dis} is the strength of dislocations.

The critical radius of NW is roughly an order of magnitude larger than the critical thickness of thin film because of the lateral relaxation relieving the strain energy. The relationship between the critical radius of NW and the strain energy caused by dislocation is given by [185,186]

$$E_{interface} = \frac{\pi(1+2\varepsilon_{\max})^3(b-4\varepsilon_{\max}r_c)^2}{(1-\nu_+)/2EY_+\lambda_- + (1+2\varepsilon_{\max})^3(1-\nu_-)/2EY_-\lambda_+} + \frac{r_c b^2 \log(\Pi r_c/b)}{2\pi(1-\nu_-^2)/EY_-} \quad (206)$$

where EY is the Young's modulus, λ is the decay length, and Π is the lower limit for the integration of the strain and dislocation. The Burger's vector terms will be ignored in the coherent situation. The strain energy reflects the sum of the elastic energy, the misfit dislocation energy and the specific system itself. The influence of surface stress on the free energy will be analyzed in the later sections. The critical radius can be simplified to a simple form to determine the critical radius numerically [180,185-189]

$$r_c = \frac{b}{8\pi\varepsilon_{mis}(1+\nu)} \ln\left(\frac{U_{core}r_c}{b}\right) \quad (207)$$

where ε_{mis} is the misfit dislocation strain, and U_{core} is the core energy factor. When the radius is smaller than the critical radius, there is no misfit dislocation, because the NW with small radius enables lateral relaxation to accommodate mismatches.

For anisotropic structure, there is a thermodynamically allowed small radius in NW growth. The thermodynamic limit on the catalyst size is given in Eq.146. Below the limit of radius, nucleation will not occur in the catalyst. The similar thermodynamic and kinetic limit occurs in the NW growth, implying there is a smallest radius existing. The droplet whose radius is lower than the critical one will evaporate into gas, resulting from the elevation of chemical potential controlled by the curvature. The difference between the existing smallest radius and Eq.146 originates from the constant coefficient, which has an influence on the curvature. For coefficient one, equation stands for the cylindrical NW; for coefficient two, equation stands for the spherical droplet. The radius limit equation can transform into the dependence of radius on the supersaturation [190]

$$r_{N\min} = \frac{V_{molar}\gamma_{VN}}{k_B T \ln(P/P_{eq})} = \frac{V_{molar}\gamma_{VN}}{k_B T \ln(\varepsilon_i n_i / \varepsilon_{ieq} n_{ieq})} = \frac{V_{molar}\gamma_{VN}}{k_B T \ln(\xi_V + 1)} \quad (208)$$

where P_{eq} is the precursor material vapor pressure over the equilibrium liquid with a concentration of n_{eq} . ε_i is the activity coefficient and is proportional to $\exp(\mu_i/k_B T)$. In summary, the minimum size is determined by the catalyst composition and size. E. I. Givargizov et al. proposed a growth rate equation of NW whose radius is larger than the minimum value. The model shows an adsorption process induces the NW growth [191],

$$\frac{dL}{dt} = k_L \left[\ln(\xi_V + 1) - \frac{2V_s \gamma_{NV}}{k_B T r_N} \right]^2 \approx \frac{\pi I r_N^2}{1 + \sqrt[3]{3(\pi I / v_{lateral})} r_N^2} \quad (209)$$

where k_L is the crystallization coefficient for liquid, I is nucleation rate in Eq.150, and v_{lateral} is the lateral velocity on the top of NW. In addition, a higher growth rate occurs at stepped inclined interfaces due to a decrease of the activation energy of nucleation.

Another advantage of VLS synthetic method for generating NW is incorporating precursor materials (including doping materials) simultaneously to realize *in situ* growth. Adsorption precursors and diffusion adatoms could dictate a local enhancement in the concentration of adatoms around the catalyst. The precursors and adatoms dissolve into the catalyst, when the chemical potential of vapor is higher than that of the catalyst. Followed by the supersaturation occurring in the catalyst, the materials precipitate on the NW surface as the chemical potential of particles exceeds that of NW material [192]. The rate controlling factor in the growth of a new phase is determined by the diffusion rate and nucleation rate at the boundary, since the atoms transfer to the nucleus by diffusion. The predictions of growth conditions for binary, ternary and more complex catalyst-group III-V depend on the phase diagrams for the catalyst and compound semiconductors of interest.

Numerous thermodynamic data and phase diagram evaluations have been published in the Bulletin of Alloy Phase Diagrams, the CALculation of PHase Diagrams (CALPHAD), and ASM Alloy Phase Diagram Database [193,194]. Phase diagrams show a representation of the thermodynamic relationships between competing phases. In the CALPHAD method, the molar Gibbs energy can be considered as the sum of reference (temperature and composition dependence), ideal random mixing, the excess Gibbs energy, the magnetic contribution and the pressure term, which have been discussed in the above section. The CALPHAD provides a method that combines the first-principles calculations with experiments and applies the model with adjustable parameters to reach the required accuracy [41,195-201]. The CALPHAD has been widely used in the metallurgical field. For

group III-V semiconductor systems, the CALPHAD assessments ignore the small degree of nonstoichiometry and the carrier concentrations. In real semiconductors, deviations from stoichiometry create antisite defects, vacancies and defect clusters, which may be ionized in different ways [202].

Early semiconductor whiskers were deposited from vapor precursors onto the metal film [203]. Initial VLS procedure was followed to grow the Au-catalyzed Si whisker [9,204]. Later the VLS mechanism was transplanted to group III-V nanowhisker growth, which was induced via an alloy droplet generated by the reactions between III-V materials and Au clusters [205]. With the introduction of a catalyst into group III-V NW growth, binary, ternary and quaternary phase diagrams about group III-V materials and transition metal-group III-V compounds have to be taken into consideration to choose the appropriate growth conditions and phases [193,194,206-223]. Precise knowledge of the thermodynamic data and phase diagrams about group III-V compounds with catalyst materials of interest is very important for the monitoring of NW growth. The most common catalyst, for example, Au and group III-V have considerably complex ternary phase diagrams. The complicated intermediate phases formed by various invariant reactions and polymorphic transformations are so complicated for the analysis of stable phases in group III-V NW growth. The eutectic temperatures for Au-III-V are higher than the actual NW growth temperature therefore it is hard to form stable binary Au-V or ternary Au-III-V at low temperature. In the case of binary reactions, Au-III produces intermetallic compound which is a clear manifestation of pseudobinary cutting through the phase diagram, and Au-V produces new solid phase in the phase diagram [220,221]. In the NW growth, group-III precursors dissolve into the catalyst to form alloy because there is high solubility limit for group-III in Au. On the contrary, group-V materials have little observed in the alloy [224]. Group-V precursors may diffuse

through the eutectic alloy fast along the dislocations or grain boundaries, and adatoms may diffusion along the solid-liquid interface to reach the local reaction points. At the interface, supersaturated liquid alloys precipitate on the top of NW. Detailed ternary phase diagrams need to be investigated further.

With the tougher request for compositionally abrupt and structurally perfect growth interface of NW [225], some circumstances under which the catalyst can be solid [224-243] and others in which the catalyst can be solution [10,244-251] are investigated for the NW growth. In the VLS mechanism, the precursive reactants are supplied in the vapour phase and the experimental temperature is above the eutectic melting point. However, some experimental results show that the temperatures of precursors dissolving into the catalyst were insufficient to form the liquid phase but formed atomic abruptness on the interface [225-227]. This mechanism was proposed as the Vapor-Solid-Solid (VSS) NW growth mechanism. In the VSS mechanism, growth is assisted by a solid phase particle and the growth rate approximately reduces to zero if the temperature exceeds the melting point of the eutectic alloy due to the preferential dissolution of the materials in the liquid catalyst. In addition, there may be a hysteresis corresponding to the supercooling of liquid catalyst metal, so the nucleation barrier at a temperature window prevents the formation of solid phase. The alloyed catalysts are affected by temperature fluctuations, pressure fluctuations and incubation time. Although the experimental temperatures exceeded the eutectic point sometimes, the NW growth was still catalyzed by solid particles [224]. On the contrary, the catalyst can be buried by substrate growth, if the temperature is lower than the lower temperature limit in the VSS mechanism. Experimental temperature, pressure, precursor molar fraction and V/III ratio, orientation relation, catalyst shape and some other parameters can affect the morphology of NW and growth rates in the VSS growth [233-236]. The

presence of solid phase catalyst can induce an unstable kinked growth because adatoms diffusion, deposition and nucleation processes are hindered [224,237-239]. On the other hand, lower temperature growth in VSS can reduce or eliminate the twinning defects and provide a better control of growth orientation. The advantageous in fabricating NW are not only low temperature growth, but also abrupt interfaces due to the lower solubility of precursors in the solid [224,239-244]. With the size of particle reducing, the solubility of precursors in catalyst is further reduced due to the Gibbs-Thompson effect [233,236,244]. Thus it also reduces the tapering phenomenon and the effects of imperfect growth in the situations of after precursor supply or at temperature cooling. Meanwhile, the particle ripening by diffusion could be mitigated under low temperature, and the incorporation of impurities caused by catalyst diffusion will be reduced due to the reduction in diffusivity.

The SLS mechanism is also similar to the VLS growth process, except for using simple, low temperature, solution phase reactions [10]. In the SLS mechanism, the precursors are delivered and react in the solution rather than in the vapor. For the solution phase semiconductor synthesis, catalyst elimination occurs at the interface between the reaction solution and the group-III flux droplet. Then the production of amorphous semiconductor condenses on the top of whiskers and crystallizes to proceed with whisker growth. Elimination-condensation processes operate at lower temperature because the catalyst lowers the energy barriers for precursor decomposition and the interfacial nonmolecular growth. Because the droplet-whisker interface is the most active interface, the growing whisker acquires 1D structure until the precursor delivery is discontinued [245-249]. The shape of crystal depends on the relative specific surface energies, and growth kinetics associated with the facets of crystal [252].

Numerous related mechanisms have been investigated in which one of the states is replaced by other phases. These mechanisms include Supercritical-Fluid-Liquid-Solid (SFLS) mechanism [249,253,254], Supercritical-Fluid-Solid-Solid (SFSS) mechanism [255-258], Solid-Liquid-Solid mechanism [229, 259-261], and some other VLS-like mechanisms.

III. C. The Catalysts in Nanowire

The catalysts are involved in numerous NW growth mechanisms. Bottom-up mechanisms induced by catalysts avoid top-down etching processes that damage the crystalline structure. In catalytic synthesis of NW, processes commonly rely on metal clusters or colloids such as Au, Ag, Pt, Pd, Ru, Rh, Ir, Pb, Cu, Cr, Nb, Mo, Ta, W, Ni, Mn, Fe, Ti and Co, which act as preferential sites for the adsorption of their surrounding vapour reactants. With the requirements for low melting temperature and noncontamination catalysts introduced, some low melting metals such as Al, Ga, In, Bi and Sn are introduced to serve as the catalysts. Melting points, solvating abilities, reactivities, thermal stability, resistant to oxidation, work function, and diffusivity are all important criteria for judging candidate metals as catalysts to form alloys. The choice of an appropriate catalytic material has the benefits of controlling over the radius, orientation, structure, and growth rate of NW. The role of catalyst played in NW growth is not chemically inert with respect to semiconductors, but rather reducing the barriers for incorporation of material and catalytic decomposition of precursor molecules at the surface of alloy and decreasing the activation energy of nucleation at the growth interface.

In much of research, Au has dominated on the catalytic behavior of inducing semiconductor NW synthesis [9,19,106,204,225,227,228,231,262-272], because of the metal

particle acting as a good physical catalyst and forming a variety of intermetallic compounds. The first silicon whisker was grown by using liquid alloys above the eutectic point based upon the VLS mechanism, in which liquid Au served as a preferential site for the adsorption of precursors and the formation of a variety of Au-Si compounds [9]. In III-V systems, the group-III species have much higher solubilities in Au than the group-V solubilities and form numerous intermediate compounds across the entire composition range. The alloy maintains stable steady-state nonequilibrium, and its chemical potential gradient provides a driving force for the reaction. A chemical potential gradient or an easier measured concentration gradient would be maintained and steady state growth would occur when a constant supply of supplied phase materials are maintained.

Generally the atomic diffusion mechanisms in a catalyst are roughly divided into substitutional diffusions and interstitial diffusions. The phase diagram of alloy can be simulated in the CALPHAD, and the calculation of diffusional phase transformations can be accurately simulated with a DICTRA that accounts for diffusivity variations. The diffusion model takes into consideration of thermal gradients and potential gradients in determining mass diffusion for the interstitial flux,

$$J_i = -\frac{L_{iQ}}{T} \nabla T - L_{ii} \nabla \mu_i - L_{is} \nabla \mu_s \quad (210)$$

$$J_s = -\frac{L_{sQ}}{T} \nabla T - L_{si} \nabla \mu_i - L_{ss} \nabla \mu_s \quad (211)$$

$$J_Q = -\frac{L_{QQ}}{T} \nabla T - L_{Qi} \nabla \mu_i - L_{Qs} \nabla \mu_s \quad (212)$$

where the subscript i indicates interstitial atom, s indicates substitutional atom, and Q is the thermodynamic flux expression. L is the corresponding kinetic factor.

Furthermore, the analysis of substitutional diffusion is taken into consideration in binary alloy, because group-V species have low solubilities in catalyst. Ternary phase diagram is more complicated since a series of compounds with catalyst. Many stable compounds have melting points intermediate between the melting point of Au and the melting of the corresponding group-III materials but no stable Au and group-V phases exist, except of Sb. The substitutional fluxes are obtained with the assumption of the absence of thermal gradients.

$$J_A = -L_{AA}\nabla\mu_A - L_{AB}\nabla\mu_B - L_{AV}\nabla\mu_V \quad (213)$$

$$J_B = -L_{BA}\nabla\mu_A - L_{BB}\nabla\mu_B - L_{BV}\nabla\mu_V \quad (214)$$

$$J_V = -L_{VA}\nabla\mu_A - L_{VB}\nabla\mu_B - L_{VV}\nabla\mu_V \quad (215)$$

where the subscript A indicates catalyst atom, B indicates group-III or V atom, and V indicates vacancy. μ_V equals to zero at an equilibrium concentration. In the real cases of $D_B \gg D_A$ [273], the fluxes can be transformed into the concentration gradient,

$$J_A = -D_A \nabla c_A = -\left(\frac{L_{AA}}{x_A} - \frac{L_{AB}}{x_B}\right) x_A \Omega_{sub} \left(\frac{\partial \mu_A}{\partial x_A}\right) \nabla c_A \quad (216)$$

$$J_B = -D_B \nabla c_B = -\left(\frac{L_{BB}}{x_B} - \frac{L_{BA}}{x_A}\right) x_B \Omega_{sub} \left(\frac{\partial \mu_B}{\partial x_B}\right) \nabla c_B \quad (217)$$

$$J_V = D_A \nabla c_A + D_B \nabla c_B \quad (218)$$

The microscopic physics of diffusion can be regarded as the result of a series of thermally activated discrete movements between the neighboring positions with local minimum energies [19,106,274-276]. The elementary atomic hop frequency can be approximated as,

$$\Gamma_{hop} = \frac{\prod_{j=1}^N \nu_j}{\prod_{j=1}^{N-1} \nu'_j} \exp\left(-\frac{\Delta E_B}{k_B T}\right) \quad (219)$$

where ΔE_B is the activation energy needed to carry a defect from an initial equilibrium position to a saddle point, and ν_j is the characteristic frequencies of the three vibrational modes for each harmonic mode. N is the normal frequencies of the entire system at the starting point of the transition, and $N-1$ is the normal frequencies of the system constrained in the saddle point. The interstitial diffusion and substitutional diffusion can be obtained based on the jump distance α separately,

$$D_{inter} = \frac{1}{6} \Gamma_{hopinter} \alpha^2 \quad (220)$$

$$D_{sub} = \frac{1}{6} \Gamma_{hopsub} \alpha^2 \quad (221)$$

The jump frequency for atoms migrating along the defects is higher than that for diffusion on the surface, and the jump frequency on the surface is greater than that in the crystal, so dislocations in the catalyst and interfaces between catalyst and NW provide high conductivity path for the group-III/V species to reach the reaction positions. And adatoms which come from the incoming flux intercepted by the substrate and sidewalls also have a relatively high conductivity path for diffusing into the catalyst droplet. If the length of NW exceeds the diffusion length, adatoms will incorporate at the sidewalls to promote the radial growth. The diffusion length in the system is affected by the substrate and NW temperatures, as well as the V/III ratio in normal conditions [271]. Because the diffusion velocity of group-V atoms, such as As, is much slower than that of group-III atoms, such as Ga, the arriving group-V atoms impinge into the catalyst center or the vicinity of three phase

periphery. Therefore the arriving group-V will also play a role in determine the growth rate owing to the dependence of rate on the species with low diffusivities.

In a substitutional solid, random walk analysis yields a probability distribution for the position of atom at a particular time. The probability of finding a random walker,

$$P \approx \exp\left(\frac{-x^2}{2\alpha^2 t / \tau^*}\right) \quad (222)$$

$$D_{random} = \frac{\alpha^2}{2d} Z_{hop} \Gamma_{hop} x f \quad (223)$$

where Z_{hop} is the number of pathways to hop, d is dimension, and f is correlation factor accounting for the history effect. f equals to 1 for interstitial diffusion, but is less than 1 for substitutional diffusion.

The activation energy for diffusion can be expressed as a function of the degree of order. The diffusion behavior of ordered intermetallics is more complex and its diffusion coefficient is much larger than that of disordered phase [277]. The conserved order and non-conserved order kinetic equations are given in Eq.177 and 181. The drift velocity superimposed on the random hopping motion is related to the activation energy Q_B for diffusion,

$$v_B = -M_B^0 \frac{\partial \mu_B}{\partial x} = -\frac{M_B^0}{RT} \exp\left(-\frac{Q_B}{RT}\right) \frac{\partial \mu_B}{\partial x} \quad (224)$$

where the mobility M_B of species involved in the interaction is divided into the frequency factor M_B^0 . Comparison with the Fick's 1st law, the tracer diffusion coefficient D_B can be obtained

$$D_B = RTM_B \left[1 + \frac{\partial \ln \gamma_B}{\partial \ln x_B} \right] \quad (225)$$

The group-III and V species reach the reaction sites and induce the NW growth through diffusional transformations. Meanwhile, the species and catalyst atoms form several intermetallic compounds through diffusion couples. For low solubility and miscibility of group-V species in group III-catalyst alloy, diffusion path dominates alloy atom transport. And the multiphase diffusion arises when diffusion couples are employed in the solution and intermetallic compounds of catalytic alloy. Consider the multiphase binary system, the interdiffusion coefficient can be written

$$\begin{aligned}\tilde{D} &= (x_B D_A + x_A D_B) \left[1 + \frac{\partial \ln \gamma_A}{\partial \ln x_A} \right] = (x_B D_A + x_A D_B) \left[1 + \frac{\partial \ln \gamma_B}{\partial \ln x_B} \right] \\ &= (x_B D_A + x_A D_B) \frac{x_A x_B}{RT} \frac{d^2 G}{dx^2}\end{aligned}\quad (226)$$

For atoms expelled through different phases, the relationship between interface velocity (diffusion) and the atom flux is given by

$$v_{interface} = \frac{J_i^\beta}{c_i^\beta - c_i^\alpha} = \frac{1}{c_i^\beta - c_i^\alpha} \left[\tilde{D}^\alpha \frac{\partial c_i^\beta}{\partial x} - \tilde{D}^\beta \frac{\partial c_i^\alpha}{\partial x} \right] \quad (227)$$

In the catalytic sphere, the Fick's 1st and 2nd laws are solved by the scaling method. The dependence of supersaturation ξ on the boundary condition and initial condition parameter based on the scaling method with $\eta_R = R(t)/(\sqrt{4Dt})$ can be written as,

$$\xi = \frac{c_B^\beta - c(r=\infty)}{c_B^\beta - c_B^\alpha} = 2\eta_R^3 \frac{e^{-\eta_R^2} / \eta_R - \sqrt{\pi} \operatorname{erfc}(\eta_R)}{e^{-\eta_R^2}} \quad (228)$$

The diffusion growth rate depends on the scaling method coefficient η_R , hence the diffusion rate will be determined by the supersaturation. Meanwhile, the geometry and dimension of particle also make a contribution to the diffusion growth rate,

$$v_{diffusion} \propto S(\theta) \sqrt{\frac{k_B T_V}{2\pi m \tau^2}} D n_{eq} \xi \quad (229)$$

where $S(\theta)$ is the geometric coefficient of variation which is proportional to the available surface area. The equilibrium concentration can be solved in stationary diffusion equation with the corresponding boundary conditions. From the above equations, diffusion induced contribution will affect the overall NW growth rate directly. From Eq.229, growth rate will increase under a positive supersaturation, on the contrary vaporation occurs with a negative supersaturation. In the real NW growth, one attempts to control the NW to forward equally on the surface under an appropriate supersaturation. During the NW growth process, the supersaturation remains almost constant because of the semiconductor atoms refilling from vapor state continuously.

In the NW growth, the nucleation process spends less time than the process of refilling the consumed atoms. Thus the nucleation rate depends on the limitation of diffusion atoms incident into the nucleation sites and the available surfaces for nucleation. The nucleation barrier tends to be large as the supersaturation tends to be zero. On the contrary, the nucleation barrier can be ignored as the supersaturation has a tendency to infinity. The maximum supersaturation can be derived from the balance between atoms incident and nucleation process. The time of established balance is the incubation time. M. A. Herman et al. summarized the dependence of epitaxial nucleation mechanisms on the supersaturation in the metastable phase [105].

Unlike the multiphase binary system with single phase product layers separated by parallel interfaces, the diffusion zone caused by reaction couple will be developed in ternary system. The complex stoichiometries and structures of multiphase compounds make the phase behavior and the synthetic processes more complicated. The diffusion path on the appropriate ternary isotherm provides a relationship between the kinetics and thermodynamics of alloy, and these develop in an effort to eliminate supersaturation in the

system [278,279]. Specific diffusion coefficients and phase diagrams corresponding to the group III-V and catalyst materials determined by diffusion multiples make contributions to develop the diffusion processes in catalysts [279-287].

For the nucleation at corresponding phase of NW, semiconductor atoms within a catalyst phase must first diffuse together to form a small volume with the NW composition, and then, the atoms rearrange into the NW crystal structure [19]. Not only the crystal structure of NW, but also the growth rate and abruptness are all governed by the nucleation processes. The overall processes are all influenced by the activation energy barriers given in Eq.188-191, and 194.

Nucleation dependence of position in the catalyst-NW interface is divided into the nuclei emerging in the center and at one location of triple phase periphery [89,288]. In the second case, the surface energy variation is caused owing to nuclei contacting to vapor phase directly. The activation barrier for 2D nucleus formation is given,

$$\Delta G^* = \frac{a_1^2}{4a_2} V_s \frac{\left[(\gamma_{surf} - \gamma_{VL} \sin \theta) \omega + \gamma_{LN} (1 - \omega) \right]^2}{\Delta \mu_{III-V} - \Delta \mu_{WZ-ZB}} \quad (230)$$

where a_1 and a_2 are the 2D nucleus shape constants, V_s is the layer volume per III-V atomic pair, $\Delta \mu_{III-V}$ is the chemical potential difference per two atoms of III and V atoms in the catalyst, $\Delta \mu_{WZ-ZB}$ is the difference of volume energies between WZ and ZB structures ($\Delta \mu_{WZ-ZB} \sim 0$ for pure ZB cubic structure), and γ_{surf} is the corresponding surface energy of ZB or WZ. ω is the “antagonization” angle between liquid phase and solid phase.

Once the nuclei reach the critical size, it will spread out laterally on the whole interface, the process repeats to induce NW growth. A catalyst cannot be exactly spherical for no matter WZ or ZB. The cross section of NW behaves as a regular hexagon that has six equivalent lateral facets. The structure of NW is highly dependent on the parameters

affecting the catalyst properties [289]. The WZ nucleation is favored at the triple phase line, when the requirements for certain suitable surface energies and a sufficiently high supersaturation are satisfied. Eq.188, 189, 192 and 193 give critical homogeneous and heterogeneous nucleation barriers for NW growth. The nucleation probability for different phases is dominated by the driving force, nucleus effective energy, and the interface between a truncated sphere catalyst and a hexagonal NW [289],

$$P \propto \int \exp(-\Delta G^*) d\omega = \int \exp\left(-\frac{\gamma_{\text{tot}}^2(\omega)}{k_B T \Delta\mu}\right) d\omega \quad (231)$$

where γ_{tot} is the total nuclei surface energy dependence on the nuclei structure. The interfacial energies for no matter top or side-wall of NW have a serious influence on γ_{tot} . The driving force dominated by the temperature and supersaturation is given in the foregoing paragraphs. The driving force difference between ZB and WZ depends on the atomistic coordinates related to the orbital radii in the local density formalism,

$$\Delta\mu_{\text{WZ}} - \Delta\mu_{\text{ZB}} = \mu_0 + c_0 \left[\frac{\left| (r_p^A + r_s^A) - (r_p^B + r_s^B) \right| + c_1 \left(\left| r_p^A - r_s^A \right| + \left| r_p^B - r_s^B \right| \right)}{(r_p^A + r_s^A)(r_p^B + r_s^B)} \right] \quad (232)$$

where r is the screened nonlocal pseudopotential or wavefunction orbital radii with a angular momentum s or p . μ_0 , c_0 and c_1 equal to 8.137 meV, -22.152, and -1.13 in the pseudopotential model, or 22.67 meV, -85.74, and 1.742 in the wavefunction model, respectively [290]. The critical chemical potentials, group-V influx, and the concentration of group-III elements in a catalyst all affect the percentage content of ZB or WZ phase in polytypism. For bulk structures, ZB structure is more stable than WZ structure, except for nitrides, otherwise the polytypism issue in NW is more complicated than the phenomena in bulk structures [289-312].

In most case, the growth orientation $\{111\}/\{\bar{1}\bar{1}00\}$ or $\{\bar{1}\bar{1}0\}/\{11\bar{2}0\}$ for group III-V NW is parallel to the $[111]$ axis of ZB substrates, because of these directions inducing the lowest energy crystal structure in group III-V compounds. The crystal symmetry will change from cubic to hexagonal or rotational twin layers. High index side facets can be less probability occurred in NW, due to their roughness and possible higher dangling bond densities. Surface normal directions are parallel to high symmetry orientations in NW. The predictions for the corresponding energies with varying facet orientations and bondings can be implemented in the calculations based on density functional theory (DFT) based on the local density approximation and the repeated slab method [292]. A first-principles pseudopotential study for the III-V polytypism under a highly accurate local density approximation provides a reliable method to predict the structure of NW [290,301-303]. A wide variation in ionicity and bond length for III-V semiconductors should be taken into consideration. Detailed calculations were summarized and calculated in software [304-308].

Cohesive energy of NW depends on its radius and its surface dangling bonds. The number of dangling bonds for ZB is larger than that of WZ structure. WZ is favored when surface energy gain is larger than the difference of volume cohesive energy between WZ and ZB structures [293,299]. Bond length of WZ is smaller than that of bulk. The smaller calculated diameter of NW is more favorable to WZ structure, due to the surface dangling bonds on facets. With the diameter increasing, bistability of ZB and WZ structure changes to rotational twin structures. For a larger diameter of NW, ZB is more favorable over WZ structure, and thus likes a cubic structure. ZB structure contains rotated 60° twin blocks with respect to each other, hence these blocks can transform into WZ segments. For a hexagon, the ratio between dangling bonds and the total number of atoms in each diameter is the lowest in this case. Strain energy caused by lattice constraints, and electrostatic energy

caused by bond charges and ionic charges make contribution to the system energy of polytypism based on an empirical interatomic potential calculation [309-311],

$$E_{NW} = E_{coh} + E_{surf} + \Delta E_{WZ-ZB} = \frac{1}{2} \left(\sum_{i,j} U_{ij} + \sum_{i,j} \frac{q_i q_j}{\epsilon |r_i - r_j|} + \sum_{i,j} U_{elecstatic} \right) \quad (233)$$

where U_{ij} is the conventional empirical interatomic potential. $U_{elecstatic}$ is the electrostatic energy affected by the distance between atoms, the effective coordination of atom and the ionicity of semiconductors. The surface energy model can be studied to calculate the equilibrium shapes by the software Surface Evolver [312], which combines of surface tension, gravitational energy, squared mean curvature or defined surface integrals.

In real thermodynamic systems, heterogeneous nucleations are much easier than homogeneous nucleations [313-315]. Nucleation process will be dominated when nucleus has the minimum activation energy barrier. Followed by a supersaturation process, semiconductor atoms start to precipitate. Dependence of the constructed crystalline phase on NW radius, incubation time for nucleation and nucleation on a triple phase line or in the center of NW, remain under the polytypic influence of the concentration of group-III in droplet and group-V flux. R. M. Walser et al. developed an empirical rule explaining that the first phase formed was the congruently melting phase closest to the lowest eutectic point on the bulk equilibrium phase diagram [315]. The first phase nucleated is highly temperature dependent, and thus this induces a different interfacial behavior and a radically variable NW growth. In an non-barrier nucleation transformation, spinodal decomposition occurs when alloy composition locates in the coherent miscibility gaps [19,53-55,106]. The phase separation occurs spontaneously, but it requires an appropriate thermal activation to maintain the rate. The rate of spinodal transformation is controlled by the interdiffusion given in Eq.226. The decomposited phases depend on the nucleation processes under a

homogeneous or heterogeneous mechanism. The specific situations mentioned in NW growth need to be taken into consideration for the corresponding phase diagrams and the more detailed experimental conditions. However, the phase separation can induce the properties of semiconductor to vary dramatically. With a development for understanding and a further study on NW structures, controllable pure ZB, WZ, 4H polytypism, and artificial twinning or superlattices can be grown in NW as people wish.

III. D. Nanowire Induced by Foreign Catalysts

In some preceding reports, some binary catalytic compositions such as Al-Au [242], Ag-Au [316] were used to grow Si/Ge NW. These binary alloy catalysts can minimize the solubilities of growth species and reduce the reservoir effect to get atomically abrupt interface. Meanwhile, exploiting the VSS mechanism reduces atom interdiffusion during growth. Compositional catalysts in group III-V NW growth need to be further analyzed to improve the interface and create abrupt heterojunctions.

Although Au catalysts can provide a moderate melting point, high resistance to oxidation and other parasitic reactions, and appropriate diffusion coefficients for inducing NW growth, the existence of substitutional impurities, interstitial impurities, intrinsic defects, complexes, and dislocations leads to extra electron states pinning in the bandgap. Because it is inevitable to introduce small amounts of foreign gold atoms into NW. Au introduces a range of energy levels into the bandgap and thus has detrimental effects on performance [262,317-325]. A gold catalyst is detrimental to internal quantum efficiency because of Au atoms and Au related complexes behaving as nonradiative recombination

centers. Therefore this presents a significant barrier to the integration of NW building blocks into the conventional semiconductor industry.

For avoiding the drawbacks of introduction of gold, some other foreign metal seeds are exploited in NW growth. Common catalysts, such as other period IV, V and VI transition metals, have been widely applied in silicon and silicide NW growth. In general, common transition metals usually have a much higher ability to chemisorb active molecules compared to noble metals. Introduced foreign species can maintain themselves not being consumed in the process of NW growth, and thus have smaller influences on the changes in NW growth parameters. Meanwhile this provides a much greater freedom for controlling NW properties under a greater flexibility of tuning growth conditions. Ti, Co, Fe, and Ni exhibit their eutectic temperatures that greatly exceed the decomposition temperatures of organic solvents. So these transition metals have a potential for NW growth under solid phase and provide more alternative phases that cannot be achieved via a gold catalyst.

A lot of non-gold foreign metals have been studied in Si NW growth and most of them have been explained based upon the Au-Si system. Ni is a common catalyst, which is compatible with silicon, as a good seed particle metal in Si NW growth [255,313,326-331]. In the NW synthesis, Ni catalyzes the decomposition of precursors and induces Si crystallization through the solid phase alloy of Si in Ni seeds [255]. During the synthesis process, Si-Si bonds are cracked to form NW, Ni-Si solid phase alloy are formed, and Ni is the dominant diffusion species in the phases of Ni-Si. Meanwhile, Nickel monosilicide behaves as an attractive Ohmic contact with p-type Si and the surface of original Si NW plays a significant role in determining the first silicide segment. In the reaction procedures of producing Ni on the top of Si NW, Ni atoms show a larger indiffusion than the outdiffusion of Si, the interdiffusion process takes place inhomogeneously in a catalyst, and

the diffusion-induced high stress is caused by the generation of nonuniform interdiffusion and cracks in the couples [330]. All thermodynamically stable phases grow whose thicknesses are proportional to their relative interdiffusion coefficients, and these coefficients become the highest values as the reaction temperatures are reduced to low levels.

Ti and titanium disilicide with excellent conductivities are compatible with the integrated technology [332-336]. However, Ti also forms deep levels in silicon meanwhile its diffusion coefficient and solubility are relatively low in Si. Ti catalysts accelerate the decomposition of Si-related gases during NW growth procedure. Some other catalytic metals, such as Pd and Pt, behave many similar properties in Si NW growth. Pd and Pt are both noble metals, that are resistant to corrosion and oxidation. The solubility and diffusivity of Pd in Si are lower than that of Au in a silicon catalyst respectively. Pd as a catalytic material is continuously expelled from the growing NW during growth [239]. Pt-Si catalyst has a much higher eutectic temperature, and this property is similar to catalyst Ti in the NW growth. Pt plays roles in enhancing the decomposition of silane and aiding the adsorbed Si species to diffuse through or around the catalyst then precipitate at the top of NW [337-339]. The contact between Pt/PtSi forms a relatively low Schottky barrier height or an attractive Ohmic contact to p-type Si, and thus allows carriers tunnelling through [340,341]. Some different morphology occurred in Si NW via Pt and Pd catalysts were observed compared to via an Au catalyst. However, Pt also has detrimental effects on the electronic properties for Si [337], otherwise, Pd can provide more favorable electronic states in Si.

Al, as a standard metal in silicon process line, is another kind of attractive catalytic metal in NW growth [244]. The real growth temperature can be lowered below 490°C, because the VSS mechanism occurs in the Al-catalyzed NW growth. Meanwhile, the VSS

mechanism provides a sharp interface on the top of NW but there is a tendency of tapered NW occurring in NW growth under the catalysis of Al.

Mn can change the properties of materials towards magnetic semiconductors and has potential applications in spintronics, photovoltaics, and thermoelectrics. Self-assembled Mn catalyst can mediate the growth of Si NW below 600°C based on the VSS mechanism [243,339]. The growth rate is limited by the decomposition of silane at the tip of NW. The nucleation phase can be derived from the congruently melting phase closest to the lowest eutectic point [314]. Fe catalyst was first used in laser ablation cluster formation method for the synthesis of Si NW by C. M. Lieber et al. [173]. Fe can also behave as a kind of ferromagnetic material in NW. Actually, Fe, Mn or Co with silicon constituting compositional NW shows attractive electromagnetic properties. Some ferromagnetic Heusler alloy NW were fabricated through the diffusion driven crystal structure transformation method [343]. The origin FeSi and CoSi NW can be grown by vapor transport method [343-345], or by Co nanodots [313,346]. The metal rich Heusler alloy can be grown radically on the origin NW to form heterostructures. Si NW catalyzed by Co can be grown in hydrogen environment (Hydrogen is essential to Si NW growth) [347]. Likewise the detrimental properties occur in Au-catalyzed NW, mid gap electronic states formed in Si are inevitable. Another drawback for Fe is highly sensitive to oxidation. Co is not particularly reactive with oxygen, except for in high temperature environment. Besides of Fe nanodots as catalysts, some Fe-silicide [348] or Ni-silicide [349] thin films can be annealed in ambient containing Ta vapor to induce Ta₂Si NW growth. In addition, Fe-Si powders were hot pressed then placed on the holey carbon grid to catalyze the NW growth [350].

Another catalyst Cu is very similar to Au in Si NW growth [351-354]. The dependence of the incubation time on the activation energy (0.98eV for Cu) is given by [351].

$$\tau_{incubation} \approx \frac{h_{catalyst}^2}{D \exp(-E_{ac}/k_B T)} \quad (234)$$

where $h_{catalyst}$ is the catalyst height, and E_{ac} is the activation energy that depends on different material catalyst. Cu catalysts induce the Si NW synthesis at a temperature window from 600°C to 650°C based on the VSS mechanism. During growth, Si atoms diffuse into Cu droplet and form Cu_3Si precipitation. The structure and morphology of silicon NW depend on the distinct crystalline structure of Cu_3Si , the size of catalyst and the temperature of synthesis [352].

Compared with 500°C for an Au catalyzed synthesis temperature, the temperatures for the above mentioned transition metals are relatively high. Some low melting point metals, such as Ga, In, Sn, and Bi, can also be used as catalysts for Si NW synthesis [355-363]. Si NW can grow with a molten Ga catalyst under exposing to hydrogen plasma [356-358], or by the hydrogen radical assisted deposition method [359]. In the Ga mediated VLS growth of Si NW, Ga plays a role in decomposition of silane. The crystalline orientations of NW depend on the catalyst size and growth temperature. The preferential growth orientation was $[\bar{1}11]$ at nearly 600°C, and more NW with preferred $\langle 112 \rangle$ directions were observed at a lower temperature [358]. In the radical assisted deposition, the orientations of NW have a relationship with the diameter, owing to the surface energy becoming to be dominated with the enhancement of aspect ratio as a diameter decreasing [359]. Hydrogen is necessary for Ga catalyzed NW growth, because the hydrogen rich can reduce the gallium oxide of the droplet. Indium originating from heated In_2O_3 substrate [360] or In-Si eutectic liquid drop [361] can also catalyze silicon NW growth at low temperature. Moreover, Sn metal thin film

[362] and Bi catalyst atoms [363] have abilities to induce catalyzed Si NW growth at relatively low eutectic temperatures respectively.

The influences of catalytic metals in Si NW have been widely studied for a long time, but still no satisfactory explanation for catalyzed growth in silicon NW has been given. Catalyzed phenomena in group III-V semiconductors are more complicated to study. Vertically growing group III-V NW on different low cost substrates under suitable reaction conditions is also an attractive and challenging issue with freshness and rigour. Non-gold foreign metals are widely used for catalytic growth of NW, especially for III-nitride NW. Au exhibits a poor solubility for N and thus provides insufficient N sources for nucleation interface [220]. For non III-nitride NW, Au still exhibits a superior catalytic ability. Different catalysts can induce different structures of NW, growth rate and densities of defects.

Ni is one of the most common catalysts in group III-V NW growth, especially for GaN NW [364-384]. No matter in the VLS mechanism or in the VSS mechanism, a Ni-Ga alloy droplet will reach supersaturation, followed by the nucleation event further GaN NW growth then occurs. The nanoparticle consists of catalytic metal, gallium and nitrogen, meanwhile some impurities seems inevitable to be introduce, i.e., H, O, and C, whereas the NW can almost only be composed of gallium and nitrogen. Metal Ni powders, bi-metallic alloy, i.e., cobalt-nickel and gold-nickel, or metal complex nickel phthalocyanine can also be used as catalysts to produce GaN NW. Ga atoms have a higher concentration in Ni catalyst than that of Au, thus this results in a higher supersaturation of Ga in Ni. Compared with an Au droplet, Ga-Ni has lower surface energy than that of Ga-Au. These will lead to a higher nucleation rate, a higher growth rate, and probably higher stacking faults formation in the Ni catalyzed GaN NW growth procedure.

Ni catalyzed GaN NW are typically grown by either chemical vapor deposition (CVD) or MBE. In CVD [364-369,371,373,374,377-383] synthesized process, trimethylgallium (TMGa) and ammonia source materials were used as Ga and N precursors carried by hydrogen or nitrogen, and molten Ga species and ammonia were injected into isothermal quartz tube CVD reactors. Ni catalyst provides energetically favorable site for forming NiGa transition alloy at 760°C~1000°C and prevents the formation of interfacial layer. Meanwhile, Ni should be catalytically active in the decomposition of ammonia gas. The reactions were studied in Ni and GaN [385-388], Ni-Ga alloy formation energies [388], and the Ni-Ga system phase diagrams [385,386]. First-principles calculations based on DFT and the MC simulation are always used to describe the order-disorder transformation in the multicomponent systems. In the procedure of species dissolving into the catalyst, disordered FCC nickel catalyst solid solution will transform into ordered intermetallic compounds. The order-disorder phase transition kinetics is given in Eq.181. The molar Gibbs energies of L1₂ structure Ni₃Ga, B₂ structure NiGa, hexagonal structure Ni₃Ga₂, and NiGa₄ can be expressed by Eq.71-74. When the order-disorder transition occurs followed by the structure of catalyst varying from cubic to hexagonal, extra Ga atoms will react with the decomposed ammonia species at the interface of catalyst. The detailed interaction parameters for different structures were discussed in [386]. Gold in Au/Ni bi-metallic catalyst plays a role in lower the catalyst formation temperature as well as the activation energy. Therefore the growth temperature can be reduced [380-382]. The NW density and the degree of alignment are sensitive to the size of Ni, due to the high activation energy for Ni diffusion [371].

In MBE synthesized process [370,372,375,376,384], Gallium and nitride precursors were evaporated from Knudsen cells at 730°C~825°C. Ni as a catalytic droplet accumulates Ga atoms meanwhile N species reach the reaction sites through diffusion. The ratio between

the fluxes of group-V and group-III elements should be controlled precisely, because the impinging N flux not only behaves as a rate limitation for NW, but also controls the radial growth under Ga-rich environment [370]. Ga atoms are accumulated till the NW length reaches the diffusion length of Ga on the side facets.

Table 1. The orientations of Ni-catalyzed GaN NW.

| Growth Tech. | Substrate & Orientation | Nanowire Direction | Ref. |
|--------------|---|---|-------|
| CVD | Si (100) | Hexagonal [110] ($\langle \bar{1}100 \rangle$) and [100] | [364] |
| CVD | (0001) sapphire | Triangular cross section [110] and [001] | [368] |
| CVD | (100) LiAlO ₂ (111) MgO | Triangular cross section [$\bar{1}10$] ($\langle \bar{1}100 \rangle$) Texagonal cross section [001] ($\langle 0001 \rangle$) | [369] |
| CVD | ($\bar{1}102$) sapphire | $\langle 1\bar{1}20 \rangle$ | [371] |
| MBE | (0001) sapphire | [0001] | [372] |
| CVD | (0001) sapphire | $\langle 1\bar{1}20 \rangle$ | [374] |
| MBE | (0001) sapphire Si (111) Si (100) | [0001] | [375] |
| CVD | (0001) sapphire | [101] | [377] |
| CVD | (0001) sapphire | Triangular cross section [0001] | [378] |
| CVD | ($\bar{1}102$) sapphire | $\langle \bar{1}100 \rangle$ | [379] |
| CVD | Si (100) | [0001] | [380] |
| CVD | (0001) sapphire | Triangular cross section [0001] | [381] |
| CVD | ($\bar{1}102$) sapphire (100) LiAlO ₂ | Au-rich $\langle \bar{1}100 \rangle$ Ni-rich $\langle 1\bar{1}20 \rangle$ | [382] |
| MBE | ($\bar{1}102$) sapphire | Pentagon cross section [$1\bar{1}20$] | [384] |

--Au/Ni-bimetallic catalysts were used in [380-382].

--CVD stands for metal organic chemical vapor deposition.

The role of Ni catalysts during GaN NW growth and their influences on the resultant structure of NW still remain unclear. Direction-controllable NWs are desirable to achieve for controlling the electronic, photonic, and magnetic properties of NW. The types of species, catalysts and substrates, the orientations of substrates, as well as the growth mechanisms all have important influences on the structures of NW. Table 1 gives the dependence of orientations of GaN NW on different substrates and growth mechanisms.

Actually, the orientations given in Table 1 are the directions of the majority of GaN NW in experiments. Other growth orientations are inevitable because it is hard to control the vertically alignment for III-V NW in real experiments. Stacking faults for ZB structure were observed in some above experiments. ZB configuration preferentially occurs at the interfaces because it enables a more favorable bond orientation between cubic Ga-Ni and Ga atoms in NW [375]. GaN can be also grown on a graphene film, but the morphology of NW were not controlled well [383].

Ni-catalyzed growth can be used to synthesize some non-GaN, group III-V NW. Ni catalyzed InAs NW were grown on amorphous silicon oxide substrates by a contact printing process at 475°C-520°C [389]. The NW density depends on the thickness of catalyst film and growth temperature. Ni catalyzed GaAs NW synthesis was realized on Si/SiO₂ substrates at 580°C-620°C [235,390]. The growth procedures are similar to Ni-catalyzed GaN, in which Ga precursors impinge or diffuse into the Ni droplets then Ga-Ni alloys are formed. Followed by supersaturated Ga atoms precipitates, Ga atoms will next react with As species. The morphologies of seeds will influence the corresponding phases of GaAs during NW growth, which is attributed to the interfacial lattice mismatch and diffusion mechanisms. Moreover, the substrate orientations, the source and substrate temperatures, and the V/III precursor ratio all influence the morphologies of NW. In addition, Ni-Au bi-metallic catalyst can be used to fabricate the axial or radial heterostructure GaN/InGaN NW [381]. More and more heterostructure group III-V NW will provide better performances for future electronic and optoelectronic devices.

In catalyzed group III-V NW growth, Pd as a catalyst is usually used for synthesizing InAs NW [391-395]. Compared with a wide bandgap material GaN (~3.4 eV), InAs has a relatively narrow bandgap (~0.36 eV), high mobility, and low contact resistance. Moreover,

Pd behaves as an attractive catalyst, because it allows for the formation of good Ohmic contacts with semiconductors. The morphologies and growth rates of NW depend on the critical radius that is influenced by the growth temperature, the sizes of catalysts, and the compressive strain on interface. The synthesis of InAs NW oriented along the $[111]_A$ direction on the InAs $(111)_A$ surface (In bonding terminated) with zigzagged side-walls would occur when its radius was below a critical value, otherwise a smooth sidewall in NW would be formed, because a varied contact angle for the catalyst-NW interface inducing an alternating inward/outward force would construct a faceted side wall under a small tip-NW radius [391]. InAs NW grow along different directions on the different substrate with varied orientations. The majority of InAs NW grew along $[\bar{1}\bar{1}1]_A$ or $[111]_A$, while others grew along $[\bar{1}\bar{1}1]_B$ or $[1\bar{1}\bar{1}]_B$ on a (100) wafer [392]. InAs NW grew along $\langle\bar{1}10\rangle$ direction on $(111)_B$ GaAs substrates [393-395]. Distinct from Au catalyzed InAs NW in general exhibiting WZ structures, Pd catalyzed InAs NW have a cubic ZB structure, resulting from the precursor catalyst, the corresponding substrate orientation, and growth directions. The sizes of catalysts that originate from annealing the uneven catalyst material film have an important influence on the morphologies of InAs NW. A larger catalyst constituted in a BCC single crystal with B_2 structure exhibited a faceted geometry, while a smaller catalyst would become a liquid hemispherical geometry due to the enhancement of In concentration in the catalyst [220,396]. For small droplets, the diffusion ability of precursors will enhance when the aspect ratio of catalyst increases with the reduction of catalyst size. It is found that the phenomenon in the morphologies of InAs NW affected by the size of catalysts appeared to contradict remarks in [391,394,395], because the growth of NW was controlled by the synergetic effects that were composed of a lot of experimental factors and processes. These synergetic effects need to be studied and analyzed further.

Pd/Au alloys can be used to deposit on silicon substrates to catalyze GaN NW. The direct writing techniques using focused ion beams had been used to decompose the precursors and deposit Pt to realize Ohmic contacts on n-type GaN NW [397,398]. In some other experiments, the contact exhibited a Schottky barrier but the barrier height was relatively low when the diameter of GaN NW was large, because the localized states pinned into Fermi level [399,400]. The large diameter of Pt contact GaN NW exhibited the behavior like the thin film Pt contact structure [401]. Through controlling an ammonia flow rate, Pd/Au catalyzed GaN NW exhibited a smooth side wall morphology along the direction perpendicular to $\langle 0001 \rangle$, otherwise a corrugated side wall along the $\langle 0001 \rangle$ direction [397].

Deposited Pt using the Focused ion beam technology [398] or annealing Pt film based on the VLS mechanism [377,402] are applied to grow GaN NW directly. There are no reports about Pt may have detrimental effects on the electronic properties of group III-V NW, so Pt has a potential to be an appropriate catalyst for group III-V material electronic devices. Meanwhile, Pt can form Ohmic contacts with GaN NW. However, Pt catalyzed GaN NW has a lower growth rate than Ni catalyzed NW growth, because the barrier of nucleation for Pt catalyzed GaN might be higher [402].

C. M. Lieber et al. predicted the laser-assisted Ag or Cu catalyzed group III-V NW growth [403-405]. The crystal structures and electronic structures of Ag and Cu are similar to that of Au, while Ag is chemically stable and Cu is easy to oxidize. There is no a high solubility for In species in Ag or Au, this thus can induce sharper interfaces than the interfaces catalyzed by Au. The growth of InAs quantum rods or NW with Ag catalyst were applied in a similar method exploited for the Au particle catalyzed approach [406,407]. High quality InAs NW may be grown on the Si (111) substrate seamlessly. Low density pure WZ structure in NW system can be achieved through the control for the diameter of NW,

because the strain can be released from the Ag film. Through improving the annealing procedure, i.e., Ag film size, annealing temperature and time, small and uniform diameters of NW can be obtained [407]. A special high annealing temperature being favorable to lead to a high NW density was observed. Initiative conditions have influences on not only the morphology of NW, but also the direction with respect to the substrate. The orientation of Ag catalyzed InP NW on Si (111) was controlled by the lattice mismatch and the precursor conditions [408]. The parasitic phenomenon for a homoepitaxial growth of Ag catalyzed InSb NW on a InSb substrate can be relieved through changing the material of substrate, resulting from improving the procedures of diffusion and desorption procedures for the precursor species [409]. Cu was used to catalyze InP NW growth on a InP (111)B substrate in a limited temperature range [410-412]. Compared with an Au catalyst, there are higher eutectic temperatures for group-III materials in a Cu catalyst, but the real growth temperature for Cu catalyzed NW can be lowered. The morphologies and growth rates of InP NW are very sensitive to the growth temperature and V/III ratio. A tendency for kinked in NW was observed when the V/III ratio and growth time were enhanced above the certain thresholds in Cu catalyzed InP NW growth [411]. A higher V/III ratio induces the structure of catalyst to be faceted, the dimensions of NW to be shorter, and the growth rate to be slower. The post growth compositional analysis shows the catalysts were composed of In shell and Cu rich part or only liquid In rich particle. These two states of catalysts can coexist in the procedures of InP NW growth. However, post growth analysis is not an approach that aids to analyze and understand a real time situation for NW growth. The post growth analysis cannot reflect a real situation because the atoms diffusion and distribution vary with the temperature change after growth. The role of Cu played in a catalyst can be the collection sites for the In diffusion atoms, and the seeds for facilitating to crack gaseous

phosphine precursors. Cu catalyzed heterostructure InP/InAs NW were grown by controlling the corresponding V/III ratios via switching the precursor materials on/off reasonably [412]. A dynamic change process for the composition variation of particles affected the growth rates of NW, resulting from the time variation caused by the establishment of new steady states. A transient state (4H structure) between ZB and WZ can be performed in the heterostructure, because the corresponding supersaturation during growth is appropriate to construct the transient state.

Mn particle can act as a catalysts and a dilute magnetic source to fabricate ferromagnetic semiconductor NW. Mn atoms and group-V atoms, i.e., As, can form a MnAs alloy droplet to catalyze GaAs or InAs NW growth. Meanwhile, diffusion Mn atoms can act as dopants behaving like 1D spintronics. GaAs NW were grown on SiO₂ and GaAs(100) substrates in a narrow temperature window [413,414]. Below or above the temperature window, the characteristic performance of quasi-2D structure becomes more obvious. In a worse-case scenario, quasi-2D structures present both WZ and ZB polytype in NW. InAs NW were grown on SiO₂, GaAs(100), and GaAs(111)B substrates at a relatively lower and narrower temperature range [415,416]. The specific catalyst-material may play a minor role in the determination of growth mechanism. Till now the Mn catalyzed GaAs or InAs NW on all substrates are randomly distributed. There is an amorphous region surrounding the Mn catalyzed NW, because Mn and NW outer layers have a tendency to be oxidized. In addition, GaAs and InAs NW show a hexagonal structure that is not affected by the kinds of catalysts, while some ZB structures formed in NW are characterized by defects, twins, or stacking faults. Diffusion Mn atoms can be applied as substitutional dopants, so ferromagnetic MnGaAs NW can be grown through self-assembled method via using MnAs catalysts [417-419]. Fe or Co was exploited to induce GaN NW growth through the laser assisted catalytic

growth [420], CVD [364,368,421], or a pyrolysis route [422]. A variety of growth orientations for Fe catalyzed GaN NW occurred on no matter Si, a-plane sapphire, or c-plane sapphire substrates because Fe droplets may change the predominant growth orientations in comparison with Au catalyzed GaN NW. Fe catalyzed GaN NW exhibit a hexagonal WZ structure, but its cross section can be transformed into a triangular cross section when its radius is smaller than a critical value. Otherwise, there are ZB defects or twins occurred when the radius of NW is above the critical radius. Fe particles can be also used to catalyze GaAs NW growth on a GaAs(111)B substrate [423]. Fe catalyzed GaAs NW with taper structures were grown at a narrow temperature range, and the orientations of NW are preferential growth along non-coincidence directions related to the normal of substrate, i.e., [100] and [110] as well as their equivalent directions.

Indium, Gallium, Bismuth, and Tin are low-melting point group-III/V metals that can form low eutectic alloys with group-III metals. Bi is widely used for the SLS synthesis in group III-V NW. Bi catalyzed InAs, InP, and GaP NW exhibited cubic crystal structure with a good dispersion stability of Bi particles [424,425], and GaAs NW also exhibited the conventional ZB crystal structure [424,426]. The effective bandgaps can be modulated through controlling the diameters of NW. The SLS growth mechanism was applied via an In catalyst to induce GaAs NW growth, and thus constructed a smaller NW diameter. A linear relationship between the diameters of In catalysts and that of GaAs NW was established [249]. The solution method is one kind of non-steady state growth technology, so it is hard to control the morphology of NW. In catalyzed GaN NW growth were ascertained in [421,427,428]. There were no uniform radii or vertically aligned NW synthesized in the experiments. In catalysts provide a possible way to induce the GaN NW growth at a relatively low temperature. Tin is one kind of uncommon foreign catalyst that is used to

assist group III-V NW growth. Sn provides a potential area to develop GaAs NW growth because Sn can be compatible with the conventional semiconductor processing [429]. Meanwhile, some phenomena caused by stacking defects were improved through substituting an Au catalyst for a Sn catalyst.

Industrially incompatible Au has been a catalyst particle of choice to initiate the group III-V NW growth [89,192,205,227-233,254,262,267-272,298,325,369,380,381,404,408,430-455], due to its chemical inertness, thermal stability, superior catalytic ability, the ability of forming relatively low temperature eutectic alloys, and the ability of producing NW system with controllable morphology and composition. An Au droplet provides a preferential site for decomposition of precursor materials and precipitation from the supersaturated alloys. One of the major advantages of gold in NW system is that it is easier to achieve high quality growth accompanied with a broad growth parameter window, resulting from the most of precursor materials being soluble in an Au catalyst to form proper alloys and having high diffusivities in an Au seed. Precisely controlling physical dimensions and chemical composition, especially in heterostructures, is of paramount importance for the growth of Au catalyzed group III-V NW.

Compared with other transition element alloys, the phase diagrams of Au-group III or Au-group V binary systems and Au-group III-V ternary as well as even quaternary systems have been studied extensively, but enormous alloy compositional information in wider temperature ranges needs to be studied further for predicting the compounds in NW [216-221]. For the pseudo-1D structure in NW, the extent of size dependent on a melting point reduction should be also taken into consideration [456-458]. Local eutectic points in catalysts have relationships with a series of compounds of binary or ternary systems, and thus lead to precipitate different compounds of NW. The special size effects in NW will

tremendously affect the properties of NW. The growth rate and chemical reaction rates can be increased by exploiting gold as catalyst, because of the catalysts reducing the activation energy and providing preferential deposition sites. In addition, the relevant surface energies and the nucleation sites in catalysts have influences on the morphologies of NW and the properties of semiconductor devices effectively.

However, using foreign metals can inadvertently introduce some significant negative consequences. Although foreign seeds are preferred to control NW diameters and heterointerfaces, transition-metal incorporation strongly influences the morphology and phase of NW. Diffusion (i.e., Au diffuses easily on the surface of Si or in the bulk silicon) and impurities (i.e., transition elements) induce disorder structures in semiconductors, and thus complicate the structure of NW and affect the properties of devices [262,459-461]. Besides of Au can introduce deep levels that work as nonradiative recombination centers in the semiconductors, common catalysts of period IV, V and VI transition metals also present formidable contaminations and introduce a range of energy levels into the bandgap. Meanwhile, foreign catalysts assisted NW growth has to be limited in the corresponding system where their growth-parameter ranges have to be compatible with the extra catalyst materials, and the more complicated supersaturation conditions have to be controlled to satisfy the situations of material decomposition, dissolving, nucleation and precipitation. As well as the extra preparation for catalyst particles [436], i.e., particles made from thin films, particles produced by lithography technique, colloidal particles produced by a chemical reduction reaction, or aerosol particles suspended in a gas. These extra procedures require additional steps, and thus add the complexity for group III-V NW growth.

III. E. Self-Catalyst Group III-V Nanowire

The growth of group III-V NW can be achieved by using group-III metallic species that have high boiling points and low melting points, as self-catalysts. Parts of self-catalyzed group III-V NW are listed in Table 2. In a self-catalyst system, the seed material is the constituent of NW, so the self-catalyzed process is a kind of comparatively clean growth. Self-catalyzed group III-V NW are synthesized through controlling the addition of group-V elements and the proper of group-III elements during vapor precursor transport and condensation deposition procedures. A so-called self-catalyst is not a real definition catalyst, because a real group-III droplet will act with group-V species in the chemical reactions. The group-III species of reactions will be offset by the impinging vapor atoms as well as the adatoms diffusing from the surface. Self-catalysts can provide simplicity and cleanliness for NW fabrication and avoid unintentional contamination with impurity level incorporation. Although the incorporation of a reasonable precursor ratio and the Ostwald ripening can conspire to control the sizes of NW in the situations of applying foreign metals, self-catalyst will be more complex in controlling the morphologies of NW, resulting from the group-III atoms in a droplet naturally being consumed as group-V species supply maintains too high. So maintaining the dynamic balance between consumption and accumulation of group-III species is very important for controlling the size of a droplet on the top of NW. Further work is needed to clarify that the nucleation of group III-V anywhere other than on the top of NW must be suppressed, through reducing the activation energy of nucleation at the top facet meanwhile tuning the curvature and the chemical potential of droplet based on the Gibbs-Thomson effect.

Indium particles as seeds can be employed to induce the In-group V NW growth, and thus remove the possibility of contamination from other foreign metals. Self-catalyzed

phenomenon caused by indium particles was first described in InN whisker growth, resulting from a similar growth mechanism observed to the traditional VLS growth [462]. Because there are no foreign metals reducing the nucleation barriers, the growth temperatures of self-catalyzed growth may not as low as using foreign metal catalysts. However, Al, In and Ga themselves are all low melting point metals, leading to their real growth temperatures not too high, resulting from no high melting point metals in self-catalyst NW growth systems. For a relatively low growth temperature, only chunks were grown, otherwise for too low growth temperatures, even no chunks or islands were grown [463]. While for too high growth temperature, pillars or cones, even flat growth can be fabricated [464,465].

In-catalyzed single crystalline InN, InP, InAs, InSb, ternary phase, or heterostructure NW have been produced, and their grow mechanisms have been studied widely. The synthesis of compound NW can be achieved by using MOCVD (MOVPE) or MBE. The deposition materials of compounds are incorporated by using the pyrolysis of single molecule precursors [462], the atoms decomposed from substrates transported by a carrier flux [466-468], or metal organic precursor fluxes [469,470] as group III-V sources in MOCVD reactors. Metal organic species, i.e., trimethylindium (TMIn), tertiarybutylphosphine (TBP)/phosphine (PH₃), tertiarybutylarsine (TBAs)/arsine (AsH₃), trimethylantimonide (TMSb) and so other species, are injected into the chambers during MOVPE for In, P, As, Sb, or other elemental precursors, respectively. MBE technology allows group III-V NW growth at a lower temperature and lower impurity incorporation due to an ultrahigh vacuum environment and introduced pure elemental species. Group-III elemental fluxes are produced by thermal effusion cells, and group-V, such as As₄, is

provided by a thermal valve cracker cell to initiate the group III-V NW on a preheated substrate in MBE system.

The dimensions and phases of NW are very dependent on the growth parameters. The temperature, pressure, flux rate, supersaturation, and NW radius sensitively influence the growth morphology, composition and crystal structure. In general, the higher temperature is, the larger diameter of NW is, and the longer dimension of NW is. Moreover, the higher incident flux is, the higher elemental content is in NW, and the higher growth rate is.

The diameter variation along the axial direction can be controlled by optimizing the V/III ratio [463-465,469,471-474], therefore tapering or uniform controlling can be realized through tuning the influx ratio. At a low V/III ratio, NW become reverse tapered, where their radius are larger on the top than at the base, because too much group-III precursors are supplied to droplets. Enough group-III elemental atoms will lead to the diameter of NW increase slowly. The enhancement of the V/III ratio will reverse the behavior, so the NW become tapered structures at a high V/III ratio, because group-V atoms are not easy to dissolve into droplets compared to group-III species. A uniform diameter can be obtained by controlling an optimal ratio. Further, the group-III droplets can be removed through modifying the V/III ratio for convenience of future integration [463].

The density of NW can be modulated by the growth temperatures [474-477], resulting from the diffusivity and migration length of atoms dependence on surface temperatures. In general, the density decreases with an increasing temperature, because the diffusion of atoms is higher at high temperature and atoms are much easier to reach the reaction sites at the top of NW. The migration length, diffusivity, and incorporation probability are significantly affected by the growth temperature and influx, resulting in a higher aspect ratio at a lower temperature, a larger flow rate, and a larger V/III ratio [464,465,469,471,475].

But the optimal temperature and V/III ratio are relative narrow compared with the methods of using foreign catalysts. A too high temperature or a too large V/III ratio will cause radial overgrowth. Meanwhile, a too high temperature is easy to induce the thermal decomposition of materials [478].

The size of a droplet mainly depends on the deposition time and temperature. The curvature of a droplet has a relationship with its contact angle, supersaturation, and surface roughness. The high curvature means that the droplet has an ability to attract more reaction atoms. The diameter of NW, curvature of droplet, supersaturation, binding energy and the ionicity of materials will significantly influence the crystal structures and the orientations of NW [469,479-483]. Some vertical In catalyzed NW have been grown by controlling the growth parameters and choosing the appropriate substrates [463,464,477,478,481,484-487]. InP and InAs NW have been grown nearly one-hundred percent vertically on Si(111) substrates at 350-380°C and 450-480°C, respectively. Below 500°C growth temperatures can be compatible with the typical CMOS growth condition. The evolution of In catalyzed NW morphologies is correlated with the local stoichiometry change, which varies from pure In to In rich to group-V rich in the VLS or VLS-like modes. The phase purity is still a challenge for self-catalyzed NW and a high density of rotational twins and stacking faults were observed in nearly all of them.

Table 2. Self-catalyzed group III-V NW.

| Growth Tech. | Substrate & Orientation | Nanowire Material & Morphology | Ref. |
|--------------|-------------------------|--|-------|
| CVD | sapphire (0001) | WZ InN $\langle 1\bar{1}00 \rangle$ | [462] |
| CVD | SiC, Si & sapphire | Triangular cross section ZB InAs $\langle 100 \rangle$ & $\langle 110 \rangle$ | [466] |
| CVD | SiO ₂ | ZB InAs [111] | [406] |
| CVD | InP | GaInP $\langle 111 \rangle$ & $\langle 113 \rangle$ | [467] |
| CVD | InP (111)B | InP [111]B | [471] |
| VPE | Si (111) | WZ InP $[10\bar{1}0]$ & $[0001]$ | [472] |

| | | | |
|------|-------------------------------|---|-------|
| VPE | (111)B InP | WZ InAs [$000\bar{1}$] | [475] |
| | (001)InAs | InAs [$\bar{1}\bar{1}\bar{1}$] | |
| | Si (001) | InAs <111> | |
| CVD | Si,SiC&sapphire | InAs,InN,InGaAs,InGaN,&InGaAsN | [468] |
| CVD | Si,SiC&sapphire | GaN,InAs,InN,InGaN,InGaAs&InGaAsN | [488] |
| CVD | (111)B InAs | InAs | [469] |
| CVD | Si(100),SiC(001) | InN,GaN&AlN | [489] |
| CVD | Non | WZ or ZB structures of InN,GaN&AlN | [479] |
| MBE | GaAs (111)B | InGaAs/GaAs [$\bar{1}\bar{1}\bar{1}$] | [490] |
| VPE | InP (111)A | InP <111> | [491] |
| VPE | InP (111)B | InP | [464] |
| VPE | Si(111),(100) | ZB InP<111> | [484] |
| CVD | Si(100) | ZB InP [111] | [470] |
| MBE | Si(111) | ZB InAs [111] | [478] |
| CVD | InP (111)B | ZB&WZ InP _{1-x} Sb _x | [473] |
| VPE | InAs (111)B | InSb [$\bar{1}\bar{1}\bar{1}$]&[$000\bar{1}$] | [480] |
| CVD | InP (111)B | ZB InP&polytypic InSb | [481] |
| VPE | InP (111)B | WZ InP/InAsP [0001] | [492] |
| VPE | InP (111)B | InP _{1-x} Sb _x ZB <111>&WZ<0001> | [465] |
| VPE | Si (111) | InAs | [493] |
| VPE | InP (111)B | ZB InP <111> | [463] |
| VPE | InP (111)B | ZB InAs<111> | [474] |
| CVD | Si (111) | ZB InAs<111> | [485] |
| MBE | Si (111) | InAs <111>&<0001> | [494] |
| MBE | GaAs (111)B | InAs | [482] |
| MBE | Si (111) | InAs | [486] |
| VPE | GaAs(100), (111)B | InAs [111],[100] | [483] |
| VPE | Si(111), InAs(111)B | InAs [111] | [476] |
| MBE | Si (111) | InAs [0001]&[111] | [477] |
| MBE | Si (111) | InAs [111] | [487] |
| MBE | Si (111) | GaAs <111> | [495] |
| CVD | Non | WZ GaN | [496] |
| MBE | Si(111), Sapphire(0001) | WZ GaN | [497] |
| CBE | Si(001),(111), (110)&(113) | GaP | [498] |
| CVD | Non | GaN | [266] |
| MBE | Si (100) | GaN <0001> | [499] |
| CVD | Sapphire(0001) | GaN <0001> | [500] |
| VPE | Sapphire(0001) | Along or 30° away from GaN<0001> | [501] |
| MBE | Si (111) | GaN <0001> | [502] |
| MBE | Si (111) | GaN&AlGaN | [503] |
| VPE | Non | AlN | [504] |
| &PVT | | | |
| MBE | Si (111) | GaN [0001] | [505] |
| CVD | Si (100) | WZ AlGaN <0001> | [506] |
| MBE | Si (111) | GaN [0001]&AlGaN | [507] |
| MBE | Si (111) | GaN <0001> | [508] |
| CVD | InP | GaInP&GaP <111>&<311> | [509] |
| CVD | Quartz& GaSb(111),(100) | Rectangular&Hexagonal GaSb [110], Diamond cubic InSb [111] | [510] |

| | | | |
|-----|--|--|-------|
| VPE | GaAs (111)B,(001), (311)B&(110) | GaAs [111]B | [511] |
| MBE | Si (111) | GaN [0001] | [512] |
| MBE | Si (111) | GaN [0001] | [513] |
| MBE | GaAs (111)B /SiO ₂ | GaAs | [514] |
| MBE | GaAs(001)& (111)B/SiO ₂ | GaAs perpendicular to (111)B or 35° away from (001) | [515] |
| MBE | GaAs(001)& (111)B/SiO ₂ | GaAs perpendicular to (111)B or 35° away from (001), ZB [1 $\bar{1}$ 1] | [516] |
| MBE | Si (100) | GaAs ZB&WZ | [517] |
| MBE | GaAs(001)& (111)B/SiO ₂ | GaAs ZB<1 $\bar{1}$ 1>&WZ<0001> | [518] |
| MBE | GaAs(001),(111) A,(111)B/SiO ₂ | GaAs 34° away from (001) or perpendicular to (111)B | [519] |
| MBE | GaAs(111)B /SiO ₂ | GaAs | [520] |
| MBE | GaAs (111)B | GaAs ZB[1 $\bar{1}$ 1]&WZ[0001] | [521] |
| CVD | Non | ZB GaP <111> | [522] |
| MBE | Si(111) | GaAs,GaAs/AlGaAs | [523] |
| MBE | Sapphire(0001), Si(111)/(001) | GaN WZ[0001] | [375] |
| MBE | Si (001) | GaN/InGaN [0001] | [524] |
| MBE | Si (111) | WZ GaAs/ZB GaAsSb <111> | [525] |
| MBE | Si (111) | ZB/WZ/4H GaAs <111> | [526] |
| MBE | Si(111)/(001) | GaN [0001] | [527] |
| MBE | GaAs (111)B /SiO ₂ | GaAs | [528] |
| MBE | Si (111) | ZB GaAs <111> | [529] |
| CVD | Si (111) | GaP <111>/GaInP | [530] |
| MBE | Si (111) | ZB GaAs [111] | [531] |
| CVD | InP(111)B | ZB InP [111] | [532] |
| VPE | Sapphire(0001) | WZ GaN [0001] | [533] |
| MBE | GaAs ($\bar{1}\bar{1}\bar{1}$) | ZB[111]&WZ[0001] GaAs | [534] |
| MBE | Si (111) | GaAs | [291] |
| MBE | Si (111) | WZ GaN<0001> | [535] |
| MBE | Si (111) | GaAs [111] | [536] |
| MBE | Si (111) | GaAs/InGaAs | [537] |
| MBE | Si (111) | GaN | [538] |
| MBE | Si (111) | GaN [0001] | [539] |
| MBE | GaAs (001)/Si | ZB GaAs along <111>&34.5° away from substrate | [540] |
| MBE | Si (111) | ZB&WZ GaAs/WZ AlGaAs | [325] |
| MBE | Si (111) | ZB &WZ GaAs | [541] |
| MBE | GaAs (111)B | ZB GaAs [111]B | [542] |
| MBE | Si (111) | GaAs ZB[111]&WZ[0001] | [543] |
| MBE | Si (111) | Hexagonal GaAs WZ<0001>&ZB<111> Pentagonal GaAs WZ<0001>&ZB<111> | [544] |
| MBE | Si (111) | GaN | [545] |
| MBE | Si (111) | GaN | [546] |
| MBE | Si (111) | GaN | [547] |
| MBE | Graphite/SiC | ZB GaAs [111]/WZ [0001] | [548] |

| | | | |
|-----|---|----------------------|-------|
| MBE | GaAs(111)B | ZB&WZ GaAs | [549] |
| MBE | Si (111) | GaAs <111> | [550] |
| MBE | GaAs (111)B | ZB&WZ GaAs&InAs | [551] |
| MBE | Si (111) | ZB&WZ GaAs/GaAsSb | [552] |
| MBE | GaAs (111)B | GaAs/AlGaAs [001] | [553] |
| MBE | Si (111) | ZB GaAs/AlGaAs <111> | [554] |
| MBE | Si (111) | GaAs/AlGaAs | [555] |
| CBE | Si (111) | ZB GaAs <111> | [556] |
| MBE | GaAs (111)B | GaAs | [557] |
| MBE | Si(111)/ Sapphire(11 $\bar{2}$ 0) &(0001) | GaN | [558] |
| MBE | SiO ₂ /GaAs(100) | ZB GaAs | [559] |
| MBE | Si (111) | GaAs | [560] |
| MBE | Si (111) | GaP&GaAsP <111>B | [561] |
| MBE | Si (111) | GaAs | [562] |
| MBE | Si (111) | GaAs | [563] |

--Non in Substrate&Orientation column means that NW grew on boat, plate, or wall of reaction vessel.

--The references [406,462-494,532] are In-catalyzed NW synthesis (Ga/In alloy in [490,537]), the others are Ga catalyzed NW growth (Al powders or Al layers were used in [504,506,507]).

--NW orientations are the preferential growth directions, and the structures of NW are the intermixing of ZB and WZ. The detailed phases depend on the growth conditions at most of time. The real NW cannot behave as pure crystal structures, especially for non-nitride semiconductor materials.

--CVD stands for the metal organic CVD (except for [468,488]), and VPE stands for the metal organic VPE or hydride VPE. MOVPE belongs to one of chemical vapor depositions with using metalorganic compounds. Except for using metalorganic precursors, hydrides, oxides, or halides are widely used in the CVD technique. O and M in the acronyms are exchanged sometimes.

In the past ten years, Ga self-catalyst NW has been widely studied, whose growth behavior is different from that of In catalyzed NW, and whose growth processes have been better controlled through much research done especially since MBE technology was introduced. In the 1960s, Ga catalyzed gallium-group V whiskers had been grown intentionally [564] or by chance [565]. However, no matter the intentional grown GaAs whiskers, or undesirable GaAs and GaP whiskers induced as imperfections, whose advantages of pseudo 1D structure had not been understood and studied till planar semiconductor manufacturing process hitting the bottleneck and the ever-increasing demand

of size shrinkage of semiconductor devices provided. Till now, much uncertainty remains on the mechanisms driving Ga catalyzed NW growth.

In a Ga catalyzed NW growth procedure, Ga droplet acts as a solvent to gather group-V solutes. Although well-controlled vertical NW were seldom reported [507,508,536,563], good control over morphology, yield and position by tuning growth temperature, V/III ratio, influx rate, patterned oxide, and other growth parameters were studied exhaustively. Through changing the overall growth conditions, the nucleation and surface diffusion mechanisms can be altered, therefore the growth morphologies will be modulated.

The morphologies of Ga catalyzed NW depends principally on the growth temperature and its gradient. The normal growth temperatures for GaN, GaP, GaAs, and GaSb are 700-830°C, 480-700°C, 560-680°C, and 1100°C respectively. The detailed temperature windows for different material NW growth may vary with different growth technologies and substrates. For MOCVD, the growth temperatures affect the preferential decomposition of the metalorganic precursors on the semiconductor surfaces. While for MBE, the temperatures alter the sticking coefficients of the species on the semiconductor surfaces with respect to their oxide patterns. Meanwhile, the supersaturation of a Ga droplet is sensitive to the temperature dependent on the pyrolysis efficiencies. For a relative low temperature in MBE growth, the sticking coefficient of Ga adatoms on oxide is close to unity, meaning that Ga atoms will precipitate on the oxide patterns. Only when the growth temperature increases above the critical value, the sticking coefficient on oxide could be reduced, and Ga atoms would desorb from the oxide [519]. During the NW growth process, the sticking coefficient on the top surface maintaining a larger value relative to the coefficient on the sidewalls has to be well controlled and preserved, for example the sticking coefficient on the c-plane is required to be higher than that on the m-plane along [0001] growth direction. When the

growth temperature is increased above the growth temperature window, there is no tendency to induce NW growth due to decomposition, dissociation and reevaporation. The desorption of group-V atoms caused by a high temperature may reduce the number of bonds available for group-III atoms hence the growth rate will be suppressed. A low temperature can also suppress the growth and thus always be used as cooling down process to interrupt the growth at the end. In general, the length, radius, and growth rate of Ga catalyzed NW increase for higher growth temperatures, resulting from the enhancement of diffusion length at high temperatures. Different surface diffusions exhibit on the different surfaces, comprising the top and sides of NW. A relative high diffusion on the sidewalls and a relative low diffusion on the top facet are favored for NW growth. For too high growth temperatures, the absorption of species and their diffusion lengths will be suppressed, due to the reduction of the incorporation into reaction sites, too high reevaporation from the surfaces, and the decreases of the dissociation efficiencies for triethylgallium (TEGa), TBP, TBAs, TMSb [538,556]. When one half of interwire distance is larger than the diffusion length of adatoms, the adatoms far from the bottom of NW will be out of the capture area, and therefore adatoms will not make any contributions to NW growth directly. Based on the same diffusion mechanism, the saturation of growth rate and the maximum growth length should be also affected by the diffusion length. During the growth, the growth rate will reach a saturated bottleneck as the growth time going on. Besides of the diffusion length, the growth temperatures strongly affect the nucleation processes and the nucleated crystal structures [526,529]. The dependence of temperatures on the nucleation rate, growth rate, and incubation time are given in Eq.150, 151, and 234 respectively. In general, a low temperature will reduce the nucleation probability. The density and diameter of NW can be also influenced by the changes in temperatures [505,535,539]. In a similar manner as the

growth length, there is a maximum density in the intermediate temperature. Too high or too low temperatures will result in the reduction of densities, because the diffusion length and the desorption rate are affected by the temperature. A two-temperature growth strategy was studied to enhance the NW density [548]. The temperature seemed to have little influences on the phases of NW, but the effect of tapering was exacerbated with the temperature increasing [542]. The phenomena of crystal defects, the parasitic bulk growth, or the coalescence processes were suppressed by raising the growth temperatures [505,526,539]. A nonmonotonic relationship between the temperature and the fraction of vertical NW was studied in [529]. At an intermediate temperature in the temperature window, a lower fraction of vertical NW was observed because the majority of NW favored along other three nonpolar low energy $\langle 111 \rangle$ orientations.

The different V/III ratio, magnitude of the influx rate, and partial pressure, will induce different stoichiometry, deposition rates and morphologies in the Ga catalyzed NW growth. However, the relationships between them are neither simple nor linear because all growth parameters are interrelated and interact on each other. The injected precursor quantity and the pressure in self-catalyst NW growth are much smaller than that of standard planar growth. The effective V/III ratio and the absolute flux quantity impinging on the facets of NW may be lower than the measurements.

The V/III ratio has an important influence on the saturation and the size of Ga droplet, meanwhile induces the morphological and crystallographic variations in the NW formation. High supersaturation could easily induce the NW nucleation and improve the nucleation probability. Tuning the V/III ratio can alter the contact state between the droplet and NW, i.e., the contact angle, and the situation of wetting or nonwetting for a droplet atop a NW. The change of V/III ratio or the tuning the flux interruptions caused the droplet consumption

accompanied by variations of the contact angles, and thus changed the phases of NW [551,552]. When a contact angle is larger than 90° , the droplet will wet NW sidewalls. The fraction of nucleation on the triple phase line with respect to the nucleation at the center of a droplet will have a significant influence on the phase formation. Part of a droplet covering atop NW or the NW growth entering the domain of a droplet both may contribute to improving the stacking defects [556], furthermore the corresponding radial growth has to be taken into consideration. The enhancement of supersaturation by increasing V/III ratio can also improve the vertical fraction in NW growth [529].

The droplet formation and the equilibrium stoichiometry are unfavorable under a group-V atom rich condition [507,511,519,524], meanwhile the grow rate relies on the group-V rate limitation. In general, the length, radius, growth rate, and density are non-monotonic dependence on the V/III ratio and the magnitude of influx rates. The high influx quantity can offset the desorption effect caused by the high temperature. However, a higher flux can induce the NW broaden and individual NW coalesced near the substrate segment. There is an optimal V/III ratio in the Ga catalyzed NW growth, because no matter too low or too high ratios will induce the diameter becoming large and parasitic growth increasing [523,529,533,550]. A reduction of Ga incorporation rate or the enhancement of V/III ratio will decrease the growth rate, because of the effective incorporation group-V atoms decreasing with a collection area shrinking. But the density of twins will be reduced with a lower Ga incoming rate [542]. A high Ga influx quantity or a low V/III ratio can lead to an inverse tapered [514,526,556,557,563], because the droplet is not fed with enough Ga atoms to compensate for the consumption in the Ga particle, and a similar phenomenon was exhibited in In catalyzed NW too. A reverse tapered behavior was exhibited in [542]. The dependence of a V/III ratio on the density was studied in [526,535,539,542,550,562], and

the density can saturate at a certain value caused by the diffusion effect. The pressure correlation with the incorporation material rate, chamber geometry, and temperature plays an important role in determining the growth behavior of self-catalyzed NW. The partial pressure P_{III-V} for the precursors is defined by [88]

$$P_{III-V} = \frac{I_{III-V}}{I_{total}} \cdot \frac{P}{P_{const}} \exp\left(m - \frac{n}{T}\right) \quad (235)$$

where I is the flow introduced, and P_{const} is a defined fixed pressure in the bubble. m and n are the vapor pressure parameters to account for the relationship between the temperature and materials respectively. The impinging vapor flux and the adsorption rate dependence on the pressure are given in Eq.182 and 158. A. F. i Morral et al. obtained a linear relationship between As_4 pressure and the growth rate v in the experiments [514],

$$v_{GaAs} = M_{As_4} + N_{As_4} \cdot P_{As_4} \quad (236)$$

where M_{As_4} and N_{As_4} are the experimental data. They equal to -7.37×10^{-2} and 5.26×10^5 respectively for Ga catalyzed GaAs NW on a GaAs (111)B substrate. The higher group-V partial pressure is, the faster coalescence and growth are for self-catalyzed NW growth [511,513,514]. The stable dimers or trimers on the surfaces can be formed at a high pressure, and the production of these polymers may retard the growth process.

III. F. Template-Assisted & Selected-Area Nanowire Growth

The drawbacks of pseudo 1D NW growth can be further magnified, resulting from having troubles in controlling the morphology and uniform arrays. Membrane templates or partially masked substrates, can be applied by controlling the nanopores to realizing the uniform diameter, vertical growth, and desired diffusion mechanisms. In these

circumstances, not only the advantages of well controlling of the morphology in a foreign-metal catalyzed technology, but also the advantages of prevention of introducing the contaminations in a self-catalyzed technology, are expressed at the same time. In the 1990s, a template synthesis method was proposed by C. R. Martin et al. [566-568]. Now exploiting the pores of nanoporous membranes and patterned substrates with oxide assist have been the most common methods.

Group II-VI semiconductors were synthesized in nanopores with monodisperse diameters [566], and the overall morphologies were improved by a template restriction for the growth dimensions. The density and distribution of pores in alumina performed much better than that of a polycarbonate template [567,568]. The synthesis of group III-V NW can be achieved in an anodic alumina membrane that has a packed array of hexagonal cells. Highly ordered porous alumina cells can be produced through anodization under appropriate conditions. A two-step molding process was proposed to fabricate the alumina membrane [569], whose hexagonal columnar array favored to induce hexagonal WZ GaN NW growth along the channel axis [570,571]. A similar method based on a mixed template comprised of carbon nanotube and porous alumina was developed for the GaN NW fabrication [572]. Although graphene lacked of dangling bonds for fabricating heterostructure growth, graphene layers still were developed for templates to induce InAs [573], GaAs [548] vertical NW growth, due to the lattice mismatch accommodation, and a larger grain size in the graphene.

Oxides are commonly used to realize the physical confinement growth, and the growth methods can be separated into using chemical oxide composition assisted and using oxide or nitride pattern mask. The oxides assisted method was used to assist Si or Ge NW growth previously [574-576]. The mechanisms of oxides inducing NW growth with significant

distinction for above mentioned catalyst induced or self-catalyzed mechanisms are not entirely understood. The differences in the different mechanisms are expressed, mainly resulting from oxygen exhibiting the inhibiting effect in VLS growth [577]. In oxide assisted group III-V NW growth, precursors made by laser ablation decomposition or pyrolysis of group III-V semiconductor sources will react with suboxides. Precursors caused by the decomposition of group III-V semiconductors reacted with Ga_2O_3 [578,579] or In_2O_3 [580], then the volatile productions of reactions and group-V atoms fabricated group III-V NW surrounded by the thin passivating gallium oxide or indium oxide films. The volatile oxides induce the nucleation processes, and the amorphous suboxide shells retard the radial growth. The oxide assisted growth mechanisms can stem from the melting point depression at the tip of NW, where precursors are preferentially absorbed then deposite. Meanwhile, a high density of defects and dislocations provide plenty of channels to facilitate atoms diffusion. Strain energies, bonding energies, surface energies and the fraction of oxide in group III-V semiconductors and oxides need to be studied further to improve the randomly oriented and ununiformed diameters.

Oxide or nitride patterned masks are always employed to assist the group III-V NW growth. A selective area growth combines both top-down mature fabrication and bottom-up atomically precise controllable epitaxial technologies. The synergy between these technologies can reduce the adverse effects caused by the dimension fluctuations of NW. However, there is a tradeoff between the compatibility with traditional lithographic techniques and etching technologies, and the faults and limitations caused by lithography and chemical etching. On the whole, the vertical array growth can be substantially improved and the morphologies can be modulated further through oxide or nitride masks. The pattern mask method can be categorized into exploiting the additive processes to introduce oxide or

nitride masks [475,476,482,511,514-516,518-520,528,559,581-591] or applying native oxide plates on silicon substrates [325,472,475,485,544,560,562,592-594, and the most of references in which silicon substrates used in Table 2].

Hexagonal or circular mask openings are etched on no matter sputtered films, native oxides, thermal oxides or spinning HSQ for preparing uniform arrays for hexagonal NW growth. Circular openings may be created unintentionally due to the lithographic resolution and wet chemical etching limitations. Hexagonal cross-section group III-V NW are grown from the nanoholes on substrates, therefore the lateral growth and the coarsening effect at the bottom of NW can be suppressed by the masked oxides. The radial sizes of NW are modulated by the lithographic dose and the shapes of nanoholey arrays. The length and the growth rate of NW depend on the fraction of openings on the whole substrate, because of the NW growth deriving from the diffusion of adatoms incorporated onto the NW facets and the masked substrate. In general, the length of NW decreases with the enhanced nanohole size or the reduced interwire distance. The dependence of morphologies of NW on the growth parameters has been discussed above. For NW growth on an oxide mask, the variations of growth parameters may affect the oxide mask, and therefore modulate the morphology and position as well as the density of NW array further. The temperature window has to be limited more stringently because a too high temperature may lead to the decomposition of oxides and impair the patterns on the mask. The position and density of NW are determined by the initial ensemble of droplets and the thickness of oxides. Nucleation preferentially occurs at the edges of nanoholes in a mask [592], meanwhile, the nucleation process and vertical fraction can be improved through modulating the microstructures of substrates [558]. The yield of NW nucleation covering the nanoholes depends on the sizes of the nanoholes and increases with the reduction of oxide thickness.

Small nanoholes with smaller capture areas may retard the adatom diffusion into the holes therefore the yield of NW will decrease in the situation of extremely small holes. Meanwhile, the higher diffusion length is, the lower density is, because of the adatoms near the nucleation sites assembling together. The nucleation and density of NW can be also affected by the surface roughness that is correlated to the interface between oxide and substrate. The dependence of the critical thicknesses, the qualities, and the interfacial roughness of oxides on different preparing methods is summarized and systematically compared by A. F. i Morral et al. [560]. The drawbacks of an oxide template are not only high-cost and complex lithographic processes, but also the uncontrollability of wet chemical etching processes. An improved droplet predeposition method was used [562], in which droplets were first grown on the oxide-free substrates, followed by the substrates were oxidized to assist the NW growth. This method can dumb down the complexity of fabrication process. Nanopatterned fabrication with an oxide template makes wet chemical etching hard to reach the required depth. Some other problems emerge in nanopatterned methods. The initiating NW growth on the oxides may cause the nonvertical directions, meanwhile unremoved-oxides or reoxidized openings will reduce the density of NW. The situation of growth occurred on oxides and the phenomenon of NW growth preferentially along nonpolar low energy $\langle 111 \rangle$ directions can exacerbate the nonvertical growth, but this case can be improved through suppressing the oxide thickness [514].

III. G. Summary

This chapter presents the bottom-up compatible with the mature optical lithography. The developing E-beam, EUV, nano-imprint, and directed self-assembly methods provide

diversity, flexibility, and low-cost in the design of NW and allow more advanced functionalities for NW devices. These advanced sub-10 nm lithographic techniques take advantages of the precision and repeatability of the top-down fabrication to produce vertical and uniform NW arrays on pattern masks. For randomly aligned NW, they have to be assembled by some assembly techniques, such as Langmuir-Blodgett assembly [595,596], field driven assembly [446], microfluidic assembly [597], and some other chemically driven techniques. The bottom-up growth has been discussed in detail by reviewing the VLS and VLS-like growth mechanisms. In the VLS, reactants from vapor phase form supersaturated liquid alloys, and then crystallize at the droplet-NW interface. The processes make sure that the condensation assisted by catalysts is much faster than the growth on the substrate. For the VSS, a solid catalyst can induce the multigrain unintentionally, but the solid phase can reduce the atom interdiffusion. No matter extrinsic catalysts, or intrinsic group-III elements, can control the anisotropic growth, determine the phase of NW, and incorporate dopants accompanied with *in situ* growth simultaneously. Meanwhile, these catalysts can induce compositionally abrupt and structurally perfect under appropriate growth parameters. The complex phase diagrams for transition metal-group III-V need to be further studied to determine and analyze the phases of NW. Appropriate catalysts for group III-V NW growth should be chosen to meet many criteria about alloy melting point, extra electron states, resistance to parasitic reactions, high-efficient diffusion, and some key thermodynamic parameters.

IV. Controllable Physical, Chemical, Electronic, and Photonic Properties of Nanowire

A more comprehensive description for group III-V NW growth will have to include the understanding for the detailed growth techniques. NW growth occurs far from the thermodynamic equilibria in the common techniques of growing group III-V semiconductors, i.e., MOCVD (MOVPE) as an advanced industrial growth technique, and MBE as a high-quality laboratorial growth technique. Many continuously improved models facilitate a better understanding for the physical and chemical procedures in NW growth and predict quantitatively experimental observations. The precursors of different growth processes stem from the volatile species containing the constituent elements and the compound or its constituent elements from amorphous sources or polycrystalline species. The growth processes are not only controlled by the mechanics of thermodynamics and kinetics, but also affected by the chemical reactions, mass transport, and hydrodynamics. Heat transfer, temperature distribution, and the species velocity field depend on the geometry of reactors or the growth techniques. Actually, the effect of each parameter that controls the group III-V NW growth has not been revealed clearly till now. Reduced computational cost and relatively simple models or empirical equations are provided to analyze the changing tendency in experiments. No matter exploiting chemical methods, or applying physical methodologies, would be expected to alter the overall growth morphology, and subsequently affect the properties and qualities of NW by changing the overall growth conditions.

IV. A. Physical and Chemical Processes

In MOCVD (MOVPE) growth technique, metalorganic compounds in vapor phase are supplied as precursors to the substrate with an inert carrier gas, such as hydrogen, deuterium, helium, or nitrogen [88,105,598,599]. Meanwhile, the carrier gas is also used as a coolant in the reactors and outer tubes. The influxes saturated with the metalorganic precursors are injected into a reactor under well controlled fluxes. The component elements of crystal are transformed into volatile agents through thermal evaporation, sputtering, or laser ablation. Large temperature gradients and concentration gradients take place in the reactor, and the elimination reaction occurs under appropriate growth conditions. However the details of reactions are uncertain, there seem to be dozens of species and several hundred detailed reactions in real chemical deposition procedures [599,600]. The reactions mention the processes of decomposition, recombination, adsorption, desorption and surface reactions. Forward and reverse reactions make the proposed mechanisms involve complicated species participating in a large number of gas-phase or surface reactions. The fluxes of reactants are controlled by switches, and the chosen species are easy for decomposition but can still store for mass transport formation in a long period to promise the compounds growing on the required sites. The rate of chemical reaction k obeys the Arrhenius law related to the activated energies of precursors E_{pre} ,

$$k = C_{Arr} \exp(-E_{pre}/RT) \quad (237)$$

where C_{Arr} is the preexponential factor. The ratio between the concentration of initial state n_i and that of final state n_f is determined by the Gibbs free energy difference between the chemical reactions, and the ratio equals to the inverse ratio of the kinetics between the forward and reverse reactions [599],

$$\frac{n_i}{n_f} = \exp\left(\frac{\Delta G}{RT}\right) = \frac{k_{rev}}{k_{for}} \quad (238)$$

The interreactions and pyrolytic decomposition of organometallic reactants are considerably complicated. The group-III organometallic compounds are planar with sp^2 bonding and their pyrolysis is studied in low temperatures. The transition states involved in the abstraction by different kinds of radicals, i.e., atomic H radical, and alkyl radicals, involve the breaking and formation of different kinds of bonds, such as H-C, H-metal, C-metal, H-H, C-C, and metal-metal. The bond strength of C-C decreases as the enhancement of the number of C atoms bonding to the central carbon in the alkyl. In the homolytic fission processes for decomposition of group-III organometallic compounds, trimethyl-III decomposes into dimethyl-III and monomethyl-III through the loss of the methyl radicals, in which monomethyl-III can be a more stable product in the decomposition. The methyl radicals produced from the decomposition can subsequently react with group-V organometallic compounds or atomic hydrogen radicals. The hydrogen can react with trimethyl-III or dimethyl-III in the hydrogenolysis reactions, and dimethyl-III or monomethyl-III and methane are produced in the reactions. Hydrogen or radicals can also react with dimethyl-III or monomethyl-III, and these processes produce by-products. The corresponding by-products can recombine with atomic hydrogen or radicals to produce methylated-III products. In the situation of a high input cation alkyl concentration, the free radicals favor to recombine with hydrogen and methyl radicals. The activated ethane is produced through the methyl radical recombination, and some reactions occurred with ethyl and propyl radicals are indispensable, thus alkenes are produced in the reactions. The detailed mechanisms of the reactions and decompositions occurring in group-V organometallic or hydridic species are still unclear. The common homolytic fission and

hydrogenolysis reactions are also the major reactions in the group-V organometallic and hydridic species. The pyrolysis of group-V organometallic species produces different reactions through different types of intramolecular coupling reactions. Methane is produced as methyl radicals recombines with the H radical from the group-V hydrides.

The surface reactions in MOCVD are extremely complicated because of involving a large number of reactions and species absorbed on the different orientations of surfaces. At first, the adatoms bound to surfaces only by a weak physisorbed effect and subsequent form stable chemical bonds with the atoms at bottom layers. The surface and H radicals can catalyze the decomposition of trimethyl-III organometallic species. Controlling the growth parameters suppresses the processes of the atomic H or methyl radicals and carbene species adsorbed on the surface free sites. The fractional coverage dependence on the adsorption or desorption rates are given in Eq.158 and 159. Considering the sticking coefficients affected by the steric factor, the fraction coverage, and the activation barrier for adsorption of species, the adsorption rate can be written by [600,601]

$$k_{ads} = \left(P / \sqrt{2\pi m_i RT} \right) x^i s^i \propto \frac{P_i}{\sqrt{2\pi m_i k_B T}} \exp \left(-\frac{\Delta E_{ads}}{k_B T} \right) \quad (239)$$

where m_i , x^i , s^i are the molecular mass, molar fraction, and sticking coefficient of the species i , respectively. The dependence of transition state on the distance from a layer to vapor phase is plotted in Fig. 2. When the growth temperature is controlled below the eutectic temperature of group-III and catalytic metals, the sticking coefficient will become near to unity.

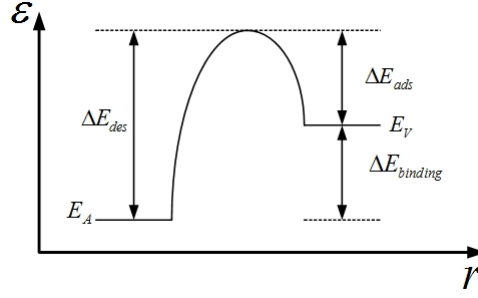


Figure 2. The dependence of transition energy on the transition distance.

In a MOCVD system, the growth occurs as the existence of a driving force between different phases. The driving force caused by a chemical potential difference stems from the supersaturation variation caused by a temperature difference in the tube. The supersaturation is defined as a difference in chemical potential between a supply phase and an accept phase. If a three phase system is referred, the driven force between vapor and liquid, vapor and substrate, vapor and NW side-wall, liquid and solid, liquid and NW top can be expressed in terms of the difference of the chemical potentials (Actually, the top facet and sidewall facet of NW have different supersaturations due to the varied surface structures.),

$$\xi_V = \exp\left(\frac{\Delta\mu_{VN}}{k_B T}\right) - 1 \approx \frac{d\delta}{dt} \frac{J\tau_{des}}{n_{eq}\sqrt{S_{atom}}/\pi} - 1 \geq \xi_A = \exp\left(\frac{\Delta\mu_{AN}}{k_B T}\right) - 1 > \xi_L = \exp\left(\frac{\Delta\mu_{LN}}{k_B T}\right) - 1 = \frac{n}{n_{eq}} - 1 \quad (240)$$

where

$$\begin{aligned} \Delta\mu_{VL} &= \mu_V(n_V) - \mu_L(n_{supersaturation}) \\ \Delta\mu_{VS} &= \mu_V(n_V) - \mu_S(n_{eq-substrate}) \\ \Delta\mu_{VN} &= \mu_V(n_V) - \mu_N(n_{eq-nanowire}) \\ \Delta\mu_{LS} &= \mu_L(n_V) - \mu_S(n_{eq-substrate}) \\ \Delta\mu_{LN} &= \mu_V(n_V) - \mu_N(n_{eq-nanowire}) \end{aligned} \quad (241)$$

$$\Delta\mu_{VN} > \Delta\mu_{VL} > 0 \quad \text{and} \quad \Delta\mu_{VS} > \Delta\mu_{VL} > 0 \quad (242)$$

When S_{atom} is the surface area per atom in a monolayer, and the chemical potential of a droplet is below the upper bound $\Delta\mu_{\text{VN}}$, the droplet accommodates or collects precursors from ambient vapor. The supersaturation is defined in terms of the chemical potentials in Eq.240, as the thermodynamic driving force. And the system is maintained supersaturation when the difference of chemical potentials is positive in Eq.242. In general, the chemical potential difference between a vapor phase and a solid phase will decrease with the temperature. When the chemical potential differences in Eq.241 decreases to zero, the system will have a tendency towards the state of equilibrium, or the system keeps undersaturated with a negative chemical potential difference.

NW growth occurs as the supersaturation of adatoms is lower than that of the impinging gas, thus the force between vapor or diffusion fluxes to a catalyst is positive and the catalyst can accommodate the impinging species. When the driving force decreases to zero, the system will maintain at equilibrium. The absorbed atoms can be reevaporation or desorption if the driving force is negative. Eq.242 compares to the driving forces at different sites, thus suggests that the supersaturation has to be controlled above a certain value to satisfy the growth requirement. The supersaturation of a catalyst is always maintained nearly constant as far as possible in the experiment through controlling nucleation processes and influxes. Meanwhile, a high supersaturation preferably promotes an axial over radial growth in NW.

In general, the chemical reactions are temperature activated. The heat generated or consumed of reactions is ignored because of the precursors being diluted in the carrier gas, and therefore the reactions will not induce a temperature disturbance in MOCVD. Meanwhile, the flow pattern and transport phenomena are also temperature sensitive, so the temperature and its distribution are very critical in group III-V NW growth. At a low

temperature, the decomposition of precursors is limited due to the thermally activated processes. As the temperature increasing, the available free adsorption sites are enhanced resulting from the degree of precursor precracking and the arrival of species improved by the growth temperature. If the growth temperature is raised too high, the growth rate decreases with a too large desorption rate. The higher the deposition rate is, and the larger temperature gradient normal to the substrate is.

In the reactor of MOCVD, group-III precursors decompose to intermediate species, and transport to the surface via the convection and diffusion mechanisms. The transport of energy and mass by diffusion and convection mechanisms play an important role in determining the chemical reactions and the fluid behaviors in MOCVD. Near the substrate, the effect of convective flows is relatively small, so the surface diffusion will be dominant. The driven flux of adatoms is described in Eq.161, and 163-167. Far away from the substrate, the diffusion in gas phase is driven by convective flow, thermodiffusion, or concentration gradient. The flux of species i controlled by its partial pressure and temperature is given by

$$J_i = \frac{1}{k_B T} \left[P_i u - D_i \nabla P_i - D_i \alpha_i \frac{P_i}{T} \nabla T \right] \quad (243)$$

where α_i is the thermal diffusivity in heat transfer, and u is the flow velocity. In the view of adsorption and desorption, the incidence of flux on the surface in Fig. 1 can be written,

$$J_i = \frac{s^i (P_{i-eq} - P_i)}{\sqrt{2\pi k_B T m_i}} \quad (244)$$

The partial pressure has an important influence on not only the change in the temperature field, but also the extent of decomposition of organometallic species. Actually, the influences caused by sticking coefficients and temperatures are relatively small, so the

incident flows in above equations are controlled mainly by the partial pressure in experiments. Low partial pressure induces the reduction of surface coverage, and promotes the trimethyl-III precursors decomposition. The axial velocity relative to the entrance velocity in the horizontal reactor depends on its local temperature [600],

$$u_{axis} = 2 \langle u_{axis} \rangle_{in} \left[\frac{(r_{rea}^2 - r_{loc}^2) T_{loc}}{T_0 r_{rea}^2} \right] \quad (245)$$

where the subscripts rea and loc indicate the reactor and the location in reactor respectively, and the subscript in stands for the parameters in the entrance.

The actual flow field in MOCVD reactors is 3D without a particular symmetry, due to the complex heat transfer, convection, buoyancy effects, and complicated reactor geometries. Therefore complicated nonlinear transport phenomena with multiple flows exist in the reactors. The heat transfer encompasses the radiation heat transfer between solid surfaces, conduction in the gas, walls and a susceptor, as well as the convection in the gas phase species. A destabilizing temperature gradient caused by a heat flow and different temperature walls will induce convection in the gas phases. The forced convection may be caused by the rotation of a susceptor. Natural convection produces flow recirculations in the reactors resulting from different temperature gradients and concentration gradients. Meanwhile, the flow is generated by buoyancy due to the existent of a large temperature gradient between the cold walls and a hot susceptor. A phenomenon that small particles in the reactor are driven away from a hot surface and towards a cold one is called thermophoresis. This mechanism dominates to induce mass transfer in the situation of existence of temperature gradient. The phenomenon of vortices can occur at a high density of species or a large temperature gradient.

For different geometrical reactors in MOCVD growth technique, the actual convection, diffusion, and flow recirculation are totally different. The geometries of reactors can be roughly divided into horizontal [602-614] and vertical [606,612,615-620] structures. Some chemical kinetic models and transport phenomena models are provided to simulate the fluid mechanisms, heat transfer and their influences on the growth. Actually, there is no appropriate or precise models provided for group III-V NW growth in MOCVD. Fortunately, fluid mechanics and heat transfer in film growth models can be applicable in NW growth. Even if the surface of substrate in the traditional film model is different with the substrate of NW growth, the fluid mechanics and heat transfer in the reactor are roughly similar. But the mechanisms of mass transfer are different for the zones near and on the substrate surface. So the diffusion mechanism dominates for mass transfer near and on the substrate. However, the unflatness of structure is indispensable to disturb flows in the reactors.

In horizontal MOCVD reactors, the fluid flow models are described to simulate the fluid mechanics involving the momentum, energy, and species conservation. The conservation of linear momentum is described by the Cauchy momentum equation (The Cauchy momentum equation transforms into the Navier-Stokes equations under different fluid conditions) [621],

$$\frac{\partial u}{\partial t} + (u \cdot \nabla)u - \frac{1}{\rho} \nabla P_{dy} = g + \nu_k \nabla^2 u \quad (246)$$

where dyadic P_{dy} is the component of stress, ρ is the density that consists of the product of the concentration of gas species and its mole fraction, g is the gravity, and ν_k is the kinematic viscosity that depends on temperature and pressure. The terms in Eq.246 stand for the local acceleration, the convective acceleration, the pressure acceleration, the gravity acceleration, or the viscous deceleration of the species, respectively. The 2D fluid flows in a

horizontal reactor can be written as the Cauchy momentum equation (Define the axial direction as z-direction, the vertical direction as y-direction, and the transverse direction as x-direction) [602-605,609],

$$\frac{\partial u}{\partial t} + \left(u_y \frac{\partial u_z}{\partial y} + u_z \frac{\partial u_z}{\partial z} \right) + \frac{1}{\rho} \frac{\partial P}{\partial z} - \frac{1}{\rho} \frac{\partial}{\partial y} \left(\frac{\partial u_z}{\partial y} + \frac{\partial u_y}{\partial z} \right) - \frac{\partial}{\partial z} \left[v_k \left(\frac{4}{3} \frac{\partial u_z}{\partial z} - \frac{2}{3} \frac{\partial u_y}{\partial y} \right) \right] = g \cos \phi \quad (247)$$

$$\frac{\partial u}{\partial t} + \left(u_y \frac{\partial u_y}{\partial y} + u_z \frac{\partial u_y}{\partial z} \right) + \frac{1}{\rho} \frac{\partial P}{\partial y} - \frac{\partial}{\partial z} \left[v_k \left(\frac{\partial u_z}{\partial y} + \frac{\partial u_y}{\partial z} \right) \right] - \frac{\partial}{\partial y} \left[v_k \left(\frac{4}{3} \frac{\partial u_y}{\partial y} - \frac{2}{3} \frac{\partial u_z}{\partial z} \right) \right] = g \sin \phi \quad (248)$$

where ϕ is the orientation angle with respect to the horizontal position. The conservation of mass is described by a continuity equation [105,609,611,621], consisted of a local change and a convective change.

$$\frac{\partial \rho}{\partial t} + \nabla \cdot (\rho u) = \frac{\partial (x^i n_i)}{\partial t} + \nabla \cdot (x^i n_i u_i) = 0 \quad (249)$$

In an ideal gas model, the momentum conservation equations are coupled with the energy balance [105,604,605,609],

$$C_p \frac{\partial T}{\partial t} + C_p \left(u_y \frac{\partial T}{\partial y} + u_z \frac{\partial T}{\partial z} \right) - \frac{1}{\rho} \frac{\partial}{\partial y} \left(k_v \frac{\partial T}{\partial y} \right) - \frac{1}{\rho} \frac{\partial}{\partial z} \left(k_v \frac{\partial T}{\partial z} \right) = 0 \quad (250)$$

where C_p is the heat capacity of vapor, and k_v is the thermal conductivity of the carrier gas.

The mass conservation equation is coupled with the energy balance [105,611],

$$\frac{\partial (x^i n_i)}{\partial t} + \nabla \cdot \left[n_i D_i (\nabla x^i + k_{vi} \nabla \ln T) \right] = 0 \quad (251)$$

where D_i is the thermodiffusion coefficient. The thermodiffusion is very important due to a large temperature gradient in the growth process. The heat conduction for NW nucleation has been given in Eq.187, and the heat conduction in reactor is described by,

$$k_w \nabla^2 T_w = 0 \quad (252)$$

where k_w is the heat conductivity of reactor walls. The temperature of wall is determined via a combination of heat transfer by radiation, conduction, and convection. The speed of heat conduction process related to the convection velocity depends upon the flow rate. From Eq.250-252, energy transfer and momentum transfer gives rise to temperature gradients and velocity gradients.

The flow pattern can be modulated not only by the geometries of sidewalls, but also the tilting susceptor with an angle diverging from the horizontal, as well as the introduction of baffles. a tilting susceptor can provide a more uniform temperature layer above the susceptor due to transverse temperature variations across the susceptor, and thus improve the uniformity of growth process [604,606,607]. The vorticity including eddies caused by turbulence can be written as the curl of velocity [621,622],

$$\zeta = 2\omega_{angular} = \nabla \times u \quad (253)$$

where $\omega_{angular}$ is the angular velocity. The vorticity transport can be derived from the curl of Eq.246,

$$\frac{\partial \zeta}{\partial t} + (u \cdot \nabla) \zeta - (\zeta \cdot \nabla) u = \frac{1}{\rho} \nabla \times \nabla P_{dy} + \nabla \times g + \nu_k \nabla^2 \zeta \quad (254)$$

The cold finger effect in the upper part of a reactor induces the asymmetry of temperature gradient, transverse rolls, as well as the disturbances of thermal-diffusion, convection, and chemical reactions [609,623], meanwhile the heat transfer and the heat radiation from a hot wall to cold flows are involved in the phenomenon. Therefore the cold finger phenomenon becomes more pronounced at gases with a lower thermal conductivity. The cold finger effect in MOCVD can be suppressed as conduction is maintained sufficiently faster than convection.

The boundary conditions are especially important for the above differential equations. For a incompressible flow, the tangential velocities of species should be zero near the outside boundary. For a slip flow, the viscosity of species may affect the fluid. The boundary conditions can be controlled by the geometry of the reactor, and the growth parameters in detailed experiments. The actual boundary conditions and the detailed growth parameters should be divided into several regions along the direction of flow in a horizontal reactor due to the different growth rate, pressure, and temperature in different regions, such as a susceptor is isotherm as a whole region, otherwise its front or back region is colder than itself as different regions.

In vertical MOCVD reactors, reactants are incorporated with a carrier gas and impinge perpendicularly on the rotated substrate. A fluid flow model is described to transfer energies and species through an axisymmetric conduit structure. The momentum conservation of laminar pipe flow can be written as the Navier-Stokes equations in cylindrical coordinates (Define the axial direction as z-direction, the radial direction as r-direction, and the azimuthal direction as ϕ -direction) [615-617,621],

$$\begin{aligned} & \left(\frac{\partial u_r}{\partial t} + u_r \frac{\partial u_r}{\partial r} - \frac{u_\phi^2}{r} + u_z \frac{\partial u_r}{\partial z} \right) - \frac{1}{r} \frac{\partial}{\partial r} \left\{ v_k r \left[\frac{4}{3} \frac{\partial u_r}{\partial r} + \frac{2}{3} \left(\frac{u_r}{r} + \frac{\partial u_z}{\partial z} \right) \right] \right\} \\ & = g_r - \frac{1}{\rho} \frac{\partial P}{\partial r} + \frac{\partial}{\partial z} \left[v_k \left(\frac{\partial u_z}{\partial r} + \frac{\partial u_r}{\partial z} \right) \right] - \frac{v_k}{r} \left[\frac{4}{3} \frac{u_r}{r} - \frac{2}{3} \left(\frac{\partial u_r}{\partial r} + \frac{\partial u_z}{\partial z} \right) \right] \end{aligned} \quad (255)$$

$$\left(\frac{\partial u_\phi}{\partial t} + u_r \frac{\partial u_\phi}{\partial r} + \frac{u_\phi u_r}{r} + u_z \frac{\partial u_\phi}{\partial z} \right) + \frac{1}{r^2} \frac{\partial}{\partial r} \left[v_k \left(r^2 \frac{\partial u_\phi}{\partial r} - r u_\phi \right) \right] = g_\phi - \frac{1}{\rho r} \frac{\partial P}{\partial \phi} + \frac{\partial}{\partial z} \left(v_k \frac{\partial u_\phi}{\partial z} \right) \quad (256)$$

$$\left(\frac{\partial u_z}{\partial t} + u_r \frac{\partial u_z}{\partial r} + u_z \frac{\partial u_z}{\partial z} \right) - \frac{1}{r} \frac{\partial}{\partial r} \left[v_k r \left(\frac{\partial u_z}{\partial r} + \frac{\partial u_r}{\partial z} \right) \right] = g_z - \frac{1}{\rho} \frac{\partial P}{\partial z} + \frac{\partial}{\partial z} \left\{ v_k \left[\frac{4}{3} \frac{u_z}{z} - \frac{2}{3} \left(\frac{\partial u_r}{\partial r} + \frac{\partial u_r}{\partial r} \right) \right] \right\} \quad (257)$$

The actual mass conservation, the momentum and mass conservations coupled with the energy balance, as well as vorticity transport in a vertical reactor are also the Navier-Stokes

equations based on cylindrical coordinates in similar representations in a horizontal reactor. For a vertical reactor, jet penetrating should be prevented, because the jet phenomenon increases the mass transfer in the center and reduces the mass transfer near the edge due to upflows in the convection [616]. The enhanced of spinning speed or the increase of susceptor rotating can assist to improve the poor uniformity caused by jet.

For no matter horizontal or vertical reactors, the simulation models are transformed into a set of nonlinear coupled partial differential and algebraic equations. The nonlinear equations can be discretized by the Petrov-Galerkin finite element method [624-628], and the computational domain is discretized into a mesh on which the solution field is approximated by piecewise continuous Lagrangian polynomials. Massively parallel computer codes, i.e., MPSalsa code [629], N3S-MUSCL industrial code [630], or SPIN code [631] can be used to simultaneously solve a set of coupled partial differential equations. The properties of gas-phase multicomponent, viscosities, diffusion coefficients, thermal conductivities, and thermal diffusion coefficients can be evaluated by a FORTRAN code [632] and a TRANSPORT code [633] in CHEMKIN library, as well as a FORTRAN code in TRANLIB library [634]. Coupled fluid flow, heat transfer, multicomponent species transport and chemical reactions governed by equations of continuity, momentum balance, energy balance, and mass transport, can be solved quantitatively.

There is a tradeoff between lost accuracy in excessively oversimplified assumption and computational cost savings. However, Oversimplified models are unable to predict the group III-V semiconductor growth, and thus cannot produce the results in agreement with experimental data quantitatively, resulting from the complex geometry, wrong empirical coefficients and correlations, as well as the oversimplified properties of fluids such as mass diffusivity, kinematic viscosity, surface tension, and so on. Constructing a fully 3D flow

structural model for group III-V NW growth will contribute to predict the growth processes quantitatively and qualitatively.

MBE technique operates via physical vapor depositions and chemical reactions of thermal atoms or molecules directly to form an ordered structure at an ultrahigh vacuum. The early collimated molecular beams were used to grow GaAs layers in the late 1960s [635-638]. Through exploiting molecular beams under a high vacuum, the production of pure epitaxy semiconductors and the controlling of the composition at the atomic level became feasible. NW growth in MBE under high nonequilibrium conditions is driven by the differences in surface energies, sticking coefficients, and diffusion coefficients on different crystal planes. In gas source MBE, group III-V materials deposit and condense on the substrate, whose growth mechanisms are similar with the mechanisms described in CVD section. The pyrolysis and cracking of group-III metalorganic species and group-V hydrides provide group-III and group-V elements separately meanwhile some by-products are produced in the reactions. In common solid source MBE, either group III-V compounds or high purity group III/V elements are used as the sources of molecular beams, which can be externally stored and renewed in Knudsen effusion cells.

The MBE assembly consists of the generation region, the mixing region, and the condensed region [105]. The decomposition of compounds or the evaporation of condensed sources from a cracker tube or a Knudsen cell provides mixture of dimers and tetramers, as well as elemental molecular beams. The ratio of tetramers to dimeric molecules depends on the growth temperature in a chamber. The state of a effusion system can be modulated by its pressure and temperature. According to the Gibbs phase rule, only one degree of freedom in the system because of one component existing under the solid-vapor phase transformation, so pressure and temperature in cells are interrelated (If existing solid and liquid phases for a

component, the degree of freedom is two, hence temperature and pressure are independent). The pressure in the cell and the effect of pressure on the phase transformation can be estimated by the Clausius-Clapeyron equation,

$$dT^{\alpha \rightarrow \beta} = \frac{T^{\alpha \rightarrow \beta} \Delta V^{\alpha \rightarrow \beta} dP}{\Delta H^{\alpha \rightarrow \beta}} \quad (258)$$

The change of temperature is linear with the change of the applied pressure. The exponential prefactor E_{cell} is affected by the material and the geometry of cell.

$$P = E_{\text{cell}} \exp\left(-\frac{\Delta H}{k_B T}\right) \quad (259)$$

where ΔH is the latent heat or the enthalpy of vaporization. In Knudsen cells, the driving flux generation bases on the solid-vapor phase equilibrium. The equilibrium pressure is maintained when a solid source material in thermodynamic equilibrium with its vapor under the pressure $P_{\text{eq-V-E}}$. Actually, the equilibrium pressure can be maintained in the whole cell, due to a very small orifice of cell. According to Eq.259, the equilibrium pressure inside a cell at different growth temperature can be derived,

$$\ln\left(\frac{P_{\text{eq-V-E}}}{P_{\text{eq-T}_0}}\right) = -\frac{\Delta H}{k_B} \left(\frac{1}{T} - \frac{1}{T_0}\right) \quad (260)$$

where $P_{\text{eq-T}_0}$ is the equilibrium pressure at temperature T_0 . The outcoming flux from a orifice into the chamber has to be replenished by the equal quantity of material evaporated from the condensed phase to maintain the equilibrium pressure in the cell. The outcoming flux and the replenished quantity satisfy the mass conservation and the dynamic equilibrium.

Followed by the generation processes, the constituent elements are transported from a effusion cell to substrate via molecular beams. There is a checks and balances between the phases and the equilibrium partial pressures for outcoming species. In a chamber, extremely

low pressure reduces the collisions and the interactions between molecular beams and background gas-phase matters. The macroscopic equilibrium of interactions is governed by thermodynamics and kinetics,

$$\prod_i P_i = \varepsilon_{\text{compound}} \exp\left(\frac{\Delta S - \Delta H}{k_B T}\right) \quad (261)$$

where $\varepsilon_{\text{compound}}$ is the activity coefficient of compound and it is proportional to $\exp(\mu_i/k_B T)$. P_i is the corresponding partial pressure of species i including the outcoming elements and the residue gas. Based on Eq.261, the detailed partial pressure of specie can be derived. The actual pressure of MBE system is much lower than that of MOCVD system, and the common order of magnitude of background pressure may be reduced to 10^{-9} - 10^{-10} Torr in the MBE chamber. In general, the partial pressure of group-V ($\sim 10^{-5}$ - 10^{-7} Torr) is considerably greater than that of group-III ($\sim 10^{-7}$ Torr) [477,534,552]. Group-V partial pressure is modulated to be larger than the partial pressure of group-III atom in an experiment, because group-V atoms will not stick to the surface in the absence of group-III atoms [172,635-637]. Therefore the actual growth rate is governed by the arrival rate of group-III atom. Based on the mechanism of group-III atoms providing adsorption sites, an extra group-III elemental pre-deposition step was introduced sometimes [536,562].

During mass transport, one or more molecular beams with different azimuth angles are injected toward the substrate and intersect each other. The fluxes of molecular beams are influenced by the geometry of assembly of Knudsen cells and substrates, the inside partial pressures and the inner temperatures. The effusion rate from the orifice of cell is the product of an outcoming flux and the surface of the orifice opening S_{effusion} ,

$$\Gamma_{\text{eff}} = JS_{\text{effusion}} = \frac{(P_{\text{eq-V-C}} - P_{\text{res}})S_{\text{effusion}}}{\sqrt{2\pi k_B T m}} = \frac{(P_{\text{eq-V-E}} - P_{\text{res}})S_{\text{sublimation}}}{\sqrt{2\pi k_B T m}} \quad (262)$$

where P_{res} is the partial pressure of residual gas, which is commonly smaller than 10^{-10} - 10^{-11} Torr. P_{eq-V-C} is the equilibrium pressure in the chamber. $S_{sublimation}$ is the sublimation area of a condensed source in the cell, and $S_{effusion}$ is the area of orifice. The actual effusion rate may be much smaller than the ideal rate due to the reaction between atoms with the wall. In an ideal situation of ignoring the orifice wall thickness, the angular distribution of the evaporated molecular beam follows a cosine law,

$$\frac{dJ(\vartheta_{cell})}{d\omega_{angle}} = \frac{J \cos \vartheta_{cell}}{\pi} \quad (263)$$

where ϑ_{cell} is the inclined angle referred to the normal direction of cell opening, and ω_{angle} is the incident angle corresponding to the incident flux direction. The angular distribution increases with the thickness of wall increasing. The angular distribution of flux can be simplified. The flux is inversely proportional to the square of the distance,

$$J \propto \frac{S_{effusion} (P_{eq-V-C} - P_{res})}{l_{OS}^2 \sqrt{2\pi k_B T m}} \quad (264)$$

where l_{OS} is the distance from the opening site.

The heat transfer between the substrate and the mixed gas depends on the thermal accommodation coefficient given in Eq.160. The temperature difference ratio reflects the energy transferred between the intersecting gas and the arriving atoms on the substrate,

$$\gamma_{accommodation} = \langle E_i - E_e \rangle / \langle E_i - E_s \rangle \quad (265)$$

where the subscripts are the same in Eq.160. The adsorption fluxes of species i controlled by their partial pressures and temperatures are given in Eq.243 and 244. In the adsorption process, the material with low pressure has a higher sticking coefficient. This phenomenon seems to be not applicable to the residual gas in MBE system. The partial pressure of residual gas is smaller than 10^{-10} - 10^{-11} Torr, while its sticking coefficient is much smaller

than unity. For the catalyzed NW growth, the sticking probability is considerably high on the particle and vanishingly small elsewhere. For the template-assisted NW growth, the sticking coefficient is near to unity, while the sticking coefficient on the mask is near to zero. Some group III-V NW growth rates with different growth parameters are listed in Table 3.

Table 3. Growth parameters of group III-V NW via MBE technique.

| Material | Temperature | Group-III Rate & Partial Pressure | Group-V Partial Pressure | Nanowire Growth Rate | Ref. |
|-----------------|-------------|---|-----------------------------|----------------------------|-------|
| InAs | 480°C | 0.24 Å/s | 1.95×10 ⁻⁶ Torr | 1.51 Å/s | [487] |
| | | | 3.90×10 ⁻⁶ Torr | 3.02 Å/s | |
| | | | 0.75×10 ⁻⁵ Torr | 6.04 Å/s | |
| GaAs | 630°C | 0.25 Å/s | 1.50×10 ⁻⁶ Torr | 2.94 Å/s | [514] |
| GaAs | 630°C | 0.25 Å/s | 2.03×10 ⁻⁶ Torr | 15.00 Å/s | [528] |
| GaAs/ InGaAs | 560°C | 1.70×10 ⁻⁷ Torr (Ga) | 3.20×10 ⁻⁷ Torr | 75 Å/s (GaAs) | [537] |
| | | 1.00×10 ⁻⁵ Torr (In) | | 47 Å/s (InGaAs) | |
| GaAs | 590°C | 0.205 Å/s | 8.00×10 ⁻⁷ Torr | 4.64 Å/s | [542] |
| GaAs | 640°C | 4.20×10 ⁻⁷ Torr | 4.80×10 ⁻⁶ Torr | 2.52 Å/s | [552] |
| GaN | 700°C | 1.70×10 ⁻⁷ Torr | 5.10×10 ⁻⁷ Torr | 0.3367 Å/s | [639] |

--Group-V Partial Pressure is the beam equivalent pressure.

--For a gas phase reaction, concentrations are replaced by partial pressures sometimes.

--The actual NW growth rate may be not a constant rate [546].

--The data derived from the different geometrical equipments has no practical significance to do a horizontal comparison.

No matter the associative adsorption in a solid MBE chamber, or the dissociative adsorption in a MOCVD reactor, exhibit the processes of physisorption and chemisorption. A genuine physisorption holds the atoms together via van der Waals' forces that are smaller than 20 kJ/mol at most of time. If the absorbed adatoms want to be compatible with the substrate, a stronger chemical bonding formation should be held. The strength of bonding is beyond 50 kJ/mol, which is enough high to localize the atom. The adsorption depends not only on the interaction between adatom and substrate, but also on the forces between adatoms. Sometimes, the adsorbate atoms are not on the surface, but rather locate at the

lower layers or the sites between the lower layers. The formation of adsorption process is reflected by the residence time. The adsorption residence time can be written,

$$\frac{1}{\tau_{ads}} = \nu_{thermal} \exp\left(-\frac{E_{ads}}{k_B T}\right) \quad (266)$$

where the vibration frequency $\nu_{thermal}$ is the same with Eq.183 caused by thermal, and the oscillation frequency is typically larger than the diffusion frequency in Eq.184. E_{ads} is the adsorption energy, which is typically several times E_{des} . The adsorption energy can be obtained by measuring the change of work function via an adsorption microcalorimeter [640,641]. In the microcalorimeter method, the change of adsorption heat reflects the adsorption energy indirectly. The desorption process behaves reversely as the adsorption manner, but expresses in a similar manner. Desorption activation energy equals to the differential heat of adsorption [642]. Thermal desorption induces the decomposition of chemical binding, and aggravates at a high temperature. Therefore desorption at a high temperature or kinetics at a low temperature is the limitation of mass transport, and they reduce the group III-V growth rate both. The dependence of desorption time on the activation energy is given in Eq.183. The activation of desorption process can be measured by thermal desorption spectroscopy [642-644].

In general, the processes of arriving, adsorption, desorption, reevaporation, capture, diffusion, and nucleation maintain a dynamic balance and mass conservation. The dependence of mass transfer on the Fick's law is described in Eq.166 and 167, and the lifetime can be obtained from the Matthiessen's rule,

$$\frac{1}{\tau} = \frac{1}{\tau_{des}} + \frac{1}{\tau_{ads}} + \frac{1}{\tau_{diff}} \quad (267)$$

For the adatoms on the mask, the preferentially diffusion and desorption processes dominate in mass transfer. In the process, the diffusion flux to the reaction site is written [645,646],

$$J_{D-mask} \propto \frac{v_{diff} v_{thermal}}{D_{sur}} \exp\left(-\frac{2E_{des} - E_d}{k_B T}\right) \quad (268)$$

And the direct impinging flux into a catalyst can be described by,

$$J_{imping-top} \propto \frac{v_{thermal}^2}{D_s} \exp\left(\frac{E_{ads} - E_{des}}{k_B T}\right) \quad (269)$$

Eq.269 gives the dependence of the activation energies on the accommodation flux of atoms. The activation energy can be also macroscopically reflected from the slope of curve in the Arrhenius plot by measuring the relationship between the NW growth rate and growth temperature. In a similar manner with group III-V bulk (film) growth, the enhancement of the growth rate of NW is induced by the reduced activation energy for pseudo-1D structure. The net flux in MBE can be obtained from the sum of all fluxes.

$$\frac{dN}{dt} = JS_{surf} \approx J_{imping-top} S(\theta) + J_{D-mask} [S_{surf} - S(\theta)] + \frac{n_{surf}}{\tau_{des}} \quad (270)$$

where the order of magnitude of diffusion length is much longer than the magnitude of NW. J is the incident flux impinging on the surface in MBE and it can be calculated in Eq.263 and 264, and n_{surf} is the number of adatoms on the surface. The reaction rate depends on the activation barrier, and the high barrier will suppress the reaction rate. A common method for reducing the activation barrier is a technique of exploiting catalysts. The catalyst provides an easier reaction path. In section III.B, a catalyst reacting with group-III atoms to form a eutectic alloy has been explained [192,226,228]. Actually, the eutectic alloy may provide an intermediate state with a much lower activation energy barrier compared to the reactions

without catalysts. In the catalyzed process, the energy varies from an origin state jumping to an intermediate state with a relatively small barrier, instead of covering a very large barrier to a final state directly. Then the energy transfers from the intermediate state to a final state with a similarly small barrier. Therefore the catalyst exploits a barrier reduction to induce a highly anisotropic pseudo-1D manner.

The catalysts are not only used to lower an activation energy barrier, but also applied to provide a high degree of precision regarding morphology, site location, and the orientation of NW. There are some direct methods based on the top-down lithography. Lithography techniques are exploited to decide the size of catalyzed seeds, such as E-beam lithography [647,648], and nanoimprint lithography [649,650]. E-beam lithography accompanied by the traditional metal evaporation, lift off and chemical etching, is used to define the pattern on a substrate. Meanwhile, E-beam lithography and dry etching can be also used to define a stamp for the nanoimprint. In nanoimprint lithography, mechanical contact replaces chemical etching to replicate the pattern into materials by a pattern transfer method. Therefore it prevents the drawbacks caused by chemical etching (except for the procedure of etching oxides), meanwhile, reduces cost and enhances throughput. After the lithography processes, samples are transferred to the chamber or the reactor immediately, then are deoxidized under a group-V pressure to form a catalyst-group-III eutectic alloy.

Another indirect method for synthetic strategy is the fabrication of a colloidal solution droplet of monodisperse nanocrystalline on a suitable substrate. The droplets with diameters below 100 nm for no matter foreign metal catalyzed NW or self-catalyzed NW can be deemed as aerosols of solid particles or liquid droplets in gas. Accurate size control for droplets is important to tune the uniformity of NW. Many aerosol researches originate from the problems caused by the contaminants deposition onto product surfaces during

manufacturing process. The contaminations induce the loss of product yields and lead to a malfunctions of electronic circuits. Conventional methods for generating monodisperse nanoparticles include high temperature thermolysis [651], laser pyrolysis [652], milling, vaporization/deposition [171,653-655], sputtering/deposition, spark discharge [656], collision, and sol-gel technique, etc. In NW growth, some simple and continuous aerosol technologies are used to produce catalysts to induce NW growth, and monodisperse aerosols are selected by some filtering means. Actually, high purity monodisperse aerosols with desirable sites, size, morphology, and crystalline phase can provide not only controllable catalysts, but also possible applications for independent building blocks attached to NW in electronic, photonic and energy applications. In the aerosol synthesis, evaporation or condensation in a kinetic model involves a series of atom diffusion, nucleation, growth, preparative size fractionation and filtering processes.

For suppressing the random size distribution of aerosols, the growth of nuclei should occur before its Ostwald ripening process where a large cluster increases with time and small particles dissolve into the large one. According to the Gibbs-Thompson effect described in Eq.138, larger particles with lower chemical potentials will grow at the expense of small particles with higher chemical potentials. The driving force inducing the asymptotic particle size distribution in a diffusion limited situation, can be expressed by the Gibbs-Thompson effect [106,657,658],

$$n(r) = n_0 \left(1 + \frac{2\gamma V_{molar}}{rRT} \right) \quad (271)$$

where $n(r)$ and n_0 are the solubilities of particles with radii r and bulk. $\gamma V_{molar}/RT$ is the capillary constant and it is of the order of several nanometers for solid-liquid interfaces typically. According to Eq.138 and 271, the aerosol growth and dissolution processes are

size dependent. Besides the aggregation effect, diffusion and sintering also have influences on nanoparticle size, density and distribution on the substrate. The aerosol growth rate can be written [657],

$$J_{ae} = 4\pi r^2 D n_0 \left[\frac{n_{mono}/n_0 - \exp\left(\frac{2\gamma V_{molar}}{rRT}\right)}{r + \frac{D}{C_{activation}} \exp\left(\frac{\Delta\mu}{RT} + C_{transfer} \frac{2\gamma V_{molar}}{rRT}\right)} \right] = \frac{8\pi r D V_{molar} n_0}{RT} \left(\frac{1}{r_c} - \frac{1}{r} \right) \quad (272)$$

where n_{mono} is the monomer concentration in bulk, $C_{activation}$ and $C_{transfer}$ are the activation energy parameter and transfer coefficient respectively, and r_c is the critical radius given in Eq.154 where the growth and dissolution rates are equal. The nanoparticle distribution was discussed in [659-661], and the distribution can be derived according to the asymptotic distribution parameters and the activation energy parameter of the reaction. In the diffusion limited, the concentration of aerosols per unit surface area, depends on the size and time, meanwhile satisfies mass conservation for the absorption atoms,

$$\frac{\partial N_{ae}}{\partial t} = - \frac{\partial}{\partial r} \left(N_{ae} \frac{\partial r}{\partial t} \right) \quad (273)$$

And mass conservation can be written by,

$$\int \frac{\pi(2 - 3\cos\theta + \cos^3\theta)}{3} N_{ae} r^3 dr = I_{abs} - I_{des} \quad (274)$$

The aerosol growth rate can be derived from the Thomson-Freundlich equation [662],

$$\frac{dr}{dt} = \frac{2M_{gram} S \sigma}{3\pi N_A v_{vis} d_D \rho^2 r} \left(\frac{1}{\langle r \rangle} - \frac{1}{r} \right) \quad (275)$$

where S is the solubility of aerosol in a saturated solution, M_{gram} is the molecular weight, σ is the interfacial tension, N_A is the Avogadro's number, v_{vis} is the viscosity, d_D is the diameter of the diffusion atom, and ρ is the density of the molecular.

In the situation of source limited, the equilibrium of concentration may be not limited by diffusion processes. However absorption and desorption can determine the equilibrium. The average concentration is written by [106],

$$\langle n(r) \rangle = n_0 \left(1 + \frac{2\gamma V_{molar} \langle r \rangle}{\langle r^2 \rangle RT} \right) \quad (276)$$

Actually, the processes of convection, diffusion, sedimentation, aggregation, sintering, electrical force caused by polarity, thermophoretic force, and turbulence, as well as high vacuum and high temperature growth condition, all may interfere with the spatial uniform aerosol formation. According to the distribution equation, the most frequent size of aerosol in the steady state distribution is in the range of $1.00\langle r \rangle$ to $1.15\langle r \rangle$, and the number of aerosols whose sizes are above $1.5\langle r \rangle$ tends to a very small number.

An indirect method for separating aerosols was used according to their electric mobilities [171,653,655,663-666], because the mobility is inversely proportional to the aerosol size. Although the electrostatic classification reduces the concentration substantially, monodisperse aerosols can be produced effectively. When the size of an aerosol is larger than 20nm, the bipolar charge distribution of aerosols is in good agreement with the Gaussian distribution [667,668]. The charging efficiency and the fraction of charged aerosols may decrease with the reduction of aerosol size. When the size of aerosol is smaller than 10nm, the probability of uncharged aerosol exceeds 99% [171,653]. In a differential mobility analyzer, size selection can only be done for charged particles. So the generated aerosols should be charged by photoelectric charging after evaporated in the furnace. Then aerosols are classified according to their sizes, and the monodisperse aerosols can be obtained from the controllable voltage and temperature. In the apparatus, the stream function J_{stream} and the electric flux function Φ_E in a analyzer apparatus can be used to define the

particle path, and they can be written in cylindrical coordinates (The coordinates are the same with Eq.255) [663],

$$J_{stream} = \int_{r,z} (ru_r dz - ru_z dr) \quad (277)$$

$$\Phi_E = \int_{r,z} (rE_r dz - rE_z dr) \quad (278)$$

where u and E are the velocity and electric field in a analyzer apparatus respectively.

After the charged aerosols remain airborne then pass the analyzer, the filtered and classified aerosols can be deposited on the substrate by means of electric field, laser, fluid dynamics or van der Waals interactions. Charged aerosols can be attracted onto a charged substrate by electrostatic precipitation, so a site-controllable aerosol deposition can be realized by controlling the electrostatic precipitator [664,669]. Sometimes, charged aerosols are neutralized by a radioactive source for avoiding unwanted electrostatic effects. The actual neutralized aerosol efficiency will be affected by the ion concentration and its mobility in the chamber [667]. Fluid dynamics has an important influence on the aerosol deposition too. The randomness of distribution caused by Brownian motion, gas phase mixing, and the complex coupling of different mechanisms is inevitable, but the uniformity can be improved via the control of the kinetics mechanisms and the thermal treatment processes. In general, a smaller quantity of fluid and a smoothing temperature gradient can give smaller geometric standard deviations.

Capillary forces not only induce the aerosol coarsening according to the LSW theory [659,662], but also alter the morphologies of NW, as well as promote NW growth. Capillary is an important driven force for the motion of internal interfaces and free surfaces as illustrated in Fig. 3, especially when the size of aerosol approaching or being smaller than the critical radius r_c [670]. The capillary effect has an important influence on the droplet.

The equilibrium of droplet is under the balance of gravity, hydrostatic pressure, and capillary pressure. The capillary effect rise when the contact angle θ is less than 90° , whereas the capillary phenomenon will be depressed. Capillary pressure and hydrostatic pressure may affect the characteristic length for a droplet. The capillary length is given by [671],

$$\lambda_{ca} = \sqrt{\gamma_{VL} / g \Delta \rho} \quad (279)$$

where g is the acceleration of gravity, and $\Delta \rho$ is the density difference caused by the surfacial fluids. When a droplet is larger than the capillary length, the droplet tends to flatten, whereas the droplet will remain to wet the NW.

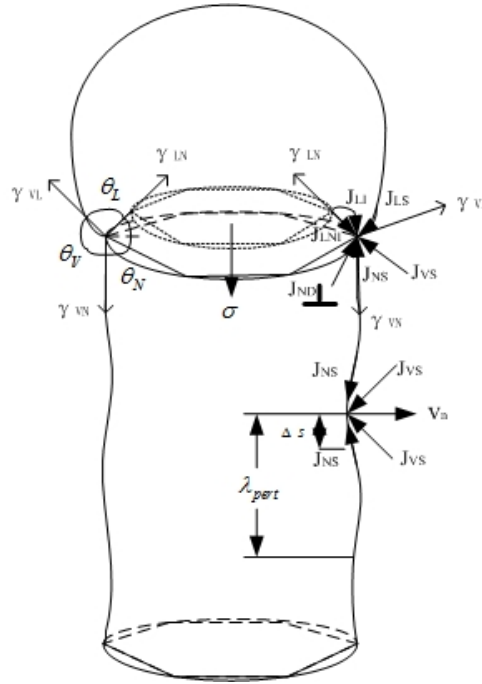


Figure 3. The NW model with capillary forces. The subscripts S, I, and D stand for surface, interface, and dislocation, respectively. The lowercase letter s stands for the arc length along the NW surface. σ is the stress. λ_{pert} is the perturbation wavelength on NW surface. v_n is the normal velocity. The other subscripts and signs are the same symbols in Figure 1.

In Fig. 3, local distortions of the droplet occur in the vicinity of the triple line. The displacement caused by distortion may be displaced either towards or away from the biphasic interfaces. These distortions induce the variations of Gibbs free energy of interface between droplet and NW, the changes of truncated angles on the top of NW, meanwhile lead to the fluctuations of NW radius [91,298]. Atom diffusion caused by capillary is concerned with the diffusion potential that is influenced by the local interface curvature. The diffusion potential with the isotropic curvature ($K \sim 1/r$) for a undistorted sphere can be given by,

$$\Phi_{diff} = \mu_0 + \gamma V_{molar} K \quad (280)$$

Take into consideration of the surface stress hence the curvature is influenced by the stress [672],

$$K = \frac{6\sigma_+ h_+}{EY_- h_-^2} \quad (281)$$

The potential in a convex region is higher than that of concave region, so the atoms will diffuse from convex to concave. Mean curvature can play a role in the basic physical driving force arising from the difference in curvature. For any curved isotropic surfaces [673,674],

$$\nabla \cdot \xi(n) = \gamma (K_1 + K_2) \quad (282)$$

where $\xi(n)$ is the capillarity vector for an isotropic or anisotropic interface and it can be expressed as the product of the scalar surface energy γ and the orientation \vec{n} . The term of $K_1 + K_2$ is the mean curvature, which is also an isotropic weighted mean curvature [674-676]. For an isotropic interface, γ is independent on the orientation, while for an anisotropic interface, stress σ on different orientations having torque components.

Eq.167 gives that the surface flux arises from the difference of atom concentrations on the NW surface. The surface atom flux caused by a capillary force can be expressed as the surface gradient of curvature [106],

$$J_{NS} = -\frac{D_{Nf}\gamma_{VN}}{RT} \frac{\partial K}{\partial s} \quad (283)$$

Through a flux, atom diffusion from a large curvature surface to a low curvature surface. A local driven force is derived from the variation of local curvature. Flux J_{LS} on a droplet has a similar expression as Eq.283. The geometric surface normal velocity is proportion to the accumulation of fluxes and it is a result of the divergence of flux caused by a capillary force,

$$v_{nN} = -V_{ph} \nabla \cdot J_{NS} = C_{caN} \frac{\partial^2 K}{\partial^2 s} \quad (284)$$

where V_{ph} is the volume phase change on the NW surface, and C_{caN} is the capillary parameter in the geometric motion velocity where the interface is capable of moving. For an anisotropic surface, the surface diffusivity is anisotropic. In this case, the surface derivatives can be obtained,

$$K_{an} = \nabla_{surf} \cdot \xi(n) \quad (285)$$

The anisotropic curvature can be simplified as $\gamma\Delta rS/V_{ph}$ on the NW surface. According to the geometric motion, the surface roughness Δr can be derived based on the Fourier transformation method,

$$\Delta r(z, t) = \frac{\lambda_{pert}}{2} \cos\left(\frac{2\pi z}{\lambda_{pert}}\right) e^{-C_{caN}\left(\frac{2\pi}{\lambda_{pert}}\right)^4 t} \quad (286)$$

where the surface roughness has a relationship with a fourth-order spatial derivatives of the NW surface. According to the instability theory, there may be no normal velocity occurring on NW surface when the perturbation wavelength is less than the circumference of NW.

The vapor transport on NW surface is affected by the ambient and equilibrium pressure. Mass transport occurs from large curvature region to low curvature region. The vapor transport normal velocity is given by [106],

$$v_{nV} = V_{ph} J_{VS} = V_{ph} K (P_{environ} - P_e) = -C_{caV} K \quad (287)$$

where C_{acV} is the capillary parameter in vapor transport. Actually, the normal velocity caused by vapor transport is a second-order spatial derivatives of the NW surface.

IV. B. Surface Structure, Morphology, Crystallography, and Strain Effect of Nanowire

Any attempts to systematically investigate the properties of NW, it is extremely important to analyze the surface structure including the static surface relaxation and reconstruction in different NW phases, orientations, or sizes. In bulk materials, the proportion of surface atoms can be negligible or have a relatively small effect. A high aspect ratio in NW structure makes the atomic structure of surface play a more significant role in semiconductor devices. The atomic structure of surface is different with that of bulk due to the absence of neighboring atoms on the outer side. Actually, the surfacial structure of NW may not coincide with that of bulk too.

Comparing with metal materials, group III-V semiconductor materials have strongly directed covalent bonds with the direction of the tetrahedral coordination. For a group-III atom, trigonal molecule has three ligands separated by 120°, and three covalent bonds have a

hybridized sp^2 bonding configuration. For a group-V atom, sp^3 hybridization exhibits a tetragonal bonding configuration, and the ligands are separated by 109.5° . In the NW facets, the outermost atomic bonds will redistribute with the shifted atomic positions, and the surface energy distribution will change with the charge redistribution on the facets of NW. The surface energetically favors a facet with a low surface energy to reduce the whole free energy in the system however twins, stacking fault, polytypes, relaxation and reconstruction make the oversimplified model impossible to satisfy the experimental observation.

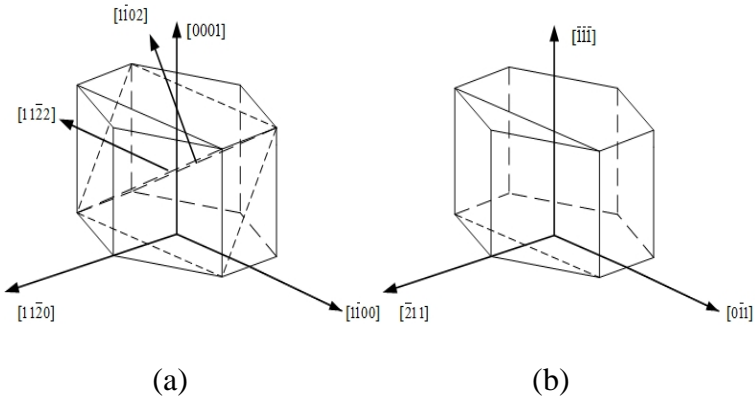


Figure 4. The crystallographic directions of (a) WZ structure and (b) ZB structure. In (a), $\{11\bar{2}2\}$ and $\{\bar{1}102\}$ planes are semipolar. In (b), $(\bar{1}\bar{1}\bar{1})$ surface can be denoted (111)B surface. B-surface is terminated by group-V atoms.

For a cubic structure, group III-V materials favor to exhibit a ZB structure, except for nitrides. The actual phase and surface structure of NW are determined by the specific growth conditions, concrete growth parameters, the dimensions of NW and the growth kinetics. Many experiments exhibit some indistinct, but referential tendencies for the phase transformation of NW. Through the observation of the atom consumption in the VLS or VLS-like process, the ZB structure formation occurs at relatively low supersaturation described in Eq.240-242, while the WZ structure formation is preferred at high

supersaturation. The WZ structure is conducted when nucleation occurs at the triple line, while the nucleation formation at the center of catalyst-NW interface favors to induce the ZB structure [89]. For a small diameter of NW, the WZ structure is favorable, and the polytypes occur with the diameter increasing [89,677,678]. Growth parameters of NW seem to have no distinct rules to control the morphologies of NW. NW may be predominantly ZB at a low temperature [679,680], or a low temperature condition may induce the exhibition of ZB structure [681].

For solar cells or LED, NW ensembled with more or less random orientations and placements, or short range order may be not required to induce the vertical growth compulsively. But conducting vertical growth and precise controlling the surface structure of NW are necessary to improve the properties of NW. The most common WZ NW orientation along $\langle 0001 \rangle$ and the most common ZB NW orientation along $\langle 111 \rangle$ are schematized in Fig. 4. No matter WZ or ZB structure with hexagonal cross sections are restricted by the specific low-index facets, whose outermost atoms are stretched on the surfaces.

Although the surface energy of $\{1100\}$ is lower than that of (100) or (111) A/B in ZB structure, polytypes associated with ZB/WZ and ZB structure possibly appear as the whole crystal structure or only in small segments. WZ and ZB crystal structures exhibit repeating ABAB (2H) and ABCABC (3C) stacking sequences along NW axis directions. Polytypes exhibit different stacking sequences along the NW growth direction. The most common polytypes are 4H and 6H crystal structures, with ABCB and ABCACB stacking sequences in Fig. 5 respectively. Fig. 5 gives the atomic models of the crystal structures of 2H, 3C, 4H and 6H. Some possible polytypic stacking sequences, such as 3Ct, 2Hs, and M, as well as their formation possibilities in NW are summarized in [293,682].

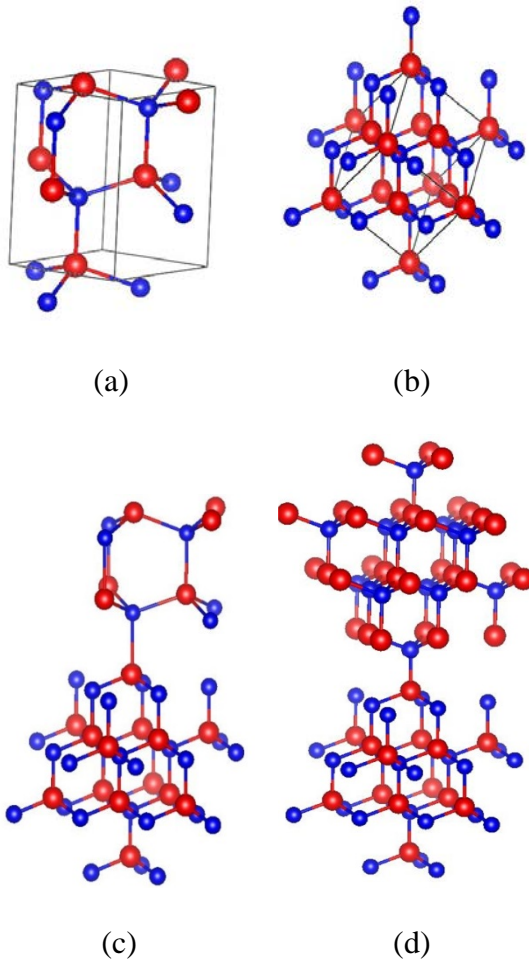


Figure 5. The models of (a)WZ (2H), (b) ZB (3C), (c) 4H (ABACABAC...), and (d) 6H (ABCACBABCACB...). The red (large) ball is the group-III atom, and the blue (small) ball is the group-V atom. At least 2, 3, 4, and 6 layer stacking sequences exhibit in 2H, 3C, 4H, and 6H crystal structures respectively.

The most of polytypism is rare, except for 4H and 6H, and randomly intermixes in the stacking sequences of NW. 4H is the most common intermediate segment between WZ and ZB, because of 4H dominating in the intermediate supersaturation [100,293,683,684]. Twins can also be formed with a gradual change in the supersaturation by tuning the influx quantity or changing the V/III ratio. The mirror plane is a twin plane and the segments above and below the mirror plane have different twin orientations. The driven force for

phase formation with respect to the supersaturation is given in Eq.240-242. Through reducing the chemical potential difference $\Delta\mu_{LN}$, the ZB phase crystal structure can be formed at a low supersaturation. When the chemical potential difference $\Delta\mu_{LN}$ is increased above the critical $\Delta\mu_C$, 4H structure formation starts to occur. The hexagonal WZ structure growth has to be controlled at a high supersaturation environment. In a variation process of supersaturation, the proportion of hexagonal structures increases continuously with the enhanced supersaturation. The proportion of hexagonality (WZ) in crystallographic purified phase and polytypes varies from 0% for 3C, 25% for 3Ct, 33.3% for 6H, 50% for 4H, 75% for 2Hs, to 100% for 2H [91,682,685].

In Fig. 4 (a), WZ (2H) $\langle 0001 \rangle$ -oriented NW is surrounded by six symmetry low energy $\{ \bar{1}100 \}$ facets or by six higher energy $\{ 1\bar{1}20 \}$ facets. In Fig. 4 (b), ZB (3C) $\langle 111 \rangle$ -oriented NW is restricted by six equivalent low energy $\{ 110 \}$ planes or by six higher energy $\{ 112 \}$ planes. Fig. 6 schematizes that the $\{ 110 \}$ and $\{ 112 \}$ planes and their respective $\{ 1\bar{1}20 \}$ and $\{ \bar{1}100 \}$ counterparts differ by a 30° angular rotation.

Because of the highly asymmetrical environment caused by missing atoms on the outside for the outmost layer, relaxation follows a bond rotation and a bond contraction, as well as reconstruction changes the atomic positions on NW surfaces. The existence of corners of edges, surface curvature, and the small adsorbates, such as H, C, N, and O, will deteriorate the surface structure and change the surface energy distribution further. The growth of group III-V NW on different substrates is still facing a variety of challenges, resulting from lattice mismatches, polar/nonpolar interfacial growth, the differences in thermal expansion coefficients, and the differences in strains or stresses for different materials, and different phases assigned to each layer as one individual segment.

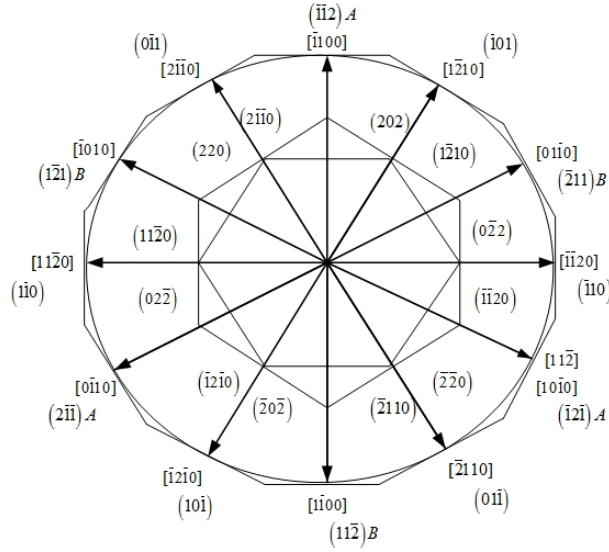


Figure 6. The schematic view of relationships between the crystallographic directions of WZ [0001]-oriented NW and ZB $[\bar{1}\bar{1}\bar{1}]$ -oriented NW on the (0001) and $(\bar{1}\bar{1}\bar{1})$ planes.

Compared to the strained and unrelaxed interface with an identical lattice constant for its overlayer and bottomlayer, the relaxation strain in NW has atomic displacements. The strain relaxation in lattice mismatch NW can accommodate a greater elastic strain (5 to 10 times) than the planar strain [686]. Therefore the atomic positions in NW will not be changed with respect to the inner atoms. In NW, an interfacial strain or a surfacial strain can be elastically accommodated. Eq.206 reflects that the strain energy equals to the sum of the elastic energy and the misfit energy. A general expression for the formation energy of NW is related to the change of the surface energy, the elastic stress relaxation, and the repulsive elastic interaction,

$$\Delta E_{form} = \Delta E_{surf} + \Delta E_{elas} + \Delta E_{edge} \quad (288)$$

$$\gamma_{form} = \gamma_{surf} + \gamma_{elas} + \gamma_{edge} \quad (289)$$

The surface energy is a function of the intrinsic surface properties (written in Eq.147 and 148) and the relative surface deformation. In general, group III-V NW can automatically choose the facets and growth directions to minimize their total free energies. The surface energies of the equilibrium facets satisfy the rule,

$$\gamma_{hkl} \leq \frac{h+k+l}{\sqrt{h^2+k^2+l^2}} \gamma_{001} \quad (290)$$

Actually, (111) is often the lowest surface energy facet, (001) is the second lowest energy facet, and the high index (211) and (311) facets will have higher surface energies. The equilibrium crystal shape of NW may be restricted by the Bibbs-Curie-Wulff rule and the Neumann Relationship [88,680],

$$\frac{\gamma_1}{r_1} = \frac{\gamma_2}{r_2} = \frac{\gamma_3}{r_3} = \dots \quad (291)$$

$$\frac{\gamma_i}{h_i} = \frac{\gamma_{LN} - \gamma_{VN}}{h_r} \quad (292)$$

$$\frac{\gamma_{VL}}{\sin \theta_N} = \frac{\gamma_{LN}}{\sin \theta_V} = \frac{\gamma_{VN}}{\sin \theta_L} \quad (293)$$

where r_i is the distance between the center of crystal to the facet, h_i is the distance from the center of droplet to the i th facet, h_r is the distance to the interface between a droplet and NW, and θ_i is the angle in Fig. 3. According to the Wulff's theory, the lower the surface energy of equilibrium facet is, the simpler the indices of surface are, the larger the facet area is, and the shorter the distance to the center of crystal remains.

Internal or surfacial strains and stresses are a consequence of the mismatch of lattice constants or the difference in the thermal expansion coefficients for the individual layer. The surface energy with respect to the strain is given by,

$$\gamma_{strain} = \int \sigma_{s\alpha\beta} \varepsilon_{s\alpha\beta} dS = \int_S \int_0^{\varepsilon_{s\alpha\beta}} e_{\alpha\beta} \sigma_{\alpha\beta} de_{\alpha\beta} dS \quad (294)$$

where $e_{\alpha\beta}$ is the integration variable representing a surface strain, and $\sigma_{s\alpha\beta}$ is the surface stress tensor. In general, the surface strain $\varepsilon_{s\alpha\beta}$ and tensor $\sigma_{s\alpha\beta}$ are different from the bulk Lagrange strain ε_{ij} and the bulk transformation tensors $\sigma_{\alpha i}$ and $\sigma_{\beta j}$ for the deformed surface. The relationship between the surface strain and the bulk strain is written,

$$\varepsilon_{s\alpha\beta} = \sigma_{\alpha i} \sigma_{\beta j} \varepsilon_{ij} \quad (295)$$

In a bulk structure, the eigenvalues ε_i of the principal axis of strain can be written as,

$$\varepsilon^3 - \sigma_{ii} \varepsilon^2 + \frac{1}{2} (\sigma_{ii} \sigma_{jj} - \sigma_{ij} \sigma_{ji}) \varepsilon - Det \begin{pmatrix} \varepsilon_1 & 0 & 0 \\ 0 & \varepsilon_2 & 0 \\ 0 & 0 & \varepsilon_3 \end{pmatrix} = 0 \quad (296)$$

and the tensor for an isotropic bulk material,

$$\sigma_{ij} = \frac{EY}{1+\nu} \left(\varepsilon_{ij} + \frac{\nu}{1-2\nu} \delta_{ij} \varepsilon_{kk} \right) \quad (297)$$

For the NW surface follows the bond rotation and the bond contraction in Fig. 7, the surface strain caused by the group-III atom shifted can be derived from the transformation vectors,

$$d\vec{y} = d\vec{x} + d\vec{w} = d\vec{x} + d\vec{x} \cdot \nabla \vec{w} \quad (298)$$

$$\varepsilon_{s\alpha\beta} \approx \frac{\left(\vec{p} \sqrt{d\vec{x} \cdot d\vec{x}} + \sqrt{d\vec{x} \cdot d\vec{x}} \vec{p} \cdot \nabla \vec{w} \right) \cdot \left(\vec{q} \sqrt{d\vec{x} \cdot d\vec{x}} + \sqrt{d\vec{x} \cdot d\vec{x}} \vec{q} \cdot \nabla \vec{w} \right)}{d\vec{x} \cdot d\vec{x}} \quad (299)$$

A surface strain for the right part in Fig. 7 can be separated into the relaxation for a group-III atom, the relaxation for a group-V atom, and the strain of bonding between these two atoms.

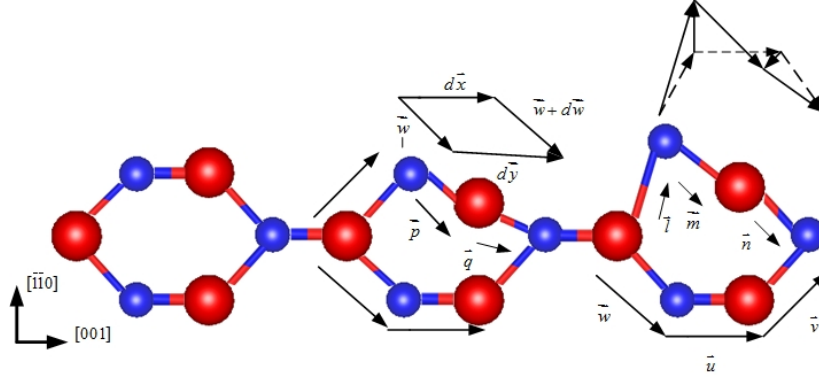


Figure 7. The bond rotation and the bond contraction exhibit on a relaxed {110} surface in group III-V NW. The left part is the unrelaxed schematic structure. The middle part or the right part exhibit a distortion of bulk structure due to the different relaxations.

For the group III-V NW with lattice mismatched interfaces, such as axial or radial heterostructures and different material substrates, etc., the NW can relax the stress over a strained area near the interface. The lattice mismatch can be accommodated by an elastic strain of the interfacial layer. When materials can accommodate their natural lattice structures, the elastic energy in a coherent structure is given by,

$$E_{elas-heteo} = \frac{EY_{N-}}{1-\nu_{N-}} \varepsilon_-^2 h_- S + \frac{EY_{N+}}{1-\nu_{N+}} (\varepsilon_- + \varepsilon_0)^2 h_+ S \approx \frac{C_{elas} EY_{N+} EY_{N-} (1+a_0) \pi r_N^3 a_0}{(1-\nu_{N-}) EY_{N+} + (1+a_0)(1-\nu_{N+}) EY_{N-}} \quad (300)$$

where lattice mismatch a_0 , and mismatch strain ε_0 . EY_{N+} and EY_{N-} are the Young's modulus of the above and below heterostructure segments respectively. Subscript N- can be regarded as the substrate. $h_{+/-}$ is the thickness, and C_{elas} is the elastic coefficient in NW. In group III-V NW, not only the interfacial tension but also the edge tension should be taken into consideration. Therefore the interfacial free energy can be written,

$$\gamma_{interf} = 6l_{facet} \varepsilon_{edge} + \frac{3\sqrt{3}}{2} l^2 \sigma_{LN} \approx 2\pi r \sigma_N \Delta z + \pi r_N^2 \sigma_{LN} \quad (301)$$

where l_{facet} is the facet edge length, and Δz is the interfacial thickness on the NW. When the stress induced by surface capillarity and the edge tension are taken into consideration, the elastic energy in one segment without the electrostatic and ions effects can be written,

$$E_{\text{elas}} = \int_S \int_0^{\epsilon_{\text{sa}\beta}} e_{\alpha\beta} \sigma_{\alpha\beta} de_{\alpha\beta} dS + \frac{1}{2} \int \lambda_{ijlm} \epsilon_{ij} \epsilon_{lm} dV + 2\pi r \sigma_N \Delta z + \pi r_N^2 \sigma_{LN} \quad (302)$$

where λ is the elastic modulus. The elastic constants of anisotropic or isotropic define the proportionality between stresses and strains when the atoms are subjected to external loads. Different crystals, phases, or orientations have different elastic constants and variable interfacial bonds [178,179]. In general, there are 21 anisotropic elastic constants in crystals. The effective elastic constant is related to the interfacial modulus of rigidity G [178],

$$1/\lambda_{\text{effect}} = (1-\nu_+)G_+ + (1-\nu_-)G_- \quad (303)$$

Actually, the elastic moduli on the surface are different from that in bulk, due to the effects caused by the stress and the surface bondings.

Thermal expansions in group III-V NW are also important, because both the changing thermal gradients and heat treatment processes cause extrinsic stresses due to unequal thermal expansions, especially in heterostructures [687]. Stress affects device bandgap and reliability, induces dislocation generation, and even leads to NW cracking [688]. When the material is isotropic, the thermal expansion of bulk coefficient is equal to three times that of linear coefficient [45,47,689],

$$\alpha_v(T) = \frac{1}{V} \frac{\partial^2 G}{\partial P \partial T} = 3\alpha_L(T) = \frac{C_V \gamma_{\text{Gru}}}{V_{\text{ato}} B} = -\frac{1}{\rho} \left(\frac{\partial \rho}{\partial T} \right)_P \quad (304)$$

where V_{ato} is atomic volume, B is bulk moduli, C_V is the heat capacity, γ_{Gru} is the average Gruneisen parameters. The Gruneisen parameter is a measure of the effect of the anharmonic interactions,

$$\gamma_{Gru-i} = -\frac{V}{v_i} \frac{dv_i}{dV} \quad (305)$$

where v_i is the corresponding vibration frequency. γ_{Gru} is a weighted average of the γ_{Gru-i} that is the measurement for each vibrational mode. In anisotropic situations, the thermal expansions on principal axes are expressed as the sum of the vibrations on the principal crystallographic axes,

$$\alpha_i = \sum_{j=1}^6 \frac{C_p \lambda_{ij} \gamma_{Gru-i}}{V} \quad i = 1, 2, 3 \quad (306)$$

For hexagonal and tetragonal crystal symmetries, $\lambda_{ij}(j=4,5,6)=0$. During the heat treatment, the rate of vibrational entropy variation caused by the thermal expansion at zero pressure is given by [47],

$$\left(\frac{\partial S_{vib}}{\partial T} \right)_{P=0} = \frac{(C_V \gamma_{Gru})^2}{V_{ato} B} = \frac{1}{V_{ato} B} \left[\frac{1}{M} \sum_q \frac{k_B (\hbar \omega_q / k_B T)^2}{4 \sinh^2 (\hbar \omega_q / 2 k_B T)} \times \frac{1}{M N_{ato}} \sum_q \gamma_q \right]^2 \quad (307)$$

At the both sides of a heterojunction where thermal expansion differences exist, the cooling process induces a tensile thermal strain in the material with a larger thermal expansion coefficient [672]. A tensile strain can be compensated by a compressive strain. In the heat process, the material with a larger thermal expansion coefficient behaves in compression. In NW, the thermal expansion mismatch can also be accommodated by the twist bonded. As the strain caused by a thermal expansion is increased above a critical value, dislocation and plastic deformation occurs. And external stresses might induce phonon frequency shifts and affect the performances of NW devices [690].

In general, the thermal expansion coefficients of Si and SiC substrates are much smaller than that of group III-V compound semiconductors [691-696]. The thermal expansion coefficient of Ge substrate is larger than that of group III-V compound semiconductors

[697], except for GaAs and GaSb. And the thermal expansion coefficient of a sapphire substrate is much larger than that of group III-V compound semiconductors [698], except for GaSb. For group III-V compounds themselves, the thermal expansion coefficients of indium compounds are smaller than that of gallium compounds in nitrides (c-/a-axis), arsenides, phosphides, and antimonides respectively.

The formation of the NW facets without relaxation or reconstruction creates a great deal of dangling bonds that are energetically unfavorable. For different surfaces of NW, not only the surface energies, but also the surface kinetics, as well as the equilibrium crystal shapes are different. The situations and the magnitudes of the bond rotation and the bond contraction are obviously different too. In the procedures of NW growth, the electrons transfer from the half filled dangling bonds attached to group-III atoms to the half filled dangling bonds located at group-V surface atoms. Therefore this changes the atomic positions and electron distribution, meanwhile, reduces the total free energy of NW. Group III-V materials exhibit a relative large relaxation due to a large room for the bond angle variation. For an unreconstructed surface, there is a contraction of bonds for the atoms on the outmost layer due to the anisotropic environment forces. The contraction occurs mainly in the outmost layer and the second layer under the surface. The amplitudes of relaxation decay exponentially with the depth of a surface.

Group III-V (001) is a polar surface plotted in Fig. 8, and the distances between the alternate cation and anion layers are equal along $\langle 111 \rangle$ stacking sequence. Anisotropic relaxation occurs along orthogonal $[110]$ and $[\bar{1}10]$ directions on (001) facet. Each surface atom has two dangling bonds at an idea (001) surface. Each dangling bond is occurred by $3/4$ or $5/4$ electrons for cation or anion, hence the surface is unstable due to a high partial occupation. (001) facet is not the first choice for ZB structure NW because (111) facet has a

lower surface free energy. The most common (001) cross-section interface formation prefers to occur along $\langle 001 \rangle$ NW orientations on (001) substrate [699-704]. NW along [100] orientation on (100) industry standard substrate are prone to achieving the crystal structure without stacking faults. Growth on (100) surface usually exhibits at an angel of 54.7° to the perpendicular along four equivalent $\langle 111 \rangle$ directions distributed 90° apart azimuthally. {100} facets on NW sidewalls were observed in vertical NW [702-704], planar NW [705], or sawtooth microfacet [706] under different growth conditions. The outmost atoms on (100) surface will be contracted to the second surface atoms, and the bond angles may change from tetrahedral 109.5° to approximately 90° and 120° with the corresponding sites.

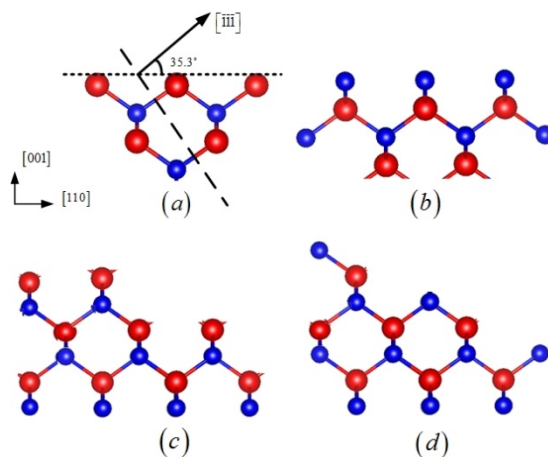


Figure 8. The schematic structures of polar group III-V {001} surfaces and the {001} undulations with facets that are close to {113}. (a) and (b) are the {001} surfaces. For no matter group-III terminated or group-V terminated surface, each surfacial atom has two dangling bonds. (c) and (d) are {113}A and {113}B respectively. The dangling bonds are occupied on {113}A surface, while unoccupied dangling bonds can cause reactions on {113}B surface.

Surface undulation occurs at (001) surface because of twinning and cracking [707]. Compared to a high twinning density in {001} facets, {113} facets can lower the density of twins. {113} facets consist of (100) terraces whose atoms have two corresponding dangling

bonds and (111) step-edge whose atoms have only one corresponding dangling bond, and thus reduces the surface energy to make the facets more stable.

Uncommon {110} surfaces in thin film growth can be compatible in NW as facets because {110} facets grow fast under a rich group-V environment [703], desorption of anions is available to control the lateral growth on these facets [593], the surface energies of these faces are lower than that of {112} facets [680], and so forth. Nonpolar group III-V {110} surface consists of one cation and one anion in the unit cell shown in Fig. 7. The surface atoms are arranged in zigzag chains along $[\bar{1}\bar{1}0]$ direction. Relaxation exhibits that the anions are protruded from the surface whereas the cations are moved inwards to the secondary surface layer with respect to the unrelaxed surface planes. On (110) facet of group III-V NW, group-III atom prefers an sp^3 or a planar sp^2 -like bonding situation and it moves outwards into a pyramidal configuration (such as $AsGa_3$ configuration with bond angles close to 90° of pure p states) with its three group-V neighbours, while group-V atom prefers an s^2p^3 or a p bonding with its three cation neighbors. Therefore, atoms on the surfaces are relaxed to the chemically favorable threefold rather than fourfold coordinated sites. Rehybridization of sp^3 tetrahedral bonds associated with atoms in the surface layer can lower the surface energy by an amount that is one order of magnitude smaller than that of the unrelaxed.

For GaAs (110) surface, As atoms are rotated out of the surface plane and Ga atoms displace inwards the secondary layer. The rotation angle of an outmost layer atom is in the range of 27° - 35° [708-710]. As atoms displace upward 0.26 \AA and Ga atoms displace from the corresponding Ga sublattice by 0.44 \AA [711]. Actually, the detailed experimental and theoretical values vary slightly in different experiments or models. The discrepancy can be caused by the variations in the second layer relaxations, the bond lengths, and the phonon

modes. In a secondary GaAs surface layer, As atoms move inwards the NW while Ga atoms are pulled outwards the surface. In this layer, the magnitudes of downward or upward displacements for As or Ga atoms reduce to 0.06 Å or less [712].

The rotation angle is defined as 0° in an unrelaxed surface. Eq.299 gives the surface strain calculation, which is described by the combination of the rotation vector and the change in bond lengths. The variation of rotation angles in different structures is relatively large. In general, the smaller the rotation angle is, and the smaller the magnitude of contraction for outmost atoms is. Ga atom is contracted 0.6 Å when the rotation angle is 34.8°, it is contracted 0.5 Å when the rotation angle becomes 27°, and it is contracted just 0.3 Å when the rotation angle reduces to only 20°. In a similar manner with the phenomenon of displacement decreasing in the secondary layer, the rotation angle on the second surface layer is reduced to 5.3° [710]. The surface bond length is contracted approximately 2-5% in the relaxed layer. Ga back bond is contracted by 0.06 Å or 2.5%, while As back bond is contracted 0.09-0.13 Å or 3.6-5% [709,711].

In general, the rotation angles of arsenides, antimonides, and phosphides are in the range of 25°-35°, and the outmost atoms are contracted 0.5-0.75 Å on the relaxed {110} surfaces [713,714]. In addition, there are smaller surface rotations and relatively large bond contractions for nitrides [712,715]. The discrepancy can be formed because the electronic structure of N atom is different with As or P meanwhile nitrides have larger covalency and polarity for the bonds. The relationship between the magnitude of ionicity and the rotation angle is fairly controversial, although there is a tendency that the rotation angle decreases with the increasing ionicity. In nitrides, the rotation angles are about 6°-16° accompanied by the contractions in surface bonds of about 4.9-7%. For the GaN atoms in the secondary

surface layer, Ga atoms move outwards 0.027 Å, while N atoms transform inwards NW by 0.052 Å.

The atomic structures of polar {111} surface are one of the most common facets in group III-V ZB NW due to their lowest surface free energies, which are schematized in Fig. 9. The surface atoms are bond to three corresponding atoms of the layer underneath, yielding one dangling bond to the surface and three hybrid orbitals bond to NW. There is a vertical compressed double layer that consists of group-III and group-V atomic layers on the (111) surface. In the outer compressed double layer of GaAs (111) facet, there is a shift 0.08 Å for one fourth layer As atoms towards the NW, while a 0.04 Å displacement for three fourths layer As atoms towards the surface, meanwhile, Ga atoms on the first double layer move inwards NW 0.706 Å [716]. In the secondary layer of the double layer, As atoms are unrelaxed, while there is a shift 0.08 Å for one fourth layer Ga atoms inwards NW and a 0.01 Å displacement for three fourths layer Ga atoms outwards NW.

For group III-V ZB NW growth on (111)A substrate, there are three equivalent <111> directions 19.6° tilted from the substrate because of its nonpolar nature. For NW on (111)B substrate, vertical growth can occur dominantly. If group III-V NW growth on Si (111) substrate, group-V- Si³⁺ or group-III- Si¹⁺ structure is equal to the so-called (111)B surface, and the other situations can be regarded as (111)A surface [717,718]. ZB NW vertical growth on (111)B surface has a relative large twinning density, and twin planes consist of repeated {111} lamellar twinning with two different zone axes [234,311,703,719-723]. These {111} facets are polar and they are neither parallel nor perpendicular to the growth direction. Twinning stacking sequences can be expressed as ABC'A'CBA, and the sequences before in the mirror plane 'A' are mirrored to the sequences after in the mirror plane. The repeated {111} twinning planes conduct the structures of NW to be octahedral

shape whose facets are terminated by $\{111\}$ facets [311,719,724]. Each truncated octahedron is restricted by six facets, and each is composed of two $\{111\}$ microfacets on its top and bottom. The real cross section of NW varies along its axis length due to these nonparallel side facets.

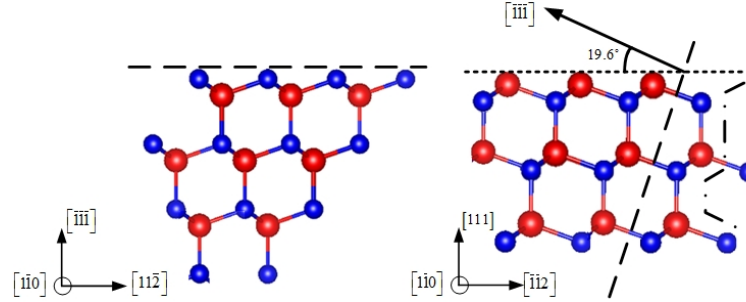


Figure 9. Atomic structures of group III-V $\{111\}$ surface from the side views. (a) $(111)B$ or $(\bar{1}\bar{1}\bar{1})$ facet is terminated by group-V atoms. (b) $(111)A$ facet is terminated by group-III atoms. Polar $\{112\}$ oriented surfaces are flat in a dash dotted line.

The Reduction of supersaturation can improve the twin plane density [719,722,723]. When the alternating microfacets $\{111\}A$ and $\{111\}B$ overgrow on the sidewalls of NW, the facets might transform to be flat macrofacets $\{112\}$ [234,311,703,721,724-729] or $\{110\}$ [234,721,728-730]. The overgrowth might start from the base and then propagate along its length. These transformations might occur when the twinning segment thickness is beyond the critical thickness. The flat facets $\{112\}$ cost more energy than the formation energy of twinning planes. For $\{112\}$ facets, two three-fold coordinated group-III atoms and one two-fold coordinated group-V atom are in the surface unit cell. For $\{1\bar{1}\bar{2}\}$ facet, there are one two-fold coordinated group-III and two three-fold coordinated group-V atoms in the surface unit cell.

Temperature and V/III ratio can affect the energy fluctuation of nucleation and have a significant influence on the choice of facets. In general, increasing temperature or

supersaturation can enhance the probability of random mixture of structures. In InAs NW, $\{11\bar{2}\}$ facets occur at a low temperature, $\{111\}$ microfacets and periodic twin planes appear at an intermediate temperature, and $\{\bar{1}10\}$ facets grow at a high temperature [234]. In GaP/GaAs heterostructure NW, six fold symmetry $\{112\}$ facets arise at an intermediate temperature, while only a threefold symmetry with three large and three small $\{112\}$ facets are restricted the NW under a higher temperature and a high V/III ratio [727]. In GaAs NW, $\{112\}$ facets appear at a relative low temperature, and facets are transformed to $\{110\}$ with the temperature increasing [680,721,727]. The NW along $\langle 111 \rangle_A$ direction favors three fold symmetry $\{11\bar{2}\}$ facets, while the facets of NW along $\langle 111 \rangle_B$ are composed of six fold symmetry $\{112\}$ [725].

$\{112\}$ facets consist of not only the alternating $\{111\}_A$ and $\{111\}_B$, but also $\{113\}$ [726] or $\{200\}$ [727] microfacets. High-index facets are relative unstable because of their larger surface free energies, higher dangling bond densities, and roughness. The atomic structure of a sawtooth facet is plotted in Fig. 10. For two type compressed double layers, $\{111\}_A$ microfacets might have a larger and flatter area than $\{111\}_B$ microfacets. Most of the time, the lengths of microfacets and their angles to the parallel side-plane of NW are different. In Fig. 10, the free energy of the total sawtooth facets per unit area is the sum of all contributions from their constituent parts,

$$\gamma_{surf-sawtooth} = \gamma_{(111)A} \frac{\sin \theta_2}{\sin(\theta_1 + \theta_2)} + \gamma_{(111)B} \frac{\sin \theta_1}{\sin(\theta_1 + \theta_2)} \quad (308)$$

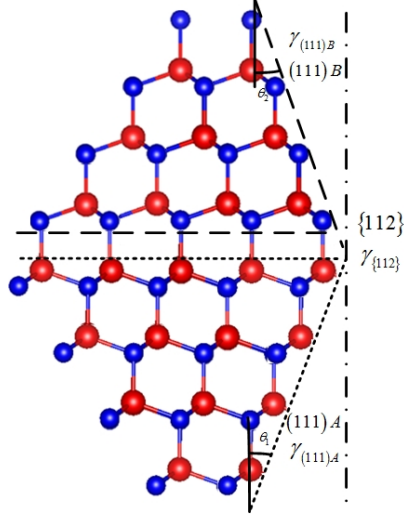


Figure 10. Atomic structures of macrofacet $\{112\}$ consist of microfacets $(111)A$ and $(111)B$. The lamellar twinning plane is the group III-V polarity. Some other polarities, such as the group III-III or V-V polarities are unstable.

A large number of group III-V NW exhibit WZ structure or WZ segment accompanied with ZB phase [91,544,552,678,706,725,726,731-735], partly due to the smaller density of surface dangling bonds and the smaller surface energies. The third nearest neighbour atom spacing of WZ is smaller than that of ZB hence this causes the energetic difference between two phases [678]. The most common WZ facets are the nonpolar $\{10\bar{1}0\}$ shown in Fig. 11 and nonpolar $\{11\bar{2}0\}$ plotted in Fig. 12, as well as polar $\{0001\}$ and semipolar $\{11\bar{2}2\}$ facets [733,734]. In general, a nonpolar surface is more stable compared to a polar surface or a semipolar surface, meanwhile, a polar surface suffers from deleterious polarization effects. Actually, the so-called nonpolar surface that is characterized by chains of equal numbers of cations and anions, might exhibit polar characteristics, as cations are shifted inwards NW to induce zigzag chains with uneven numbers of group III-V atoms on a surface or the normal of facet is not perpendicular to the growth direction. In a similar manner with the relaxation phenomenon occurred in ZB structure, the electron transfer is coupled with the relaxation of

WZ facet, accompanied with bond contraction and bond rotation [736,737]. The relaxation of configurations for group-III or group-V in WZ is similar to the atomic transformation in ZB configuration.

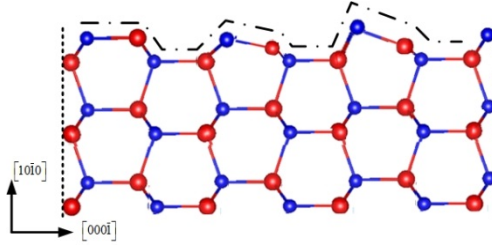


Figure 11. A schematic stick and ball representation of group III-V $\{10\bar{1}0\}$ facets in WZ structure from the side view. The red (large) ball stands for the cation, and the blue (small) ball presents the anion.

In $\{10\bar{1}0\}$ facets, the relaxation of the tetrahedrally coordinated atoms is mainly confined to the first surface layer in Fig. 11. On an unrelaxed nonpolar GaN ($\bar{1}100$) facet comprised of Ga and N atoms, cations and anions exhibit one surface bond and two back bonds. In general, the rotation angle exhibits 5° - 8° , accompanied with the bond contraction 4-8% [737-740]. When relaxation occurs on the GaN ($\bar{1}100$) facet, Ga atom relaxes inward and shifts toward a more planar three fold sp^2 coordination with its neighboring N atoms, N atom rehybridizes outward into a pyramidal configuration with p^3 coordination. The rehybridization changes the bond angles in tetrahedrally coordinated to 118° , 118° , and 113° for Ga atoms, and 105° , 105° , and 114° for N atoms. After the relaxation, the Ga-N bond is contracted 6-7% with a 7° rotational angle. On the first GaN ($\bar{1}100$) surface layer, Ga atom move inwards 0.2\AA and N atom shifts outwards 0.02\AA . On the second surface layer, both Ga and N atoms relax outwards 0.05\AA [738]. Besides the vertical relaxation, lateral relaxations cause the N and Ga atoms shift along $[000\bar{1}]$ and $[1\bar{1}20]$ in the same order of

magnitude of the vertical displacements [737]. For WZ structures of phosphides or arsenides, the bond rotations might enhance to 15°-20°, while the contractions might be reduced, due to the interaction for different electron configurations.

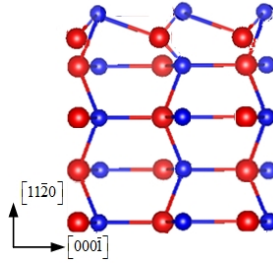


Figure 12. The atomic structure of group III-V $\{1\bar{1}20\}$ facets in WZ structure from the side view.

Compared with $\{1\bar{1}00\}$ facets, $\{1\bar{1}20\}$ facets might have larger surface energy [738] and smaller dangling densities [292]. On the unrelaxed nonpolar GaN ($1\bar{1}20$) facet comprised of Ga and N atoms, cations and anions exhibit two surface bonds and one back bond. The relaxed ($1\bar{1}20$) facet is schematized in Fig. 12. On the relaxed facet, the rehybridization changes the bond angles in tetrahedrally coordinated to 115°, 116°, and 119° for Ga atoms, and 101°, 106°, and 107° for N atoms with a bond contraction of 4-5%. On the first relaxed surface layer, Ga atoms move inwards 0.17 Å, while N atoms move outside 0.05 Å. On the secondary layer, Ga and N atoms shift outwards 0.05 Å and 0.02 Å respectively.

In fact, the above mentioned atomic structure parameters, such as the vertical shear Δ_{\uparrow} accompanied with rotation angle ω_{buckling} and the contraction bond length is $d_{\text{contraction}}$ on the outmost layer, might be not independent of each other. The relationship of these parameters can be given with a lattice constant a_0 ,

$$\Delta_{\uparrow} = \sqrt{d_{\text{contraction}}^2 - \left(\frac{a_0}{2\sqrt{2}}\right)^2} \sin \omega_{\text{buckling}} \quad (309)$$

According to Eq.309, the magnitude of contraction will decrease with the enhancement of rotation angle and bond length. Actually, the formations of bond contraction and rotation relaxation have involved not only the atomic vertical relaxation, but also the rearrangements and reconstructions of atoms on facets. On NW facets (especially on polar facets), the surface reconstruction not only conducts the atomic lateral displacement, but also reduces the periodicity and the symmetry of surface structure compared to the bulk structure. The displacement of atomic reconstruction (atomic scale or tenths of angstroms) is larger than that of relaxation, even if the symmetry exhibition on the facet is the same as that of bulk. In addition, vertical relaxation on the surface barely reduces the density of states around the chemical potentials of a material. The reconstruction is accompanied by opening of a surface bandgap near the Fermi energy hence a significant reduction of density of states performs in this energy range. Actually, the reconstruction of a semiconductor interface has been developed for more than fifty years. Principles for semiconductor surface reconstruction are proposed by C. B. Duke in the literature [741]. J. P. LaFemina discussed the calculation of surface energy and the simulation of semiconductor surface reconstructions [742]. The atomic surface structure and the kinetics of tetrahedrally coordinated semiconductor are reviewed by A. Kahn [743], J. Neugebauer [744], and Ph. Ebert [745].

Dangling bonds or unfilled atoms on NW facets keep electronically labile and tend to rearrange to form stable species and neutral charge. The driving force for reconstruction tends to reduce the dangling bond density and the surface stress, and thus minimizes the surface free energy kinetically meanwhile causes the passivation of dangling bonds and the surface stoichiometry variation. For the facet reconstruction of a semiconductor, the facet

automatically attempts to minimize the dangling bond density by the rehybridization of dangling bonds with the enhanced energy stored in the surface field or by the formation of new bonds. And therefore the electronic states of dangling bonds will be filled for anions or be empty for cations. Meanwhile, the facet automatically attempts to maintain charge neutrality and compensate charges. This constraint limits the stoichiometries and geometries of compound semiconductor surfaces and retains no charge accumulation on the facets.

Besides the relaxation and zigzag chain structures on facets preserve the surface free energy minimum, the dimerization and the passivation of dangling bonds can also have an influence on the determination of allowable composition and geometry. For a m-fold periodicity dimerization of $2 \times m$ reconstructions, dimers are the basic building block for the facet reconstructions. The relationship for the formation of dimers to minimize their electronic energies can be given by,

$$2N_{Dimer} = \frac{N_{m-Dimer}N_{valence}}{N_{valence} - 1} = \frac{3N_{valence}}{2} \quad (310)$$

where N_{Dimer} is the dimers per unit cell, $N_{m-Dimer}$ is the missing dimers, and $N_{valence}$ is the number of valence electrons. On group III-V NW facet, $N_{valence}$ is the number of valence electrons for the group-III (equals to 3). So for common (2×4) reconstructions, N_{Dimer} will equal to 3, hence surface reconstructions are formed with three outmost dimers in the unit cell. Actually, many of constructed surface compositions and structures are metastable meanwhile the transitions of reconstructions between all regions might be reversible. The actual composition and geometry can be controlled by the growth kinetics and experimental growth parameters.

For the surfaces of group III-V compounds, there are a wide variety of compositions and geometries on polar facets as functions of growth conditions and stoichiometries of

compounds. Meanwhile, the varieties of dimers and missing dimers on the polar facets vary with the growth parameters. The surfaces have been studied enormously by employing the plane wave pseudopotential methods, and ab initio tight binding calculations, as well as observed by scanning tunneling microscopy, reflectance difference spectroscopy, X-ray scattering and so on. The ideal $\{100\}$ A or $\{100\}$ B surfaces are composed of the single atom model in the (1×1) unit cell, each of which has two dangling bonds, while (1×1) structure is unstable and energetically highly unfavorable. The energetically favorable reconstructions and compositions are characterized by the completely occupied anions and empty cations on the outmost layer for polar facets.

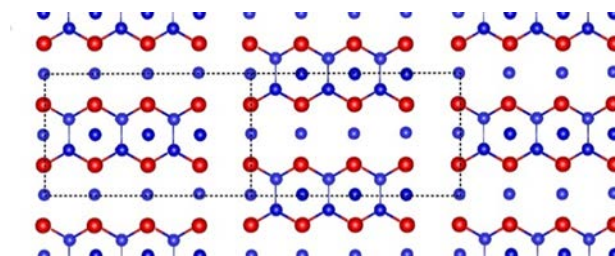


Figure 13. Group III-V (100) B- $c(2\times 8)$ or (2×4) . c denotes a centered unit mesh. Actually, (2×4) in this figure is $\beta(2\times 4)$ with three group-V dimers and one missing dimer. Cation dangling bonds and $\times 4$ missing row period preserve along $[110]$, meanwhile anion dangling bonds and $\times 2$ repetition period maintain along $[\bar{1}10]$. The bond lengths in the outmost layer are slightly contracted. When the group V/III ratio or the temperature is changed in experiments, other substructures designated by $\beta 2(2\times 4)$, $\alpha(2\times 4)$, $\alpha'(2\times 4)$, $\gamma(2\times 4)$, etc., can be synthesized [741,746].

The transition of common reconstructions on $\{100\}$ surfaces can be controlled by the growth temperature and the group V/III ratio [741,746]. In theory, group-V dimers favor on a group-V terminated surface, meanwhile, group-III dimers are the energetically most stable on a group-III terminated surface. There are a small number of second nearest neighbor atoms on $\beta(2\times 4)$ or $c(2\times 8)$ dimer structure, and these structures reduce the Coulomb

correlation energy to make themselves are relatively stable. (2×4) , $c(2\times 8)$ or the coexistence of these two reconstructions is the most common structure on group-V terminated (100)B surfaces for GaAs [636,637,741-743,746-756], InP [757-761], InAs [761-764], GaP [765,766] and even ternary InGaAs [767,768]. $c(2\times 8)$ structure is a small perturbation of the (2×4) with the phase shift caused by an As vacancy, and it is slightly more stable than the (2×4) structure [Fig. 13]. The surface free energy of $c(2\times 8)$ might be $1 \text{ meV}/\text{\AA}^2$ smaller in surface energy than that of (2×4) . In Fig. 13, group-V dimer vacancies on GaAs (100)B or InAs (100)B cause a four-fold missing periodicity along the $[110]$ direction to form an eight-fold periodicity.

For $\beta(2\times 4)$, unit cells are composed of rows of three group-V dimers and one missing group-V dimer [748,753,755,762,766] or two neighboring group-V dimers and two missing group-V dimers [749-752]. D. J. Chadi proposed the unit cell energy of two dimers is 0.2 eV larger than that for three dimers on GaAs (100)B- (2×4) surface [769]. For $\beta_2(2\times 4)$ unit cell, there are two neighboring group-V dimers and two missing dimers, as well as one row of group-III on the secondary layer missing with one group-V dimer along $[\bar{1}10]$ on the third layer exposed as the outmost layer in the unit cell [753,754,760]. The surface free energy of $\beta_2(2\times 4)$ on GaAs (001) is $2\text{-}3 \text{ meV}/\text{\AA}^2$ smaller than that of $\beta(2\times 4)$ with three dimers, while $\beta_2(2\times 4)$ unit cell is 0.2eV higher than $\beta(2\times 4)$ with two dimers in energy [750]. For $\alpha(2\times 4)$ reconstruction, there are two neighboring group-V and another two neighboring group-III dimers stacks perpendicular to V-V dimer bonds [754,755,760]. $\alpha'(2\times 4)$ phase is in a similar manner with $\beta(2\times 4)$ reconstruction, while the middle group-V dimer is replaced by group III-V dimer [753]. And $\gamma(2\times 4)$ reconstruction exhibits one extra group-V dimer stacking on the top of the group-V dimers of $\beta(2\times 4)$ surface [741,760,762]. The phases of reconstructions can be changes through adjusting temperature and group V/III ratio. With

the temperature increasing, the transition of phases occur $c(4\times4) \rightarrow \gamma(2\times4) \rightarrow \beta(2\times4) \rightarrow \alpha(2\times4) \rightarrow (4\times2)$ [746,762]. With the group V/III ratio decreasing, the phases of reconstructions change $\beta(2\times4) \rightarrow \beta_2(2\times4) \rightarrow \alpha(2\times4)$ [741]. Besides group V/III ratio and temperature, the atomic concentration in ternary alloy can also affect the phases of reconstruction, such as $\text{In}_{0.27}\text{Ga}_{0.73}\text{As}/\text{GaAs}$ exhibiting $\alpha_2(2\times4)$ structure, while $\text{In}_{0.81}\text{Ga}_{0.19}\text{As}/\text{InP}$ showing $\beta_2(2\times4)$ structure [767].

Phosphides $(001)-(2\times4)$ with two dimers and two missing dimers might be stable in the view of electron counting, while P is hard to suffer high temperatures above 350°C . Even in the conditions of low temperatures and a high P-supplied environment, group-V rich (4×2) reconstruction is unstable [757,758,765]. Besides the reason of unstable phosphides at high temperature, the larger radius differences of atoms for phosphides than that of arsenides can also induce that mixed-dimer or heterodimer on (2×4) structure can be energetically favorable. The mixed-dimer or heterodimer on In-rich (2×4) [760,761], Ga-rich (2×4) [765,766], or some ternary alloy (2×4) [767,768] is shown in Fig. 14.

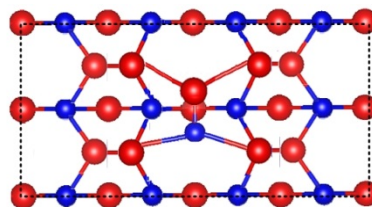


Figure. 14. The heterodimer or mixed-dimer on InP or GaP $(001)A-(2\times4)$ reconstruction. The surface is terminated by In or Ga atoms, each which possesses two dangling sp^3 hybrids along $[111]$ and $[\bar{1}\bar{1}\bar{1}]$ directions. Some other reconstructions can be formed when the middle III-V bond is replaced by a P dimer as $\sigma(2\times4)$ [761,762,766], a Ga dimer [766], or a three-fold symmetry group-V trimerlike unit [757].

The relationship between phases and growth parameters is plotted in [770], and the reversible phase transformations among various phases are proposed. Some $(n \times 3)$ or $(n \times 6)$ intermediate phases and their coexistence phases appear in the transition process between (2×4) and (4×2) [742,743,746-748,751,767,768,770-773], in the ternary reconstructions [767,768,774], or in antinodes [771,773,774]. The common (2×3) dimer consists of one group-V dimer along $[\bar{1}10]$ direction each of whose atoms bonds to two group-III atoms on the second layer, and one adjacent group-V dimer along $[110]$ each of whose atoms bonds to two group-V atoms on the second layer. More complicated $(n \times 3)$ and $(n \times 6)$ reconstructions have the similar surface structure with a (2×3) dimer.

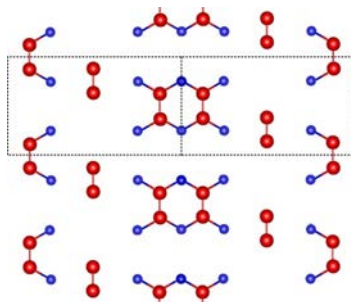


Figure. 15. A surface phase diagram of $(100)A$ - $c(8 \times 2)$ or (4×2) is the counterpart of the corresponding group-V terminated (2×4) structure.

In the situation of high temperature or low group V/III ratio, (4×2) or $c(8 \times 2)$ structure emerge on the $(001)A$ surface for GaAs [636,637,741,742,746,748,751,754], InAs [761,763,764], InSb [771,775], and InGaAs [766]. Unlike $(100)B$ - $\beta(2 \times 4)$ phase, there seems a contradiction about which one is more stable for surfaces containing three or two dimers on the outmost layer. The phase of $(100)A$ - (4×2) surface made up of two dimers and two missing dimers is energetically favorable [754]. Fig. 15 shows the surface phase diagram for (4×2) or $c(8 \times 2)$ reconstruction. On the surface, each (4×2) unit cell consists of two

neighboring group-III dimers and two missing dimers on the outmost layer, which are adjacent to another group-III dimer at the third layer. The group-V atoms stack on the second layer. The whole (4×2) reconstruction exhibit a mirror image of the corresponding $(100)\text{B}-(2 \times 4)$ structure.

On (100) surface, $c(4 \times 4)$ phase is formed with excessive amounts of group-V atoms [747,748,770] or at lower temperatures [746,752,758,759,762]. Adjusting high V/III ratio or quenching to low temperatures can grow $c(4 \times 4)$ reconstruction in GaAs [741-743,746,748,752,754,776], InP [758,759,777], InAs [764], and InSb [771,774]. A group III-V $c(4 \times 4)$ pattern is shown in Fig. 16. It is a possible model for $c(4 \times 4)$ that corresponds to sets of three group-V dimers along $[110]$ adsorbed on a monolayer of group-V atoms.

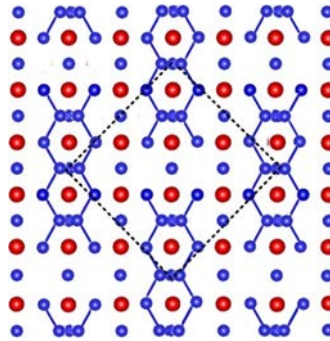


Figure. 16. Possible $(100)\text{B}-c(4 \times 4)$ reconstruction with extra group-V atoms replacing group-III vacancies to form the disordered structure. It involves the adsorption of excess group-V atoms.

In the rectangular unit of top layer, group-V dimers trigonally bond to the group-V atoms on the second layer. The saturated three dimers phase should be more stable than one dimer or two dimers phase in $c(4 \times 4)$ reconstructions due to a smaller surface free energy for three dimers reconstruction.

For GaN (001) surface, (1×1) phase is unstable due to Peierls transition, but it can exist under a N-rich environment. In general, Ga-rich conditions make contributes to improve the surface stability. With the decreasing of group V/III ratio, the phase transition (1×1) → (2×2) → c(2×2) will occur. Compared with (1×1) structure, (001)A-(2×2) and c(2×2) reconstructions are the relative stabilized surfaces with 50% and 100% Ga-terminated coverages respectively. (2×2) reconstruction exhibits one row of Ga dimers growing along [110] direction adjacent to one missing row of dimers on the outmost layer. The Ga atoms of dimer back bond to the Ga atoms below, which are adjacent to N atoms stacking on the second layer. In c(2×2) reconstruction, one row of Ga dimers shifted to half periodicity along [110] covers the Ga vacancies and enhances the polarity of surface [778,779]. Under N-rich or high temperature environments, the surface reconstruction might exhibit an intrinsic (1×4) phase, but the surface will degrade in the situation of extreme N-rich. The degradation can be relieved through the enhancement of Ga concentration. (1×4) reconstructure is constructed by a row of three continuous Ga dimers and one missing dimer neighboring to the dimer row. Each outmost Ga dimer has two back bonds to the N atoms below. It might be slightly more stable than (2×2) and c(2×2) reconstructions on (100) surface. However, the introduction of As can significantly improve the stability of (2×2) and c(2×2) phases [780,781].

Ideal sawtooth {111} microfacets are illustrated in Fig. 10, while the real (111)A/B facets exhibit (2×2) or ($\sqrt{19} \times \sqrt{19}$) R23.4° reconstruction [782]. Unlike Si(111) surface exhibits a (2×1) π -bonded structure at low temperature or room temperature, or else (5×5) and (7×7) structure at high temperature, most of group III-V {111} surfaces produce (2×2) vacancy-buckling reconstruction where the surfaces are saturated via surface dangling bonds by rehybridization or converting into nonbonding electronic states.

For the reconstruction on polar (111)A surface, a variety of group III-V materials are widely studied, such as GaAs [716,754,756,783-791], InAs [791], GaP [792,793], GaSb [793,794], InSb [794,795], and so on. The geometries of different materials are remarkably similar, but there is a larger magnitude of distortion in the reconstructions of antimonides [793-795]. In general, (111)A-(2×2) reconstructions might be energetically favorable because of their low surface free energy and their electrostatic neutrality where the dangling bonds of group-III atoms are the equivalent of that of group V atoms. The neutrality can be realized through either adding group-V atoms to, or removing group-III atom from, every unit cell. Therefore there are several substructures on the (111)A surface, including group-III vacancy, group-V adatom and group-V trimer replacing the vacancy.

No matter under group-III rich or group-V rich, vacancy structure is the most stable reconstruction for (111)A-(2×2). Trimer reconstruction might be stable only in the extreme group-V rich environment. The formation of vacancy reconstruction is the result of the charge compensation. The top view of the (111)A composed of the (2×2) vacancy is plotted in Fig. 17(a). In the unit cell, the removal of one cation generates three group-V dangling bonds to accompany three corresponding group-III dangling bonds. In the process of rehybridization, the electrons of group-III atoms transfer to the dangling bonds of group-V atoms. Meanwhile, three planar sp^2 cation dangling bonds and three p-type anion dangling bonds are formed. The rehybridized orbitals are slightly contracted together, and the tetrahedral bond angles are changed, i.e., 119.2° and 93.8° for Ga and As atoms respectively on GaAs surface [754].

The compounds and geometries of (111)B surface are more complicated than that of (111)A. Besides group-III adatom, group-III trimer, group-V vacancy, and group-V trimer in (2×2) phase [716,743,754,783-787,796], ($\sqrt{3}\times\sqrt{3}$) [756], (3×3) [756], ($\sqrt{19}\times\sqrt{19}$)-R23.4°

[743,754,797-801] and $(\sqrt{7}\times\sqrt{7})\text{-R}19.1^\circ$ [798,799] reconstructions can also be formed on (111)B surface. Under group-V rich environment, (2×2) phase with group-V trimer yields the lowest surface energy compared with other (2×2) reconstructions [754,796,797]. Fig. 17 (b) plots that the threefold coordinated symmetry of group-V adatoms which is formed via slightly strained V-V bondings and 60° bond angles to the neighboring group-V adatoms. Each atom in a trimer unit back bonds to one group-V atom on the outmost layer. Compared with the bulk bondings, the intertrimer bondings become shorter and stronger.

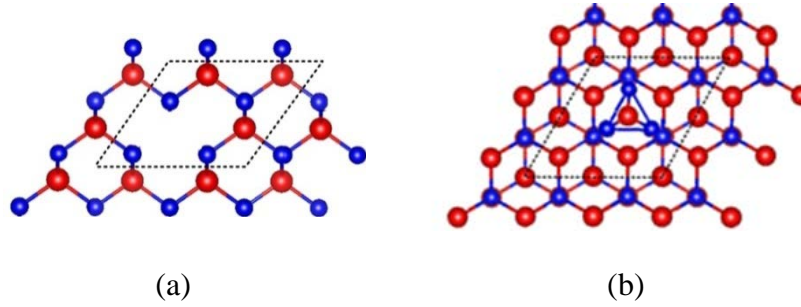


Figure. 17. Top view of group III-V (111)A- (2×2) vacancy reconstruction (a) and (111)B- (2×2) reconstruction with the group-V trimer (b). (a) In (111)A- (2×2) unit cell, the fourth group-III atom is removed. Meanwhile, the fourth group-V atom tetrahedrally bonds to three group-III atoms on the surface and another one stacking below. (b) In (111)B- (2×2) unit cell, the trimer is formed to saturate three dangling bonds and leave a rest atom with one dangling bond.

Under group-III rich or high temperature environment, a more complex and less strain $(\sqrt{19}\times\sqrt{19})\text{-R}23.4^\circ$ reconstruction exhibits the lowest surface free energy on (111)B surface. $(\sqrt{19}\times\sqrt{19})\text{-R}23.4^\circ$ phase was first studied by D. K. Biegelsen et al., while the proposed structure with an odd number of atoms per unit cell cannot be fully autocompensated [797]. H. H. Farrell et al., improved the $(\sqrt{19}\times\sqrt{19})\text{-R}23.4^\circ$ reconstruction and proposed the surface accompanying fraction electrostatic neutrality [800]. In Fig. 18, $(\sqrt{19}\times\sqrt{19})\text{-R}23.4^\circ$ unit cell is dominated by a bilayer hexagonal ring where Group-V atoms are in the top layer,

meanwhile the unit cell consists of four planar group-III atoms on the surface. The antisite of III/V atoms in the hexagonal ring might occur when the group V/III ratio varies.

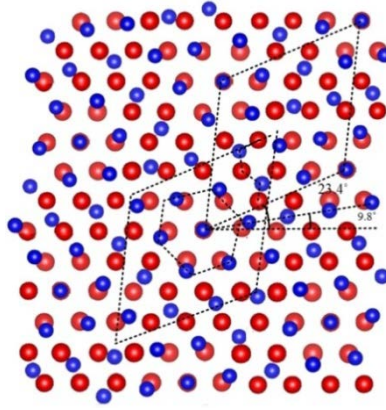


Figure. 18. (111)B ($\sqrt{19} \times \sqrt{19}$) $R23.4^\circ$ reconstruction. The atoms are located in inequivalent domains of ($\sqrt{19} \times \sqrt{19}$), which is created via a 23.4° rotation of the cell translation vector relative to the unreconstruction layer.

Compared with a mass of studies on ZB polar surfaces, there are not a large number of papers discussing about surface reconstructions for arsenides or phosphides with WZ structures. The most of polar {0001} surface reconstructions proposed were applied for nitrides [802-845]. (1×1) is the most common reconstruction on the polar {0001} surface, while the so-called (1×1) {(5.08×2.54)- $R20^\circ$ [808]} is not the same with the bulk structure. This kind of pseudo-(1×1) reconstruction might not correlate with the periodic atom arrangements on the surface, on the contrary, it maintains an incommensurate reconstruction. Under a N-rich environment, the magnitude of reconstruction might be reduced. For GaN (0001)A surface, pseudo-(1×1) might be the most Ga-rich phase, which consists of a laterally contracted Ga terminated bilayer. The stronger Ga-Ga bonds and the lateral contracted overlayer can stabilize the (0001)-(1×1) phase [811]. For InN (0001)A surface, the In-terminated surface is composed of a 3/4 monolayer of In atoms under In-rich

conditions [813]. For AlN (0001)A surface, the reconstruction surface might exhibit a (2×6) phase under a low group V/III influx ratio [809].

The reversible phase transitions of WZ structures behave in a similar manner with ZB structures, which can be controlled by changing growth parameters. For GaN (0001) surface, phase transition occurs from pseudo (1×1) → (6×4) → (5×5) → (2×2) with V/III ratio or temperature increasing [802,808]. (6×4) reconstruction is an intermediate phase, which contains (1×1) and (5×5) phases, and (5×5) reconstruction is composed of a linear chain of unevenly displaced Ga adatoms [744,807,808]. Under a N-rich environment, (0001)-(2×2) might be energetically favorable. Several kinds of morphologies, such as group III/V adatoms, trimers, and vacancies, are similar with {111} surface reconstructions. Compared with other substructures of (2×2) phase, the favored morphology is most likely the N-adatom or group-III vacancies under a N-rich environment, while a group-III adatom is preferred under a relatively small V/III ratio [744,804,808,811]. (2×2) phase can be modulated into (4×4) or the coexistence of (2×2) and (4×4) via increasing the temperature further or reducing the V/III ratio [807], or reducing the temperature with a mediate Ga concentration [812].

On (0001)B surface, nitrides with large bond energies provide a high resistance to relaxation or reconstruction. For a nitrogen-terminated surface, (1×1) is not the most group-III rich phase anymore. Phase transformation occurs from (2×2) → (1×1) → (3×3) → (6×6) → c(6×12) with reduced group V/III ratio [805,806,810]. High order reconstructions are formed by depositing excess group-III atoms. Likewise (111)B-(2×2) reconstruction, group-V trimer is also a stable structure on (0001)B surface [814,815].

The nonpolar low-index facets on group III-V NW, such as {110}, { $\bar{1}100$ } and { $1\bar{1}20$ } are the most likely unreconstructed [816,817], but still exhibit rotational and

vertical relaxations [708-716,737-740,754,818-822]. The detailed bond contraction and the specific bond rotation of nonpolar surface have been analyzed in the above section. The original nonpolar facets have satisfied the energetically favorable requirements for the orbital rehybridization. The nearest group III/V neighboring atoms contain the equal numbers of the corresponding dangling bonds, and there are equal numbers of each type of hybrids per unit cell. Therefore the nearly charge neutral and complete relaxed (1×1) phase appears on the nonpolar surfaces [715,716,738,814,819]. (1×1) periodicity can correlate with or depend on the atomic arrangement of bulk termination, while the actual surfaces are relaxed because of reducing the surface free energy. Relaxation induces the actual nonpolar surfaces exhibiting dimer tilting or zigzag chain structures, as well as non-absolute charge neutrality. By the calculations of idea unreconstructed facets, the calculated surface free energy of $(\bar{1}\bar{1}00)-(1\times 1)$ was smaller than that of $(1\bar{1}\bar{2}0)-(1\times 1)$, meanwhile $(1\bar{1}\bar{2}0)-(1\times 1)$ was a little more stable than $(110)-(1\times 1)$, furthermore $(\bar{1}\bar{1}00)-(1\times 1)$ was preferred compared with $(112)-(1\times 1)$ [738,814]. The higher order reconstructions for nonpolar facets need to be studied further in the future.

The whole cross section of group III-V NW is composed of hexagonal relaxed and reconstructed facets. The common crystallographic structures of ZB/WZ NW along [111]/[0001] are shown in Fig. 19. Actually, there might be some other crystallographic structures formed when NW grow, while those facets with high dangling bond densities are unstable. $\{\bar{1}\bar{1}0\}$ facets in Fig. 19(a) are composed of staircaselike atom chains caused by relaxation. Each atom on facets has one dangling bonds, whereas three cations and three anions have two dangling bonds at six corners. In actual NW facets, dangling bonds are easy to be passivated by hydrogen, and the free energies of passivated surfaces are obviously smaller than that of clean facets [292,678,823].

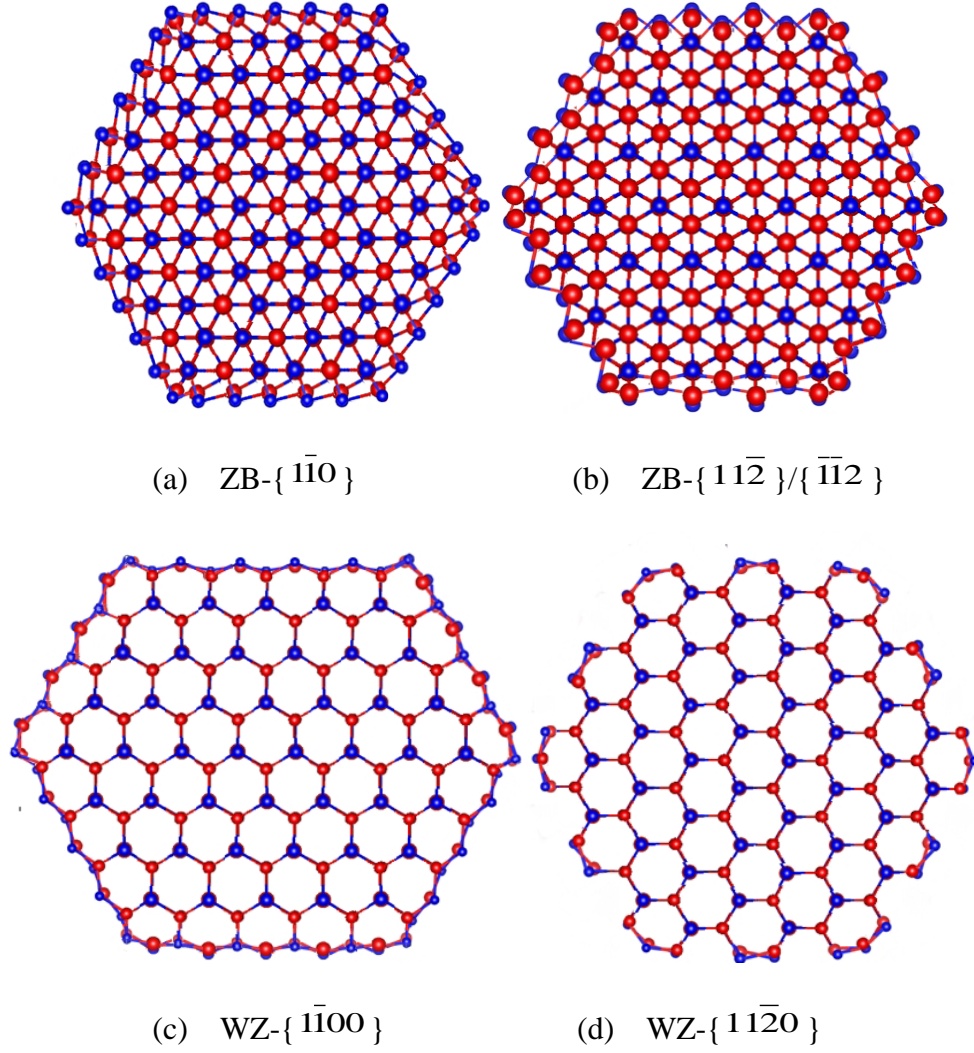


Figure 19. Schematic representation of the cross sections of relaxation, unpassivated group III-V NW facets. Rotation relaxation and contraction of the bonds on the outmost layers are visible.

For $\{ \bar{1}\bar{1}2 \} / \{ 11\bar{2} \}$ facets in Fig. 19(b), cations and anions on different facets have different numbers of dangling bonds, and each atom at outmost layer possesses $3/2$ dangling bonds in average. On $\{ 11\bar{2} \}$ facets, one twofold coordinated group-III atom has two dangling bonds, whereas one threefold coordinated group-V atom has only one dangling bond. On $\{ \bar{1}\bar{1}2 \}$ facets, one twofold coordinated group-V atom has two dangling bonds, whereas one threefold coordinated group-III atom has only one dangling bond. No matter

$\{\bar{1}\bar{1}2\}$ or $\{1\bar{1}2\}$ are unstable when the radii of NW are small. The $\{1\bar{1}2\}$ composed of microfacets $\{111\}$ A/B are plotted in Fig. 10. $\{\bar{1}\bar{1}00\}$ facets in Fig. 19(c) consist of zigzag cation-anion chains. Each of the atoms in the outlayer of bilayer has one dangling bond. For $\{1\bar{1}20\}$ facets, cations and anions form zigzag chains along the growth direction, and each atom possesses only one dangling bond on the surface.

IV. C. Defects, Dopants, and Bandgap Engineering of Nanowire

Defects and dopants are ubiquitous companions of group III-V NW growth, whereas the identification or detection for them in NW is difficult and indirect. In general, they behave as perturbations, substitutional impurities, interstitial impurities, or undesirable imperfections in NW, meanwhile, have important influences on the electronic, optoelectronic, photonic, and magnetic properties of devices. The fundamental carrier densities, Fermi levels, as well as a large number of basic equations about electron, phonon, optical and thermal properties, for nondegenerate and degenerate bulk semiconductors have been summarized well by S. M. Sze [322]. A variety of fundamental electronic, vibrational, optical and thermal properties for dopants have also been summarized by M. D. McCluskey and E. E. Haller [323]. However, the dopants in pseudo-1D structure have not been studied in great detail. Moreover, most existing studies on doping of NW, still mainly focus on the mechanisms, morphologies and measurements, rather than applications.

Defects and dopings can also be defined as unintentional impurities or intentional dopants artificially. No matter via MBE or by MOCVD, amounts of hydrogen, oxygen, carbon present during growth. Abundant H and C are particularly troublesome contaminations, which are almost impossibly removed by heating and are always present on the surfaces of

NW because of a high aspect ratio exposed to any atmospheres. For a pseudo-1D structure, a larger number of surface atoms mean not only more relaxation and reconstruction, but also different chemical environment of oxide or hydrogen termination formation. In addition, the likelihood of catalyst metals, mask materials, and atoms from substrate, as well as carrier gases, annealing gases, and residual gases can behave as dopants during NW growth. Suppressing unintentional and background impurities can control the drawbacks on performance. In contrary, reasonable intentional dopings in NW can drastically improve the characters of materials and tuning the bandgap of semiconductors effectively. For group III-V materials, defects and dopants might occur far from thermal equilibrium during growth and supply extra electron levels inside the bandgap. Impurities is an irreversible process in thermodynamics, and they induce a decrease in the Gibbs free energy by an increase in the whole configurational entropy,

$$\Delta S_{conf} = \sum_i x_i \ln x_i \quad (311)$$

The pinned levels in bandgap or near band edges act as the compensating centers, and thus deteriorate the conductivity and provide uncontrolled radiative or nonradiative recombination. For relatively small bandgap of semiconductors, dopings of shallow and deep impurities for both donors and acceptors are always achieved easily. For wide bandgap materials, dopings with either n-type or p-type with shallow and deep levels can be created, but not both [824].

Dopants can change morphologies, surface reconstruction, surface recombination, and the growth rates of facets during NW growth [636,825-837]. Meanwhile, dopants can suppress the dislocation formation [838], as well as induce the impurity intermixing [839] and impurity segregation [840,841]. Dopants can also modulate the phases for WZ, ZB, or polytypes by changing the contact angle of a catalyst and the supersaturation of a catalyst

[827,828] or by reducing the ZB/WZ structural energy difference [842]. In addition, different dopants have opposite influences on the NW growth mechanisms for inducing bending [826] or improving verticality [843].

Dopants might exhibit different phenomena compared with their behaviors in bulk with the quantum confinement arising in the low dimensional NW structure. In a low dimensional structure, dopants might auto-ionize without thermal activation, because the carrier must occupy one of confined states, hence the carrier energy increases passively with the reduced dimension [844]. Meanwhile the limitation of dopant concentration is suppressed by the quantum confinement [845]. Quantum confinement arises as a result of the changes in the density of electronic states. For 0D, density of states behaves as the discrete energy eigenfunctions. In the situation of 1D (~radius of NW lower than 50 nm), density of states behaves the characterization of a unit-step function [322,844-847],

$$n^{1D}(\varepsilon, z) = \frac{2}{\pi \hbar} \sin^2(kz) \sum_{N_m, N_n} \sqrt{\frac{2m_z^*}{\varepsilon - \left[\varepsilon_{C/V} + \hbar^2 \pi^2 (N_m^2 + N_n^2) / 2m_{mn}^* \sin^2(kz) \right]}} \quad (312)$$

where N_m and N_n are the densities of states on the cross section of NW. As the radius increases above the critical value, the 3D model will be employed to calculate the density of states. The total energy of state kz in the NW can be written as,

$$\varepsilon_{m,n}(k_z) = \varepsilon_{C/V} + \hbar^2 \pi^2 (N_m^2 + N_n^2) / 2m_{mn}^* \sin^2(kz) + \hbar^2 \pi^2 / 2m_z^* \quad (313)$$

where m^* is the effective mass.

Dopant limitation is an intrinsic property determined by the location of the semiconductor band edges, valence band maximum (VBM) and conduction band minimum (CBM), with respect to the Fermi level stabilization energy E_{Fs} in the amphoteric defect model [845,848,849] or the phenomenological p-like pinning energy E_{pin-p} and n-like

pinning energy $E_{\text{pin-n}}$ [850-853]. E_{Fs} is independent of the dopant level or the type. In the most of group III-V materials, the doping disparity is caused by the asymmetry of CBM and VBM with respect to E_{Fs} . A rough limitation rule [824,850,851] described the limits to doping of various n-type or p-type group III-V semiconductors in terms of their energy level alignment with the corresponding pinning energy. When $E_{\text{pin-n}} \ll \text{CBM}$, materials cannot be doped with n-type. When $E_{\text{pin-p}} \gg \text{VBM}$, materials cannot be doped with p-type. When $E_{\text{pin-n}} \gg \text{CBM}$, materials can be doped with heavily n-type. When $E_{\text{pin-p}} \ll \text{VBM}$, materials can be doped with heavily p-type. For NW, low dimensional structures actually have little effects on E_{F} or E_{Fs} due to a small spatial extension [854].

Take into consideration of these two models in n-type doping. In an amphoteric defect model, $E_{\text{F}} > E_{\text{Fs}}$ and acceptor-like defects are spontaneously formed resulting in pulling E_{F} towards E_{Fs} till $E_{\text{F}} = E_{\text{Fs}}$, and then doping reaches an n-type limitation. In a pinning Fermi level model, the intentional donors raise E_{F} , and thus lower the formation energy of intrinsic acceptor defects. The spontaneously formed acceptors will make the lowest $E_{\text{pin-n}}$ pin E_{F} to induce $E_{\text{F}} = E_{\text{pin-n}}$ and compensate the intentional donors. Therefore, the energy level of predominantly formed acceptors determines the n-type limitation. The maximum concentration of doping is determined by [851],

$$n_{\text{max}}^{(n/p)}(E_{\text{F}}^{(n/p)}, T) = \frac{(2m_{(n/p)}^*)^{3/2}}{2\pi^2} \int \frac{\sqrt{\varepsilon}}{\exp(\varepsilon - E_{\text{F}}^{(n/p)}/k_{\text{B}}T) + 1} d\varepsilon \quad (314)$$

The pinning level can be obtained by inverting Eq.314, because the pinning level is the bottleneck of a maximum dopant. Various solubilities of native defects in some common group III-V materials were studied in [855].

The equilibrium concentrations or the solubilities of defects can be determined by their formation energies and the growth temperatures. The formation energy depends on the

difference between the total energy and the energy of the host atoms, the chemical potential of species involved in the creation of the defect, the change of free energy required to create the defect, and the correction term. Under the thermal equilibrium, the defect concentration is defined as,

$$n_{defect} = N_{site} \exp\left(-\frac{E_{form}}{k_B T}\right) = N_{site} \exp\left(-\frac{E_{tot-def} - E_{tot-bulk} - \Delta\mu_{def} + N_e e E_F + E_{co}}{k_B T}\right) \quad (315)$$

where N_{site} equals to the ratio between the possible sites in a unit cell and the volume of the corresponding unit cell (for GaN $\sim 4.4 \times 10^{22} \text{ cm}^{-3}$). $\Delta\mu_{def}$ is the corresponding energy of vacancy atoms or substitutional impurity in a reservoir or the chemical potential of a vacancy, such as $\Delta\mu_{def} \sim -\mu_N$ for nitrogen vacancy, whereas $\Delta\mu_{def} \sim \mu_N$ for nitrogen interstitial, and $\Delta\mu_{def} \sim \mu_{Be} - \mu_{Ga}$ for substitution Be_{Ga} . N_e is composed of the charge number of the impurity and its sign, such as $N_e = -3$ for Ga vacancy on (111)A-(2×2) in Fig. 17(a), $N_e = 0$ for a neutral defect, $N_e = 1$ for one electron removed, and $N_e = -1$ for one electron added. The stable state will have the lowest formation energy via the calculation for Eq.315. E_{co} is a correction term accounts for k-point sampling, especially for a neutral defect. From Eq.315, one can get that the formation energy is raised up as the increasing of E_F linearly. And the decrease in formation energy can enhance the solubility of a defect exponentially.

In the situation of NW, the distribution of dopants might be changed compared with the distribution in bulk, owing to the defect formation energy of NW behaving different from that of bulk. The surface relaxation and reconstruction as well as electronic effects will have significant influences on the formation energy. The Fermi level respect to band edges can be shifted due to atomic asymmetry and dangling bonds on the facets of NW. As the radius of NW r_{NW} decreases, especially lower than the critical radius, the surface potential barrier will be suppressed with the reduction of the radius [834],

$$\Phi_{sb(r \leq r_c)} = \frac{r_{NW}^2 e^2 N_d \Phi_{sb-c}}{4\epsilon_{s-NW} [\Phi_{sb-c} - k_B T \ln(N_C / N_d)]} \quad (316)$$

where Φ_{sb-c} is the barrier as the radius is larger than the critical value, ϵ_{s-NW} is the dielectric constant, and N_C is the effective density of states in the conduction band. The bent band will reduce the formation energy of dopants on the surface and thus enhance the solubility and diffusivity for defects [856-858]. The concentration of defects at inner NW might still maintain the bulk solubilities for defects due to the loss of surface effects.

Actually, any one kind of defect has several charge states and thus can introduce the corresponding energy levels in the bandgap. Some of them are stable state, some of them are metastable, and others are unstable, such as Ga_i interstitials in GaN, only 3+ charge state is stable, 1+ and 2+ charge states are metastable, whereas others are unstable. The formation energies of a positive charged defect and a negative charged defect can be written as,

$$E(D^+) = E(D^0) - \epsilon(0/+) + E_F \quad (317)$$

$$E(A^-) = E(A^0) + \epsilon(-/0) - E_F \quad (318)$$

In an n-type doping situation, more energy is needed to form D^+ or produce electron due to a large E_F in Eq.317. Meanwhile, the formation energy of acceptor reduces resulting from E_F moving up in bandgap, and this increases the spontaneous acceptor concentration in Eq.318, such as native acceptor, or cation vacancy V_C . The opposite behaviors occur in p-type doping NW. The thermodynamic transition level $\epsilon(q_1/q_2)$ is defined as the ratio of the Fermi-level position to the corresponding charge states. When Fermi level is defined as zero or VBM, the transition level is given by,

$$\epsilon(q_1 / q_2) = [E_{form}(q_1) - E_{form}(q_2)] / (q_2 - q_1) \quad (319)$$

When E_F is below $\varepsilon(q_1/q_2)$, charge state q_1 is stable, whereas q_2 will be stable, when $\varepsilon(q_1/q_2)$ is above the transition level. When E_F equals to $\varepsilon(q_1/q_2)$, both charge states have the same formation energy. Defects, whose $\varepsilon(+/-)$ locate within the bandgap, will behave the amphoteric characteristic. If $\varepsilon(+/-)$ is positioned above CBM, donor has the lowest formation energy, while a defect acts as an acceptor for $\varepsilon(+/-)$ below VBM.

The position of a transition level compared to the thermal ionization energy ($\sim k_B T$) determines the defects to be a shallow level or a deep level. In general, the defects with shallow states have only a small impact on the crystal lattice. The properties of shallow levels are primarily determined by the growth temperature, effective masses, and the dielectric constant. Their wavefunctions are delocalized and formed mostly out of the states close to CBM or VBM, owing to weak perturbations by central cells and small ionization energies. On the deep levels, electrons required to remove from the valence band or to add to conduction band need much more energy than the thermal ionization energy. The defects with deep levels cause significant local strains and their wavefunctions are localized in deep levels. These deep levels can trap carriers and reduce the mobilities.

For an n-type doping, the statistical mechanics equation can be written with considering the degeneracy for the occupations of the donors,

$$\langle N \rangle = \frac{\sum N_m g_m \exp\left(-\frac{\varepsilon_m - N_m E_F}{k_B T}\right)}{\sum g_m \exp\left(-\frac{\varepsilon_m - N_m E_F}{k_B T}\right)} = \frac{1}{1 + \frac{1}{2} \exp\left(\frac{E_D - E_F}{k_B T}\right)} \quad (320)$$

when $N_m=0$, $\varepsilon_m=0$, and $g_m=1$ due to no electrons; when $N_m=1$, $\varepsilon_m=E_D$, and $g_m=2$ due to an occupation by an electron with either spin up or down. In Eq.320, the donor energy is $E_D=E_g-E_{D\text{binding}}$, where the binding energy $E_{D\text{binding}}$,

$$E_{D\text{binding}} = 13.6\text{eV} \cdot m_e^* / m_e \epsilon_{r-d}^2 = Ry \cdot m_e^* / m_e \epsilon_{r-d}^2 \quad (321)$$

where ϵ_{r-d} is the permittivity of semiconductor. Ry is the Rydberg constant.

When n-type NW are doped by shallow donors, it can be described in analogy to a hydrogen atom. The concentration of occupied neutral donors N_d^0 can be derived from Eq.320.

$$N_d^0 = \frac{N_d}{\frac{1}{2} \exp\left(\frac{E_c - E_d - E_F}{k_B T}\right) + 1} \quad (322)$$

where N_d is the shallow donor concentration, E_d is the donor ionization energy or donor binding energy. E_d ($\sim E_C - E_D$) is the energy difference between CBM and the donor level. For an n-type doping, the hole concentration can be neglected due to the charge neutrality. So the electron concentration with an n-type shallow doping can be written,

$$n \approx N_d^+ = N_d - N_d^0 = \frac{1}{2} \left(\frac{m_e k_B T}{2\pi \hbar^2} \right)^{3/2} e^{-\frac{E_d}{k_B T}} \left[-1 + \sqrt{1 + \frac{4N_d}{(m_e k_B T / 2\pi \hbar^2)^{3/2}} e^{\frac{E_d}{k_B T}}} \right] \quad (323)$$

Obviously, the electron concentration and the Fermi level will be affected by the variation of growth temperature. The electron concentration and the corresponding Fermi level will transition from an intrinsic region at a high temperature, to a saturation region, at last to a freeze-out region with the result of temperature decreasing.

When n-type NW are doped by deep donors, the equation that consists of the charge neutrality and statistical mechanics can be given by,

$$n \approx N_d^+ + N_{\text{deep}}^+ = 2 \left(\frac{m_e k_B T}{2\pi \hbar^2} \right)^{3/2} \exp\left(\frac{E_F - E_C}{k_B T}\right) = \frac{N_d}{1 + 2 \exp\left(\frac{E_F - E_D}{k_B T}\right)} + \frac{N_{\text{deep}}}{1 + 2 \exp\left(\frac{E_F - E_{\text{deep}}}{k_B T}\right)} \quad (324)$$

The electron concentration is similar with the shallow doping. In the freeze-out region, N_{deep} is much larger than N_d at a low temperature. E_F coincides with the deep level, hence $k_B T \ll E_d \ll E_{\text{deep}}$. So the concentration can be calculated by,

$$n = \frac{1}{2} \left\{ - \left(\frac{m_e k_B T}{2\pi \hbar^2} \right)^{3/2} e^{-\frac{E_d}{k_B T}} + N_{\text{deep}} + \sqrt{4 \left(\frac{m_e k_B T}{2\pi \hbar^2} \right)^{3/2} e^{-\frac{E_d}{k_B T}} (N_d - N_{\text{deep}}) + \left[\left(\frac{m_e k_B T}{2\pi \hbar^2} \right)^{3/2} e^{-\frac{E_d}{k_B T}} - N_{\text{deep}} \right]^2} \right\} \quad (325)$$

As the temperature increases, the electron concentration reaches the saturation region, where $E_d \ll k_B T \ll E_{\text{deep}}$. The electron concentration becomes $N_d + N_{\text{deep}}$, with the temperature increasing further to an intrinsic regime, and carriers are excited across the bandgap. The electron concentration expression is the same with the result of shallow donor doping.

For a p-type doping, the statistical mechanics equation can be written with considering the degeneracy for the occupation of the acceptors,

$$\langle N \rangle = \frac{\sum N_m g_m \exp\left(-\frac{N_m E_F - \varepsilon_m}{k_B T}\right)}{\sum g_m \exp\left(-\frac{N_m E_F - \varepsilon_m}{k_B T}\right)} = \frac{1}{1 + \frac{1}{4} \exp\left(\frac{E_F - E_A}{k_B T}\right)} \quad (326)$$

when $N_m=0$, $\varepsilon_m=0$, and $g_m=1$ due to no electrons; when $N_m=1$, $\varepsilon_m=E_A$, and $g_m=2$ due to an occupation by light and heavy holes with spin up and down.

When p-type NW are doped by shallow acceptors whose chemical valence are lower than that for the host atoms. The concentration of occupied neutral acceptor N_a^0 can be derived from Eq.326.

$$N_a^0 = \frac{N_a}{1 + \frac{1}{4} \exp\left(\frac{E_V + E_a - E_A}{k_B T}\right)} \quad (327)$$

where E_a is the acceptor ionization energy. E_a ($\sim E_A - E_V$) is the energy difference between VBM and the acceptor level. Take into consideration of the charge neutrality, and the electron concentration is neglected. The hole concentration can be written,

$$p \approx N_a^- = N_a - N_a^0 = \frac{1}{4} \left(\frac{m_h k_B T}{2\pi \hbar^2} \right)^{3/2} e^{-\frac{E_a}{k_B T}} \left[-1 + \sqrt{1 + \frac{8N_a}{\left(\frac{m_h k_B T}{2\pi \hbar^2} \right)^{3/2} e^{\frac{E_a}{k_B T}}}} \right] \quad (328)$$

Take into consideration of the situation of deep donor (with charge 1+) dopings into p-type NW. Deep donors will cause compensation and reduce the free carrier density. When the deep donor concentration N_{deep} is larger than acceptor concentration N_a , E_F will be close to the deep donor level $E_V + E_{deep}$, and the major donor will be neutral with a small number $N_{deep}^+ \approx N_a \approx N_a^-$. When N_{deep} is smaller than the acceptor concentration N_a , the material shows the p-type characteristic. The equilibrium equation consists of charge neutrality and the statistical mechanics,

$$p \approx N_a^- - N_{deep}^+ = 2 \left(\frac{m_h k_B T}{2\pi \hbar^2} \right)^{3/2} \exp\left(\frac{-E_F}{k_B T}\right) = \frac{N_a}{1 + 4 \exp\left(\frac{E_a - E_F}{k_B T}\right)} - \frac{N_{deep}}{1 + 2 \exp\left(\frac{E_F - E_{deep}}{k_B T}\right)} \quad (329)$$

At a low temperature freeze-out regime, the acceptor concentration can be calculated by,

$$p = \frac{1}{2} \left\{ -8 \left(\frac{m_h k_B T}{2\pi \hbar^2} \right)^{3/2} e^{-\frac{E_a}{k_B T}} - N_{deep} + \sqrt{32 \left(\frac{m_h k_B T}{2\pi \hbar^2} \right)^{3/2} e^{-\frac{E_a}{k_B T}} (N_a - N_{deep}) + \left[8 \left(\frac{m_h k_B T}{2\pi \hbar^2} \right)^{3/2} e^{-\frac{E_a}{k_B T}} + N_{deep} \right]^2} \right\} \quad (330)$$

In the saturation regime, the acceptor concentration becomes to $N_a - N_{deep}$. Besides the doping situations discussed above, the situation of p-type NW doped by acceptors is similar like the case of n-type NW doped by deep donors in Eq.323, and the situation of n-type NW doped by acceptors is similar like the case of p-type NW doped by deep donors in Eq.329. Some

n/p-type dopings in NW are given in Table 4. The mechanisms and behaviours of dopings in NW display the similar behaviors for dopants in bulk.

Table 4. Nanowire with n/p-type dopants.

| n-type | | | p-type | | |
|-------------|--|-----------|--------|-------------------------------------|---------------|
| NW | Dopant | Ref. | NW | Dopant | Ref. |
| GaAs | Si _{Ga} | [262,859] | GaAs | Zn _{Ga} | [866] |
| GaAs | Sn _{Ga} | [860] | GaAs | C _{As} | [867] |
| GaAs | Te _{As} | [861] | GaAs | Si _{As} , Be _{Ga} | [859] |
| AlGaAs/GaAs | Si _{Ga} | [862] | GaP | N | [868] |
| GaN | Si _{Ga} | [843] | GaN | Mg _{Ga} | [500,547,826] |
| GaN | V _N | [366,863] | GaN | V _{Ga} -O _N | [869] |
| GaP | S _P , Ga-O | [864] | InAs | Be _{In} | [870] |
| InAs | Si _{In} | [837] | InAs | Zn _{In} | [871] |
| InAs | Si _{In} , S _{As} , Te _{As} , C _{In} | [836] | InP | Zn _{In} | [827,828,830] |
| InAs | Si _{In} , S _{As} , Sn _{In} , Se _{As} | [833] | | | |
| InN | H _N , Si _{In} | [865] | | | |
| InP | Si _{In} | [831] | | | |
| InP | Sn _{In} | [830] | | | |

For GaAs, native defects are abundant in Ga-rich or As-rich environments. In undoped GaAs, As_{Ga} dominates as a deep double donor under As-rich growth condition, while the equilibrium concentration of V_{Ga} increases rapidly as E_F moves towards CBM. In a Ga-rich environment, acceptor Ga_{As} and shallow donor V_{As} will dominate, and V_{Ga} concentration increases with E_F approaching CBM [872-875]. In an n-type case, V_{Ga} is a dominant center as a shallow acceptor, whereas As_{Ga} becomes dominant as a deep donor in a p-type situation [873,874,876-878]. Interstitials as isolated impurities are thermodynamically much less likely under all conditions. But electrically nonactive As_i might become to dominate in the vicinity of melting point [855]. The equilibrium concentration of Ga_i might increase as E_F reaching VBM in p-type GaAs, and Ga_i will decrease with As concentration increasing. In a high aspect ratio situation, a large number of As dangling bonds and Ga dangling bonds present on the surface, whose energy levels locate near VBM or CBM separately [874].

Various extrinsic impurities are incorporated into GaAs as dopings during growth. In general, impurities form acceptors on group-III sites (shallow levels such as Be_{Ga} , Mg_{Ga} , Zn_{Ga} , Cd_{Ga} ; deep level such as Cu_{Ga}) [873,879-883] and on group-V sites (shallow levels such as C_{As} , Ge_{As} ; deep level such as Si_{As}) [636,873,880,884], or form donors on group-III sites (shallow levels such as C_{Ga} , Si_{Ga} , Ge_{Ga} ; deep levels such as N_{Ga} , Sn_{Ga}) [884,885] and on group-V sites (shallow levels such as S_{As} , Se_{As} , Te_{As} , Sb_{As} ; deep levels such as O_{As}) [872,876,886,887]. In addition, some neutral deep defect, such as N_{As} or O_{i} complexes can also cause nonradiative recombination meanwhile reduce the minority carrier lifetime [853,876,883].

Hydrogen and group-IV atoms can behave amphoteric nature in group III-V semiconductors. These amphoteric characteristics can be controlled by tuning the group V/III ratio during growth,

$$\ln \frac{IV_{\text{Ga}}}{IV_{\text{As}}} = \ln \left(C_{IV-\text{GaAs}} \frac{J_{\text{As}}}{J_{\text{Ga}}} \right) - \frac{\Delta G}{RT} \quad (331)$$

where $C_{IV-\text{GaAs}}$ is the experimental parameters for group-IV defects in GaAs, and ΔG is the free energy difference between IV_{As} and IV_{Ga} . As the V/III ratio is low, IV_{As} will dominate and the nature of acceptors behaves preferentially in amphoteric dopants. While donors are favored as V/III ratio is high. Isolated H can occupy V_{A} and it acts as a shallow donor, or locates at V_{C} to act as a shallow acceptor. Amphoteric nature and a small size H can be used to passivate acceptors or donors to form neutral complexes, such as $\text{As}_{\text{Ga}}\text{-H}$, $\text{C}_{\text{As}}\text{-H}$, $\text{Si}_{\text{Ga}}\text{-H}$, or $\text{O}_{\text{i}}\text{-H}$, $\text{V}_{\text{Ga}}\text{-H}$ [883,888,889]. In addition, hydrogen passivation can remove the energy levels in bandgap associated with the dangling bonds. The solubility of hydrogen can be calculated in Eq.315, where the free energy of H can be obtained by,

$$\mu_H = \frac{1}{2} \left\{ E(H_2) + k_B T \ln \left[\frac{Ph^3}{k_B T (2\pi m k_B T)^{\frac{3}{2}}} \right] - k_B T \ln \left(\frac{8\pi^2 m_{red} r^2 k_B T}{2h^2} \right) - k_B T \ln \left[\frac{\exp\left(-hc/2k_B T \lambda\right)}{1 - \exp\left(-hc/k_B T \lambda\right)} \right] \right\} \quad (332)$$

where the third term on the right side of equation is the rotation term, and the forth term is the vibration term. m_{red} is the half mass of hydrogen and λ is 4160 cm^{-1} for a hydrogen atom. The free energy can also be obtained from the JANAF Table in [890].

Various complexes involving combinations of two or more impurities or native defects present in GaAs and they affect the properties of NW. The most common complexes that are composed by native defects are $V_{Ga}-Ga_i$, $V_{As}-As_i$, $As_{Ga}-As_i$, $As_{Ga}-V_{Ga}$, and $As_{Ga}-V_{As}$ [885]. For the vacancy-interstitial pair, atom moves from a regular lattice site to an interstitial position and then several charge transfer energies are introduced within the bandgap. No matter interstitial, antisite, or substitutional impurities will induce the lattice relaxation. Another lattice relaxation is the formation of DX or AX centers. For a DX, the donor transports from the substitutional site to a relaxed site (lower symmetry C_{3v}) along one of the $\langle 111 \rangle$ directions and thus form deep acceptors, such as $Ge_{Ga}-V_{Ga}$, $Si_{Ga}-V_{Ga}$, $Si_{Ga}-O_i$ [854,872,873,883,884,891,892]. A DX center is highly localized for their wavefunctions and converts an intentional shallow dopant to a deep level impurity.

For GaN, native defects are also abundant. Under Ga-rich conditions, the equilibrium concentration of single shallow donor V_N increases as E_F moves away from CBM (p-type), while the equilibrium concentration of triple acceptor V_{Ga} is enhanced as E_F moves towards CBM (n-type) [893]. Spontaneous V_N donor dominates in “intrinsic” GaN and induces an n-type autodoping. Antisites GaN and N_{Ga} , as well as interstitials Ga_i and N_i have higher formation energies than vacancies and therefore their concentrations are suppressed. Because N_i , GaN , and N_{Ga} have not only one stable charge state, they will behave amphoteric

nature. For Ga_i , $3+$ is its only stable charge states, so Ga_i acts as a donor in GaN [894]. Under a N-rich environment, the formation energy of V_N becomes large, and the concentration of V_N will be reduced compared with the situation in a Ga-rich condition.

Various intentional impurities are studied as the dopants in GaN. The most common n-type dopings are Si_{Ga} , Ge_{Ga} , C_{Ga} , Be_i as shallow levels, as well as O_N as deep and shallow levels [834,880,895-905]. Moreover, Be_{Ga} [898,900], Mg_{Ga} [834,880,896,899,900,906-910], Zn_{Ga} [906,907], Ca_{Ga} [908,909], C_N [880,904,905,908,909,911], and Si_N [900] are widely studied as acceptors in p-type GaN. The biggest problem for acceptors is their too large ionization energies. Amphoteric hydrogen plays a significant role in GaN. It not only suppresses the native defects, but also forms complexes with other impurities. In a p-type doping, acceptor H^+ has a very low formation energy (smaller than V_N) and locates at the N-antibonding site. In an n-type doping, H^- resides at the center of hexagonal channel along c-axis. The enhancement in H^- induces E_F to increase, and thus increases the formation energy of donor V_N and suppresses the native defect in process. Hydrogen behaves as negative-U formation energy in GaN, because H^0 is thermodynamically unfavorable under all conditions [912]. Likewise hydrogen in GaAs, H can passive native defects and form complexes, such as double donor $V_N\text{-H}$, double acceptor $V_{\text{Ga}}\text{-H}$, single acceptor $V_{\text{Ga}}\text{-H}_2$, neutral complex $V_{\text{Ga}}\text{-H}_3$, and single donor $V_{\text{Ga}}\text{-H}_4$. Although hydrogen can form the corresponding complexes with p-type impurities, H atom has no bonds with impurities directly. Actually, H atom resides at the N-antibonding site. Native defects might form some more stable complexes with extrinsic impurities compared with those unfavorable isolated native defects themselves, such as double acceptors $V_{\text{Ga}}\text{-O}_N$ and $V_{\text{Ga}}\text{-Si}_{\text{Ga}}$, shallow acceptor $V_N\text{-Mg}_{\text{Ga}}$, and deep acceptor $V_{\text{Ga}}\text{-C}_N$ [869,897,900,911,913,914]. Similarly, the complexes

composed by two dopants, such as $\text{Mg}_{\text{Ga}}\text{-O}_{\text{N}}$ [900], or $\text{C}_{\text{N}}\text{-O}_{\text{N}}$ [915] have lower formation energies than their isolated constituents in GaN.

In general, dopants in arsenides [833,836,837,870-872,874,879,916,917] and in phosphides [827,876,918,919] behave the similar doping mechanisms with dopants in GaAs. And dopants in nitrides [880,897,902,903,905,910,920-922] behave the similar doping mechanisms with dopants in GaN. However, the magnitude of detailed relaxation and the properties caused by relaxation are different.

In the above segment of the foreign-metal catalysts in NW, various transition metals are used to catalyze NW growth. During growth, transition-metallic atoms are incorporated into NW inevitably. However, the solubilities of the transition metal impurities in group III-V materials are rather low. Some concentrations of defects might be too low to be detected. Mn is the only exception, whose solubility limit is much higher than other transition metals. In catalyzed growth, these inevitable impurities introduce a range of energy levels into the bandgap [322,323,923-925]. The wavefunctions of metal electrons are localized in deep levels, meanwhile, they also tunnel into the semiconductors and decay exponentially.

Transition-metallic atoms substitute group-III atoms and form bonds with group-V atoms. These bonds behave partly ionic character and give rise to intrinsic electric dipoles, meanwhile, the bond lengths are reduced slightly due to the partial ionic character. In general, substitution impurities act as deep donors, acceptors, or neutral substitutions in semiconductors. For transition metallic impurities, the neutral states behave as $3+(3d^3)$ charge state, acceptors show $1+(3d^5)$ or $2+(3d^4)$ states, and donors act as $4+(3d^2)$ charge state, via the transitions of tetragonally Jahn-Teller distorted.

Titanium [923,926], vanadium [923], and chromium [923,927-930] in group III-V fabricate not only deep donors, but also construct double acceptors as hole traps. For iron

[923,926-929], manganese [923,926,929], and nickel [923,928], the most common charge states are the neutral 3+ and acceptor 2+. The semi-insulating materials are obtained as dopants are with 3+ charge state. Dopings with cobalt [923,928] and copper [928,931] will lead to double acceptors in n-type materials. These deep levels are taken into account as the compensation centers of charges.

A series of point defects can segregate and absorb excess vacancies or interstitials. Therefore this induces the formation of dislocations in NW during growth. The elastic strain energy of an edge dislocation with a distance d_{dis} in NW can be obtained [183]

$$E_{edge-dis} = \frac{C_{edge-dis} r_{NW} G b^2}{4\pi(1-\nu)} \left(\ln \frac{d_{dis}}{b} + 1 \right) \quad (333)$$

where b is Burger's vector, G is the shear modulus, $C_{edge-dis}$ is the dislocation constant in NW. The most common dislocation in group III-V NW is the 60° dislocation, where the Burgers vector lies in a $\{111\}$ plane. The 60° dislocation often splits into two partial dislocations with 30° and 90° . The density of threading dislocations for GaN film on a sapphire substrate is 10^8 - 10^{11} cm $^{-2}$. Assuming the order of magnitude of threading dislocation in NW is similar with that in bulk. So the number of threading dislocations in a NW with 50 nm radius is 10^{-1} .

In general, the band structures of NW can be determined by the wavefunctions and the relative positions of the composed atoms in NW. The strain caused by relaxation and reconstruction, as well as the electric fields caused by piezoelectric polarization and spontaneous polarization will have significant influences on the energy bands.

The dependence of strain on band leads to band splitting with strain, due to the reduced symmetry. In the simplified model provided by C. G. Van de Walle [932], the influence of the hydrostatic strain component on the offsets of the conduction band and the valence band

is described. Shear strain reduces the symmetry and causes the valence band degeneracy lifting and the splitting of indirect conduction band. For compressive strain, the bandgap is widened and the splitting between HH and LH is increased; for tensile strain, the bandgap is shrunk and the splitting will be reduced [88,846,933]. Strain also affects the interaction between electron and phonon. Compression or dilation will induce the band up or down, whose magnitude is proportional to the strain accompanied with the deformation coupling to longitudinal acoustic phonons and the polar coupling to longitudinal optic phonons.

The lower symmetry of materials will cause a piezoelectric polarization. However, a reduced strain distribution might lead to a weaker piezoelectric polarization field in NW. The spontaneous polarization and the piezoelectric polarization arised from stained and polarized atoms will influence the shape of band edges and the carrier distribution [736,934,935]. An electrostatic field can be modulated by the piezoelectric polarization that can be written by,

$$P_{polar} = \begin{pmatrix} e_{15}\epsilon_{xz} \\ e_{15}\epsilon_{yz} \\ e_{33}\epsilon_{zz} + e_{31}(\epsilon_{xx} + \epsilon_{yy}) \end{pmatrix} \quad (334)$$

where e_{31} and e_{33} are the piezoelectric coefficients. Assume zz is the NW growth direction. The cross section strains are $\epsilon_{xx} = \partial u / \partial x$ and $\epsilon_{yy} = \partial u / \partial y$ (where $u^2 = u_{xx}^2 + u_{yy}^2$) as well as the axial strain is $\epsilon_{zz} = (-2C_{13}/C_{33})\epsilon_{xx}$ along the growth direction. C_{13} and C_{33} are the elastic stiffness. The potential induced by the piezoelectric polarization is,

$$V_{piezo}(r) = \frac{1}{4\pi\epsilon_0} \iiint \frac{P_{polar} \cdot (r - r')}{|r - r'|} d^3r' \quad (335)$$

The electronic structure can be calculated by first-principle calculations based on density functional theory (DFT) in the local-density approximation (LDA) [936,937] or the

generalized gradient approximation (GGA) [938,939] with the modified pseudopotentials [940]. DFT provided by W. Kohn et al. [941,942] describes the many-body electronic ground state in terms of single particle equations and an effective potential with minimal use of approximations to calculate band structure and density of states. The electronic structure calculations can be described by the plane wave basis [943] or the localized Gaussian type orbitals. The advantages of using the plane wave basis are easy to change from a real-space via a Fast Fourier Transformation to momentum-space where the kinetic energy is diagonal and is easy to realize convergence of total energy. For systems containing 3d or 4f electrons, Gaussian basis is a more appropriate choice [944].

The approximation treatment for core electrons can exploit the fully pseudopotential method [945], the Gaussian pseudopotential method [946], or the projector augmented wave (PAW) method [947]. A more accurate and higher cost method via quasiparticle calculations can also be employed in [948]. The introduced pseudopotentials avoid the need for an explicit treatment of the chemically inert core electrons, meanwhile ignore the nonlinearity of the exchange between valence and core electrons.

The perfect crystal can be described by the Hamiltonian with the average potential $V(r)$. The one electron Schrodinger equation with pseudowave ψ_k is given by

$$\left[\frac{p^2}{2m} + V(r) \right] \psi_k(r) = \varepsilon_k \psi_k(r) \quad (336)$$

where the pseudopotentials in group III-V (A-B) materials is given by,

$$V(r) = \sum_G (V_{GA} S_{GA} + V_{GB} S_{GB}) \exp(iG \cdot r) = \frac{1}{V_{cell}} \int [V_A(r) \exp(-iG \cdot r_A) + V_B(r) \exp(-iG \cdot r_B)] \exp(-iG \cdot r) dr \quad (337)$$

where G is the reciprocal vector, S_{GA} and S_{GB} are the structure factor, and V_{cell} is the volume of a primitive cell.

The empirical pseudopotential method exploits the assumption in which the valence electrons oscillate and the core electrons are frozen to calculate the electronic structure of group III-V materials [949-951]. The symmetric and antisymmetric structure factors are given by,

$$S_{sym}(G) = \frac{1}{V} \sum_j \exp(-iG \cdot r_j) \quad (338)$$

$$S_{asy}(G) = \frac{-i}{V} \sum_j P_j \exp(-iG \cdot r_j) \quad (339)$$

The symmetric and antisymmetric structure form factors $V_{sym}(G)$ and $V_{asy}(G)$ can be obtained from the difference and sum of the spherically symmetric cation and anion,

$$V_{sym}(G) = \frac{a_1 G - a_2}{1 + \exp(a_3 + a_4 G^2)} \quad (340)$$

$$V_{asy}(G) = (a_5 + a_6) \exp(a_7 + a_8 G^2) \quad (341)$$

where a_i ($i=1-8$) is the material parameters. The $V(r)$ can be calculated by Eq.338-341,

$$\langle G | V(r) | G \rangle = V_{sym}(G' - G) S_{sym}(G' - G) + i V_{asy}(G' - G) S_{asy}(G' - G) \quad (342)$$

When $V(r)$ is taken into the Schrodinger equation and the wavefunction ψ_k and the energy $\varepsilon(k)$ can be obtained. → Then calculate the density of states etc., and compare the calculated values with the experimental values. → Then alter $V(r)$ gradually till the calculated values in good agreement with the experimental results.

In the LDA method [26,952-955], a self-interaction correction with exchange and correlation term has to be taken into consideration. Meanwhile, only the local density is used to define the exchange-correlation approximation. The LDA provides a method to completely define the Kohn-Sham (KS) equations. In the Kohn's model, the matrix $\{\mathcal{H}\}$

elements include the electronic kinetic energy, electron-nuclear attraction, electron-electron repulsive and exchange-correlation potential terms. So the KS equations have the form [956-958],

$$\mathcal{H}_{KS}\psi_i(r) = \left[-\frac{\hbar^2}{2m}\nabla^2 + V(r) \right] \psi_i(r) = \left[-\frac{\hbar^2}{2m}\nabla^2 + \sum_j \frac{Z_j}{r} (r - R_j) + \frac{2\pi e^2}{\epsilon_0} \int \frac{n(r')}{|r - r'|} d^3r' + \frac{\delta E_{XC}[n(r)]}{\delta n(r)} \right] \psi_i(r) = \epsilon_i \psi_i(r) \quad (343)$$

For applying the KS equation to find the minimum energy, a set of equations in which each equation only involves a single electron have to be solved. The KS simplifies the complicated Hamiltonian. Take the initial $V(r)$ into the Schrodinger equation and get wavefunction ψ_k and energy $\epsilon(k)$,

$$V(r) = \sum_j \frac{Z_j}{r} (r - R_j) + V_{HF} + V_{exchange-correlation} \quad (344)$$

where Z and R stand for the nuclear charge and the position of the nucleus separately. The first term on the right side is devoted to the potential energy of electrons interacting with the nuclei. The second term is the Hartree electron-electron repulsion potential. And the exchange-correlation term is given by,

$$V_{exchange-correlation} = \epsilon_{XC} [n(r), r] + n(r) \frac{\delta \epsilon_{XC} [n(r), r]}{\delta n(r)} \quad (345)$$

The exchange-correlation potential contains the exchange-correlation energy ϵ_{XC} and its local change with density. Derivative is discontinuous when the state changes discontinuously with a function of density. In the LDA, the exchange-correlation potential is deemed to be a homogeneous electron gas approximation. So $E_{XC}[n(r)]$ can be written as a function of the local spin density,

$$E_{XC}^{LDA} [n(r)] = \int \mathcal{E}_{XC}^{homo} [n_{s\uparrow}(r), n_{s\downarrow}(r)] n(r) d^3r \quad (346)$$

In the Hartree-Fock approximation, the electron-electron Coulomb interaction is included. After calculating the charge density $\rho = \psi^* \psi$, one can solve the computationally expensive Hartree-Fock approximation,

$$\nabla^2 V_{HF} = \rho / \epsilon_0 \quad \text{or} \quad V_{HF}(r) = e^2 \iiint \frac{\rho(r')}{|r - r'|} d^3 r' \quad (347)$$

$$V_{HF}(G) = \frac{e^2}{\epsilon_0 G^2} \sum_k \sum_{G'} f C_k^*(G' - G) C_k(G') \quad (348)$$

$$V_{exchange-correlation} = -e^2 \frac{\sum f \rho}{|r - r'|} = \iiint \rho \epsilon_{exchange-correlation}(n_{s\uparrow}, n_{s\downarrow}) d^3 r \quad (349)$$

where f is the occupation weights, and $C_k(G)$ is the structure factor. Through comparison and modulation, the converged result can be obtained. The Hohenberg-Kohn theorem ensures that the converged solution corresponds to the charge density in the ground state. The total ground state energy of the system is given by,

$$E_{tot}(n) = T_s(n) \int V_{ext}(r) n(r) d^3 r + \frac{1}{2} \iint \frac{n(r) n(r')}{|r - r'|} d^3 r d^3 r' + E_H + E_{exchange-correlation}(n) \quad (350)$$

The first term is the kinetic energy, and the second term shows the direct interaction called Hartree energy. The third term expresses the nuclei effect and the last term is devoted to the many-body effects.

An extra Coulomb interaction U can be added to remedy the underestimated bandgap and correct the positions of the derived narrow bands [959-961]. In the calculations, the electron self-interaction is corrected by the introduction of U , especially for transition metals. The corresponding one electron energy is changed by adding a correlation interaction $U(0.5 - n_{\alpha, \alpha})$, where $n_{\alpha, \alpha}$ is an occupation matrix involving the orbit α (x, y, z). DFT can apply for non-integer particle number [962,963]. At the moment, the derivatives of the exchange-

correlation potential $\delta V_{\text{exchange-correlation}}/\delta n$ ($\sim 1/r$) must change discontinuously by an additive constant, and thus leads to a discontinuous jump in the exchange correlation term.

To define the Hartree potential, the electron density has to be used to study in an iterative way. Define an initial electron density $n(r)$ and calculate the effective potentials \rightarrow Solve the Kohn-Sham equations with defined the initial electron density to find the single-particle wavefunction $\psi_i(r) \rightarrow$ Calculate the electron density $n_{\text{KS}}(r) = 2 \sum_i \psi_i^*(r) \psi_i(r) \rightarrow$ Compare $n_{\text{KS}}(r)$ and $n(r) \rightarrow$ If the two densities are the same, then this is the ground state electron density and the density can be used to compute the total energy; If not, change the initial density $n(r)$. This self-consistent loop is repeated until the new electron density or the new total energy does not differ much from the old one.

In the GGA method [938,964-966], gradient expansions provide systematic corrections for electron densities that vary slowly over space, and stipulate that the exchange-correlation energy density depends additionally on the gradient of the electron density. The GGA provides more physical information hence it is more accurate. The exchange-correlation energy is improved by the introduction of gradient terms,

$$V_{\text{exchange-correlation}} = \iiint f(n_{s\uparrow}, n_{s\downarrow}, \nabla n_{s\uparrow}, \nabla n_{s\downarrow}) d^3r = \iiint n [\varepsilon(r_s, \zeta) + H(r_s, \zeta, t)] d^3r \quad (351)$$

where r_s is the Fermi radius, ζ is the relative spin polarization $(n_{\uparrow} - n_{\downarrow})/(n_{\uparrow} + n_{\downarrow})$, and t is the reduced gradient given by

$$t = \frac{|\nabla n|}{k_s n \left[(1 + \zeta)^{2/3} + (1 - \zeta)^{2/3} \right]} = \frac{|\nabla n|}{k_s n \left[\left(\frac{2n_{\uparrow}}{n_{\uparrow} + n_{\downarrow}} \right)^{2/3} + \left(\frac{2n_{\downarrow}}{n_{\uparrow} + n_{\downarrow}} \right)^{2/3} \right]} \quad (352)$$

where k_s is the local screening length vector. Different correlation coefficients and expectations are discussed for exchange under various approximate conditions

[938,939,955]. Some hybrid density functions are proposed and induce the GGA results to be improved further [874,876,967-974].

The N-electron wave function without spin-orbit interaction is described by a Slater determinant to satisfy the antisymmetry principle [958,975]. For the simplest two-electron case, the Slater determinant with the vector of coordinates r_i [958],

$$\psi(r_1, r_2) = \frac{1}{\sqrt{2!}} \det \begin{bmatrix} \phi_1(r_1, s_1) & \phi_1(r_2, s_2) \\ \phi_2(r_1, s_1) & \phi_2(r_2, s_2) \end{bmatrix} = \frac{1}{\sqrt{2}} [\phi_1(r_1, s_1)\phi_2(r_2, s_2) - \phi_1(r_2, s_2)\phi_2(r_1, s_1)] \quad (353)$$

where the spin orbitals can be expressed as a product,

$$\phi_i(r_k, s_k) = \sum_{i=1}^K \alpha_{i,k}(s_k) \varphi_{i,k}(r_k) \quad (354)$$

where $\alpha_{i,k}$ are the expansion coefficients, and $\varphi_{i,k}$ are the basis set for the calculation. In the HF method, the expectation of the Hamiltonian \mathcal{H} is,

$$\langle \psi | \mathcal{H} | \psi \rangle = \frac{1}{2} \iiint \left[\phi_1^*(r_1, s_1) \phi_2^*(r_2, s_2) \mathcal{H} \phi_1(r_1, s_1) \phi_2(r_2, s_2) + \phi_1^*(r_2, s_2) \phi_2^*(r_1, s_1) \mathcal{H} \phi_1(r_2, s_2) \phi_2(r_1, s_1) \right. \\ \left. - \phi_1^*(r_1, s_1) \phi_2^*(r_2, s_2) \mathcal{H} \phi_1(r_2, s_2) \phi_2(r_1, s_1) - \phi_1^*(r_2, s_2) \phi_2^*(r_1, s_1) \mathcal{H} \phi_1(r_1, s_1) \phi_2(r_2, s_2) \right] dr_1 ds_1 dr_2 ds_2 \quad (355)$$

The expression is easy to be expanded into N-electron system in the same manner.

A semiempirical multiband $k \cdot p$ method based on the Kane's model [976] can be used to study for bandstructures and optical properties in NW [977]. In an 8-band model, bands consist of electrons, heavy holes, light holes, and split-off, each of which has two spin orientations [978,979]. Additional bands can be further introduced to provide a better description, especially for indirect bandgap cases. A 40-band model has been described to analyze group III-V materials [980]. For a nondegenerate ZB or WZ structure, the wavefunction with a small perturbation can be derived,

$$\psi_k = \psi_0 + \frac{\hbar}{m} \sum_r \frac{\langle \psi_0 | k \cdot p | \psi_{0r} \rangle}{\epsilon_0 - \epsilon_{0r}} \psi_{0r} \quad (356)$$

And its corresponding energy level and the effective mass can be given by,

$$\varepsilon(k) = \varepsilon_0 + \frac{\hbar^2 k^2}{2m} + \frac{\hbar^2}{m^2} \sum_r \frac{\left| \langle \psi_0 | k \cdot p | \psi_{0r} \rangle \right|^2}{\varepsilon_0 - \varepsilon_{0r}} \quad (357)$$

$$\frac{1}{m_c^*} = \frac{1}{m} + \frac{2}{m^2 k^2} \sum_r \frac{\left| \langle \psi_0 | k \cdot p | \psi_{0r} \rangle \right|^2}{\varepsilon_0 - \varepsilon_{0r}} \quad (358)$$

In Eq.357, the influence of spin orbit coupling on the Hamiltonian is ignored. The coupling-ignored Hamiltonian is easily diagonalized, but it cannot be used to describe the energy dispersions precisely. The Hamiltonian with spin orbit coupling term can be written by,

$$\mathcal{H} = \frac{\hbar^2 k^2}{2m} + \frac{p^2}{2m} + \frac{\hbar k \cdot p}{m} + \mathcal{H}_s + V(r) = \frac{\hbar^2 k^2}{2m} + \frac{p^2}{2m} + \frac{\hbar k \cdot p}{m} + \frac{\hbar (\nabla \bar{V} \times \vec{p}) \cdot \vec{\sigma}}{4m^2 c^2} + V(r) \quad (359)$$

where σ is the Pauli spin matrices. So the energy $\varepsilon(k)$ with spin orbit coupling can be written by,

$$\varepsilon(k) = \varepsilon_0 + \frac{\hbar^2}{2} \sum_{\alpha\beta} k_\alpha k_\beta \left[\frac{\delta_{\alpha\beta}}{m} + \frac{2}{m^2} \sum_{p \neq q} \frac{\langle \psi_{p0} | p + \mathcal{H}_s | \psi_{q0} \rangle_\alpha \langle \psi_{q0} | p + \mathcal{H}_s | \psi_{p0} \rangle_\alpha}{\varepsilon_{p0} - \varepsilon_{q0}} \right] \quad (360)$$

where the coordinate symbols $\alpha, \beta = x, y, z$.

For a degenerate band calculation, valence band wavefunctions are p-like at the zone center and they have Γ_4 symmetry. The actual valence band curve in NW might have larger slopes for energy bands than the theoretical calculations. Smaller dimensions for NW might induce a stronger confinement in NW [425,426,844]. For ZB structure, the split-off band Γ_7 is described by,

$$\varepsilon_s = -\frac{3\mathcal{H}_s}{2l \cdot s} + \frac{\hbar^2 k^2}{2m} \left\{ 1 - \frac{2}{3} \left[\frac{P^2}{m(\varepsilon_0 + 3\mathcal{H}_s/2l \cdot s)} + \frac{2Q^2}{m(\varepsilon_{0r} + 3\mathcal{H}_s/2l \cdot s)} \right] \right\} \quad (361)$$

where l and s are the angular momentum and the spin operator separately. In this case, P and Q can be expressed by,

$$P^2 = -\left[\langle \psi_{1C} | k \cdot p | \psi_{4V} \rangle\right]^2 \quad \text{and} \quad Q^2 = -\left[\langle \psi_{4C} | k \cdot p | \psi_{4V} \rangle\right]^2 \quad (362)$$

Take into consideration of dispersion band Γ_8 for heavy holes and light holes,

$$\varepsilon_{hh} = -\frac{\hbar^2}{2m} \left[1 - \frac{2}{3} \left(\frac{P^2}{m\varepsilon_0} + \frac{2Q^2}{m\varepsilon_{0r}} \right) \right] k^2 - \left[\frac{\hbar^4}{9m^2} \left(\frac{Q^2}{m\varepsilon_{0r}} - \frac{P^2}{m\varepsilon_0} \right)^2 k^4 + \frac{4\hbar^4 P^2 Q^2}{3m^4 \varepsilon_0 \varepsilon_{0r}} (k_x^2 k_y^2 + k_y^2 k_z^2 + k_z^2 k_x^2) \right]^{1/2} \quad (363)$$

$$\varepsilon_{lh} = -\frac{\hbar^2}{2m} \left[1 - \frac{2}{3} \left(\frac{P^2}{m\varepsilon_0} + \frac{2Q^2}{m\varepsilon_{0r}} \right) \right] k^2 + \left[\frac{\hbar^4}{9m^2} \left(\frac{Q^2}{m\varepsilon_{0r}} - \frac{P^2}{m\varepsilon_0} \right)^2 k^4 + \frac{4\hbar^4 P^2 Q^2}{3m^4 \varepsilon_0 \varepsilon_{0r}} (k_x^2 k_y^2 + k_y^2 k_z^2 + k_z^2 k_x^2) \right]^{1/2} \quad (364)$$

The anisotropic effective masses of HH, LH and SO can be expressed in terms of the related Luttinger parameters γ_i [981,982].

$$\gamma_1 = -\frac{2}{3} \left[\frac{3}{2} + \frac{1}{m} \sum_l \frac{\langle \psi_j | k \cdot p | \psi_l \rangle_x}{\varepsilon_0 - \varepsilon_{0l}} + \frac{2}{m} \sum_l \frac{\langle \psi_j | k \cdot p | \psi_l \rangle_y}{\varepsilon_0 - \varepsilon_{0l}} \right] \quad (365)$$

$$\gamma_2 = -\frac{1}{3} \left[\frac{1}{m} \sum_l \frac{\langle \psi_j | k \cdot p | \psi_l \rangle_x}{\varepsilon_0 - \varepsilon_{0l}} - \frac{1}{m} \sum_l \frac{\langle \psi_j | k \cdot p | \psi_l \rangle_y}{\varepsilon_0 - \varepsilon_{0l}} \right] \quad (366)$$

$$\gamma_3 = -\frac{1}{3m} \sum_l \frac{\langle \psi_j | k \cdot p | \psi_l \rangle_{xy} + \langle \psi_j | k \cdot p | \psi_l \rangle_{yx}}{\varepsilon_0 - \varepsilon_{0l}} \quad (367)$$

where j stands for states in HH, LH and split off, i stands for other states. The Luttinger parameters can be used for yielding along the different crystallographic directions for the effective masses. The effective masses ($1/m^*$) for HH, LH and split off in ZB structure are given in Table 5.

Table 5. The effective masses in ZB structure.

| | [100] | [110] | [111] |
|----|---|------------------------------------|----------------------|
| HH | $\gamma_1-2\gamma_2$ | $(2\gamma_1-\gamma_2-3\gamma_3)/2$ | $\gamma_1-2\gamma_3$ |
| LH | $\gamma_1+2\gamma_2$ | $(2\gamma_1+\gamma_2+3\gamma_3)/2$ | $\gamma_1+2\gamma_3$ |
| SO | $\gamma_1-E_P\Delta_{so}/3E_g(E_P+\Delta_{so})$ | | |

-- E_P is the momentum matrix elements between conduction and valence bands, and Δ_{so} is the spin orbit splitting.

For WZ structure, a different crystal symmetry results in a different band structure compared with ZB. ZB has the highest order of fourfold-degeneracy due to its high symmetry. The order of triply-degeneracy of WZ is smaller than that of ZB resulting from the lower symmetry in WZ. When the spin orbit coupling is ignored, the energy dispersions are given as follows [983-986]:

$$\varepsilon_s = \Delta_1 + (W_1 + W_3)k_z^2 + (W_2 + W_2)(k_x^2 + k_y^2) - W_5(k_x^2 + k_y^2) \quad (368)$$

$$\varepsilon_{hh} = \frac{1}{2} \left\{ \begin{aligned} &\Delta_1 + (W_1 + W_3)k_z^2 + (W_2 + W_2)(k_x^2 + k_y^2) + W_5(k_x^2 + k_y^2) + W_1k_z^2 + W_2(k_x^2 + k_y^2) \\ &- \left[\Delta_1 + (W_1 + W_3)k_z^2 + (W_2 + W_2)(k_x^2 + k_y^2) + W_5(k_x^2 + k_y^2) - W_1k_z^2 - W_2(k_x^2 + k_y^2) \right]^2 + 8W_6^2k_z^2(k_x^2 + k_y^2) \end{aligned} \right\}^{\frac{1}{2}} \quad (369)$$

$$\varepsilon_{lh} = \frac{1}{2} \left\{ \begin{aligned} &\Delta_1 + (W_1 + W_3)k_z^2 + (W_2 + W_2)(k_x^2 + k_y^2) + W_5(k_x^2 + k_y^2) + W_1k_z^2 + W_2(k_x^2 + k_y^2) \\ &+ \left[\Delta_1 + (W_1 + W_3)k_z^2 + (W_2 + W_2)(k_x^2 + k_y^2) + W_5(k_x^2 + k_y^2) - W_1k_z^2 - W_2(k_x^2 + k_y^2) \right]^2 + 8W_6^2k_z^2(k_x^2 + k_y^2) \end{aligned} \right\}^{\frac{1}{2}} \quad (370)$$

where Δ_1 denotes the energy splitting induced by the structure symmetry in WZ. The dependence of the splitting on the band edge energies for \mathcal{H}_{WZ} is given by (assuming the valence bands belong to Γ_{6V} and Γ_{1V}),

$$\Delta_1 = \frac{\hbar^2}{m^2} \sum_r \frac{\left| \langle \psi_{6V} | \mathcal{H}_{WZ} | \psi_{6Vr} \rangle \right|^2}{\varepsilon_0 - \varepsilon_{0r}} - \frac{\hbar^2}{m^2} \sum_r \frac{\left| \langle \psi_{1V} | \mathcal{H}_{WZ} | \psi_{1Vr} \rangle \right|^2}{\varepsilon_0 - \varepsilon_{0r}} \quad (371)$$

The band structure coefficients W_i ($i \sim 1-6$) in Eq.368-370 can be derived from the coefficients of that in ZB structure. They satisfy the following relations,

$$W_1 = \frac{\hbar^2}{3m} \left\{ \frac{1}{2} \left[1 - \frac{2}{3} \left(\frac{P^2}{m\epsilon_0} + \frac{2Q^2}{m\epsilon_{0r}} \right) \right] + \frac{2}{3} \left(\frac{Q^2}{m\epsilon_{0r}} - \frac{P^2}{m\epsilon_0} \right) + \frac{4PQ}{\sqrt{3}m^{3/2}\epsilon_0\epsilon_{0r}} \right\} \quad (372)$$

$$W_2 = \frac{\hbar^2}{3m} \left\{ \frac{1}{2} \left[1 - \frac{2}{3} \left(\frac{P^2}{m\epsilon_0} + \frac{2Q^2}{m\epsilon_{0r}} \right) \right] + \frac{2}{3} \left(\frac{Q^2}{m\epsilon_{0r}} - \frac{P^2}{m\epsilon_0} \right) - \frac{2PQ}{\sqrt{3}m^{3/2}\epsilon_0\epsilon_{0r}} \right\} \quad (373)$$

$$W_3 = -2W_4 = -\frac{2PQ}{\sqrt{3}m^{3/2}\epsilon_0\epsilon_{0r}} \quad (374)$$

$$W_5 = \frac{\hbar^2}{6m} \left\{ -\frac{1}{2} \left[1 - \frac{2}{3} \left(\frac{P^2}{m\epsilon_0} + \frac{2Q^2}{m\epsilon_{0r}} \right) \right] + \frac{1}{3} \left(\frac{Q^2}{m\epsilon_{0r}} - \frac{P^2}{m\epsilon_0} \right) - \frac{4PQ}{\sqrt{3}m^{3/2}\epsilon_0\epsilon_{0r}} \right\} \quad (375)$$

$$W_6 = \frac{\hbar^2}{3\sqrt{2}m} \left\{ -\left[1 - \frac{2}{3} \left(\frac{P^2}{m\epsilon_0} + \frac{2Q^2}{m\epsilon_{0r}} \right) \right] + \frac{2}{3} \left(\frac{Q^2}{m\epsilon_{0r}} - \frac{P^2}{m\epsilon_0} \right) - \frac{2PQ}{\sqrt{3}m^{3/2}\epsilon_0\epsilon_{0r}} \right\} \quad (376)$$

Actually, there is an interaction between LH band and SO band, which will determine the coefficient W_7 . The interaction will affect band structures and the effective masses in WZ structure. The spin orbit splitting will induce the transformations of Eq.368-370 by introducing the spin orbit splitting terms Δ_2 and Δ_3 into the equations. The splitting terms are parameterized by \mathcal{H}_{WZ} (adding a spin orbit coupling term into Eq.358).

$$\Delta_2 = \frac{i\hbar^2}{m^2} \sum_r \frac{\left| \langle \psi_{6V} | \mathcal{H}_{WZ} | \psi_{6V'r} \rangle \right|^2}{\epsilon_0 - \epsilon_{0r}} \quad \text{and} \quad \Delta_3 = \frac{i\hbar^2}{m^2} \sum_r \frac{\left| \langle \psi_{6V} | \mathcal{H}_{WZ} | \psi_{1Vr} \rangle \right|^2}{\epsilon_0 - \epsilon_{0r}} \quad (377)$$

The band structure coefficients W_i (i~1-6) in Eq.372-376 are similar with the ZB Luttinger parameters γ_i in Eq.365-367. Therefore, the effective mass ($1/m^*$) for HH, LH and split off described by W_i in WZ structure are summarized in Table 6.

Table 6. The effective masses in WZ structure.

| | [0001] | [11 $\bar{2}$ 0] | [1 $\bar{1}$ 00] |
|----|------------|------------------|------------------|
| HH | $-W_1-W_3$ | $-W_2-W_4-W_5$ | $-W_2-W_4-W_5$ |
| LH | $-W_1-W_3$ | $-W_2-W_4+W_5$ | $-W_2-W_4+W_5$ |
| SO | $-W_1$ | $-W_2$ | $-W_2$ |

--The spin orbit splitting is ignored.

--The data from [983]

Different effective matrix $\{\mathcal{H}\}$ are studied in various models. The effective matrix $\{\mathcal{H}\}$ elements were constructed in 6×6 [983,985,987,988], 8×8 [987], or 16×16 [989,990] for WZ structures, and in 6×6 [991,992], or 8×8 [978,979,993] for ZB structures. The matrix can be diagonalized with some approximations, such as the spherical band or the band dispersion parabolic. When the slowly varying field caused by defects is taken into consideration, the Hamiltonian can be changed via an addition of the defect term.

$$\mathcal{H} = \frac{\hbar^2 k^2}{2m} + \frac{(p + eV_d)^2}{2m} + \frac{\hbar k \cdot (p + eV_d)}{m} + \frac{\hbar [\nabla V \times (p + eV_d)] \cdot \sigma}{4m^2 c^2} + V(r) + \frac{e\hbar}{2m} \sigma \cdot (\nabla \times V_d) \quad (378)$$

For defects, a supercell model can be constructed by an artificial unit cell composed of several primitive unit cells and one impurity [898]. In the supercell approach, the total energy is the sum over the special k-points. The dispersion can be estimated [994],

$$\varepsilon(k) = \varepsilon_d + \frac{\sum_r \langle \psi_d | \mathcal{H} - \mathcal{H}_{iso} | \psi_{dr} \rangle e^{ik \cdot r}}{1 + \sum_{r \neq 0} \langle \psi_d | \psi_{dr} \rangle e^{ik \cdot r}} \quad (379)$$

where \mathcal{H}_{iso} is the Hamiltonian operator with the change caused by a defect, ψ_d is the normalized isolated states, and ψ_{dr} is the state with a superlattice vector r .

Band offset in heterostructure is one of the most important characteristics that determine the transport, quality of contact or barrier, and quantum confinement. Not only quantum confinement, but also tunneling, correlation and interference phenomena will affect the quantum transport in NW. The hetero- and reduced structures play an important role in

electron-phonon coupling, impurity scattering, phonon interaction and some other physical phenomena. Quantum confinement can change the bandgap by over 1 eV, thus has an important influence on the bandgap engineering.

The basic rule for heterojunction band lineups is the electron affinity rule, where the Fermi levels of compounds tend to be aligned by transferring electrons. However, exploiting the reference potential in practice might be neither reliable nor precise. So the valence band offsets rather than the conduction band offsets are the more fundamental parameters. First-principles calculations are also widely used for theoretical studies of valence band offsets in heterostructures [995-998]. There is no doubt that group III-V NW can bring the heterostructural superiorities into full play. In an ideal, straddling GaAs/AlAs, GaSb/AlSb, GaAs/GaP, GaN/AlGaN, InGaN/GaN, GaAs/AlGaAs, InGaAs/InAlAs, InGaAs/InP, GaN/AlN, GaAs/GaSb, InN/GaN, InN/AlN, and staggered GaAs/InP, GaAs/InAs, InGaAs/GaSbAs, InP/AlInAs; InP/InAlAs, InAs/AlSb, GaAs/AlGaAs, as well as broken-gap (misaligned) InAs/GaSb, all of these heterostructures, might be realized in a pseudo-1D configuration. Even for homomaterials, heterostructures can be realized in NW by tuning WZ/ZB segments [730,989,999,1000]. In the ZB/WZ interface, the lowest electron state is confined in ZB layers, because HH states always behave double degenerate in WZ. Therefore this presents a staggered structure for direct bandgap semiconductors. This phenomenon has been proved in GaAs NW [534,541,543,735,816,1001], InP NW [1002,1003], and InAs [730,1004,1005]. Appropriate p/n-dopings can improve the carrier tailoring further.

However, some phenomena in heterostructures may interfere with the properties of NW, such as, group III-V heterostructures always suffer from persistent interface compositional grading; the valence electrons locating on the high-valence-band side may induce deep

states within the bandgap for low-valence-band materials; excess potentials can be generated by dipoles due to heterostructures [1006,1007], piezoelectric polarization due to strain, and polarization originating from the atomic arrangement along polar directions; the temperature dependence on bandgap may have different effects due to different components [1008,1009]. For optoelectronic devices, the heterojunction interface might induce the loss of carriers due to non-radiative recombination at centers originating from lattice mismatch. The reduction of dimension in NW also interferes with the properties of NW strongly due to high inhomogeneities in NW system [1010-1014]. The interfacial correlation effects altering electrical characteristics need to be calculated based upon the many-body GW approximation [1015,1016]. The method improves the Coulomb interaction in HF approximation for group III-V semiconductors. The bare Coulomb interaction is replaced by a dynamically screened Coulomb interaction. The interaction between the electron and its image charge caused by the inhomogeneity can be predicted based on a long-range correlation effect in the quasiparticle energy theory. The quasiparticle model provides a good description for charge transport in group III-V NW. In the quasiparticle energy calculations, the exchange-correlation potential is expressed as a non-local electron self-energy operator [1015,1017],

$$\left[\frac{\hbar^2 k^2}{2m} + V_H(r) \right] \psi_i(r) + \int \sum(r, r', \varepsilon_i) \psi_i(r') d^3 r' = \varepsilon_i \psi_i(r) \quad (380)$$

where \sum is a Hermitian that is the Fourier transform of GW function [1018]. In general, the GW approximation improves the quasiparticle energies relative to the LDA eigenvalues. The excited state spectrum can be described in the Green functions based upon the wavefunctions in the quasiparticle equation. In the simplified GW schemes, the exchange-

correlation potentials for conduction and valence states in the static Coulomb-hole and screened-exchange (COHSEX) approximation are given by [1015,1018],

$$V_{XC-C} = -e^2 \sqrt[3]{3\rho(r)/8\pi} \left[1 - \frac{E_g^2}{E_g^2 + (\hbar\omega_p)^2} \right] - \frac{C_{ex} (\hbar\omega_p)^2}{2 \left[E_g^2 + (\hbar\omega_p)^2 - E_g \sqrt{E_g^2 + (\hbar\omega_p)^2} \right]} \quad (381)$$

$$V_{XC-V} = -e^2 \sqrt[3]{3\rho(r)/8\pi} \left[1 + \frac{E_g^2}{E_g^2 + (\hbar\omega_p)^2} \right] - \frac{C_{ex} (\hbar\omega_p)^2}{2 \left[E_g^2 + (\hbar\omega_p)^2 + E_g \sqrt{E_g^2 + (\hbar\omega_p)^2} \right]} \quad (382)$$

where $\rho(r)$ is the local electronic density, $\hbar\omega_p$ is the plasmon energy and the exchange interaction C_{ex} is,

$$C_{ex} = \int \left[\phi_{v-C}(r-T) \phi_{v-V}^*(r-T) \right]^* v(r-r') \left[\phi_{v'-C}(r'-T) \phi_{v'-V}^*(r'-T) \right] d^3r d^3r' \quad (383)$$

In the exchange energy C_{ex} , v stands for the bare Coulomb interaction, ϕ is the Wannier function localized in bond v -C and v -V, respectively. And T is defined as a crystal translation vector. The GW approximation gives a prediction about bandgap change between WZ and ZB under strains [1019]. The corresponding strain deformation potentials are introduced into the band structures, and play an important role on the transport and optical properties in group III-V NW.

IV. D. Summary

This chapter is devoted to growth techniques and their corresponding mechanisms, including convection, diffusion, and capillary forces in NW system. Surface relaxation and reconstruction for different phases in NW are summarized. Not only quantum confinement, but also dopants have a strong influence on the bandgap and energy states in group III-V semiconductors. Effective dopings can be introduced by the incorporation from

a liquid catalyst or vapor species from sidewalls based on *in situ* dopings. Some ex situ doping approaches, such as ion-beam implantation, dopants diffusion and deposition, or annealing NW in the dopant ambient, can also be applied. Heterojunctions provide diversity and flexibility in the design of bandgap and allow more complex and advanced functionalities for applications. Heterostructures in NW are promising in the applications of tunnelling transistor, high electron mobility transistor, photodetector, laser, sensor, and solar cell. The treatment of the bandgap engineering in heterostructure NW bases upon the analysis of band structures. First-principles calculations based on DFT is a phenomenally successful approach to describe the quantum behaviors. The core of DFT is the calculations of the ground-state energy for electrons associated with a set of defined-position nuclei. The result of the iterative procedures converges toward a self-consistent solution of the equations only until a designed convergence is satisfied. A variety of calculations based on different approximations and experimental measurements are exploited to study the band structures. The calculation results are used to compare with the experimental measurements from optical measurements or photoemission and inverse photoemission experiments, meanwhile, the calculation approximations and methods can be remedied continually through the introduction of correction data. The dependence of exchange-correlation potentials on the bandgap in group III-V NW is still an open question. Neither methods nor approximations are panaceas up to now. The comprehensive introduction of some approximations in first-principles calculations are described in this chapter. The large surface dimension in NW due to a high aspect ratio plays a more important role in correlations and ionized impurities to alter electrical, optical, and magnetic characteristics. Some challenges, i.e., lattice mismatch, thermal expansion coefficient mismatch, polar/nonpolar surface nature, as well as other dopant and defect problems, need to be studied further.

V. Conclusion and Outlook

Nanowires have gained wide attention during the last decade. Today, advances in the science of NW show no signs of abating. On the contrary, people spend more on this versatile building block for developing group III-V semiconductor devices with excellent performances. A large number fundamental researches and current efforts already under way clear a path for future avenues of study. In this thesis, group III-V NW growth and characterization are systematically elucidated. In the first part of this thesis, thermodynamics and kinetics, as well as concerned phase equilibrium or transformation were described. The CVM and the MC simulation were presented to explain the dependence of free energy on entropy and lattice properties by analyzing topology, electronic distribution and vibrational states. The corresponding supersaturation caused by chemical potential and the Gibbs-Thomson effect are the driving force for nucleation during NW growth. The kinetic model was provided to give a summary of the dependence of rates on the adsorption, desorption, diffusion and nucleation. The model summarized the kinetic equations on every interface in the NW system, then the kinetic equations provided the growth rate and the critical dimension. Although the results are qualitative rather than quantitative, the model gave a good prediction for the characterization of NW. Then, top-down and bottom-up growth mechanisms were described systematically. Modern sub-10 nm resolution lithography can take advantage of the techniques developed by the existing semiconductor industry and control uniform NW arrays growth. Under the particular growth conditions, the VLS and VLS-like mechanisms were given to fabricate compositionally abrupt and structurally perfect NW. Foreign catalysts not only provide preferential sites but also reduce nucleation barriers. Choosing appropriate metals accompanied with moderate melting points, solvating abilities, thermal stability and other suitable chemical properties is key in the VLS

mechanism. However, the detrimental influences of transition metals during NW synthesis impact the electronic or optoelectronic performance due to the non-radiative recombination at deep levels. Group-III species via self-catalyzed processes were introduced to present a more comprehensive analysis of growth mechanism accompanied with preventing the drawbacks of introduction of transition metals. Moreover, the dependence of dimensions, phases, and density of group III-V on the growth parameters was given to consummate the NW growth model. Phases of the resultant NW depend on the details of temperature, pressure, influx rate and V/III ratio. Furthermore, the mechanisms of MOCVD and MBE for NW growth were analyzed, and the mechanisms provided strong evidence for the roles of the kinetics model and phase equilibriums. In addition, a generalized morphology analysis in the presence of surface relaxation and reconstruction were systematically investigated, meanwhile, the influences of dopants and defects were elucidated. The dependence of bandgap and states on the doping, strain, as well as low-dimension was described based upon the first-principles calculations. Doping affecting the electron density, strain having an impact on the effective masses of carriers, and quantum confinement modulating the material anisotropy were discussed in detail. The precise state analysis is attributed to advanced experimental measurements and a variety of code packages. According to the bandgap engineering in heterostructures, the capability of band offset combined with unrestricted lattice-mismatch in NW is opening up possibilities beyond devices by the international technology roadmap for semiconductors.

In recent days, the argument that Moore's law is nearing its end has become increasingly prevalent [1020], but it does not mean that the last hour of semiconductor has come. On the contrary, there is a lot of development worth pursuing for scientists. The cores of development for transistor are not only going smaller, but also going faster and consuming

less. Group III-V tunneling field-effect transistor (TFET) based on NW structure is a promising candidate to meet the above requirements. It overcomes the thermodynamic barrier and breaks the limitation of subthreshold swing (SS) of MOSFET, 60 mV/dec, at room temperature. The steeper SS provides lower power consumption and faster speed switching in group III-V TFET NW. TFET NW consume less power under a lower supply voltage, because the power is proportional to the square of the supply voltage. Tunneling mechanism can be realized when carriers tunnel through a potential barrier if the barrier is sufficiently thin [322]. Band to band tunneling is based on the breakdown mechanism, where the Zener tunneling occurring controlled by a breakdown voltage.

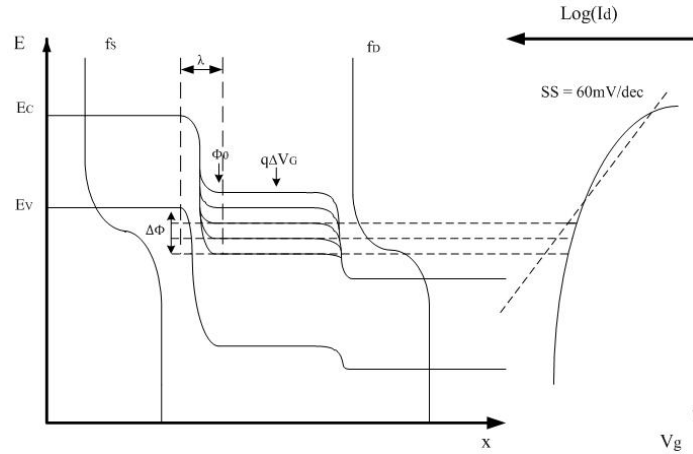


Figure 20. Principles of operation of an n-type TFET. The TFET operates like a gated p-i-n diode, and behaves like an energy band pass filter so only the carriers in the states in $\Delta\Phi$ can be allowed to tunnel through the barrier. The number of available states is determined by the transmission factor and Fermi levels in the source and the drain, respectively.

In Fig. 20, the electrons in the source tunnel through the bandgap barrier into the channel, when a positive gate voltage V_G moves the energy band in the conduction band down, resulting in overlapping with the states in the valence band of the source. In opposite, the unoccupied bands in the channel are pulled up with a negative gate voltage. Meanwhile,

hole tunneling behavior shows a opposite process where holes tunnel from the channel into the source. Because carriers can only move to empty states in the overlap band regime, those nonoverlapping states in the channel are cut off. In conclusion, only the states in the bandgap window $\Delta\Phi$ contribute to a tunneling current, as shown in Fig. 20. In the off state, the overlapping states in the window are negative, so the off-current is suppressed to a considerably low level.

The basic principle of TFET is based upon tunneling phenomenon, so the current of TFET is controlled by a tunneling probability. The tunneling probability of TFET depends on the material bandgap and the bandgap window in Fig. 20 [1021-1023]. Group III-V heterostructure NW reduce the influence of lattice-mismatch, meanwhile provide a large band to band current under a forward bias [1024,1025]. There is a tradeoff in heterostructures between the suppression for the off-current leakage due to a band discontinuity and the extra tunneling channels caused by defects on the interface [1026,1027]. Type-II or type-III heterostructures can improve the on-current and the I_{on}/I_{off} ratio effectively by using appropriate bandgap and small effective masses materials in NW [1028-1031]. Another advantage for TFET NW is easy to realize tight gate control wrapped by gate to suppress parasitic leakage currents. However, no TFETs can behave perfect performances on all parameters till now, meanwhile, fabricating tunneling transistors requires a complete redesign the structure to accommodate the asymmetric property and the fabrication processes in engineering.

Recently, an electronic-photonic chip including a large number of photonic components was integrated to overcome the bandwidth and power density limitations of traditional microprocessors with pure electrical components [1032]. This opens up future optical communication in a semiconductor integrated circuit. Group III-V type-I

heterostructure NW is much more appropriate than Si to serve as a laser source, an electro-optic/electro-absorption modulator, an illuminated photodetector, and an optical amplifier in an electronic-photonic integrated circuit [1033]. Group III-V semiconductors can provide direct bandgap and large refractive index materials for laser gain media. In the range of group III-V compounds laser emission, short distance and minimum attenuation data communication bands are ~ 850 nm (AlGaAs/GaAs NW, AlAs, InN) [1034,1035] and ~ 1.31 μm (GaAs/AlGaAs, InP/InGaAsP [1034], InGaAs QD [1036], GaAsSb QW [1037]), as well as long distance optic communication window is ~ 1.55 μm (InP/InGaAsP) [1034]. Some other wavelength windows, such as ~ 980 nm (InGaAs/AlGaAs, InGaAs/GaAs) [1034], ~ 533 nm (InGaN/GaN [1038]), ~ 380 nm UV (GaN NW [561,1039], GaN/AlGaN [1040]), and shorter wavelengths UV (AlGaN NW [1041], InGaN/GaN NW [1042]), have been demonstrated widely.

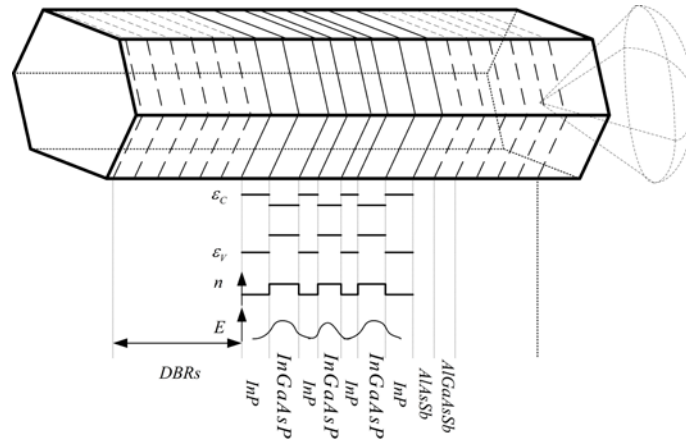


Figure 21. Illustration of a simplified axial InP/InGaAsP (~ 1.55 μm) NW laser. The cavity between the distributed Bragg reflectors (DBRs) consists of InGaAsP ($E_g \sim 0.8$ eV @300K) QWs, separated by InP ($E_g \sim 1.351$ eV @300K) barriers, and clad on each side by another InP barrier. The DBRs consists of AlAsSb/AlGaAsSb, where AlAsSb matches to the outside barrier InP lattice. The corresponding energy diagram, the refractive index profile, and the electric field/the photon density profile along axis are schematized.

NW laser system. The NW laser in Fig. 21 is designed as a vertical cavity surface emitting laser and the wave propagates along NW axis. The outside low index air provides a lateral confinement efficiently meanwhile the surface passivation improves the radiative efficiency or the quantum efficiency [1043]. The NW laser in Fig. 22 is the edge emission laser with a strong lateral confinement, and its output optical waveguide is provided from the edge of NW. The radial index change induces to guiding photons along NW axis, and the outside barrier can limit optical losses. The output wavelength or mode can be modulated by designing the well width and barrier height [1034], changing the NW length, or tuning the refractive index of the cladding [1044]. The precise mode calculation for NW is more complicated than that of fibers, but the hexagonal cross section calculations in NW can be approximated by the circular cross section calculations based upon the Maxwell's equations [1044]. Besides of lasers, photodetectors, electro-optic/electroabsorption modulators, and optical amplifiers can be fabricated based upon NW structures. The capability of dense integration with NW components into an integrated circuit needs to study further.

No matter whether the future roadmap departs the route of Moore's law or not, quantum computing that focuses on building and running algorithms promises exponential speedup for calculations [1045-1054]. The quantum algorithms originate from initializing qubits, applying evolution operators, controlling reasonable decoherence time, measuring qubits, and implementing appropriate quantum gates. NW represent a platform to investigate the dependence of physical realizations on the quantum calculations, because its extremely low dimension makes large electrostatic charging energies easier to achieve, complicated heterostructures are simpler to construct, and the phenomena of decoherence and imperfect quantum gates are more likely to be improved. Until now, the most promising physical implementations for quantum computers are single photon source, artificial quantum dot

(QD)/trapped nanostructure, and superconductor, which have to satisfy the requirements of logic criterion and correctability. In encoded quantum information, the state of system is represented by a vector in a 2D Hilbert space, where the vector can be written as a linear combination of the eigenstates. The state of a single qubit is shown in Fig. 23. A qubit can be used to describe the polarization of a photon from a polarized photon, or the spin of electrons, protons, and neutrons in a QD. The evolution operator causes the manipulation of quantities that depend on the state of a system. Some general criteria for qubits are summarized by D. P. DiVincenzo [1055].

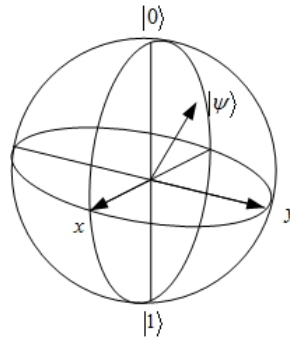


Figure 23. Illustration of a general qubit as a Bloch sphere, where the poles represent the eigenstates (or classical bits). Quantum mechanics allows a qubit to be in a linear superposition of the basis states, $|\psi\rangle = a|0\rangle + b|1\rangle$, where $|a|^2 + |b|^2 = 1$.

In quantum information processing, a high-efficiency single photon source based on a single QD or a trapped ‘atom’ can be well applied for computation, storage and communication, because photons are free of decoherence and are able to carry quantum information over a long distance [1056-1059]. The qubit state can be encoded in the polarization of a single photon on the basis of location and timing. The excitation pulse generates a single-photon pulse by controlling only QD ground-excitation recombination implemented [1056], or adjusting the phase of laser illuminating the trapped rubidium atom

[1057]. NW with embedded QDs can provide a promising technique for application in quantum photonics [1060,1061]. A QD and its corresponding Bragg mirrors cladding the QD can be grown in NW system to fabricate a cavity directly [1058,1062-1068]. The insertion of QD and the morphology of QD in NW can be controlled during NW growth.

For group III-V semiconductors, artificial atoms/QDs have ability to confine electrons or holes and their spin states can provide a logical qubit. Electron spins in QD [1069,1070] or nuclear spins can be used to encode quantum information. Quantum logic can be operated by changing an electrostatic gate voltage or a magnetic field. Coupled QDs can serve as a basic building block for a quantum computer [1071]. NW provide an alternative choice for fabricating double QDs and confining electrons in a low dimension. In real, nonuniform QDs, imperfect quantum gates, and the low quality of contact interface all induce the detrimental performances of quantum information processing. The electron spins in a QD can also be changed through the spin-orbit interaction in group III-V materials with a strong spin-orbit coupling [1072]. The qubit in this system consists of spin states and the orbital degrees of freedom, where spin states have some orbital characteristics. The perturbation of orbit caused by an electric field can induce the change of spin states. Group III-V NW with embedded QDs are expected to provide a platform to control spins in a fast qubit operation [1072,1073]. The coupling of QD spin qubits in a long distance can be realized by introduction of a superconducting microwave cavity into the NW system [1074]. The coupling microwave cavity in semiconductor superconductor NW generating hybrid qubits through the Josephson junction provides another approach for electrical control in future quantum implementation [1075]. These qubits can be controlled by not only microwaves, but also a magnetic field, voltages and currents. Other recent advances for the manipulation of quantum information also attempt to construct physical realizations on an ideal NW

platform. Moore's law is not a physical law in the manner of Newton's laws or Maxwell's equations, and it may be coming to a natural end one day. The thoroughly research on quantum calculations and quantum computers might pave the way for another new Moore's law.

Last but not least, the research of photovoltaic NW solar cell targets a compromise between higher conversion efficiency and a lower cost. Throughout the history of development of humans, every advancement of human civilization is accompanied by the improvements in utilizing solar energy, from producing and maintaining crops in the agricultural society, to exploiting coal, petroleum and natural gas in the industrial society. As worldwide energy demand increases, accompanied with a global tendency to lower fuel consumption and the emission of greenhouse gases, continued development of clean energy emerges as an important aspect of harnessing nature. In the future, the ability of direct solar energy conversion from incident light into electricity will determine the level of human development directly. Although the price of group III-V materials are much higher than Si, CdTe, and copper indium gallium selenide (CIGS), group III-V solar cells based on NW structure provide various advantages over most existing thin film or planar wafer based solar cells on the market.

Most of the sun's power distributes in the range of 400 nm to 2 μm , and the maximum solar cell efficiency lies in the range 1.4-1.6 eV. Group III-V materials provide appropriate bandgaps that are larger than 1.4 eV. Besides of GaAs, GaN, InGaN, InAs, GaAsP, GaInP, GaAs/AlGaAs, and InGaP/InGaAs have the optimal bandgap energies for applications. NW circumvent the lattice-mismatch, and are used to fabricate radial cells in which the radial structure ensures a sufficient optical absorption length while reducing the carrier extraction distance [1076,1077]. The needs for no matter extremely high efficiency at aerospace or

higher efficiency at a lower cost at terrain can be met through absorbing sunlight over a broad range of wavelengths and incident angles. NW radial multi-junction heterostructure will solve the problem by applying multiple group III-V materials, in which each material p-n junction will absorb the corresponding wavelength of light and produce electric currents. In Fig. 24, a homojunction p-n radial NW solar cell is plotted. The photon energy absorption induces exciton creation and separation to free carriers, and then carriers are collected by the electrodes, such as Al, Fe, or conductive glass. The type-II heterojunction offset or QD attached on NW [1078] provides alternative choices for solar cells based on NW systems. A tunnel junction needs to be added at the interface of heterojunctions for multi-junction NW. In a photovoltaic system, a photocurrent increases with the decreasing of bandgap exponentially, and an open circuit voltage can be enhanced with the enhancement of bandgap logarithmically. So to obtain a maximum output power, there exists an optimum value for the bandgap of group III-V semiconductor [322].

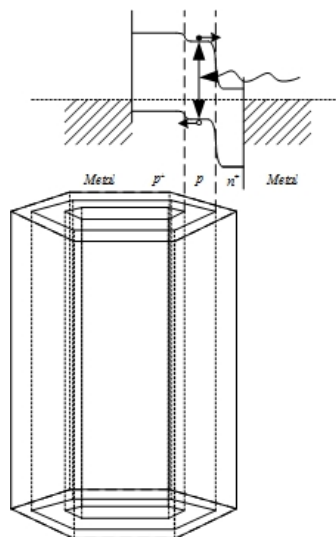


Figure 24. Schematic structure of an n^+p-p^+ radial GaAsP NW solar cell. Solar cell operates on the principle of photovoltaic effect, in which sunlight creates electron-hole pairs that are collected in an external circuit. The forward current can be dominated by the recombination current in the depletion region.

Annual results about photovoltaic cell efficiencies and module techniques were summarized in published tables [1079]. Expectations of group III-V material quality should be concomitantly raised to satisfy the requirements of high conductivity and low recombination rate. NW systems can improve the efficiencies through reducing reflections, providing extreme light trapping, improving bandgap modulations, and increasing strain and defect tolerance [1080]. Antireflection coatings can address reflection loss, arising from a difference in refractive indices between two media to eliminate the reflection at both interfaces. Cladding NW or a surface passivated process improves the efficiency via the reduction of surface recombination [1076,1081]. Changing radial layer thickness can control the light trapping to improve absorption meanwhile ordered NW arrays provide excellent light trapping and enhanced absorption [1082,1083]. In a NW system, carrier propagation is driven by wavefunctions as well as the possible resonance and interference caused by external fields. The coupling effects within NW or between NW need to be studied further.

References

1. R. P. Feynman, There's plenty of room at the bottom, *Engineering and Science*, pp. 22-36, 1960.
2. H. Kroemer, Theory of a wide-gap emitter for transistors, *Proc. IRE.*, 45, 1535, 1957.
3. H. Kroemer, Quasi-electric and quasi magnetic fields in a non-uniform semiconductor, *RCA Rev.*, 28, 332, 1957.
4. H. Kroemer, A proposed class of heterojunction injection lasers, *Proc. IEEE*, 51, 1782, 1963.
5. Zh. I. Alferov, R. F. Kazarinov, Semiconductor laser with electric pumping, Inventor's Certificate, no. 181737 [in Russian], Application, no. 950840, Mar. 1963.
6. C. Thelander, P. Agarwal, S. Brongersma, J. Eymery, L. F. Feiner, A. Forchel, M. Scheffler, W. Riess, B. J. Ohlsson, U. Gosele, and L. Samuelson, Nanowire-based one-dimensional electronics, *Mater. Today*, vol. 9, no. 10, p. 28, Oct. 2006.
7. L. Esaki and R. Tsu, Superlattice and negative conductivity in semiconductors, *IBM Res. Note RC-2418*, 1969.
8. L. Esaki, R. Tsu, Superlattice and negative differential conductivity in semiconductors, *IBM J. Res. Develop.*, 14, p. 61, Jan. 1970.
9. R. S. Wagner, W. C. Ellis, Vapor-Liquid-solid mechanism of single crystal growth, *Appl. Phys. Lett.*, vol. 4, no. 5, p. 89, Mar. 1964.
10. T. J. Trentler, K. M. Hickman, S. C. Goel, A. M. Viano, P. C. Gibbons, and W. E. Buhro, Solution-liquid-solid growth of crystalline III-V semiconductors: An analogy to vapor-liquid-solid growth, *Science New Series*, vol. 270, no. 5243, p. 1791, Dec. 1995.
11. M. S. Gudiksen, L. J. Lauhon, J. Wang, D. C. Smith, and C. M. Lieber, Growth of nanowire superlattice structures for nanoscale photonics and electronics, *Nature*, vol. 415, p. 617, Feb. 2002.
12. L. J. Lauhon, M. S. Gudiksen, D. Wang, and C. M. Lieber, Epitaxial core-shell and core-multishell nanowire heterostructures, *Nature*, vol. 420, p. 57, Nov. 2002.
13. M. Johnson, R. H. Silsbee, Interfacial charge-spin coupling: Injection and detection of spin magnetization in metals, *Phys. Rev. Lett.*, 55, 1790, Oct. 1985.
14. M. N. Baibich, J. M. Broto, A. Fert, F. N. V. Dau, F. Petroff, P. Etienne, G. Creuzet, A. Friederich, and J. Chazelas, Giant magnetoresistance of (001)Fe/(001)Cr magnetic superlattices, *Phys. Rev. Lett.*, 61, 2472, Nov. 1988.
15. G. Binasch, P. Grunberg, F. Saurenbach, and W. Zinn, Enhanced magnetoresistance in layered magnetic structures with antiferromagnetic interlayer exchange, *Phys. Rev. B*, Mar. 1989.
16. S. Datta, B. Das, Electronic analog of the electro-optic modulator, *Appl. Phys. Lett.*, 56, 665, 1990.
17. J. Y. Tsao, *Materials fundamentals of molecular beam epitaxy*, Academic Pre. Inc., 1993.
18. A. R. Miedema, P. F. de Chaterl, and F. R. de Boer, Cohesion in alloys-Fundamentals of a semi-empirical model, *Physica* 100B, 1, 1980.
19. D. A. Porter, K. E. Easterling, and M. Y. Sherif, *Phase transformations in metals and alloys*, 3rd edition, CRC Pre., 2008.

20. R. Kikuchi, A theory of cooperative phenomena, *Phys. Rev.*, vol. 81, no. 6, Mar. 1951.
21. R. Kikuchi, A theory of cooperative phenomena. II. Equation of states for classical statistics, *J. Chem. Phys.*, 19, 1230, 1951.
22. M. Kurata, R. Kikuchi, and T. Watari, A theory of cooperative phenomena. III. Detailed discussions of the cluster variation method, *J. Chem. Phys.*, 21, 434, 1953.
23. J. M. Sanchez, D. de Fontaine, The fcc Ising model in the cluster variation approximation, *Phys. Rev. B*, vol. 17, no. 7, Apr. 1978.
24. J. M. Sanchez, F. Ducastelle, and D. Gratias, Generalized cluster description of multicomponent systems, *Physica* 128A, 334-350, 1984.
25. Z. W. Lu, S. -H. Wei, A. Zunger, S. Frota-Pessoa, and L. G. Ferreira, First principles statistical mechanics of structural stability of intermetallic compounds, *Phys. Rev. B*, vol. 44, no. 2, Jul. 1991.
26. R. Lesar, Introduction to computational materials science: Fundamentals to applications, MRS, Cambridge Uni. Press, 2013.
27. J. M. Sanchez, Cluster expansions and the configurational energy of alloys, *Phys. Rev. B*, vol. 48, no. 18, Nov. 1993-II.
28. A. F. Kohan, P. D. Tapesch, G. Ceder, and C. Wolverton, Computation of alloy phase diagrams at low temperatures, *Comp. Mater. Sci.*, 9, pp. 389-396, 1998.
29. M. E. J. Newman, G. T. Barkema, Monte Carlo methods in statistical physics, Oxford Univ. Press, 1999.
30. G. Ceder, A derivation of the Ising model for the computation of phase diagrams, *Comp. Mater. Sci.*, 1, pp. 144-150, 1993.
31. B. Dunweg, D. P. Landau, Phase diagram and critical behavior of the Si-Ge unmixing transition: A Monte Carlo study of a model with elastic degrees of freedom, *Phys. Rev. B*, vol. 48, no. 19, Nov. 1993-I.
32. R. Magri, J. E. Bernard, and A. Zunger, Predicting structural energies of atomic lattices, *Phys. Rev. B*, vol. 43, no. 2, Jan. 1991-I.
33. T. Dietl, K. Sato, T. Fukushima, A. Bonanni, M. Jamet, A. Barski, S. Kuroda, M. Tanaka, P. N. Hai, H. Katayama-Yoshida, Spinodal nanodecomposition in semiconductors doped with transition metals, *Rev. Mod. Phys.*, vol. 87, no. 4, Oct.-Dec. 2015.
34. F. Ducastelle, Order and phase stability in alloys, Elsevier Science, 1991.
35. J. A. Barker, Methods of approximation in the theory of regular mixtures, *Proc. R. Soc.*, A216, 45, 1953.
36. J. Hijmans, J. De Boer, An approximation method for order-disorder problems I, *Physica*, 21, pp. 471-484, 1955; J. Hijmans, J. De Boer, An approximation method for order-disorder problems II, *Physica*, 21, pp. 485-498, 1955; J. Hijmans, J. De Boer, An approximation method for order-disorder problems III, *Physica*, 21, pp. 499-516, 1955; J. Hijmans, J. De Boer, An approximation method for order-disorder problems IV, *Physica*, 22, pp. 408-428, 1956; J. Hijmans, An approximation method for order-disorder problems V, *Physica*, 22, pp. 429-442, 1956.
37. T. Mohri, J. M. Sanchez, and D. De Fontaine, Binary ordering prototype phase diagrams in the cluster variation approximation, *Acta metall.*, vol. 33, no. 7, pp. 1171-1185, 1985.
38. R. Kikuchi, C. M. van Baal, Phase diagrams of FCC and BCC ordered alloys, *Scripta Metall.*, vol. 8, pp. 425-430, 1974.

39. D. Gratias, J. M. Sanchez, and D. De Fontaine, Application of group theory to the calculation of the configurational entropy in the cluster variation method, *Physica* 113A, pp. 315-337, 1982.
40. J. L. Murray, Calculation of the Titanium-Aluminum phase diagram, *Metal. Transac. A*, vol. 19A, pp. 243-247, Feb. 1988.
41. H. L. Lukas, S. G. Fries, and B. Sundman, *Computational thermodynamics: The Calphad Method*, Cambridge University Press, 2007.
42. J. M. Soler, E. Artacho, J. D. Gale, A. Garcia, J. Junquera, P. Ordejon, and D. Sanchez-Portal, The SIESTA method for ab initio order-N materials simulation, *J. Phys.: Condens. Matter*, 14, 2745-2779, 2002.
43. A. van de Walle, G. Ceder, The effect of lattice vibrations on substitutional alloy thermodynamics, *Rev. Mod. Phys.*, vol. 74, pp. 11-45, 2002.
44. D. de Fontaine, Cluster approach to order-disorder transformations in alloys, *Solid State Phys.*, 47, 33, 1994.
45. V. Ozolins, B. Sadigh, and M. Asta, Effects of vibrational entropy on the Al-Si phase diagram, *J. Phys.: Condens. Matter*, 17, pp. 2197-2210, 2005.
46. G. M. Stocks, D. M. C. Nicholson, W. A. Shelton, B. L. Gyorffy, F. J. Pinski, D. D. Johnson, J. B. Staunton, B. Ginatempo, P. E. A. Turchi, and M. Sluiter, First principles theory of disordered alloys and alloy phase stability, *Statics and Dynamics of Alloy Phase Transform.*, vol. 319, pp. 305-359, 1993.
47. M. Asta, V. Ozolins, Structural, vibrational, and thermodynamic properties of Al-Sc alloys and intermetallic compounds, *Phys. Rev. B*, vol. 64, 094104, 2001.
48. V. Ozolins, C. Wolverton, and A. Zunger, First-principles theory of vibrational effects on the phase stability of Cu-Au compounds and alloys, *Phys. Rev. B*, vol. 58, no. 10, Sep. 1998-II.
49. W. A. Oates, H. Wenzl, The cluster/site approximation for multicomponent solutions-A practical alternative to the cluster variation method, *Scripta Mater.*, vol. 35, no. 5, pp. 623-627, 1996.
50. W. A. Oates, F. Zhang, S. Chen, Y. A. Chang, Improved cluster-site approximation for the entropy of mixing in multicomponent solid solutions, *Phys. Rev. B*, vol. 59, no. 17, May 1999.
51. M. Laradji, D. P. Landau, and B. Dunweg, Structural properties of $\text{Si}_{1-x}\text{Ge}_x$ alloys: A Monte Carlo simulation with the Stillinger-Weber potential, *Phys. Rev. B*, vol. 51, no. 8, Feb. 1995-II.
52. A. van de Walle, M. Asta, Self-driven lattice-model Monte Carlo simulations of alloy thermodynamic properties and phase diagrams, *Modelling Simul. Mater. Sci. Eng.*, 10, pp. 521-538, 2002.
53. P. D. Fleming III, A. J. M. Yang, and J. H. Gibbs, A molecular theory of interfacial phenomena in multicomponent systems, *J. Chem. Phys.*, 65, 7, 1976.
54. A. D. J. Haymet, D. W. Oxtoby, A molecular theory for the solid-liquid interface, *J. Chem. Phys.*, 74, 2559, 1981.
55. A. G. Khachaturyan, *Theory of structural transformations in solid*, Dover edition, Dover Pub. Inc., 2008.
56. L. G. Ferreira, S. -H. Wei, and A. Zunger, First-principles calculation of alloy phase diagrams: The renormalized-interaction approach, *Phys. Rev. B*, vol. 40, no. 5, Aug. 1989-I.

57. M. J. Wainwright, M. I. Jordan, Graphical models, exponential families, and variational inference, *J. Found. Tre. Mach. Learning*, vol. 1, no. 1-2, pp. 1-305, Jan. 2008.
58. A. Pelizzola, Cluster variation method in statistical physics and probabilistic graphical models, *J. Phys. A: Math. Gen.*, 38, pp. R309-R339, 2005.
59. S. Matsumura, N. Kuwano, and K. Oki, Ordered structures and phase states in epitaxial layers of III-V semiconductor alloys, *Jpn. J. Appl. Phys.*, vol. 29, no. 4, pp. 688-695, Apr. 1990.
60. S. Froyen, A. Zunger, Surface-induced ordering in GaInP, *Phys. Rev. Lett.*, vol. 66, no. 16, Apr. 1991.
61. G. Wagner, Thermodynamics of phase diagrams of binary systems involving compounds, *ACTA Metall.*, vol. 6, p. 309, May 1958.
62. G. B. Stringfellow, P. E. Greene, Calculation of III-V ternary phase diagrams: In-Ga-As and In-As-Sb, *J. Phys. Chem. Sol.*, vol. 30, pp. 1779-1791, 1969; G. B. Stringfellow, Calculation of ternary phase diagrams of III-V systems, *J. Phys. Chem. Sol.*, vol. 33, pp. 665-677, 1972; G. B. Stringfellow, Calculation of ternary and quaternary III-V phase diagrams, *J. Cryst. Growth*, 27, 21-34, 1974.
63. G. B. Stringfellow, Calculation of regular solution interaction parameters in semiconductor solid solutions, *J. Phys. Chem. Solids*, vol. 34, pp. 1749-1750, 1973.
64. G. B. Stringfellow, Epitaxy, *Rep. Prog. Phys.*, 45, 469, 1982.
65. N. Saunders, A. P. Miodownik, *CALPHAD Calculation of Phase Diagrams: A Comprehensive Guide*, Pergamon, 1998.
66. L. M. Foster, A lattice parameter criterion for miscibility gaps in the III-V and II-VI pseudobinary solid solutions, *Latt. Param. Crit.*, vol. 121, no. 12, 1974.
67. M. Hillert, Empirical methods of predicting and representing thermodynamic properties of ternary solution phases, *Calphad*, 4, 1, pp. 1-12, 1980.
68. J. Nakano, P. J. Jacques, Effects of the thermodynamic parameters of the hcp phase on the stacking fault energy calculations in the Fe-Mn and Fe-Mn-C systems, *CALPHAD: Comp. Coupling Phase Diagrams Thermochem.*, 34, pp. 167-175, 2010.
69. M. B. Panish, M. Ilegems, Phase equilibria in ternary III-V systems, *Prog. Solid State Chem.*, 7, 39, 1972.
70. M. Ilegems, J. Pearson, Phase studies in III-IV, II-VI, and IV-VI compound semiconductor alloys systems, *Annu. Rev. Mater. Sci.*, 5, 345, 1975.
71. L. J. Vieland, Phase equilibria of III-V compounds, *ACTA Metall.*, vol. 11, p. 137, Feb. 1963.
72. M. Hillert, Empirical methods of predicting and representing thermodynamic properties of ternary solution phases, *Calphad*, vol. 4, no. 1, pp. 1-12, 1980.
73. L. Kaufman, J. Nell, K. Taylor, and F. Hayes, Calculation of ternary systems containing III-V and II-VI compound phases, *Calphad*, vol. 5, no. 3, pp. 185-215, 1981.
74. K. Chou, W. Li, F. Li, and M. He, Formalism of new ternary model expressed in terms of binary regular-solution type parameters, *Calphad*, vol. 20, no. 4, pp. 395-406, 1996.
75. Z. Wang, R. Luck, and B. Predel, A general regular-type geometric model for quaternary and higher-order systems, *Calphad*, vol. 17, no. 3, pp. 303-333, 1993.
76. B. Sundman, B. Jansson, and J. Anders, The thermo-calc databank system, *Calphad*, vol. 9, no. 2, pp. 153-190, 1985.

77. J. Andersson, A. F. Guillermet, M. Hillert, B. Jansson, and B. Sundman, A compound-energy model of ordering in a phase with sites of different coordination numbers, *ACTA Metall.* vol. 34, no. 3, pp. 437-445, 1986.
78. G. Eriksson, K. Hack, ChemSage-A computer program for the calculation of complex chemical equilibria, *Metall. Trans. B*, vol. 21B, 1013, Dec. 1990.
79. S. Chen, K. Chou, and Y. A. Chang, On a new strategy for phase diagram calculation I. Basic principles, *Calphad*, vol. 17, no. 3, pp. 237-250, 1993.
80. S. Chen, K. Chou, and Y. A. Chang, On a new strategy for phase diagram calculation II. Binary systems, *Calphad*, vol. 17, no. 3, pp. 287-302, 1993.
81. A. Altomare, M. C. Burla, M. Camalli, G. L. Cascarano, C. Riavazzo, A. Guagliardi, A. G. G. Moliteri, G. Polidori, and R. Spagna, A new tool for crystal structure determination and refinement, *J. Appl. Cryst.*, 32, 115-119, 1999.
82. M. Emelianenko, Z. Liu, and Q. Du, A new algorithm for the automation of phase diagram calculation, *Comp. Mater. Sci.*, 35, 61-74, 2006.
83. S. Pizzini, *Physical chemistry of semiconductor materials and processes*, Wiley, 2015.
84. V. G. Dubrovskii, Self-regulated pulsed nucleation in catalyzed nanowire growth, *Phys. Rev. B*, 87, 195426, 2013.
85. M. Yamaguchi, J. -H. Paek, and H. Amano, Probability of twin formation on self-catalyzed GaAs nanowires on Si substrate, *Nanoscale Res. Lett.*, 7:558, 2012.
86. A. A. Koryakin, N. V. Sibirev, D. A. Zeze, and V. G. Dubrovskii, Modeling of axial heterostructure formation in ternary III-V nanowires, *J. Phys. Conf. Series*, 643, 012007, 2015.
87. F. Glas, Chemical potentials for Au-assisted vapor-liquid-solid growth of III-V nanowires, *J. Appl. Phys.*, 108, 073506, 2010.
88. U. W. Pohl, *Epitaxy of semiconductors, Introduction to physical principles*, Springer, 2013.
89. F. Glas, J. C. Harmand, and G. Patriarche, Why does wurtzite form in nanowires of III-V zinc blende semiconductors, *Phys. Rev. Lett.*, 99, 146101, 2007.
90. A. J. M. Yang, P. D. Fleming III, and J. H. Gibbs, Molecular theory of surface tension, *J. Chem. Phys.*, 64, 3732, 1976.
91. P. Krogstrup, H. I. Jorgensen, E. Johnson, M. H. Madsen, C. B. Sorensen, A. F. i Morral, M. Aagesen, J. Nygard, and F. Glas, Advances in the theory of III-V nanowire growth dynamics, *J. Phys. D: Appl. Phys.*, 46, 313001, 2013.
92. N. Li, T. Y. Tan, and U. Gosele, Transition region width of nanowire hetero- and pn-junctions grown using vapor-liquid-solid processes, *Appl. Phys. A*, 90, pp. 591-596, 2008.
93. V. G. Dubrovskii, N. V. Sibirev, J. C. Harmand, and F. Glas, Growth kinetics and crystal structure of semiconductor nanowires, *Phys. Rev. B*, 78, 235301, 2008.
94. E. Gil, V. G. Dubrovskii, G. Avit, Y. Andre, C. Leroux, K. Lekhal, J. Grecenkov, A. Trassoudaine, D. Castelluci, G. Monier, R. M. Ramdani, D. Robert-Goumet, L. Bideux, J. C. Harmand, and F. Glas, Record pure zincblende phase in GaAs nanowires down to 5nm in radius, *Nano Lett.*, 14, pp. 3938-3944, 2014.
95. V. G. Dubrovskii, I. P. Soshnikov, G. E. Cirlin, A. A. Tonkikh, Y. B. Samsonenko, N. V. Sibirev, and V. M. Ustinov, On the non-monotonic lateral size dependence of the height of GaAs nanowhiskers grown by molecular beam epitaxy at high temperature, *Phys. Stat. Sol. (b)*, 241, no. 7, pp. R30-R33, 2004.

96. D. N. McIlroy, A. Alkhateeb, D. Zhang, D. Eric, Aston, A. C. Marcy, and M. G. Norton, Nanospring formation-unexpected catalyst mediated growth, *J. Phys.: Condens. Matter*, 16, R415-R440, 2004.
97. S. Kodambaka, J. Tersoff, M. C. Reuter, and F. M. Ross, Diameter-independent kinetics in the vapor-liquid-solid growth of Si nanowires, *Phys. Rev. Lett.*, 96, 096105, 2006.
98. L. Schubert, P. Werner, N. D. Zakharov, G. Gerth, F. M. Kolb, L. Long, U. Gosele, and T. Y. Tan, Silicon nanowhiskers grown on <111> Si substrates by molecular-beam epitaxy, *Appl. Phys. Lett.*, 84, 4968, 2004.
99. S. A. Kukushkin, A. V. Osipov, New phase formation on solid surfaces and thin film condensation, *Prog. Surf. Sci.*, vol. 51, no. 1, pp. 1-107, 1996.
100. V. G. Dubrovskii, N. V. Sibirev, Growth rate of a crystal facet of arbitrary size and growth kinetics of vertical nanowires, *Phys. Rev. E*, 70, 031604, 2004.
101. E. I. Givargizov, Fundamental aspects of VLS growth, *J. Cryst. Growth*, 31, 20-30, 1975.
102. V. G. Dubrovskii, G. E. Cirlin, I. P. Soshnikov, A. A. Tonkikh, N. V. Sibirev, Y. B. Samsonenko, and V. M. Ustinov, Diffusion-induced growth of GaAs nanowhiskers during molecular beam epitaxy: theory and experiment, *Phys. Rev. B*, vol. 71, p. 205325, 2005.
103. V. G. Dubrovskii, N. V. Sibirev, G. E. Cirlin, I. P. Soshnikov, W. H. Chen, R. Larde, E. Cadel, P. Pareige, T. Xu, B. Grandidier, J. -P. Nys, D. Stievenard, M. Moewe, L. C. Chuang, and C. Chang-Hasnain, Gibbs-Thomson and diffusion-induced contributions to the growth rate of Si, InP, and GaAs nanowires, *Phys. Rev. B*, 79, 205316, 2009.
104. V. G. Dubrovskii, Y. Y. Hervieu, Diffusion-induced growth of nanowires: Generalized boundary conditions and self-consistent kinetic equation, *J. Cryst. Growth*, 401, 431-440, 2014.
105. M. A. Herman, W. Richter, and H. Sitter, *Epitaxy: physical principles and technical implementation*, Springer, 2003.
106. R. W. Balluffi, S. M. Allen, and W. C. Carter, *Kinetics of materials*, Wiley-interscience, 2005.
107. V. G. Dubrovskii, N. V. Sibirev, G. E. Cirlin, A. D. Bouravleuv, Y. B. Samsonenko, D. L. Dheeraj, H. L. Zhou, C. Sartel, J. C. Harmand, G. Patriarche, and F. Glas, Role of nonlinear effects in nanowire growth and crystal phase, *Phys. Rev. B*, 80, 205305, 2009.
108. D. Turnbull, Formation of crystal nuclei in liquid metals, *J. Appl. Phys.*, 21, 1022, 1950.
109. M. J. Mandell, J. P. McTague, and A. Rahman, Crystal nucleation in a three-dimensional Lennard-Jones systems: A molecular dynamics study, *J. Chem. Phys.*, 64, 3699, 1976.
110. T. Ito, S. Okazaki, Pushing the limits of lithography, *Nature*, vol. 406, pp. 1027-1031, Aug. 2000.
111. M. Neisser, S. Wurm, ITRS lithography roadmap: 2015 challenges, *Adv. Opt. Techn.*, 4(4), pp. 235-240, 2015.
112. R. F. Pease, S. Y. Chou, Lithography and other patterning techniques for future electronics, *Proc. IEEE*, vol. 96, no. 2, Feb. 2008.
113. S. A. Campbell, *Fabrication engineering at the micro- and nanoscale*, 4th edition, Oxford Univ. Press, 2013.

- 114.H. Butler, Position control in lithographic equipment, *Control Systems, IEEE*, 31, pp. 28-47, Oct. 2011.
- 115.J. van Schoot, K. van I. Schenau, C. Valentin, and S. Migura, EUV lithography scanner for sub-8nm resolution, *Proc. SPIE*, vol. 9422, 94221F, 2015.
- 116.N. Mojarad, M. Hojeij, L. Wang, J. Gobrecht, and Y. Ekinici, Single-digit-resolution nanopatterning with extreme ultraviolet light for the 2.5 nm technology node and beyond, *Nanoscale*, 7, 4031, 2015.
- 117.H. Kim, W. Li, S. Danylyuk, W. S. Brocklesby, M. C. Marconi, and L. Juschkina, Optical properties of 2D fractional Talbot patterns under coherent EUV illumination, *J. Phys. D:Appl. Phys.*, 48, 375101, 2015.
- 118.T. S. Kulmala, M. Vockenhuber, E. Buitrago, R. Fallica, and Y. Ekinici, Towards 10 nm half-pitch in EUV lithography: Results on resist screening and pattern collapse mitigation techniques, *Proc. SPIE*, vol. 9422, 942204, 2015; T. S. Kulmala, M. Vockenhuber, E. Buitrago, R. Fallica, and Y. Ekinici, Toward 10 nm half-pitch in extreme ultraviolet lithography: results on resist screening and pattern collapse mitigation techniques, *J. Micro/Nanolith. MEMS MOEMS*, 14, 3, 033507, Jul.-Sep. 2015.
- 119.N. Mojarad, D. Fan, J. Gobrecht, and Y. Ekinici, Broadband interference lithograph at extreme ultraviolet and soft x-ray wavelengths, *Optics Lett.*, vol. 39, no. 8, p. 2286, Apr. 2014.
- 120.Y. Hirai, S. Hafizovic, N. Matsuzuka, J. G. Korvink, and O. Tabata, Validation of X-ray lithography and development simulation system for moving mask deep X-ray lithography, *J. Microelectromech. Syst.*, vol. 15, no. 1, Feb. 2006.
- 121.A. Heuberger, X-ray lithography, *J. Vac. Sci. Technol. B*, 6, 107, 1988.
- 122.D. Fleming, J. R. Maldonado, and M. Neisser, Prospects for x-ray lithography, *J. Vac. Sci. Technol. B*, 10, 2511, 1992.
- 123.S. Y. Lee, D. Y. Noh, H. C. Lee, C. Yu, Y. Hwu, and H. C. Kang, Direct-write X-ray lithography using a hard X-ray Fresnel zone plate, *J. Synchrotron Rad.*, 22, pp. 781-785, 2015.
- 124.R. Menon, H. I. Smith, Absorbance-modulation optical lithography, *J. Opt. Soc. Am. A*, vol. 12, no. 9, Sep. 2006.
- 125.S. Owa, H. Nagasaka, Immersion lithography; its potential performance and issues, *Proc. SPIE*, vol. 5040, pp. 724-733, 2003.
126. B. Streifkerk, J. Baselmans, W. Gehoel-van Ansem, J. Mulken, C. Hoogendam, M. Hoogendorp, D. G. Flagello, H. Sewell, and P. Graupner, Extending optical lithography with immersion, *Proc. SPIE*, vol. 5377, pp. 285-305, 2004.
- 127.S. Okazaki, High resolution optical lithography or high throughput electron beam lithography: The technical struggle from the micro to the nano-fabrication evolution, *Microelec. Eng.*, 133, 23-35, 2015.
- 128.Intel, Micron extend NAND flash technology leadership with introduction of world's first 128GB NAND device and mass production of 64GB 20nm NAND, <https://newsroom.intel.com/news-releases/intel-micron-extend-nand-flash-technology-leadership-with-introduction-of-worlds-first-128gb-nand-device-and-mass-production-of-64gb-20nm-nand/>, 2011.
- 129.Y. Choi, J. Zhu, J. Grunes, J. Bokor, and G. A. Somorjai, Fabrication of sub-10-nm silicon nanowire arrays by size reduction lithography, *J. Phys. Chem. B*, 107, pp. 3340-3343, 2003.

- 130.T. Ito, S. Okazaki, Pushing the limits of lithography, *Nature*, vol. 406, pp. 1027-1031, Aug. 2000.
- 131.T. Okino, Y. Kuba, M. Shibata, and H. Ohyi, 130kV high-resolution electron beam lithography system for sub-10-nm nanofabrication, *Jpn. J. Appl. Phys.*, 52, 06GB01, 2013.
- 132.W. Hu, K. Sarveswaran, M. Lieberman, and G. H. Bernstein, Sub-10 nm electron beam lithography using cold development of poly(methylmethacrylate), *J. Vac. Sci. Tech. B*, 22, 1711, 2004.
- 133.M. M. Mirza, H. Zhou, P. Velha, X. Li, K. E. Docherty, A. Samarelli, G. Ternent, and D. J. Paul, Nanofabrication of high aspect ratio (~50:1) sub-10 nm silicon nanowire using inductively coupled plasma etching, *J. Vac. Sci. Tech. B*, 30, 06FF02, 2012.
- 134.B. Lee, J. Hong, N. Amos, I. Dumer, D. Litvinov, S. Khizroev, Sub-10-nm-resolution electron-beam lithography toward very-high-density multilevel 3D nanomagnetic information devices, *J. Nanopart. Rev.*, 15:1665, 2013.
- 135.V. R. Manfrinato, L. Zhang, D. Su, H. Duan, R. G. Hobbs, E. A. Stach, and K. K. Berggren, Resolution limits of electron-beam lithography toward the atomic scale, *Nano Lett.*, 13, pp.1555-1558, 2013.
- 136.V. Sidorkin, E. van Veldhoven, E. van der Drift, P. Alkemade, H. Saleminck, and D. Maas, Sub-10-nm nanolithography with a scanning helium beam, *J. Vac. Sci. Tech. V*, 27, L18, 2009.
- 137.D. Winston, B. M. Cord, B. Ming, D. C. Bell, W. F. DiNatale, L. A. Stern, A. E. Vladar, M. T. Postek, M. K. Mondol, J. K. W. Yang, and K. K. Berggren, Scanning-helium-ion-beam lithography with hydrogen silsesquioxane resist, *J. Vac. Sci. Tech. B*, 27, 2702, 2009.
- 138.D. Winston, V. R. Manfrinato, S. M. Nicaise, L. L. Cheong, H. Duan, D. Ferranti, J. Marshman, S. McVey, L. Stern, J. Notte, and K. K. Berggren, Neon ion beam lithography (NIBL), *Nano Lett.*, 11, pp. 4343-4347, 2011.
- 139.S. Y. Chou, P. R. Krauss, Imprint lithography with sub-10nm feature size and high throughput, *Microelec. Eng.*, 35, 237-240, 1997.
- 140.S. Y. Chou, P. R. Krauss, W. Zhang, L. Guo, and L. Zhuang, Sub-10nm imprint lithography and applications, *J. Vac. Sci. Tech. B*, 15, 2897, 1997.
- 141.Y. K. Ryu, P. A. Postigo, F. Garcia, and R. Garcia, Fabrication of sub-12 nm thick silicon nanowires by processing scanning probe lithography masks, *Appl. Phys. Lett.*, 104, 223112, 2014.
- 142.H. Wolf, C. Rawlings, P. Mensch, J. L. Hedrick, D. J. Coady, U. Duerig, and A. W. Knoll, Sub-20 nm silicon patterning and metal lift-off using thermal scanning probe lithography, *J. Vac. Sci. Tech. B*, 33, 02B102, 2015.
- 143.R. Garcia, A. W. Knoll, and E. Riedo, Advanced scanning probe lithography, *Nature Nanotech.*, vol. 9, pp. 577-587, Aug. 2014.
- 144.J. W. Jeong, W. I. Park, L. Do, J. Park, T. Kim, G. Chae, and Y. S. Jung, Nanotransfer printing with sub-10nm resolution realized using directed self-assembly, *Adv. Mater.*, 24, pp. 3526-3531, 2012.
- 145.M. Asbahi, S. Mehraeen, K. T. P. Lim, F. Wang, J. Cao, M. C. Tan, and J. K. W. Yang, Template-induced structure transition in sub-10 nm self-assembling nanoparticles, *Nano Lett.*, 14, pp. 2642-2646, 2014.
- 146.M. J. Lercel, H. G. Craighead, A. N. Parikh, K. Seshadri, and D. L. Allara, Sub-10 nm lithography with self-assembled monolayers, *Appl. Phys. Lett.*, 68, 1504, 1996.

147. International Technology Roadmap for Semiconductors, www.itrs.net, 2015.
148. R. Peeters, S. Lok, J. Mallman, M. van Noordenbrug, N. Harned, P. Kuerz, M. Lowisch, E. van Setten, G. Schiffelers, A. Pirati, J. Stoeldraijer, D. Brandt, N. Farrar, I. Fomenkov, H. Boom, H. Meiling, and R. Kool, EUV lithography: NXE platform performance overview, *Proc. SPIE*, vol. 9048, 90481J, 2014.
149. R. Gronheid, H. H. Solak, Y. Ekinici, A. Jouve, and F. van Roey, Characterization of extreme ultraviolet resists with interference lithography, *Microelectr. Eng.*, 83, pp. 1103-1106, 2006.
150. A. K. Whittaker, I. Blakey, J. Blinco, K. S. Jack, K. Lawrie, H. Liu, A. Yu, M. Leeson, W. Yeuh, and T. Younkin, Development of polymers for non-CAR resists for EUV lithography, *Proc. SPIE*, vol. 7273, 72732, 2009.
151. I. Blakey, L. Chen, Y. Goh, K. Lawrie, Y. Chuang, E. Piscani, P. A. Zimmerman, and A. K. Whittaker, Non-CA resists for 193 nm immersion lithography: Effects of chemical structure on sensitivity, *Proc. SPIE*, vol. 7273, 72733X, 2009.
152. J. Yamamoto, S. Uchino, H. Ohta, T. Yoshimura, and F. Murai, Accurate critical dimension control by using an azide/novolac resist process for electron-beam lithography, *J. Vac. Sci. Tech. B*, 15, 2868, 1997.
153. J. Fujita, Y. Ohnishi, Y. Ochiai, and S. Matsui, Ultrahigh resolution of calixarene negative resist in electron beam lithography, *Appl. Phys. Lett.*, 68, 1297, 1996.
154. M. J. Rooks, A. Aviram, Application of 4-methyl-1-acetoxycalix[6]arene resist to complementary metal-oxide-semiconductor gate processing, *J. Vac. Sci. Tech. B*, 17, 3394, 1999.
155. A. E. Grigorescu, M. C. van der Krogt, C. W. Hagen, and P. Kruit, 10 nm lines and spaces written in HSQ, using electron beam lithography, *Microelectr. Eng.*, 84, pp. 822-824, 2007.
156. B. Liu, Y. Huang, G. Xu and S. Ho, Nanolithography using spin-coatable ZrO₂ resist and its application to sub-10 nm direct pattern transfer on compound semiconductors, *Nanotechnol.*, 19, 155303, 2008.
157. D. Borah, M. T. Shaw, S. Rasappa, R. A. Farrell, C. O'Mahony, C. M. Faulkner, M. Bosea, P. Gleeson, J. D. Holmes, and M. A. Morris, Plasma etch technologies for the development of ultra-small feature size transistor devices, *J. Phys. D:Appl. Phys.*, 44, 174012, 2011.
158. R. A. Farrell, N. T. Kinahan, S. Hansel, K. O. Stuen, N. Petkov, M. T. Shaw, L. E. West, V. Djara, R. J. Dunne, O. G. Varona, P. G. Gleeson, S. Jung, H. Kim, M. M. Kolesnik, T. Lutz, C. P. Murray, J. D. Holmes, P. F. Nealey, G. S. Duesberg, V. Krstic, and M. A. Morris, Large-scale parallel arrays of silicon nanowires via block copolymer directed self-assembly, *Nanoscale*, 4, 3228, 2012.
159. S. Rasappa, D. Borah, C. C. Faulkner, T. Lutz, M. T. Shaw, J. D. Holmes, and M. A. Morris, Fabrication of a sub-10 nm silicon nanowire based ethanol sensor using block copolymer lithography, *Nanotech.*, 24, 065503, 2013.
160. C. A. Ross, K. K. Berggren, J. Y. Cheng, Y. S. Jung, and J. -B, Chang, Three-dimensional nanofabrication by block copolymer self-assembly, *Adv. Mater.*, 26, pp. 4386-4396, 2014.
161. S. C. Rustagi, N. S. W. W. Fang, K. D. Buddharaju, S. R. Omampuliyur, S. H. G. Teo, C. H. Tung, G. Q. L. N. Balasubramanian, and D. L. Kwong, CMOS Inverter based on gate-all-around silicon-nanowire MOSFETs fabricated using top-down approach, *IEEE, Elec. Dev. Lett.*, vol. 28, no. 11, Nov. 2007.

- 162.N. Singh, K. D. Buddharaju, S. K. Manhas, A. Agarwal, S. C. Rustagi, G. Q. Lo, N. Balasubramanian, and D. L. Kwong, Si, SiGe nanowire devices by top-down technology and their applications, *IEEE Trans. Elec. Dev.*, vol. 55, no. 11, Nov. 2008.
- 163.G.W. Sears, A growth mechanism for mercury whiskers, *ACTA Metal.*, vol. 3, no. 4, p. 361, Jul. 1955.
- 164.G. W. Sears, A mechanism of whisker growth, *ACTA Metal.*, vol. 3, p. 367, Jul. 1955.
- 165.S. S. Brenner, G. W. Sears, Mechanism of whisker growth-III nature of growth sites, , vol. 3, no. 4, p. 268, May 1956.
- 166.J. M. Blakely, K. A. Jackson, Growth of crystal whiskers, *J. Chem. Phys.*, 37, 428, Jul. 1962.
- 167.V. Ruth, J. P. Hirth, Kinetics of diffusion-controlled whisker growth, *J. Chem. Phys.*, 41, 3139, 1964.
- 168.D. Turnbull, Kinetics of heterogeneous nucleation, *J. Chem. Phys.*, vol. 18, no. 2, p. 198, Feb. 1950.
- 169.K. Hiruma, M. Yazawa, K. Haraguchi, K. Ogawa, T. Katsuyama, M. Koguchi, and H. Kakibayashi, GaAs free-standing quantum-size wires, *J. Appl. Phys.*, 74, 3162, 1993.
- 170.K. Lew, C. Reuther, A. H. Carim, J. M. Redwing, B. R. Martin, Template-directed vapor-liquid-solid growth of silicon nanowires, *J. Vac. Sci. Technol. B*, 20 (1), Jan./Feb. 2002.
- 171.M. H. Magnusson, K. Deppert, J. Malm, J. Bovin, and L. Samuelson, Gold nanoparticles: production, reshaping, and thermal charging, *J. Nanopart. Res.*, vol. 1, pp. 243-251, 1999.
- 172.B. J. Ohlsson, M. T. Bjork, M. H. Magnusson, K. Deppert, L. Samuelson, and L. R. Wallenberg, Size-, shape-, and position-controlled GaAs nano-whiskers, *Appl. Phys. Lett.*, vol. 79, no. 20, Nov. 2001.
- 173.A. M. Morales, C. M. Lieber, A laser ablation method for the synthesis of crystalline semiconductor nanowires, *Science*, vol. 279, Jan. 1998.
- 174.M. S. Gudiksen, C. M. Lieber, Diameter-selective synthesis of semiconductor nanowire, *J. Am. Chem. Soc.*, 122, 8801, 2000.
- 175.Y. Cui, L. J. Lauhon, M. S. Gudiksen, J. Wang, and C. M. Lieber, Diameter-controlled synthesis of single-crystal silicon nanowires, *Appl. Phys. Lett.*, 78, 2214, Apr. 2001.
- 176.M. S. Gudiksen, J. Wang, and C. M. Lieber, Synthetic control of the diameter and length of single crystal semiconductor nanowires, *J. Phys. Chem. B*, 105, 4062-4064, 2001.
- 177.V. K. Lamer, R. H. Dinegar, Theory, production, and mechanism of formation of monodispersed hydrosols, *J. Am. Chem. Soc.*, vol. 72, no. 11, Nov. 1950.
- 178.J. H. Van Der Merwe, Crystal interfaces. Part I. Semiinfinite crystals, *J. Appl. Phys.*, 34, 117, Jan. 1963.
- 179.J. H. Van Der Merwe, Crystal interfaces. Part II. Finite overgrowths, *J. Appl. Phys.*, 34, 123, Jan. 1963.
- 180.J. W. Matthews, A. E. Blakeslee, Defects in epitaxial multilayers: I. Misfit dislocation, *J. Cryst. Growth*, vol. 27, p. 118, 1974.

181. J. W. Matthews, A. E. Blakeslee, Defects in epitaxial multilayers: II. Dislocation pile-ups, threading dislocations, slip lines and cracks, *J. Cryst. Growth*, vol. 29, p. 273, 1975.
182. J. W. Matthews, A. E. Blakeslee, Defects in epitaxial multilayers: III. Preparation of almost perfect multilayers, *J. Cryst. Growth*, vol. 32, p. 265, 1976.
183. J. W. Matthews, Defects associated with the accommodation of misfit between crystals, *J. Vac. Sci. Tech.*, vol. 12, no. 1, p. 126, Jan./Feb. 1975.
184. J. W. Matthews, A. E. Blakeslee, and S. Mader, Use of misfit strain to remove dislocations from epitaxial thin films, *Thin Solid Films*, vol. 33, p. 253, 1976.
185. E. Ertekin, P. A. Greaney, T. D. Sands, and D. C. Chrzan, Equilibrium analysis of lattice-mismatched nanowire heterostructures, *Mat. Res. Soc. Symp. Proc.*, vol. 737, p. F10.4.1, 2003.
186. E. Ertekin, P. A. Greaney, D. C. Chrzan, and T. D. Sands, Equilibrium limits of coherency in strained nanowire heterostructures, *J. Appl. Phys.*, vol. 97, 114325, 2005.
187. W. D. Nix, Metall. Mechanical properties of thin films, *Trans. A*, vol. 20A, p. 2217, Nov. 1989.
188. G. Kastner, U. Gosele, Stress and dislocations at cross-sectional heterojunctions in a cylindrical nanowire, *Phil. Mag.*, vol. 84, no. 35, p. 383, Dec. 2004.
189. F. Glas, Critical dimensions for the plastic relaxation of strained axial heterostructures in free-standing nanowires, *Phys. Rev. B*, vol. 74, 121302, 2006.
190. T. Y. Tan, N. Li, and U. Gosele, Is there a thermodynamic size limit of nanowires grown by the vapor-liquid-solid process, *Appl. Phys. Lett.*, vol. 83, no. 6, p. 1199, Aug. 2003.
191. E. I. Givargizov, A. A. Chernov, VLS growth rate of whiskers and the role of surface energy, *Kristallografiya* 18, 147, 1973.
192. K. A. Dick, A review of nanowire growth promoted by alloy and non-alloying elements with emphasis on Au-assisted III-V nanowires, *Prog. Cryst. Growth Character. Mater.*, 54, 138-173, 2008.
193. <http://www1.asminternational.org/asmenterprise/apd/AdvancedSearchAPD.aspx>
194. H. Baker, ASM International, Alloy Phase Diagrams, vol. 3, Mater. Infor. Co., 1992.
195. U. R. Kattner, The thermodynamic modeling of multicomponent phase equilibria, *J. Metals*, 12, pp. 14-19, Dec. 1997.
196. A. E. Kissavos, S. Shallcross, V. Meded, L. Kaufman, I. A. Abrikosov, A critical test of ab initio and CALPHAD methods: The structural energy difference between bcc and hcp molybdenum, *Comp. Coupl. Phase Diag. Thermochem.*, 29, pp. 17-23, 2005.
197. Z. -K. Liu, First-principles calculations and CALPHAD modeling of thermodynamics, *J. Phase Equil. Diff.*, vol. 30, no. 5, pp. 517-534, 2009.
198. Q. Chen, M. Hillert, B. Sundman, W. A. Oates, S. G. Fries, and R. Schmid-fetzer, Phase equilibria, defect chemistry and semiconducting properties of CdTe(s)-Thermodynamic modeling, *J. Electron. Mater.*, vol. 27, no. 8, 1998.
199. Q. Chen, M. Hillert, The compound energy model for compound semiconductors, *J. Alloys Comp.*, 245, pp. 125-131, 1996.
200. M. Hillert, The compound energy formalism, *J. Alloys Comp.*, 320, pp. 161-176, 2001.

201. J. Wang, Y. J. Liu, L. B. Liu, H. Y. Zhou, and Z. P. Jin, Thermodynamic assessment of the Au-Ga binary system, *CALPHAD: Comp. Coupling Phase Diagrams Thermochem.*, 35, pp. 242-248, 2011.
202. T. Andersson, D. de Fontaine, S. G. Fries, B. Legendre, W. A. Oates, R. Schmid-Fetzer, H.-J. Seifert, and Q. Chen, Thermodynamic modelling of solutions and alloys, *Calphad*, vol. 21, no. 2, pp. 265-285, 1997.
203. K. Takahashi, T. Moriizumi, Growth of InAs whiskers in wurtzite structure, *Jpn. J. Appl. Phys.*, vol. 5, no. 8, Aug. 1966.
204. R. S. Wagner, C. J. Doherty, Controlled vapor-liquid-solid growth of silicon crystals, *J. Electrochem. Soc.*, vol. 113, no. 12, p. 1300, Dec. 1966.
205. M. Yazawa, M. Koguchi, A. Muto, M. Ozawa, and K. Hiruma, Effect of one monolayer of surface gold atoms on the epitaxial growth of InAs nanowhiskers, *Appl. Phys. Lett.*, 61, 2051, 1992.
206. G. B. Stringfellow, P. E. Greene, Calculation of III-V ternary phase diagrams: In-Ga-As and In-As-Sb, *J. Phys. Chem. Solids*, vol. 30, pp. 1779-1791, 1969.
207. G. B. Stringfellow, Calculation of ternary phase diagrams of III-V systems, *J. Phys. Chem. Solids*, vol. 33, pp. 665-677, 1972.
208. G. B. Stringfellow, Calculation of ternary and quaternary III-V phase diagrams, *J. Cryst. Growth*, 27, 21-34, 1974.
209. G. B. Stringfellow, Miscibility gaps in quaternary III.V alloys, *J. Cryst. Growth*, 58, 194-202, 1982.
210. M. Ilegems, M. B. Panish, Phase equilibria in III-V Quaternary systems-application to Al-Ga-P-As, *J. Phys. Chem. Solids*, vol. 35, pp. 409-420, 1974.
211. A. S. Jordan, M. Ilegems, Solid-liquid equilibria for quaternary solid solutions involving compound semiconductors in the regular solution approximation, *J. Phys. Chem. Solids*, vol. 36, pp. 329-342, 1975.
212. M. Ilegems, M. B. Panish, Phase diagram of the system Al-Ga-P, *J. Cryst. Growth*, 20, 77-81, 1973.
213. M. B. Panish, A thermodynamic evaluation of the simple solution treatment of the Ga-P, In-P and Ga-As systems, *J. Cryst. Growth*, 27, 6-20, 1974.
214. M. Tmar, A. Gabriel, C. Chatillon, and I. Ansara, Critical analysis and optimization of the thermodynamic properties and phase diagrams in the III-V compounds: the In-P and Ga-P systems, *J. Cryst. Growth*, 68, 557-580, 1984.
215. M. Tmar, A. Gabriel, C. Chatillon, and I. Ansara, Critical analysis and optimization of the thermodynamic properties and phase diagrams in the III-V compounds II: the Ga-As and In-As systems, *J. Cryst. Growth*, 69, 421-441, 1984.
216. R. Beyers, K. B. Kim, R. Sinclair, Phase equilibria in metal-gallium-arsenic systems: thermodynamic considerations for metallization materials, *J. Appl. Phys.*, 61, 2195, 1987.
217. K. Terakura, T. Oguchi, T. Mohri, and K. Watanabe, Electronic theory of the alloy phase stability of Cu-Ag, Cu-Au, and Ag-Au systems, *Phys. Rev. B*, vol. 35, no. 5, Feb. 1987-I.
218. T. Mohri, K. Terakura, T. Oguchi, and K. Watanabe, First principles calculation of thermodynamic properties of noble-metal alloys, *Acta Metall.*, vol. 36, no. 3, pp. 547-553, 1988.
219. M. W. Chase Jr., J. L. Curnutt, J. R. Downey Jr., R. A. McDonald, A. N. Syverud, and E. A. Valenzuela, JANAF thermochemical tables, 1982 supplement, *J. Phys. Chem. Ref. Data*, 11, 695, 1982.

220. R. P. Elliott, F. A. Shunk, The Au-Ga (Gold-Gallium) system, *Bulletin of Alloy Phase Diagrams*, vol. 2, no. 3, 1981; H. Okamoto, T. B. Massalski, The As-Au (Arsenic-Gold) system, *Bulletin of Alloy Phase Diagrams*, vol. 5, no. 1, 1984; J. L. Murray, H. Okamoto, and T. B. Massalski, The Al-Au (Aluminum-Gold) system, *Bulletin of Alloy Phase Diagrams*, vol. 8, no. 1, 1987; J. L. Murray, The Al-Ga (Aluminum-Gallium) system, *Bulletin of Alloy Phase Diagrams*, vol. 4, no. 2, 1983; H. A. Wriedt, The Al-N (Aluminum-Nitrogen) system, *Bulletin of Alloy Phase Diagrams*, vol. 7, no. 4, 1986; H. Okamoto, T. B. Massalski, The Au-Sn (Gold-Tin) system, *Bulletin of Alloy Phase Diagrams*, vol. 5, no. 5, 1984; N. Saunders, A. P. Miodownik, The Cu-Sn (Copper-Tin) system, *Bulletin of Alloy Phase Diagrams*, vol. 11, no. 3, 1990; P. R. Subramanian, D. E. Laughlin, The Cu-In (Copper-Indium) system, *Bulletin of Alloy Phase Diagrams*, vol. 10, no. 5, 1989; H. Okamoto, Cu-In (Copper-Indium), *J. Phase. Equil. Diffus.*, 26, 645, 2005; T. L. Ngai, R. C. Sharma, and Y. A. Chang, The Ga-Sb (Gallium-Antimony) system, *Bulletin of Alloy Phase Diagrams*, vol. 9, no. 5, 1988; R. C. Sharma, T. L. Ngai, and Y. A. Chang, The In-Sb (Indium-Antimony) system, *Bulletin of Alloy Phase Diagrams*, vol. 10, no. 6, 1989; H. Okamoto, T. B. Massalski, The Au-Sb (Gold-Antimony) system, *Bulletin of Alloy Phase Diagrams*, vol. 5, no. 2, 1984; J. L. Murray, The Al-In (Aluminum-Indium) system, *Bulletin of Alloy Phase Diagrams*, vol. 4, no. 3, 1983; H. Okamoto, T. B. Massalski, The Au-P (Gold-Phosphorus) system, *Bulletin of Alloy Phase Diagrams*, vol. 5, no. 5, 1984; H. Okamoto, T. B. Massalski, The Au-N (Gold-Nitrogen) system, *Bulletin of Alloy Phase Diagrams*, vol. 5, no. 4, 1984; M. F. Singleton, P. Nash, The In-Ni (Indium-Nickel) system, *Bulletin of Alloy Phase Diagrams*, vol. 9, no. 5, 1988; H. Okamoto, Ga-Ni (Gallium-Nickel), *J. Phase Equil. Diffus.*, vol. 29, no. 3, 2008; H. Okamoto, In-Pd (Indium-Palladium), *J. Phase Equil.*, vol. 24, no. 5, 2003; H. Okamoto, Ga-Pt (Gallium-Platinum), *J. Phase Equil. Diffus.*, vol. 28, no. 5, 2007; M. R. Baren, The Ag-Ga (Silver-Gallium) system, *Bulletin of Alloy Phase Diagrams*, vol. 11, no. 4, 1990; J. Hertz, K. E. Aissaoui, and L. Bouirden, A thermodynamic optimization of the Cu-In system, *J. Phase Equil.*, vol. 23, no. 6, 2002; W. -C. Huang, C. -H. Tu, Copper-gallium alloy sputtering target, method for fabricating the same and related applications, no. EP2182083 A1, Application, no. EP20080105733, May 2010; R. Schmid-Fetzer, Stability of metal/GaAs-interfaces: a phase diagram survey, *J. Elec. Mater.*, vol. 17, no. 2, 1988.
221. C. T. Tsai, R. S. Williams, Solid phase equilibria in the Au-Ga-As, Au-Ga-Sb, Au-In-As, and Au-In-Sb ternaries, *J. Mater. Res.*, 1, 352, Mar./Apr. 1986.
222. I. Ansara, C. Chatillon, H. L. Lukas, T. Nishizawa, H. Ohtani, K. Ishida, M. Hillert, B. Sundman, B. B. Argent, A. Watson, T. G. Chart, T. Anderson, A binary database for III-V compound semiconductor systems, *Calphad*, vol. 18, no. 2, pp. 177-222, 1994.
223. M. B. Panish, Ternary codensed phase systems of Gallium and arsenic with group IB elements, *J. Electrochem. Soc.: Solid State Sci.*, vol. 114, no. 5, May 1967.
224. A. I. Persson, M. W. Larsson, S. Stenstrom, B. J. Ohlsson, L. Samuelson, and L. R. Wallenberg, Solid-phase diffusion mechanism for GaAs nanowire growth, *Nature Mater.*, vol. 3, p. 677, Oct. 2004.
225. B. J. Ohlsson, M. T. Bjork, A. I. Persson, C. Thelander, L. R. Wallenberg, M. H. Magnusson, K. Deppert, L. Samuelson, Growth and characterization of GaAs and InAs nano-whiskers and InAs/GaAs heterostructures, *Phys. E*, 13, 1126-1130, 2002.

- 226.K. Hiruma, M. Yazawa, T. Katsuyama, K. Ogawa, K. Haraguchi, M. Koguchi, and H. Kakibayashi, Growth and optical properties of nanometer-scale GaAs and InAs whiskers, *J. Appl. Phys.*, 77, 447, 1995.
- 227.K. A. Dick, K. Deppert, T. Martensson, B. Mandl, L. Samuelson, and W. Seifert, Failure of the vapor-liquid-solid mechanism in Au-assisted MOVPE growth of InAs Nanowires, *Nano Lett.*, vol. 5, no. 4, p. 761, 2005.
- 228.K. A. Dick, K. Deppert, L. S. Karlsson, L. R. Wallenberg, L. Samuelson, and W. Seifert, A new understanding of Au-assisted of III-V semiconductor nanowires, *Adv. Funct. Mater.*, 15, 1603-1610, 2005.
- 229.K. W. Kolasinski, Catalytic growth of nanowires: vapor-liquid-solid, vapor-solid-solid, solution-liquid-solid and solid-liquid-solid growth, *Current Opin. Solid State Mater. Sci.*, 10, 182-191, 2006.
- 230.J. Johansson, B. A. Wacaser, K. A. Dick, and W. Seifert, Growth related aspects of epitaxial nanowires, *Nanotechnol.*, 17, S355-S361, 2006.
- 231.M. Tchernycheva, J. C. Harmand, G. Patriarche, L. Travers, and G. E. Cirlin, Temperature conditions for GaAs nanowire formation by Au-assisted molecular beam epitaxy, *Nanotechnol.*, 17, 4025-4030, 2006.
232. H. D. Park, A. -C. Gaillot, S. M. Prokes, and R. C. Cammarata, Observation of size dependent liquidus depression in the growth of InAs nanowires, *J. Cryst. Growth*, 296, 159-164, 2007.
- 233.S. N. Mohammad, For nanowire growth, vapor-solid-solid (vapor-solid) mechanism is actually vapor-quasisolid-solid (vapor-quasiliquid-solid) mechanism, *J. Chem. Phys.*, 131, 224702, 2009.
- 234.K. A. Dick, P. Caroff, J. Bolinsson, M. E. Messing, J. Johansson, K. Deppert, L. R. Wallenberg, L. Samuelson, Control of III-V nanowire crystal structure by growth parameter tuning, *Semicond. Sci. Technol.*, 25, 024009, 2010.
- 235.N. Han, A. T. Hui, F. Wang, J. J. Hou, F. Xiu, T. Hung, and J. C. Ho, Crystal phase and growth orientation dependence of GaAs nanowires on Ni_xGa_y seeds via vapor-solid-solid mechanism, *Appl. Phys. Lett.*, 99, 083114, 2011.
- 236.N. Wang, Y. Cai, and R. Q. Zhang, Growth of nanowires, *Mater. Sci. Eng. R*, 60, 1, 2008.
- 237.C. Cheze, L. Geelhaar, A. Trampert, O. Brandt, and H. Riechert, Collector phase transitions during vapor-solid-solid nucleation of GaN nanowires, *Nano Lett.*, 10, 3426-3431, 2010.
- 238.S. -J. Tang, S. Kodambaka, W. Swiech, I. Petrov, C. P. Flynn, and T. -C. Chiang, Sublimation of atomic layers from a chromium surface, *Phys. Rev. Lett.*, 96, 126106, 2006.
- 239.S. Hofmann, R. Sharma, C. T. Wirth, F. Cervantes-Sodi, C. Ducati, T. Kasama, R. E. Dunin-Borkowski, J. Drucker, P. Bennett, and J. Robertson, Ledge-flow-controlled catalyst interface dynamics during Si nanowire growth, *Nature Mater.*, vol. 7, 372-375, May 2008.
- 240.H. J. Joyce, Q. Gao, H. H. Tan, C. Jagadish, Y. Kim, X. Zhang, Y. Guo, and J. Zou, Twin-free uniform epitaxial GaAs nanowires grown by a two-temperature process, *Nano Lett.*, vol. 7, no. 4, 921-926, 2007.
- 241.C. -Y. Wen, M. C. Reuter, J. Tersoff, E. A. Stach, and F. M. Ross, Structure, growth kinetics, and ledge flow during vapor-solid-solid growth of copper-catalyzed silicon nanowires, *Nano Lett.*, 10, 514-519, 2010.

- 242.C. -Y. Wen, M. C. Reuter, J. Bruley, J. Tersoff, S. Kodambaka, E. A. Stach, F. M. Ross, Formation of compositionally abrupt axial heterojunctions in silicon-germanium nanowires, *Science*, vol. 326, Nov. 2009.
- 243.J. L. Lensch-Falk, E. R. Hemesath, D. E. Perea, L. J. Lauhon, Alternative catalysts for VSS growth of silicon and germanium nanowires, *J. Mater. Chem.*, 19, 849-857, 2009.
- 244.Y. Wang, V. Schmidt, S. Senz, and U. Gosele, Epitaxial growth of silicon nanowires using an aluminium catalyst, *Nature Nanotechnol.*, vol. 1, 186-189, 2006.
- 245.T. Douglas, K. H. Theopold, Molecular precursors for indium phosphide and synthesis of small III-V semiconductor clusters in solution, *Inorg. Chem.*, 30, 4, pp. 594-596, 1991.
- 246.T. J. Trentler, S. C. Goel, K. M. Hickman, A. M. Viano, M. Y. Chiang, A. M. Beatty, P. C. Gibbons, and W. E. Buhro, Solution-liquid-solid growth of indium phosphide fibers from organometallic precursors: elucidation of molecular and nonmolecular components of the pathway, *J. Am. Chem. Soc.*, 119, 2172-2181, 1997.
- 247.S. D. Dingman, N. P. Rath, P. D. Markowitz, P. C. Gibbons, and W. E. Buhro, Low-temperature, catalyzed growth of indium nitride fibers from azido-indium precursors, *Angew. Chem. Int. Ed.*, 39, no. 8, 2000.
- 248.P. D. Markowitz, M. P. Zach, P. C. Gibbons, R. M. Penner, and W. E. Buhro, Phase separation in $\text{Al}_x\text{Ga}_{1-x}\text{As}$ nanowhiskers grown by the solution-liquid-solid mechanism, *J. Am. Chem. Soc.*, 123, 4502-4511, 2001.
- 249.H. Yu, W. E. Buhro, Solution-liquid-solid growth of soluble GaAs nanowires, *Adv. Mater.*, 15, no. 5, Mar. 2003; F. Wang, A. Dong, J. Sun, R. Tang, H. Yu, and W. E. Buhro, Solution-liquid-solid growth of semiconductor nanowires, *Inorg. Chem.*, 45, 19, 7511-7521, 2006.
- 250.A. J. Wooten, D. J. Werder, D. J. Williams, J. L. Casson, and J. A. Hollingsworth, Solution-liquid-solid growth of ternary Cu-In-Se semiconductor nanowires from multiple- and single- source precursors, *J. Am. Chem. Soc.*, 131, 16177-16188, 2009.
- 251.J. Sun, C. Liu, and P. Yang, Surfactant-free, large-scale, solution-liquid-solid growth of gallium phosphide nanowires and their use for visible-light-driven hydrogen production from water reduction, *J. Am. Chem. Soc.*, 133, 19306-19309, 2011.
- 252.Y. Xia, P. Yang, Y. Sun, Y. Wu, B. Mayers, B. Gates, Y. Yin, F. Kim, and H. Yan, One-dimensional nanostructures: synthesis, characterization, and applications, *Adv. Mater.*, 15, no. 5, Mar. 2003.
- 253.T. Hanrath, B. A. Korgel, Supercritical fluid-liquid-solid (SFLS) synthesis of Si and Ge nanowires seeded by colloidal metal nanocrystals, *Adv. Mater.*, 15, no. 5, Mar. 2003.
- 254.F. M. Davidson III, A. D. Schricker, R. J. Wiacek, and B. A. Korgel, Supercritical Fluid-Liquid-Solid synthesis of gallium arsenide nanowires seeded by Alkanethiol-stabilized gold nanocrystals, *Adv. Mater.*, 16, no. 7, Apr. 2004.
- 255.H. Y. Tuan, D. C. Lee, T. Hanrath, and B. A. Korgel, Catalytic solid-phase seeding of silicon nanowires by nickel nanocrystals in organic solvents, *Nano Lett.*, vol. 5, no. 4, 681-684, 2005.
- 256.H. Y. Tuan, D. C. Lee, T. Hanrath, and B. A. Korgel, Germanium nanowire synthesis: An example of solid-phase seeded growth with nickel nanocrystals, *Chem. Mater.*, 17, 5705-5711, 2005.

257. H. Y. Tuan, D. C. Lee, and B. A. Korgel, Nanocrystal-mediated crystallization of silicon and germanium nanowires in organic solvents: The role of catalysis and solid-phase seeding, *Angew. Chem. Int. Ed.*, 45, 5184-5187, 2006.
258. H. Y. Tuan, A. Ghezelbash, and B. A. Korgel, Silicon nanowires and silica nanotubes seeded by copper nanoparticles in an organic solvent, *Chem. Mater.*, 20, 2306-2313, 2008.
259. H. F. Yan, Y. J. Xing, Q. L. Hang, D. P. Yu, Y. P. Wang, J. Xu, Z. H. Xi, and S. Q. Feng, Growth of amorphous silicon nanowires via a solid-liquid-solid mechanism, *Chem. Phys. Lett.*, 323, 224-228, 2000.
260. D. P. Yu, Y. J. Xing, Q. L. Hang, H. F. Yan, J. Xu, Z. H. Xi, and S. Q. Feng, Controlled growth of oriented amorphous silicon nanowires via a solid-liquid-solid (SLS) mechanism, *Phys. E*, 9, 305-309, 2001.
261. M. Paulose, O. K. Varghese, and C. A. Grimes, Synthesis of gold-silica composite nanowires through solid-liquid-solid phase growth, *J. Nanosci. Nanotechnol.*, vol. 3, no. 4, pp. 341-346, Aug. 2003.
262. M. J. Tambe, S. Ren, and S. Gradecak, Effects of gold diffusion on n-type doping of GaAs nanowires, *Nano Lett.*, 10, 4584-4589, 2010.
263. J. Westwater, D. P. Gosain, S. Tomiya, S. Usui, and H. Ruda, Growth of silicon nanowires via gold/silane vapor-liquid-solid reaction, *J. Vac. Sci. Tech. B*, 15, 554, 1997.
264. Y. Wu, H. Yan, M. Huang, B. Messer, J. H. Song, and P. Yang, Inorganic semiconductor nanowires: rational growth, assembly, and novel properties, *Chem. Eur. J.*, 8, no. 6, 2002.
265. V. A. Nebol'sin, A. A. Shchetinin, Role of surface energy in the vapor-liquid-solid growth of silicon, *Inorganic Mater.*, vol. 39, no. 9, pp. 899-903, 2003.
266. A. M. S. Elahl, M. He, P. Zhou, G. L. Harris, L. Salamanca-Riba, F. Felt, H. C. Shaw, A. Sharma, M. Jah, D. Lakins, T. Steiner, and S. N. Mohammad, Systematic study of effects of growth conditions on the (nano-, meso-, micro) size and (one-, two-, three-dimensional) shape of GaN single crystals grown by a direct reaction of Ga with ammonia, *J. Appl. Phys.*, 94, 7749, 2003.
267. J. C. Harmand, M. Tchernycheva, G. Patriarche, L. Travers, F. Glas, and G. Cirlin, GaAs nanowires formed by Au-assisted molecular beam epitaxy: Effect of growth temperature, *J. Cryst. Growth*, 301-302, 853-856, 2007.
268. M. Tchernycheva, L. Travers, G. Patriarche, F. Glas, J. Harmand, G. E. Cirlin, and V. G. Dubrovskii, Au-assisted molecular beam epitaxy of InAs nanowires: growth and theoretical analysis, *J. Appl. Phys.*, 102, 094313, 2007.
269. J. C. Harmand, G. Patriarche, N. Pere-Laperne, M-N. Merat-Combes, L. Travers, and F. Glas, Analysis of vapor-liquid-solid mechanism in Au-assisted GaAs nanowire growth, *Appl. Phys. Lett.*, 87, 203101, 2005.
270. F. Jabeen, S. Rubini, F. Martelli, Growth of III-V semiconductor nanowires by molecular beam epitaxy, *Microelec. J.*, 40, 442-445, 2009.
271. C. Sartel, D. L. Dheeraj, F. Jabeen, and J. C. Harmand, Effect of arsenic species on the kinetics of GaAs nanowires growth by molecular beam epitaxy, *J. Cryst. Growth*, 312, 2073-2077, 2010.
272. Z. H. Wu, X. Y. Mei, D. Kim, M. Blumin, and H. E. Ruda, Growth of Au-catalyzed ordered GaAs nanowire arrays by molecular-beam epitaxy, *Appl. Phys. Lett.*, 81, 5177, 2002.

- 273.S. Nakahara, E. Kinsbron, Room temperature interdiffusion study of Au/Ga thin film couples, *Thin Solid Films*, 113, 15-26, 1984.
- 274.G. H. Vineyard, Frequency factors and isotope effects in solid state rate processes, *J. Phys. Chem. Solids*, Pergamon Press, vol. 3, pp. 121-127, 1957.
- 275.S. A. Rice, Dynamical theory of diffusion in crystals, *Phys. Rev.*, vol. 112, no. 3, Nov. 1958.
- 276.E. T. Bruk-Levinson, O. D. Chernetsov, Statistical determination of the coefficient of self-diffusion in a monatomic molecular crystal, *J. Eng. Phys.*, vol. 48, 5, pp. 602-609, May 1985.
- 277.T. Helander, J. Agren, A phenomenological treatment of diffusion in Al-Fe and Al-Ni alloys having B2-B.C.C. ordered structure, *ACTA Mater.*, vol. 47, no. 4, pp. 1141-1152, 1999.
- 278.A. D. Dalvi, D. E. Coates, A review of the diffusion path concept and its application to the high-temperature oxidation of binary alloys, *Oxida. Metals*, vol. 5, no. 2, 1972.
- 279.A. A. Kodentsov, G. F. Bastin, F. J. J. van Loo, The diffusion couple technique in phase diagram determination, *J. Alloys Compounds*, vol. 320, 2, pp. 207-217, May 2001.
- 280.P. Maugis, W. D. Hopfe, J. E. Morral, and J. S. Kirkaldy, Multiple interface velocity solutions for ternary biphasic infinite diffusion couples, *ACTA Mater.*, vol. 45, no. 5, pp. 1941-1954, 1997.
- 281.J. -C. Zhao, X. Zheng, and D. G. Cahill, High-throughput diffusion multiples, *Materialstoday*, vol. 8, 10, pp. 28-37, Oct. 2005.
- 282.H. Chen, J. E. Morral, Variation of the effective diffusivity in two-phase regions, *ACTA Mater.*, vol. 47, no. 4, pp. 1175-1180, 1999.
- 283.J. -C. Zhao, Combinatorial approaches as effective tools in the study of phase diagrams and composition-structure-property relationships, *Prog. Mater. Sci.*, 51, 557-631, 2006.
- 284.A. A. Kodentsov, A. Paul, M. J. H. van Dal, Cs. Cserhati, A. M. Gusak, and F. J. J. van Loo, On the spatial stability and bifurcation of the Kirkendall plane during Solid-State interdiffusion, *Crit. Rev. Solid State Mater. Sci.*, 33:3-4, 210-233, 2008.
- 285.A. L. Schmitt, J. M. Higgins, J. R. Szczech, and S. Jin, Synthesis and applications of metal silicide nanowires, *J. Mater. Chem.*, 20, 223-235, 2010.
- 286.M. J. H. van Dal, M. C. L. P. Pleumeekers, A. A. Kodentsov, and F. J. J. van Loo, Intrinsic diffusion and Kirkendall effect in Ni-Pd and Fe-Pd solid solutions, *ACTA Mater.*, 48, 385-396, 2000.
- 287.A. Paul, M. J. H. van Dal, A. A. Kodentsov, and F. J. J. van Loo, The Kirkendall effect in multiphase diffusion, *ACTA Mater.*, 52, 623-630, 2004.
- 288.V. G. Dubrovskii, The theory of nucleation and polytypism of III-V semiconductor nanowires, *Tech. Phys. Lett.*, vol. 41, no. 2, pp. 203-207, 2015.
- 289.P. Krogstrup, S. Curiotto, E. Johnson, M. Aagesen, J. Nygard, and D. Chatain, Impact of the liquid phase shape on the structure of III-V nanowires, *Phys. Rev. Lett.*, PRL 106, 125505, 2011.
- 290.C. -Y. Yeh, Z. W. Lu, S. Froyen, and A. Zunger, Zinc-blende-wurtzite polytypism in semiconductors, *Phys. Rev. B*, vol. 46, no. 16, Oct. 1992-II.
- 291.V. G. Dubrovskii, G. E. Cirilin, N. V. Sibirev, F. Jabeen, J. C. Harmand, and P. Werner, New mode of vapor-liquid-solid nanowire growth, *Nano Lett.*, 11, 1247-1253, 2011.

- 292.R. Leitsmann, F. Bechstedt, Surface influence on stability and structure of hexagon-shaped III-V semiconductor nanorods, *J. Appl. Phys.*, 102, 063528, 2007.
- 293.V. G. Dubrovskii, N. V. Sibirev, Growth thermodynamics of nanowires and its application to polytypism of zinc blende III-V nanowires, *Phys. Rev. B*, 77, 035414, 2008.
- 294.F. Glas, J.-C. Harmand, and G. Patriarche, Nucleation antibunching in catalyst-assisted nanowire growth, *Phys. Rev. Lett.*, 104, 135501, 2010.
- 295.E. Mendez-Villuendas, R. K. Bowles, Surface nucleation in the freezing of gold nanoparticles, *Phys. Rev. Lett.*, 98, 185503, 2007.
- 296.S. G. Ghalamestani, M. Ek, M. Ghasemi, P. Caroff, J. Johansson, and K. A. Dick, Morphology and composition controlled $\text{Ga}_x\text{In}_{1-x}\text{Sb}$ nanowires: understanding ternary antimonide growth, *Nanoscale*, 6, 1086, 2014.
- 297.V. G. Dubrovskii, Physical consequences of the equivalence of conditions for the steady-state growth of nanowires and the nucleation on triple phase line, *Tech. Phys. Lett.*, vol. 37, no. 1, pp. 53-57, 2011.
- 298.V. G. Dubrovskii, *Nucleation theory and growth of nanostructures*, Springer, Heidelberg, 2014.
- 299.T. Akiyama, K. Nakamura, and T. Ito, Structural stability and electronic structures of InP nanowires: Role of surface dangling bonds on nanowire facets, *Phys. Rev. B*, 73, 235308, 2006.
- 300.M. I. McMahon, R. J. Nemes, Observation of a Wurtzite form of gallium arsenide, *Phys. Rev. Lett.*, 95, 215505, 2005.
- 301.A. Mujica, B. J. Needs, and A. Munoz, First-principles pseudopotential study of the III-V semiconductors GaAs and AlAs, *Phys. Rev. B*, vol. 52, no. 12, Sep. 1995-II.
- 302.J. Crain, G. J. Ackland, J. R. Maclean, R. O. Piltz, P. D. Hatton, and G. S. Pawley, Reversible pressure-induced structural transitions between metastable phases of silicon, *Phys. Rev. B*, vol. 50, no. 17, Nov. 1994-I.
- 303.J. Crain, R. O. Piltz, G. J. Ackland, and S. J. Clark, Tetrahedral structures and phase transitions in III-V semiconductors, *Phys. Rev. B*, vol. 50, no. 12, Sep. 1994-II; J. Crain, R. O. Piltz, G. J. Ackland, S. J. Clark, M. C. Payne, V. Milman, J. S. Lin, P. D. Hatton, and Y. H. Nam, Erratum: Tetrahedral structures and phase transitions in III-V semiconductors, *Phys. Rev. B*, vol. 52, no. 23, Dec. 1995-I.
- 304.M. C. Payne, M. P. Teter, D. C. Allan, T. A. Arias, and J. D. Joannopoulos, Iterative minimization techniques for ab initio total-energy calculations: molecular dynamics and conjugate gradients, *Rev. Mod. Phys.*, 64, 1045, 1992.
- 305.G. Kresse, J. Furthmuller, Efficiency of ab-initio total energy calculations for metals and semiconductors using a plane-wave basis set, *Comp. Mater. Sci.*, 6, 15-50, 1996.
- 306.M. Fuchs, M. Scheffler, Ab initio pseudopotentials for electronic structure calculations of poly-atomic systems using density-functional theory, *Comp. Phys. Comm.*, 119, 67-98, 1999.
- 307.X. Gonze, J. -M. Beuken, R. Caracas, F. Detraux, M. Fuchs, G. -M. Rignanese, L. Sindic, M. Verstraete, G. Zerah, F. Jollet, M. Torrent, A. Roy, M. Mikami, Ph. Ghosez, J. -Y. Raty, and D. C. Allan, First-principles computation of material properties: the ABINIT software project, *Comp. Mater. Sci.*, 25, 478-492, 2002.
- 308.X. Gonze, B. Amadon, P. -M. Anglade, J. -M. Beuken, F. Bottin, P. Boulanger, F. Bruneval, D. Caliste, R. Caracas, M. Cote, T. Deutsch, L. Genovese, Ph. Ghosez, M. Giantomassi, S. Goedecker, D. R. Hamann, P. Hermet, F. Jollet, G. Jomard, S. Leroux, M. Mancini, S. Mazevet, M. J. T. Oliveira, G. Onida, Y. Pouillon, T. Rangel,

- G. –M. Rignanese, D. Sangalli, R. Shalta, M. Torrent, M. J. Verstraete, G. Zerah, and J. W. Zwanziger, ABINIT: First-principles approach to material and nanosystem properties, *Comp. Phys. Comm.*, 180, 2582-2615, 2009.
- 309.T. Ito, Y. Kangawa, An empirical potential approach to wurtzite-zinc blende structural stability of semiconductors, *J. Cryst. Growth*, 235, 149-153, 2002.
- 310.T. Yamashita, T. Akiyama, K. Nakamura, and T. Ito, Theoretical investigation on the structural stability of GaAs nanowires with two different types of facets, *Physica E*, 42, 2727-2730, 2010.
- 311.J. Johansson, L. S. Karlsson, C. P. T. Svensson, T. Martensson, B. A. Wacaser, K. Deppert, L. Samuelson, and W. Seifert, Structural properties of <111>B-oriented III-V nanowires, *Nature Mater.*, 5, 574, 2006.
- 312.K. A. Brakke, The surface evolver, *Exp. Math.*, vol. 1, no. 2, 141, 1992.
- 313.Y. Chou, W. Wu, L. Chen, and K. Tu, Homogeneous nucleation of epitaxial CoSi₂ and NiSi in Si nanowires, *Nano Lett.*, vol. 9, no. 6, 2337-2342, 2009.
- 314.B. J. Kim, J. Tersoff, S. Kodambaka, M. C. Reuter, E. A. Stach, and F. M. Ross, Kinetics of individual nucleation events observed in nanoscale vapor-liquid-solid growth, *Science*, vol. 322, 1070, Nov. 2008.
- 315.R. M. Walser, R. W. Bene, First phase nucleation in silicon-transition-metal planar interfaces, *Appl. Phys. Lett.*, 28, 624, 1976.
- 316.Y. Chou, C. Wen, M. C. Reuter, D. Su, E. A. Stach, and F. M. Ross, Controlling the growth of Si/Ge nanowires and heterojunctions using silver-gold alloy catalysts, *ACS Nano*, vol. 6, no. 7, 6407-6415, 2012.
- 317.C. B. Collins, R. O. Carlson, and C. J. Gallagher, Properties of gold-doped silicon, *Phys. Rev.*, vol. 105, no. 4, Feb. 1957.
- 318.V. Heine, Theory of surface states, *Phys. Rev.*, vol. 138, no. 6A, Jun. 1965.
- 319.H. G. Grimmeiss, Deep level impurities in semiconductors, *Ann. Rev. Mater. Sci.*, 7: 341-76, 1977.
- 320.P. Krispin, Thermochemistry applied to deep-level defects in III-V compounds, *Czech. J. Phys. B*, vol. 34, 5, pp. 428-435, 1984.
- 321.P. M. Mooney, Deep donor levels (D X centers) in III-V semiconductors, *J. Appl. Phys.*, 67, R1, 1990.
- 322.S. M. Sze, K. K. Ng, *Physics of semiconductor devices*, 3rd edition, Wiley-Interscience, 2007.
- 323.M. D. McCluskey, E. E. Haller, *Dopants and defects in semiconductors*, CRC Press, Taylor & Francis Group, 2012.
- 324.K. A. Dick, P. Caroff, Metal-seeded growth of III-V semiconductor nanowires: towards gold-free synthesis, *Nanoscale*, 6, 3006, 2014.
- 325.S. Breuer, C. Pfuller, T. Flissikowski, O. Brandt, H. T. Grahm, L. Geelhaar, and H. Riechert, Suitability of Au- and self-assisted GaAs nanowires for optoelectronic applications, *Nano Lett.*, 11, 3, pp. 1276-1279, 2011.
- 326.W. K. Chu, S. S. Lau, J. W. Mayer, H. Muller, and K. N. Tu, Implanted noble gas atoms as diffusion markers in silicide formation, *Thin Solid films*, 25, 393-402, 1975.
- 327.F. d'Heurle, C. S. Petersson, J. E. E. Baglin, S. J. LaPlace, and C. Y. Wong, Formation of thin films of NiSi: metastable structure, diffusion mechanisms in intermetallic compounds, *J. Appl. Phys.*, 55, 4208, 1984.
- 328.J. H. Gulpen, A. A. Kodentsov, and F. J. J. A. van Loo, Growth of silicides in Ni-Si and Ni-SiC bulk diffusion couples, *Z. Metallkd.*, 86, 8, 1995.

- 329.D. Z. Chi, D. Mangelinck, A. S. W. Wong, and S. K. Lahiri, Nickel silicide as a contact material for submicron CMOS devices, *J. Elec. Mater.*, vol. 30, no. 12, 2001.
- 330.N. S. Dellas, B. Z. Liu, S. M. Eichfeld, C. M. Eichfeld, T. S. Mayer, and S. E. Mohny, Orientation dependence of nickel silicide formation in contacts to silicon nanowires, *J. Appl. Phys.*, 105, 094309, 2009.
- 331.P. T-. Tremblay M. Guihard, S. Gaudet, M. Chicoine, C. Lavoie, P. Desjardins, and F. Schiettekatte, *J. Vac. Sci. Tech. B*, 31, 051213, 2013.
- 332.T. I. Kamins, R. S. Williams, Y. Chen, Y. -L. Chang, and Y. A. Chang, Chemical vapor deposition of Si nanowires nucleated by TiSi_2 islands on Si, *Appl. Phys. Lett.*, 76, 562, 2000.
- 333.T. I. Kamins, R. S. Williams, D. P. Basile, T. Hesjedal, and J. S. Harris, Ti-catalyzed Si nanowires by chemical vapor deposition: Microscopy and growth mechanisms, *J. Appl. Phys.*, 89, 1008, 2001.
- 334.B. Xiang, Q. X. Wang, Z. Wang, X. Z. Zhang, L. Q. Liu, and D. P. Yu, Synthesis and field emission properties of TiSi_2 nanowires, *Appl. Phys. Lett.*, 86, 243103, 2005.
- 335.S. Zhou, X. Liu, Y. Lin, and D. Wang, Rational synthesis and structural characterizations of complex TiSi_2 Nanostructures, *Chem. Mater.*, 21, 1023-1027, 2009.
- 336.H. -K. Lin, Y. -F. Tzeng, C. -H. Wang, N. -H. Tai, I. -I. Lin, C. -Y. Lee, and H. -T. Chiu, Ti_5Si_3 nanowire and its field emission property, *Chem. Mater.*, 20, 2429-2431, 2008.
- 337.S. D. Brotherton, P. Bradley, and J. Bicknell, Electrical properties of platinum in silicon, *J. Appl. Phys.*, 50, 3396, 1979.
- 338.T. Baron, M. Gordon, F. Dhalluin, C. TERNON, P. Ferret, and P. Gentile, Si nanowire growth and characterization using a microelectronics-compatible catalyst: PtSi, *Appl. Phys. Lett.*, 89, 233111, 2006.
- 339.B. Liu, Y. Wang, S. Dilts, T. S. Mayer, and S. E. Mohny, Silicidation of silicon nanowires by platinum, *Nano Lett.*, vol. 7, no. 3, 818-824, 2007.
- 340.E. C. Garnett, W. Liang, and P. Yang, Growth and electrical characteristics of platinum-nanoparticle-catalyzed silicon nanowires, *Adv. Mater.*, 19, 2946-2950, 2007.
- 341.Y. -C. Lin, K. -C. Lu, W. -W. Wu, J. Bai, L. J. Chen, K. N. Tu, and Y. Huang, Single crystalline PtSi nanowires, PtSi/Si/PtSi nanowire heterostructures, and nanodevices, *Nano Lett.*, vol. 8, no. 3, 913-918, 2008.
- 342.J. M. Higgins, A. L. Schmitt, I. A. Guzei, and S. Jin, Higher manganese silicide nanowires of Nowotny chimney ladder phase, *J. Am. Chem. Soc.*, 130, 16086-16094, 2008.
- 343.K. Seo, N. Bagkar, S. Kim, J. In, H. Toon, Y. Jo, and B. Kim, Diffusion-driven crystal structure transformation: synthesis of Heusler alloy Fe_3Si nanowires, *Nano Lett.*, 10, 3643-3647, 2010.
- 344.K. S. K. Varadwaj, K. Seo, J. In, P. Mohanty, J. Park, and B. Kim, Phase-controlled growth of metastable Fe_5Si_3 nanowires by a vapor transport method, *J. Am. Chem. Soc.*, 129, 8594-8599, 2007.
- 345.K. Seo, K. S. K. Varadwaj, P. Mohanty, S. Lee, Y. Jo, M. Jung, J. Kim, and B. Kim, Magnetic properties of single-crystalline CoSi nanowires, *Nano Lett.*, vol. 7, no. 5, 1240-1245, 2007.

- 346.Y. Chou, W. Wu, S. Cheng, B. Yoo, N. Myung, L. J. Chen, and K. N. Tu, In-situ TEM observation of repeating events of nucleation in epitaxial growth of nano CoSi_2 in nanowires of Si, *Nano Lett.*, vol. 8, no. 8, 2194-2199, 2008.
- 347.J. D. Carter, Y. Qu, R. Porter, L. Hoang, D. J. Masiel, and T. Guo, Silicon-based nanowires from silicon wafers catalyzed by cobalt nanoparticles in a hydrogen environment, *Chem. Commun.*, 2274-2276, 2005.
- 348.Y. L. Chueh, L. J. Chou, S. L. Cheng, L. J. Chen, C. J. Tsai et al., Synthesis and characterization of metallic TaSi_2 nanowires, *Appl. Phys. Lett.*, 87, 223113, 2005.
- 349.Y. L. Chueh, M. T. Ko, L. J. Chou, L. J. Chen, C. S. Wu, and C. D. Chen, TaSi_2 nanowires: a potential field emitter and interconnect, *Nano Lett.*, vol. 6, no. 8, 1637-1644, 2006.
- 350.R. J. Barsotti Jr., J. E. Fischer, C. H. Lee, J. Mahmood, C. K. W. Adu, and P. C. Eklund, Imaging, structural, and chemical analysis of silicon nanowires, *Appl. Phys. Lett.*, 81, 2866, 2002.
- 351.B. Kalache, P. R. i Cabarrocas, and A. F. i Morral, Observation of incubation times in the nucleation of silicon nanowires obtained by the vapor-liquid-solid method, *Jpn. J. Appl. Phys.*, vol. 45, no. 7, pp. L190-L193, 2006.
- 352.J. Arbiol, B. Kalache, P. R. i Cabarrocas, J. R. Morante, and A. F. i Morral, Influence of Cu as a catalyst on the properties of silicon nanowires synthesized by the vapour-solid-solid mechanism, *Nanotechnol.*, 18, 305606, 2007.
- 353.J. Arbiol, A. F. i Morral, S. Estrade, F. Peiro, B. Kalache, P. R. i Cabarrocas, and J. R. Morante, Influence of the (111) twinning on the formation of diamond cubic/diamond hexagonal heterostructures in Cu-catalyzed Si nanowires, *J. Appl. Phys.*, 104, 064312, 2008.
- 354.R. R. Chromik, W. K. Neils, and E. J. Cotts, Thermodynamic and kinetic study of solid state reactions in the Cu-Si system, *J. Appl. Phys.*, 86, 4273, 1999.
- 355.H. Chandrasekaran, G. U. Sumanasekara, and M. K. Sunkara, Rationalization of nanowire synthesis using low-melting point metals, *J. Phys. Chem. B*, 110, 18351-18357, 2006.
- 356.M. K. Sunkara, S. Sharma, R. Miranda, G. Lian, and E. C. Dickey, Bulk synthesis of silicon nanowires using a low-temperature vapor-liquid-solid method, *Appl. Phys. Lett.*, 79, 1546, 2001.
- 357.S. Sharma, M. K. Sunkara, Direct synthesis of single-crystalline silicon nanowires using molten gallium and silane plasma, *Nanotechnol.*, 15, 130-134, 2004.
- 358.I. Zardo, L. Yu, S. Conesa-Boj, S. Estrade, P. J. Alet, J. Rossler, M. Frimmer, P. R. i Cabarrocas, F. Peiro, J. Arbiol, J. R. Morante, and A. F. i Morral, Gallium assisted plasma enhanced chemical vapor deposition of silicon nanowires, *Nanotechnol.*, 20, 155602, 2009.
- 359.M. Jeon, Y. Tomitsuka, and K. Kamisako, Synthesis of gallium-catalyzed silicon nanowires by hydrogen radical-assisted deposition method, *J. Indust. Eng. Chem.*, 14, 836-840, 2008.
- 360.M. Jeon, K. Kamisako, Catalyst formation at various temperatures by hydrogen radical treatment and synthesis of silicon nanowires, *Appl. Surf. Sci.*, 254, 7703-7707, 2008.
- 361.I. Zardo, S. Conesa-Boj, S. Estrade, L. Yu, F. Peiro, P. R. i Cabarrocas, J. R. Morante, J. Arbiol, and A. F. i Morral, Growth study of indium-catalyzed silicon nanowires by plasma enhanced chemical vapor deposition, *Appl. Phys. A*, 100, 287-296, 2010.

- 362.M. Jeon, H. Uchiyama, and K. Kamisako, Characterization of Tin-catalyzed silicon nanowires synthesized by the hydrogen radical-assisted deposition method, *Mater. Lett.*, 63, 246-248, 2009.
- 363.L. Yu, F. Fortuna, B. O'Donnell, T. Jeon, M. Foldyna, G. Picardi, and P. R. i Cabarrocas, Bismuth-catalyzed and doped silicon nanowires for one-pump-down fabrication of radial junction solar cells, *Nano Lett.*, 12, 4153-4158, 2012.
- 364.C. -C. Chen, C. -C. Yeh, C. -H. Chen, M. -Y. Yu, H. -L. Liu, J. -J. Wu, K. -H. Chen, L. -C. Chen, J. -Y. Peng, and Y. -F. Chen, Catalytic growth and characterization of gallium nitride nanowires, *J. Am. Chem. Soc.*, 123, 2791-2798, 2001.
- 365.J. C. Johnson, H. Choi, K. P. Knutsen, R. D. Schaller, P. Yang, and R. J. Saykally, Single gallium nitride nanowire lasers, *Nature Mater.*, 1, 106-110, 2002.
- 366.J. -R. Kim, H. M. So, J. W. Park, J. -J. Kim, J. Kim, C. J. Lee, and S. C. Lyu, Electrical transport properties of individual gallium nitride nanowires synthesized by chemical-vapor-deposition, *Appl. Phys. Lett.*, 80, 3548, 2002.
- 367.T. Y. Kim, S. H. Lee, Y. H. Mo, H. W. Shim, K. S. Nahm, E. -K. Suh, J. W. Yang, K. Y. Lim, and G. S. Park, Growth of GaN nanowires on Si substrate using Ni catalyst in vertical chemical vapor deposition reactor, *J. Cryst. Growth*, 257, 97-103, 2003.
- 368.T. Kuykendall, P. Pauzauskie, S. Lee, Y. Zhang, J. Goldberger, and P. Yang, Metalorganic chemical vapor deposition route to GaN nanowires with triangular cross sections, *Nano Lett.*, vol. 3, no. 8, 1063-1066, 2003.
- 369.T. Kuykendall, P. J. Pauzauskie, Y. Zhang, J. Goldberger, D. Sirbulu, J. Denlinger, and P. Yang, Crystallographic alignment of high-density gallium nitride nanowire arrays, *Nature Mater.*, 3, 524-528, 2004.
- 370.L. Geelhaar, C. Cheze, W. M. Weber, R. Averbeck, H. Riechert, Th. Kehagias, Ph. Komninou, G. P. Dimitrakopulos, and Th. Karakostas, Axial and radial growth of Ni-induced GaN nanowires, *Appl. Phys. Lett.*, 91, 093113, 2007.
- 371.Q. Li, G. T. Wang, Improvement in aligned GaN nanowire growth using submonolayer Ni catalyst films, *Appl. Phys. Lett.*, 93, 043119, 2008.
- 372.L. Lari, R. T. Murray, T. J. Bullough, P. R. Chalker, M. Gass, C. Cheze, L. Geelhaar, H. Riechert, Nanoscale compositional analysis of Ni-based seed crystallites associated with GaN nanowire growth, *Phys. E*, 40, 2457-2461, 2008.
- 373.X. Weng, R. A. Burke, and J. M. Redwing, The nature of catalyst particles and growth mechanisms of GaN nanowires grown by Ni-assisted metal-organic chemical vapor deposition, *Nanotechnol.*, 20, 085610, 2009.
- 374.H. Ji, M. Kuball, R. A. Burke, and J. M. Redwing, Vibrational and optical properties of GaN NW synthesized by Ni-assisted catalytic growth, *Nanotechnol.*, 18, 445704, 2007.
- 375.C. Cheze, L. Geelhaar, O. Brandt, W. M. Weber, H. Riechert, S. Munch, R. Rothmund, S. Reitzenstein, A. Forchel, T. Kehagias, P. Komninou, G. P. Dimitrakopulos and T. Karakostas, Direct comparison of catalyst-free and catalyst-induced GaN nanowires, *Nano Res.*, 3, 528, 2010.
- 376.C. Cheze, L. Geelhaar, B. Jenichen, and H. Riechert, Different growth rates for catalyst-induced and self-induced GaN nanowires, *Appl. Phys. Lett.*, 97, 153105, 2010.

- 377.E. Park, S. Shim, R. Ha, E. Oh, B. W. Lee, and H. -J. Choi, Reassembling of Ni and Pt catalyst in the vapor-liquid-solid growth of GaN nanowires, *Mater. Lett.*, 65, 2458-2461, 2011.
- 378.S. M. Kang, B. K. Kang, and D. H. Yoon, Growth and properties of vertically well-aligned GaN nanowires by thermal chemical vapor deposition process, *Mater. Lett.*, 65, 763-765, 2011.
- 379.X. Zhou, J. Chesin, S. Crawford, and S. Gradecak, Using seed particle composition to control structural and optical properties of GaN nanowires, *Nanotechnol.*, 23, 285603, 2012.
- 380.D. Zhan, H. Huang, H. Wu, M. Ren, H. Zhu, Y. Liu, and B. Sun, Influence of Ni and Au/Ni catalysts on GaN nanowire growth, *Phys. Status Solidi A*, 210, no. 12, 2689-2692, 2013.
- 381.R. Ha, S. -W. Kim, and H. -J. Choi, Fabrication of vertical GaN/InGaN heterostructure nanowires using Ni-Au bi-metal catalysts, *Nano. Res. Lett.*, 8, 299, 2013.
- 382.T. R. Kuykendall, M. V. P. Altoe, D. F. Ogletree, and S. Aloni, Catalyst-directed crystallographic orientation control of GaN nanowire growth, *Nano Lett.*, 14, 6767-6773, 2014.
- 383.J. B. Park, N. -J. Kim, Y. -J. Kim, S. -H. Lee, and G. -C. Yi, Metal catalyst-assisted growth of GaN nanowires on graphene films for flexible photocatalyst applications, *Current Appl. Phys.*, 14, 1437-1442, 2014.
- 384.Y. Lin, B. Leung, Q. Li, J. J. Figiel, G. T. Wang, GaN nanowires with pentagon shape cross-section by ammonia-source molecular beam epitaxy, *J. Cryst. Growth*, 2015.
- 385.J. N. Pratt, J. M. Bird, Solid electrolyte cell studies of solid nickel-gallium alloys, *J. Phase Equil.*, vol. 14, no. 4, p. 465, 1993.
- 386.W. X. Yuan, Z. Y. Qian, H. Ipser, and G. Eriksson, Thermodynamic assessment of the Ni-Ga system, *J. Phase Equil. Diffusion*, vol. 25, no. 1, p. 68, 2004.
- 387.H. S. Venugopalan, S. E. Mohny, B. P. Luther, S. D. Wolter, and J. M. Redwing, Interfacial reactions between nickel thin films and GaN, *J. Appl. Phys.*, 82, 650, 1997.
- 388.J. A. Chisholm, P. D. Bristowe, Formation energies of metal impurities in GaN, *Comp Mater. Sci.*, 22, 73-77, 2001.
- 389.A. C. Ford, J. C. Ho, Z. Fan, O. Ergen, V. Altoe, S. Aloni, H. Razavi and A. Javey, Synthesis, contact printing, and device characterization of Ni-catalyzed, crystalline InAs nanowires, *Nano Res.*, 1, 32-39, 2008.
- 390.N. Han, F. Wang, A. T. Hui, J. J. Hou, G. Shan, F. Xiu, T. Hung, and J. C. Ho, Facile synthesis and growth mechanism of Ni-catalyzed GaAs nanowires on non-crystalline substrates, *Nanotechnol.*, 22, 285607, 2011.
- 391.S. Heun, B. Radha, D. Ercolani, G. U. Kulkarni, F. Rossi, V. Grillo, G. Salviati, F. Beltram and L. Sorba, Coexistence of vapor-liquid-solid and vapor-solid-solid growth modes in Pd-assisted InAs nanowires, *Small*, 6, no. 17, 1935-1941, 2010.
- 392.S. Heun, B. Radha, D. Ercolani, G. U. Kulkarni, F. Rossi, V. Grillo, G. Salviati, F. Beltram and L. Sorba, Pd-assisted growth of InAs nanowires, *Cryst. Growth Des.*, vol. 10, 4197-4202, 2010.
- 393.H. Xu, Y. Wang, Y. Guo, Z. Liao, Q. Gao, H. H. Tan, C. Jagadish, and J. Zou, Defect-free <110> zinc-blende structured InAs nanowires catalyzed by palladium, *Nano Lett.*, 12, 5744-5749, 2012.

- 394.H. -Y. Xu, Y.-N. Guo, Z.-M. Liao, W. Sun, Q. Gao, H. H. Tan, C. Jagadish and J. Zou, Catalyst size dependent growth of Pd-catalyzed one-dimensional InAs nanostructures, *Appl. Phys. Lett.*, 102, 203108, 2013.
- 395.R. Perumal, Z. Cui, P. Gille, J. -C. Harmand, and K. Yoh, Palladium assisted hetroepitaxial growth of an InAs nanowire by molecular beam epitaxy, *Semicond. Sci. Technol.*, 29, 115005, 2014.
- 396.H. -S. Kim, K. -H. Lee, M. -C. Shin, S. -Y. Kim, and M. -H. Dzo, Electrochemical behavior of palladium-indium system alloys, *Scripta Materialia*, vol. 38, no. 10, pp. 1549-1555, 1998.
- 397.C. Y. Nam, D. Tham, and J. E. Fischer, Effect of the polar surface on GaN nanostructure morphology and growth orientation, *Appl. Phys. Lett.*, 85, 5676, 2004.
- 398.C. Y. Nam, J. Y. Kim, and J. E. Fischer, Focused-ion-beam platinum nanopatterning for GaN nanowires: Ohmic contacts and patterned growth, *Appl. Phys. Lett.*, 86, 193112, 2005.
- 399.C. Y. Nam, D. Tham, and J. E. Fischer, Disorder effects in focused-ion-beam-deposited Pt contacts on GaN nanowires, *Nano Lett.*, vol. 5, no. 10, 2029-2033, 2005.
- 400.D. Tham, C. Y. Nam, and J. E. Fischer, Microstructure and composition of focused-ion-beam-deposited Pt contacts to GaN nanowires, *Adv. Mater.*, 18, 290-294, 2006.
- 401.O. Weidemann, E. Monroy, E. Hahn, M. Stutzmann, and M. Eickhoff, Influence of thermal oxidation on the electronic properties of Pt Schottky contacts on GaN grown by molecular-beam epitaxy, *Appl. Phys. Lett.*, 86, 083507, 2005.
- 402.E. Oh, B. W. Lee, S. Shim, K. -Y. Lee, H. Oh, H. -J. Choi, B. H. Son, Y. H. Ahn, and L. S. Dang, Platinum-assisted vapor-liquid-solid growth of GaN nanowires and their properties, *J. Korean Phys. Soc.*, vol. 56, no. 1, pp. 100-103, Jan. 2010.
- 403.J. Hu, T. W. Odom, and C. M. Lieber, Chemistry and physics in one dimension: synthesis and properties of nanowires and nanotubes, *Acc. Chem. Res.*, 32, 435-445, 1999.
- 404.X. Duan, C. M. Lieber, General synthesis of compound semiconductor nanowires, *Adv. Mater.*, 12, no. 4, 2000.
- 405.X. Duan, J. Wang, and C. M. Lieber, Synthesis and optical properties of gallium arsenide nanowires, *Appl. Phys. Lett.*, 76, 1116, 2000.
- 406.S. Kan, A. Aharoni, T. Mokari, and U. Banin, Shape control of III-V semiconductor nanocrystals: synthesis and properties of InAs quantum rods, *Faraday Discuss.*, 125, 23-38, 2004.
- 407.D. Pan, M. Fu, X. Yu, X. Wang, L. Zhu, S. Nie, S. Wang, Q. Chen, P. Xiong, S. von Molnar, and J. Zhao, Controlled synthesis of phase-pure InAs nanowires on Si(111) by diminishing the diameter to 10 nm, *Nano Lett.*, 14, 1214-1220, 2014.
- 408.S. T. Boles, C. V. Thompson, E. A. Fitzgerald, Influence of indium and phosphine on Au-catalyzed InP nanowire growth on Si substrates, *J. Cryst. Growth*, 311, 1446-1450, 2009.
- 409.A. T. Vogel, J. de Boor, M. Becker, J. V. Wittemann, S. L. Mensah, P. Werner, and V. Schmidt, Ag-assisted CBE growth of ordered InSb nanowire arrays, *Nanotechnol.*, 22, 015605, 2011.
- 410.K. Hillerich, M. E. Messing, L. R. Wallenberg, K. Deppert, and K. A. Dick, Epitaxial InP nanowire growth from Cu seed particles, *J. Cryst. Growth*, 315, 134-137, 2011.

- 411.K. Hillerich, K. A. Dick, M. E. Messing, K. Deppert, and J. Johansson, Simultaneous growth mechanisms for Cu-seeded InP nanowires, *Nano Res.*, 5, 5, 297-306, 2012.
- 412.K. Hillerich, D. S. Ghidini, K. A. Dick, K. Deppert, and J. Johansson, Cu particle seeded InP-InAs axial nanowire heterosturctures, *Phys. Status Solidi RRL*, 7, no. 10, 850-854, 2013.
- 413.F. Martelli, S. Rubini, M. Piccin, G. Bais, F. Jabeen, S. De Franceschi, V. Grillo, E. Carlino, F. D'Acapito, F. Boscherini, S. Cabrini, M. Lazzarino, L. Businaro, F. Romanato, and A. Franciosi, Manganese-induced growth of GaAs nanowires, *Nano Lett.*, vol. 6, no. 9, 2130-2134, 2006.
- 414.F. Martelli, M. Piccin, G. Jabeen, S. Ambrosini, S. rubini, and A. Franciosi, Photoluminescence of Mn-catalyzed GaAs nanowires grown by molecular beam epitaxy, *Nanotechnol.*, 18, 125603, 2007.
- 415.F. Jabeen, M. Piccin, L. Felisari, V. Grilo, G. Bais, S. Rubini, F. Martelli, F. D'Acapito, M. Rovezzi, and F. Boscherini, Mn-induced growth of InAs nanowires, *J. Vac. Sci. Tech. B*, 28, 478, 2010.
- 416.F. Martelli, S. Rubini, F. Jabeen, L. Felisari, and V. Grillo, On the growth of InAs nanowires by molecular beam epitaxy, *J. Cryst. Growth*, 323, 297-300, 2011.
- 417.J. Sadowski, P. Dluzewski, S. Kret, E. Janik, E. Lusakowska, J. Kanski, A. Presz, F. Terki, S. Charar, and D. Tang, GaAs:Mn nanowires grown by molecular beam epitaxy of (Ga,Mn)As at MnAs segregation conditions, *Nano Lett.*, vol. 7, no. 9, 2724-2728, 2007.
- 418.J. Adell, I. Ulfat, J. Sadowski, L. Ilver, and J. Kanski, Electron spectroscopic studies of nanowires formed by (GaMn)As growth on GaAs (111)B, *Solid State Commu.*, 151, 850-854, 2011.
- 419.A. Bouravleuv, G. Cirlin, V. Sapega, P. Werner, A. Savin, and H. Lipsanen, Ferromagnetic (Ga,Mn)As nanowries grown by Mn-assisted molecular beam epitaxy, *J. Appl. Phys.*, 113, 144303, 2013.
- 420.X. Duan, C. M. Lieber, Laser-assisted catalytic growth of single crystal GaN nanowries, *J. Am. Chem. Soc.*, 122, 188-189, 2000.
- 421.J. Zhang, L. Zhang, Growth of semiconductor gallium nitride nanowires with different catalysts, *J. Vac. Sci. Tech. B*, 21, 2415, 2003.
- 422.W. -Q. Han, A. Zettl, Pyrolysis approach to the synthesis of gallium nitride nanorods, *Appl. Phys. Lett.*, 80, 303, 2002.
- 423.I. Regolin, V. Khorenko, W. Prost, F. J. Tegude, D. Sudfeld, J. Kastner, G. Dumpich, K. Hitzbleck, and H. Wiggers, GaAs whiskers grown by metal-organic vapor-phase epitaxy using Fe nanoparticles, *J. Appl. Phys.*, 101, 054318, 2007.
- 424.D. D. Fanfair, B. A. Korgel, Bismuth nanocrystal-seeded III-V semiconductor nanowire synthesis, *Cryst. Growth Design*, vol. 5, no. 5, 1971-1976, 2005.
- 425.F. Wang, H. Yu, S. Jeong, J. M. Pietryga, J. A. Hollingsworth, P. C. Gibbons, and W. E. Buhro, The scaling of the effective band gaps in indium-arsenide quantum dots and wires, *ACS Nano*, vol. 2, no. 9, 1903-1913, 2008.
- 426.A. Dong, H. Yu, F. Wang, and W. E. Buhro, Colloidal GaAs quantum wires: solution-liquid-solid synthesis and quantum-confinement studies, *J. Am. Chem. Soc.*, 130, 5954-5961, 2008.
- 427.C. -C. Chen, C. -C. Yeh, Large-scale catalytic synthesis of crystalline gallium nitride nanowires, *Adv. Mater.*, 12, no. 10, 2000.

- 428.J. Su, G. Cui, M. Gherasimova, H. Tsukamoto, J. Han, D. Ciuparu, S. Lim, L. Pfefferle, Y. He, A. V. Nurmikko, C. Broadbridge, and A. Lehman, Catalytic growth of group III-nitride nanowires and nanostructures by metalorganic chemical vapor deposition, *Appl. Phys. Lett.*, 86, 013105, 2005.
- 429.R. Sun, D. Jacobsson, I. –J. Chen, M. Nilsson, C. Thelander, S. Lehmann, and K. A. Dick, Sn-seeded GaAs nanowires as self-assembled radial p-n junctions, *Nano Lett.*, 15, 3757-3762, 2015.
- 430.S. De Franceschi, J. A. van Dam, E. P. A. M. Bakkers, L. F. Feiner, L. Gurevich, and L. P. Kouwenhoven, Single-electron tunneling in InP nanowires, *Appl. Phys. Lett.*, 83, 344, 2003.
- 431.C. Cao, X. Xiang, and H. Zhu, High-density, uniform gallium nitride nanorods grown on Au-coated silicon substrate, *J. Cryst. Growth*, 273, 375-380, 2005.
- 432.M. C. Plante, R. R. LaPierre, Growth mechanisms of GaAs nanowires by gas source molecular beam epitaxy, *J. Cryst. Growth*, 286, 394-399, 2006.
- 433.P. Paiano, P. Prete, N. Lovergine, and A. M. Mancini, Size and shape control of GaAs nanowires grown by metalorganic vapor phase epitaxy using tertiarybutylarsine, *J. Appl. Phys.*, 100, 094305, 2006.
- 434.S. A. Dayeh, E. T. Yu, and D. Wang, III-V nanowire growth mechanism: V/III ratio and temperature effects, *Nano Lett.*, vol. 7, no. 8, 2486-2490, 2007.
- 435.M. Piccin, G. Bais, V. Grillo, F. Jabeen, S. De Franceschi, E. Carlino, M. Lazzarino, F. Romanato, L. Businaro, S. Rubini, F. Martelli, and A. Franciosi, Growth by molecular beam epitaxy and electrical characterization of GaAs nanowires, *Phys. E*, 37, 134-137, 2007.
- 436.M. E. Messing, K. Hillerich, J. Johansson, K. Deppert, and K. A. Dick, The use of gold for fabrication of nanowire structures, *Gold Bulletin*, vol. 42, no. 3, p. 172, 2009.
- 437.S. Paiman, Q. Gao, H. H. Tan, C. Jagadish, K. Pemasiri, M. Montazeri, H. E. Jackson, L. M. Smith, J. M. Yarrison-Rice, X. Zhang, and J. Zou, The effect of V/III ratio and catalyst particle size on the crystal structure and optical properties of InP nanowires, *Nanotechnol.*, 20, 225606, 2009.
- 438.Z. Zhang, K. Zheng, Z. –Y. Lu, P. –P. Chen, W. Lu, and J. Zou, Catalyst orientation-induced growth of defect-free zinc-blende structured $\langle 00\bar{1} \rangle$ InAs nanowires, *Nano Lett.*, 15, 876-882, 2015.
- 439.S. A. Fortuna, X. Li, Metal-catalyzed semiconductor nanowires: a review on the control of growth directions, *Semicond. Sci. Technol.*, 25, 024005, 2010.
- 440.J. Johansson, C. P. T. Svensson, T. Martensson, L. Samuelson, and W. Seifert, Mass transport for semiconductor nanowire growth, *J. Phys. Chem. B*, 109, 13567-13571, 2005.
- 441.W. Lu, C. M. Lieber, Semiconductor nanowires, *J. Phys. D: Appl. Phys.*, 39, R387-R406, 2006.
- 442.P. Cheyssac, M. Sacilotti, and G. Patriarche, Vapor-liquid-solid mechanisms: challenges for nanosized quantum cluster/dot/wire materials, *J. Appl. Phys.*, 100, 044315, 2006.
- 443.K. A. Dick, S. Kodambaka, M. C. Reuter, K. Deppert, L. Samuelson, W. Seifert, L. R. Wallenberg, and F. M. Ross, The morphology of axial and branched nanowire heterostructures, *Nano Lett.*, vol. 7, no. 6, 1817-1822, 2007.

- 444.N. P. Dasgupta, J. Sun, C. Liu, S. Brittman, S. C. Andrews, J. Lim, H. Gao, R. Yan, and P. Yang, 25th anniversary article: semiconductor nanowires-synthesis, characterization, and applications, *Adv. Mater.*, 26, 2137-2184, 2014.
- 445.L. Samuelson, Self-forming nanoscale devices, *Materialstoday*, vol. 6, no. 10, pp. 22-31, Oct. 2003.
- 446.X. Duan, Y. Huang, Y. Cui, J. Wang, and C. M. Lieber, Indium phosphide nanowires as building blocks for nanoscale electronic and optoelectronic devices, *Nature*, vol. 409, pp. 66-69, Jan. 2001.
- 447.J. Bauer, V. Gottschalch, and G. Wagner, The influence of the droplet composition on the vapor-liquid-solid growth of InAs nanowires on GaAs($\overline{111}$)B by metal-organic vapor phase epitaxy, *J. Appl. Phys.*, 104, 114315, 2008.
- 448.E. P. A. M. Bakkers, J. A. Van Dam, S. De Franceschi, L. P. Kouwenhoven, M. Kaiser, M. Verheijen, and H. Wondergem, Epitaxial growth of InP nanowires on germanium, *Nature Mater.*, vol. 3, pp. 769-773, Nov. 2004.
- 449.T. Martensson, C. P. T. Svensson, B. A. Wacaser, M. W. Larsson, W. Seifert, K. Deppert, A. Gustafsson, L. R. Wallenberg, and L. Samuelson, Epitaxial III-V nanowires on silicon, *Nano Lett.*, vol. 4, no. 10, 1987-1990, 2004.
- 450.S. S. Yi, G. Girolami, J. Amano, M. Saif Islam, S. Sharma, T. I. Kamins, and I. Kimukin, InP nanobridges epitaxially formed between two vertical Si surfaces by metal-catalyzed chemical vapor deposition, *Appl. Phys. Lett.*, 89, 133121, 2006.
- 451.A. L. Roest, M. A. Verheijen, O. Wunnicke, S. Serafin, H. Wondergem, and E. P. A. M. Bakkers, Position-controlled epitaxial III-V nanowires on silicon, *Nanotechnol.*, 17, S271-S275, 2006.
- 452.E. P. A. M. Bakkers, M. T. Borgstrom, and M. A. Verheijen, Epitaxial growth of III-V nanowires on group IV, *MRS Bulletin*, vol. 32, pp. 117-122, Feb. 2007.
- 453.L. C. Chuang, M. Moewe, C. Chase, N. P. Kobayashi, C. Chang-Hasnain, and S. Crankshaw, Critical diameter for III-V nanowires grown on lattice-mismatched substrates, *Appl. Phys. Lett.*, 90, 043115, 2007.
- 454.X. -Y. Bao, C. Soci, D. Susac, J. Bratvold, D. P. R. Aplin, W. Wei, C. -Y. Chen, S. A. Dayeh, K. L. Kavanagh, and D. Wang, Heteroepitaxial growth of vertical GaAs nanowires on Si (111) substrates by metal-organic chemical vapor deposition, *Nano Lett.*, vol. 8, no. 11, 3755-3760, 2008.
- 455.L. C. Chuang, M. Moewe, S. Crankshaw, and C. Chang-Hasnain, Optical properties of InP nanowires on Si substrates with varied synthesis parameters, *Appl. Phys. Lett.*, 92, 013121, 2008.
- 456.Ph. Buffat, J. -P. Borel, Size effect on the melting temperature of gold particles, *Phys. Rev. A*, vol. 13, no. 6, Jun. 1976.
- 457.J. -P. Borel, Thermodynamical size effect and the structure of metallic clusters, *Surf. Sci.*, 106, 1-9, 1981.
- 458.J. Ross, R. P. Andres, Melting temperature of small clusters, *Surf. Sci.*, 106, 11-17, 1981.
- 459.D. G. Deppe, N. Holonyak Jr., Atom diffusion and impurity-induced layer disordering in quantum well III-V semiconductor heterostructures, *J. Appl. Phys.*, 64, R93, 1988.
- 460.H. P. Ho, I. Harrison, N. Baba-Ali, B. Tuck, and M. Henini, Diffusion induced disorder in AlAs-GaAs superlattice by transition elements, *J. Elec. Mater.*, vol. 20, no. 9, 1991.

461. I. Harrison, H. P. Ho, and N. Baba-Ali, Diffusion induced disorder of GaAs/AlGaAs superlattices, *J. Elec. Mater.*, vol. 20, no. 6, 1991.
462. H. Parala, A. Devi, F. Hipler, E. Maile, A. Birkner, H. W. Becker, and R. A. Fischer, Investigation on InN whiskers grown by chemical vapour deposition, *J. Cryst. Growth*, 231, 68-74, 2001.
463. G. Zhang, K. Tateno, H. Gotoh, and T. Sogawa, Vertically aligned InP nanowires grown via the self-assisted vapor-liquid-solid mode, *Appl. Phys. Exp.*, 5, 055201, 2012.
464. R. L. Woo, L. Gao, N. Goel, M. K. Hudait, K. L. Wang, S. Kodambaka, and R. F. Hicks, Kinetic control of self-catalyzed indium phosphide nanowires, nanocones, and nanopillars, *Nano Lett.*, vol. 9, no. 6, 2207-2211, 2009.
465. H. Zhou, M. Pozuelo, R. F. Hicks, and S. Kodambaka, Self-catalyzed vapor-liquid-solid growth of $\text{InP}_{1-x}\text{Sb}_x$ nanostructures, *J. Cryst. Growth*, 319, 25-30, 2011.
466. M. He, M. M. E. Fahmi, S. N. Mohammad, R. N. Jacobs, L. Salamanca-Riba, F. Felt, M. Jah, A. Sharma, and D. Lakins, InAs nanowires and whiskers grown by reaction of indium with GaAs, *Appl. Phys. Lett.*, 82, 3749, 2003.
467. M. Sacilotti, J. Decobert, H. Sik, G. Post, C. Dumas, P. Viste, and G. Patriarche, Structural studies of nano/micrometric semiconducting GaInP wires grown by MOCVD, *J. Cryst. Growth*, 272, 198-203, 2004.
468. M. He, S. N. Mohammad, Novel chemical-vapor deposition technique for the synthesis of high-quality single-crystal nanowires and nanotubes, *J. Chem. Phys.*, 124, 064714, 2006.
469. S. A. Dayeh, E. T. Yu, and D. Wang, Excess indium and substrate effects on the growth of InAs nanowires, *Small*, 3, no. 10, 1683-1687, 2007.
470. S. Yu, G. Miao, Y. Jin, L. Zhang, H. Song, H. Jiang, Z. Li, D. Li, and X. Sun, Growth and optical properties of catalyst-free InP nanowires on Si (100) substrates, *Physica E*, 42, 1540-1543, 2010.
471. C. J. Novotny, P. K. L. Yu, Vertically aligned, catalyst-free InP nanowires grown by metalorganic chemical vapor deposition, *Appl. Phys. Lett.*, 87, 203111, 2005.
472. M. Mattila, T. Hakkarainen, H. Lipsanen, H. Jiang, and E. I. Kauppinen, Catalyst-free growth of In(As)P nanowires on silicon, *Appl. Phys. Lett.*, 89, 063119, 2006.
473. C. Ngo, H. Zhou, M. Mecklenburg, M. Pozuelo, B. C. Regan, Q. F. Xiao, V. B. Shenoy, R. F. Hicks, and S. Kodambaka, Effect of precursor flux on compositional evolution in $\text{InP}_{1-x}\text{Sb}_x$ nanowires grown via self-catalyzed vapor-liquid-solid process, *J. Cryst. Growth*, 336, 14-19, 2011.
474. G. Zhang, S. Sasaki, K. Tateno, H. Gotoh, and T. Sogawa, Au-free InAs nanowires grown in In-particle-assisted vapor-liquid-solid mode: growth, structure and electrical property, *AIP Advances*, 3, 052107, 2013.
475. B. Mandl, J. Stangl, T. Martensson, A. Mikkelsen, J. Eriksson, L. S. Karlsson, G. Bauer, L. Samuelson, and W. Seifert, Au-free epitaxial growth of InAs nanowires, *Nano Lett.*, vol. 6, no. 8, 1817-1821, 2006.
476. B. Mandl, J. Stangl, E. Hilner, A. A. Zakharov, K. Hillerich, A. W. Dey, L. Samuelson, G. Bauer, K. Deppert, and A. Mikkelsen, Growth mechanism of self-catalyzed group III-V nanowires, *Nano Lett.*, 10, 4443-4449, 2010.
477. E. Dimakis, J. Lahnemann, U. Jahn, S. Breuer, M. Hilse, L. Geelhaar, and H. Riechert, Self-assisted nucleation and vapor-solid growth of InAs nanowires on bare Si(111), *Cryst. Growth Des.*, 11, 4001-4008, 2011.

- 478.G. Koblmuller, S. Hertenberger, K. Vizbaras, M. Bichler, F. Bao, J. -P. Zhang, and G. Abstreiter, Self-induced growth of vertical free-standing InAs nanowires on Si (111) by molecular beam epitaxy, *Nanotechnol.*, 21, 365602, 2010.
- 479.M. He, A. Motayed, and S. N. Mohammad, Phase separations of single-crystal nanowires grown by self-catalytic chemical vapor deposition method, *J. Chem. Phys.*, 126, 064704, 2007.
- 480.B. Mandl, K. A. Dick, D. Kriegner, M. Keplinger, G. Bauer, J. Stangl, and K. Deppert, Crystal structure control in Au-free self-seeded InSb wire growth, *Nanotechnol.*, 22, 145603, 2011.
- 481.M. Pozuelo, H. Zhou, S. Lin, S. A. Lipman, M. S. Goorsky, R. F. Hicks, and S. Kodambaka, Self-catalyzed growth of InP/InSb axial nanowire heterostructures, *J. Cryst. Growth*, 329, 6-11, 2011.
- 482.Th. Grap, T. Rieger, Ch. Blomers, Th. Schapers, D. Grutzmacher, and M. I. Lepsa, Self-catalyzed VLS grown InAs nanowires with twinning superlattices, *Nanotechnol.*, 24, 335601, 2013.
- 483.D. Forbes, S. Hubbard, R. Raffaele, and J. S. McNatt, Au-catalyst-free epitaxy of InAs nanowires, *J. Cryst. Growth*, 312, 1391-1395, 2010.
- 484.L. Gao, R. L. Woo, B. Liang, M. Pozuelo, S. Prikhodko, M. Jackson, N. Goel, M. K. Hudait, D. L. Huffaker, M. S. Goorsky, S. Kodambaka, and R. F. Hicks, Self-catalyzed epitaxial growth of vertical indium phosphide nanowires on silicon, *Nano Lett.*, vol. 9, no. 6, 2223-2228, 2009.
- 485.Y. Jing, X. Bao, W. Wei, C. Li, K. Sun, D. P. R. Aplin, Y. Ding, Z. Wang, Y. Bando, and D. Wang, Catalyst-free heteroepitaxial MOCVD growth of InAs nanowires on Si substrates, *J. Phys. Chem. C*, 118, 1696-1705, 2014.
- 486.M. H. Madsen, M. Aagesen, P. Krogstrup, C. Sorensen, and J. Nygard, Influence of the oxide layer for growth of self-assisted InAs nanowires on Si(111), *Nanoscale Res. Lett.*, 6, 516, 2011.
- 487.S. Hertenberger, D. Rudolph, S. Bolte, M. Doblinger, M. Bichler, D. Spirkoska, J. J. Finley, G. Abstreiter, and G. Koblmuller, Absence of vapor-liquid-solid growth during molecular beam epitaxy of self-induced InAs nanowires on Si, *Appl. Phys. Lett.*, 98, 123114, 2011.
- 488.S. N. Mohammad, Self-catalysis: a contamination-free, substrate-free growth mechanism for single-crystal nanowire and nanotube growth by chemical vapor deposition, *J. Chem. Phys.*, 125, 094705, 2006.
- 489.S. N. Mohammad, Self-catalytic solution for single-crystal nanowire and nanotube growth, *J. Chem. Phys.*, 127, 244702, 2007.
- 490.M. Hei, A. Gustafsson, S. Conesa-Boj, F. Peiro, J. R. Morante, G. Abstreiter, J. Arbiol, L. Samuelson, and A. F. i Morral, Catalyst-free nanowires with axial In_xGa_{1-x}As/GaAs heterostructures, *Nanotechnol.*, 20, 075603, 2009.
- 491.H. Goto, K. Nosaki, K. Tomioka, S. Hara, K. Hiruma, J. Motohisa, and T. Fukui, Growth of core-shell InP nanowires for photovoltaic application by selective-area metal organic vapor phase epitaxy, *Appl. Phys. Exp.*, 2, 035004, 2009.
- 492.V. Evoen, H. Zhou, L. Gao, M. Pozuelo, B. Liang, J. Tatebayashi, S. Kodambaka, D. L. Huffaker, and R. F. Hicks, Self-catalyzed vapor-liquid-solid growth of InP/InAsP core-shell nanopillars, *J. Cryst. Growth*, 314, 34-38, 2011.
- 493.B. Mandl, A. W. Dey, J. Stangl, M. Cantoro, L. -E. Wernersson, G. Bauer, L. Samuelson, K. Deppert, and C. Thelander, Self-seeded, position-controlled InAs

- nanowire growth on Si: A growth parameter study, *J. Cryst. Growth*, 334, 51-56, 2011.
- 494.E. Dimakis, M. Ramsteiner, C. –N. Huang, A. Trampert, A. Davydok, A. Biermanns, U. Pietsch, H. Riechert, and L. Geelhaar, *In situ* doping of catalyst-free InAs nanowires with Si: growth, polytypism, and local vibrational modes of Si, *Appl. Phys. Lett.*, 103, 143121, 2013.
 - 495.S. Bietti, C. Somaschini, C. Frigeri, A. Fedorov, L. Esposito, L. Geelhaar, and S. Sanguinetti, Self-assisted GaAs nanowires with selectable number density on silicon without oxide layer, *J. Phys. D: Appl. Phys.*, 47, 394002, 2014.
 - 496.M. He, I. Minus, P. Zhou, S. N. Mohammed, J. B. Halpern, R. Jacobs, W. L. Sarney, L. Salamanca-Riba, and R. D. Vispute, Growth of large-scale GaN nanowires and tubes by direct reaction of Ga with NH_3 , *Appl. Phys. Lett.*, 77, 3731, 2000.
 - 497.E. Calleja, M. A. Sanchez-Garcia, F. J. Sanchez, F. Calle, F. B. Naranjo, and E. Munoz, Luminescence properties and defects in GaN nanocolumns grown by molecular beam epitaxy, *Phys. Rev. B*, vol. 62, no. 24, Dec. 2000-II.
 - 498.V. Narayanan, S. Mahajan, N. Sukidi, K. J. Bachmann, V. Woods, and N. Dietz, Orientation mediated self-assembled gallium phosphide islands grown on silicon, *Phil. Mag. A*, vol. 80, no. 3, 555-572, 2000.
 - 499.L. W. Tu, C. L. Hsiao, T. W. Chi, I. Lo, and K. Y. Hsieh, Self-assembled vertical GaN nanorods grown by molecular-beam epitaxy, *Appl. Phys. Lett.*, 82, 1601, 2003.
 - 500.Z. Zhong, F. Qian, D. Wang, and C. M. Lieber, Synthesis of p-type gallium nitride nanowires for electronic and photonic nanodevices, *Nano Lett.*, vol. 3, no. 3, 343-346, 2003.
 - 501.E. A. Stach, P. J. Pauzauskie, T. Kuykendall, J. Goldberger, R. He, and P. Yang, Watching GaN nanowires grow, *Nano Lett.*, vol. 3, no. 6, 867-869, 2003.
 - 502.Y. S. Park, C. M. Park, D. J. Fu, T. W. Kang, and J. E. Oh, Photoluminescence studies of GaN nanorods on Si (111) substrates grown by molecular-beam epitaxy, *Appl. Phys. Lett.*, 85, 5718, 2004.
 - 503.K. A. Bertness, N. A. Sanford, J. M. Barker, J. B. Schlager, A. Roshko, A. V. Davydov, and I. Levin, Catalyst-free growth of GaN nanowires, *J. Electro. Mater.*, vol. 35, no. 4, 2006.
 - 504.B. T. Adekore, K. Rakes, B. Wang, M. J. Callahan, S. Pendurti, and Z. Sitar, Ammonothermal synthesis of aluminum nitride crystals on group III-nitride templates, *J. Electro. Mater.*, vol. 35, no. 5, 2006.
 - 505.R. Meijers, T. Richter, R. Calarco, T. Stoica, H. –P. Bochem, M. Marso, and H. Luth, GaN-nanowhiskers: MBE-growth conditions and optical properties, *J. Cryst. Growth*, 289, 381-386, 2006.
 - 506.L. Hong, Z. Liu, X. T. Zhang, and S. K. Hark, Self-catalytic growth of single-phase AlGaIn alloy nanowires by chemical vapor deposition, *Appl. Phys. Lett.*, 89, 193105, 2006.
 - 507.K. A. Bertness, A. Roshko, N. A. Sanford, J. M. Barker, and A. V. Davydov, Spontaneously grown GaN and AlGaIn nanowires, *J. Cryst. Growth*, 287, 522-527, 2006.
 - 508.H. –Y. Chen, H. –W. Lin, C. –H. Shen, and S. Gwo, Structure and photoluminescence properties of epitaxially oriented GaN nanorods grown on Si (111) by plasma-assisted molecular-beam epitaxy, *Appl. Phys. Lett.*, 89, 243105, 2006.

- 509.M. Sacilotti, P. Cheyssac, G. Patriarche, J. Decobert, Th. Chiaramonte, L. P. Cardoso, M. F. Pillis, M. J. Brasil, F. Iikawa, M. Nakaema, Y. Lacroute, J. C. Vial, and F. Donatini, Organometallic precursors as catalyst to grow three-dimensional micro/nanostructures: spheres, clusters & wires, *Surface & Coatings Technol.*, 201, 9104-9108, 2007.
- 510.S. Vaddiraju, M. K. Sunkara, A. H. Chin, C. Z. Ning, G. R. Dholakia, and M. Meyyappan, Synthesis of group III antimonide nanowires, *J. Phys. Chem. C*, 111, 7339-7347, 2007.
- 511.K. Ikejiri, J. Noborisaka, S. Hara, J. Motohisa, T. Fukui, Mechanism of catalyst-free growth of GaAs nanowires by selective area MOVPE, *J. Cryst. Growth*, 298, 616-619, 2007.
- 512.K. A. Bertness, A. Roshko, L. M. Mansfield, T. E. Harvey, and N. A. Sanford, Nucleation conditions for catalyst-free GaN nanowires, *J. Cryst. Growth*, 300, 94-99, 2007.
- 513.K. A. Bertness, A. Roshko, L. M. Mansfield, T. E. Harvey, and N. A. Sanford, Mechanism for spontaneous growth of GaN nanowires, with molecular beam epitaxy, *J. Cryst. Growth*, 310, 3154-3158, 2008.
- 514.C. Colombo, D. Spirkoska, M. Frimmer, G. Abstreiter, and A. F. i Morral, Ga-assisted catalyst-free growth mechanism of GaAs nanowires by molecular beam epitaxy, *Phys. Rev. B*, 77, 155326, 2008.
- 515.A. F. i Morral, C. Colombo, G. Abstreiter, J. Arbiol, and J. R. Morante, Nucleation mechanism of gallium-assisted molecular beam epitaxy growth of gallium arsenide nanowires, *Appl. Phys. Lett.*, 92, 063112, 2008.
- 516.A. F. i Morral, D. Spirkoska, J. Arbiol, M. Heigoldt, J. R. Morante, and G. Abstreiter, Prismatic quantum heterostructures synthesized on molecular-beam epitaxy GaAs nanowires, *Small*, 4, no. 7, 899-903, 2008.
- 517.F. Jabeen, V. Grillo, S. Rubini, and F. Martelli, Self-catalyzed growth of GaAs nanowires on cleaved Si by molecular beam epitaxy, *Nanotechnol.*, 19, 275711, 2008.
- 518.D. Spirkoska, G. Abstreiter and A. F. i Morral, Size and environment dependence of surface phonon modes of gallium arsenide nanowires as measured by Raman spectroscopy, *Nanotechnol.*, 19, 435704, 2008.
- 519.D. Spirkoska, C. Colombo, M. Heiss, G. Abstreiter, and A. F. i Morral, The use of molecular beam epitaxy for the synthesis of high purity III-V nanowires, *J. Phys.: Condens. Matter*, 20, 454225, 2008.
- 520.C. Colombo, M. Heiß, M. Gratzel, and A. F. i Morral, Gallium arsenide p-i-n radial structures for photovoltaic applications, *Appl. Phys. Lett.*, 94, 173108, 2009.
- 521.I. Zardo, S. Conesa-Boj, F. Peiro, J. R. Morante, J. Arbiol, E. Uccelli, G. Abstreiter, and A. F. i Morral, Raman spectroscopy of wurtzite and zinc-blende GaAs nanowires: polarization dependence, selection rules, and strain effects, *Phys. Rev. B*, 80, 245324, 2009.
- 522.Z. Gu, M. P. Paranthaman, and Z. Pan, Vapor-phase synthesis of gallium phosphide nanowires, *Cryst. Growth Des.*, vol. 9, no. 1, 525-527, 2009.
- 523.J. H. Paek, T. Nishiwaki, M. Yamaguchi, and N. Sawaki, Catalyst free MBE-VLS growth of GaAs nanowires on (111)Si substrate, *Phys. Status Solidi C*, 6, no. 6, 1436-1440, 2009.

- 524.W. Guo, M. Zhang, A. Banerjee, and P. Bhattacharya, Catalyst-free InGaN/GaN nanowire light emitting diodes grown on (001) silicon by molecular beam epitaxy, *Nano Lett.*, 10, 3355-3359, 2010.
- 525.S. Plissard, K. A. Dick, X. Wallart, and P. Caroff, Gold-free GaAs/GaAsSb heterostructure nanowires grown on silicon, *Appl. Phys. Lett.*, 96, 121901, 2010.
- 526.S. Plissard, K. A. Dick, G. Larrieu, S. Godey, A. Addad, X. Wallart, and P. Caroff, Gold-free growth of GaAs nanowires on silicon: arrays and polytypism, *Nanotechnol.*, 21, 385602, 2010.
- 527.C. Cheze, L. Geelhaar, A. Trampert, and H. Riechert, *In situ* investigation of self-induced GaN nanowire nucleation on Si, *Appl. Phys. Lett.*, 97, 043101, 2010.
- 528.J. Dufouleur, C. Colombo, T. Garma, B. Ketterer, E. Uccelli, M. Nicotra, and A. F. i Morral, P-doping mechanisms in catalyst-free gallium arsenide nanowires, *Nano Lett.*, 10, 1734-1740, 2010.
- 529.P. Krogstrup, R. Popovitz-Biro, E. Johnson, M. H. Madsen, J. Nygard, and H. Shtrikman, Structural phase control in self-catalyzed growth of GaAs nanowires on silicon (111), *Nano Lett.*, 10, 4475-4482, 2010.
- 530.J. Tatebayashi, G. Mariani, A. Lin, R. F. Hicks, and D. L. Huffaker, Optical characteristics of GaInP/GaP double-heterostructure core-shell nanowires embedded in polydimethylsiloxane membranes, *Appl. Phys. Lett.*, 96, 253101, 2010.
- 531.G. E. Cirlin, V. G. Dubrovskii, Y. B. Samsonenko, A. D. Bouravleuv, K. Durose, Y. Y. Proskuryakov, B. Mendes, L. Bowen, M. A. Kaliteevski, R. A. Abram, and D. Zeze, Self-catalyzed, pure zincblende GaAs nanowires grown on Si (111) by molecular beam epitaxy, *Phys. Rev. B*, 82, 035302, 2010.
- 532.M. Pozuelo, S. V. Prikhodko, R. Grantab, H. Zhou, L. Gao, S. D. Sitzman, V. Gambin, V. B. Shenoy, R. F. Hicks, and S. Kodambaka, Zincblende to wurtzite transition during the self-catalyzed growth of InP nanostructures, *J. Cryst. Growth*, 312, 2305-2309, 2010.
- 533.X. J. Chen, B. Gayral, D. Sam-Giao, C. Bougerol, C. Durand, and J. Eymery, Catalyst-free growth of high-optical quality GaN nanowires by metal-organic vapor phase epitaxy, *Appl. Phys. Lett.*, 99, 251910, 2011.
- 534.M. Heiss, S. Conesa-Boj, J. Ren, H. -H. Tseng, A. Gali, A. Rudolph, E. Uccelli, F. Peiro, J. R. Morante, D. Schuh, E. Reiger, E. Kaxiras, J. Arbiol, and A. F. i Morral, Direct correlation of crystal structure and optical properties in wurtzite/zinc-blende GaAs nanowire heterostructures, *Phys. Rev. B*, 83, 045303, 2011.
- 535.K. A. Bertness, N. A. Sanford, and A. V. Davydov, GaN nanowires grown by molecular beam epitaxy, *IEEE J. Selec. Topics Quantum Elec.*, vol. 17, no. 4, Jul./Aug. 2011.
- 536.S. Plissard, G. Larrieu, X. Wallart, and P. Caroff, High yield of self-catalyzed GaAs nanowire arrays grown on silicon via gallium droplet positioning, *Nanotechnol.*, 22, 275602, 2011.
- 537.J. Paek, M. Yamaguchi, and H. Amano, MBE-VLS growth of catalyst-free III-V axial heterostructure nanowires on (111) Si substrate, *J. Cryst. Growth*, 323, 315-318, 2011.
- 538.E. Galopin, L. Largeau, G. Patriarche, L. Travers, F. Glas, and J. C. Harmand, Morphology of self-catalyzed GaN nanowires and chronology of their formation by molecular beam epitaxy, *Nanotechnol.*, 22, 245606, 2011.

- 539.V. Consonni, M. Knelangen, A. Trampert, L. Geelhaar, and H. Riechert, Nucleation and coalescence effects on the density of self-induced GaN nanowires grown by molecular beam epitaxy, *Appl. Phys. Lett.*, 98, 071913, 2011.
- 540.S. Ambrosini, M. Fanetti, V. Grillo, A. Franciosi, and S. Rubini, Self-catalyzed GaAs nanowire growth on Si-treated GaAs (100) substrates, *J. Appl. Phys.*, 109, 094306, 2011.
- 541.B. Ketterer, M. Heiss, E. Uccelli, J. Arbiol, and A. F. i Morral, Untangling the electronic band structure of wurtzite GaAs nanowires by resonant Raman spectroscopy, *ACS Nano*, vol. 5, no. 9, 7585-7592, 2011.
- 542.T. Rieger, S. Heiderich, S. Lenk, M. I. Lepsa, and D. Grutzmacher, Ga-assisted MBE growth of GaAs nanowires using thin HSQ layer, *J. Cryst. Growth*, 353, 39-46, 2012.
- 543.U. Jahn, J. Lahnemann, C. Pfuller, O. Brandt, S. Breuer, B. Jenichen, M. Ramsteiner, L. Geelhaar, and H. Riechert, Luminescence of GaAs nanowires consisting of wurtzite and zinc-blende segments, *Phys. Rev. B*, 85, 045323, 2012.
- 544.Y. H. Kim, D. W. Park, S. J. Lee, K. Kim, and Y. C. Park, Hexagonal and pentagonal shapes of self-catalyzed one-dimensional GaAs nanostructures: shape dependence of the phase evolutions, *Appl. Phys. Lett.*, 100, 133112, 2012.
- 545.K. Hestroffer, C. Leclere, V. Cantelli, C. Bougerol, H. Renevier, and B. Daudin, *In situ* study of self-assembled GaN nanowires nucleation on Si (111) by plasma-assisted molecular beam epitaxy, *Appl. Phys. Lett.*, 100, 212107, 2012.
- 546.V. G. Dubrovskii, V. Consonni, L. Geelhaar, A. Trampert, and H. Riechert, Scaling growth kinetics of self-induced GaN nanowires, *Appl. Phys. Lett.*, 100, 153101, 2012.
- 547.F. Limbach, R. Caterino, T. Gotschke, T. Stoica, R. Calarco, L. Geelhaar, and H. Riechert, The influence of Mg doping on the nucleation of self-induced GaN nanowires, *AIP Advances*, 2, 012157, 2012.
- 548.A. M. Munshi, D. L. Dheeraj, V. T. Fauske, D. -C. Kim, A. T. J. van Helvoort, B. -O. Fimland, and H. Weman, Vertically aligned GaAs nanowires on graphite and few-layer graphene: generic model and epitaxial growth, *Nano Lett.*, 12, 4570-4576, 2012.
- 549.P. Corfdir, B. Van Hattem, E. Uccelli, A. F. i Morral, and R. T. Phillips, Charge carrier generation, relaxation, and recombination in polytypic GaAs nanowires studied by photoluminescence excitation spectroscopy, *Appl. Phys. Lett.*, 103, 133109, 2013.
- 550.C. Somaschini, S. Bietti, A. Trampert, U. Jahn, C. Hauswald, H. Riechert, S. Sanguinetti, and L. Geelhaar, Control over the number density and diameter of GaAs nanowires on Si (111) mediated by droplet epitaxy, *Nano Lett.*, 13, 3607-3613, 2013.
- 551.T. Rieger, M. I. Lepsa, T. Schapers, and D. Grutzmacher, Controlled wurtzite inclusions in self-catalyzed zinc blende III-V semiconductor nanowires, *J. Cryst. Growth*, 378, 506-510, 2013.
- 552.A. M. Munshi, D. L. Dheeraj, J. Todorovic, A. T. J. van Helvoort, H. Weman, and B. -O. Fimland, Crystal phase engineering in self-catalyzed GaAs and GaAs/GaAsSb nanowires grown on Si (111), *J. Cryst. Growth*, 372, 163-169, 2013.
- 553.A. M. Graham, P. Corfdir, M. Heiss, S. Conesa-Boj, E. Uccelli, A. F. i Morral, and R. T. Phillips, Exciton localization mechanisms in wurtzite/zinc-blende GaAs nanowires, *Phys. Rev. B*, 87, 125304, 2013.

554. P. Plochocka, A. A. Mitoglu, D. K. Maude, G. L. J. A. Rikken, A. G. del Aguila, P. C. M. Christianen, P. Kacman, and H. Shtrikman, High magnetic field reveals the nature of excitons in a single GaAs/AlAs core/shell nanowire, *Nano Lett.*, 13, 2442-2447, 2013.
555. D. Rudolph, L. Schweickert, S. Morkotter, L. Hanschke, S. Hertenberger, M. Bichler, G. Koblmüller, G. Abstreiter, and J. J. Finley, Probing the trapping and thermal activation dynamics of excitons at single twin defects in GaAs-AlGaAs core-shell nanowires, *New J. Phys.*, 15, 113032, 2013.
556. C. G. Nunez, A. F. Brana, J. L. Pau, D. Ghita, B. J. Garcia, G. Shen, D. S. Wilbert, S. M. Kim, and P. Kung, Pure zincblende GaAs nanowires grown by Ga-assisted chemical beam epitaxy, *J. Cryst. Growth*, 372, 205-212, 2013.
557. G. Priante, S. Ambrosini, V. G. Dubrovskii, A. Franciosi, and S. Rubini, Stopping and resuming at will the growth of GaAs nanowires, *Cryst. Growth Des.*, 13, 3976-3984, 2013.
558. M. Sobanska, K. Klosek, J. Borysiuk, S. Kret, G. Tchutchulasvili, S. Gieraltowska, and Z. R. Zytewicz, Enhanced catalyst-free nucleation of GaN nanowires on amorphous Al₂O₃ by plasma-assisted molecular beam epitaxy, *J. Appl. Phys.*, 115, 043517, 2014.
559. K. H. Yoen, E. H. Lee, S. Y. Kim, T. E. Park, M. H. Bae, and J. D. Song, Growth of catalyst-free GaAs nanowire with As pulse injection for full zinc-blende structure, *Current Appl. Phys.*, 14, 366-370, 2014.
560. F. Matteini, G. Rutuncuoglu, D. Ruffer, E. Alarcon-Llado, A. F. i Morral, Ga-assisted growth of GaAs nanowires on silicon, comparison of surface SiO_x of different nature, *J. Cryst. Growth*, 404, 246-255, 2014.
561. G. Priante, G. Patriarche, F. Oehler, F. Glas, and J. -C. Harmand, Abrupt GaP/GaAs interfaces in self-catalyzed nanowires, *Nano Lett.*, xxx, xxx-xxx, xxxx.
562. T. V. Hakkarainen, A. Schramm, J. Makela, P. Laukkanen, and M. Guina, Lithography-free oxide patterns as templates for self-catalyzed growth of highly uniform GaAs nanowires on Si (111), *Nanotechnol.*, 26, 275301, 2015.
563. V. G. Dubrovskii, T. Xu, A. Diaz Alvarez, S. R. Plissard, P. Caroff, F. Glas, and B. Grandidier, Self-equilibration of the diameter of Ga-catalyzed GaAs nanowires, *Nano Lett.*, 15, 5580-5584, 2015.
564. R. L. Barns, W. C. Ellis, Whisker crystals of gallium arsenide and gallium phosphide grown by the vapor-liquid-solid mechanism, *J. Appl. Phys.*, 36, 2296, 1965.
565. J. R. Arthur, J. J. Lepore, GaAs, GaP, and GaAsP epitaxial films grown by molecular beam deposition, *J. Vac. Sci. Tech.*, 6, 545, 1969.
566. J. D. Klein, R. D. Herrick, D. Palmer, and M. J. Sailor, Electrochemical fabrication of cadmium chalcogenide microdiode arrays, *Chem. Mater.*, 5, 902-904, 1993.
567. C. R. Martin, Nanomaterials—A membrane-based synthetic approach, *Science*, vol. 266, no. 5193, pp. 1961-1966, Dec. 1994.
568. C. R. Martin, Template synthesis of electronically conductive polymer nanostructures, *Acc. Chem. Res.*, 28, 61-68, 1995.
569. H. Masuda, K. Fukuda, Ordered metal nanohole arrays made by a two-step replication of honeycomb structures of anodic alumina, *Science*, vol. 268, no. 5216, pp. 1466-1468, Jun. 1995.

570. G. S. Cheng, L. D. Zhang, Y. Zhu, G. T. Fei, L. Li, C. M. Mo, and Y. Q. Mao, Large-scale synthesis of single crystalline gallium nitride nanowires, *Appl. Phys. Lett.*, 75, 2455, 1999.
571. G. S. Cheng, S. H. Chen, X. G. Zhu, Y. Q. Mao, and L. D. Zhang, Highly ordered nanostructures of single crystalline GaN nanowires in anodic alumina membranes, *Mater. Sci. Eng., A* 286, 165-168, 2000.
572. W. Han, S. Fan, Q. Li, and Y. Hu, Synthesis of gallium nitride nanorods through a carbon nanotube confined reaction, *Science*, vol. 277, no. 5330, pp. 1287-1289, Aug. 1997.
573. Y. J. Hong, W. H. Lee, Y. Wu, R. S. Ruoff, and T. Fukui, van der Waals epitaxy of InAs nanowires vertically aligned on single-layer graphene, *Nano Lett.*, 12, 1431-1436, 2012.
574. S. T. Lee, N. Wang, Y. F. Zhang, and Y. H. Tang, Oxide-assisted semiconductor nanowire growth, *MRS Bulletin*, vol. 24, no. 08, pp. 36-42, Aug. 1999.
575. S. T. Lee, Y. F. Zhang, N. Wang, Y. H. Tang, I. Bello, C. S. Lee, and Y. W. Chung, Semiconductor nanowires from oxides, *J. Mater. Res.*, vol. 14, no. 12, pp. 4503-4507, Dec. 1999.
576. R. Q. Zhang, Y. Lifshitz, and S. T. Lee, Oxide-assisted growth of semiconducting nanowires, *Adv. Mater.*, 15, no. 7-8, Apr. 2003.
577. H. D. Park, S. M. Prokes, M. E. Twigg, R. C. Cammarata, and A. -C. Gaillot, Si-assisted growth of InAs nanowires, *Appl. Phys. Lett.*, 89, 223125, 2006.
578. W. Shi, Y. Zheng, N. Wang, C. Lee, and S. Lee, A general synthetic route to III-V compound semiconductor nanowires, *Adv. Mater.*, 13, no. 8, Apr. 2001.
579. W. S. Shi, Y. F. Zheng, N. Wang, C. S. Lee, and S. T. Lee, Oxide-assisted growth and optical characterization of gallium-arsenide nanowires, *Appl. Phys. Lett.*, 78, 3304, 2001.
580. C. Tang, Y. Bando, Z. Liu, and D. Golberg, Synthesis and structure of InP nanowires and nanotubes, *Chem. Phys. Lett.*, 376, 676-682, 2003.
581. T. Hamano, H. Hirayama, and Y. Aoyagi, New technique for fabrication of two-dimensional photonic bandgap crystals by selective epitaxy, *Jpn. J. Appl. Phys.*, vol. 36, part 2, no. 3A, pp. L286-L288, March 1997.
582. J. Takeda, M. Akabori, J. Motohisa, T. Fukui, Formation of $\text{Al}_x\text{Ga}_{1-x}\text{As}$ periodic array of micro-hexagonal pillars and air holes by selective area MOVPE, *Appl. Surf. Sci.*, 190, 236-241, 2002.
583. M. Akabori, J. Takeda, J. Motohisa, and T. Fukui, InGaAs nano-pillar array formation on partially masked InP (111)B by selective area metal-organic vapor phase epitaxial growth for two-dimensional photonic crystal application, *Nanotechnol.*, 14, 1071-1074, 2003.
584. J. Motohisa, J. Noborisaka, J. Takeda, M. Inari, and T. Fukui, Catalyst-free selective-area MOVPE of semiconductor nanowires on (111)B oriented substrates, *J. Cryst. Growth*, 272, 180-185, 2004.
585. J. Motohisa, J. Takeda, M. Inari, J. Noborisaka, and T. Fukui, Growth of GaAs/AlGaAs hexagonal pillars on GaAs (111)B surfaces by selective-area MOVPE, *Phys. E*, 23, 298-304, 2004.
586. M. Inari, J. Takeda, J. Motohisa, and T. Fukui, Selective area MOVPE growth of InP and InGaAs pillar structures for InP-based two-dimensional photonic crystals, *Phys. E*, 21, 620-624, 2004.

- 587.J. Noborisaka, J. Motohisa, and T. Fukui, Catalyst-free growth of GaAs nanowires by selective-area metalorganic vapor-phase epitaxy, *Appl. Phys. Lett.*, 86, 213102, 2005.
- 588.P. Mohan, J. Motohisa, and T. Fukui, Controlled growth of highly uniform, axial/radial direction-defined, individually addressable InP nanowire arrays, *Nanotechnol.*, 16, 2903-2907, 2005.
- 589.K. Romioka, P. Mohan, J. Noborisaka, S. Hara, J. Motohisa, T. Fukui, Growth of highly uniform InAs nanowire arrays by selective-area MOVPE, *J. Cryst. Growth*, 298, 644-647, 2007.
- 590.K. Ikejiri, T. Sato, H. Yoshida, K. Hiruma, J. Motohisa, S. Hara, and T. Fukui, Growth characteristics of GaAs nanowires obtained by selective area metal-organic vapour-phase epitaxy, *Nanotechnol.* 19, 265604, 2008.
- 591.H. Paetzelt, V. Gottschalch, J. Bauer, G. Benndorf, G. Wagner, Selective-area growth of GaAs and InAs nanowires—home- and heteroepitaxy using SiN_x templates, *J. Cryst. Growth*, 310, 5093-5097, 2008.
- 592.S. Hertenberger, D. Rudolph, M. Bichler, J. J. Finley, G. Abstreiter, and G. Koblmuller, Growth kinetics in position-controlled an dcatalyst-free InAs nanowire arrays on Si (111) grown by selective area molecular beam epitaxy, *J. Appl. Phys.*, 108, 114316, 2010.
- 593.K. Toioka, T. Tanaka, S. Hara, K. Hiruma, and T.Fukui, III-V nanowires on Si substrate: selective-area growth and device applications, *IEEE J. Sel. Top. Quantum Electron.*, vol. 17, no. 4, Jul. /Aug. 2011.
- 594.P. D. Kanungo, H. Schmid, M. T. Bjork, L. M. Gignac, C. Breslin, J. Bruley, C. D. Bessire, and H. Riel, Selective area growth of III-V nanowires and their heterostructures on silicon in a nanotube template: towards monolithic integration of nano-devices, *Nanotechnol.*, 24, 225304, 2013.
- 595.D. Whang, S. Jin, and C. M. Lieber, Nanolithography using hierarchically assembled nanowire masks, *Nano Lett.*, vol. 3, no. 7, pp. 951-954, 2003.
- 596.D. Whang, S. Jin, Y. Wu, and C. M. Lieber, Large-scale hierarchical organization of nanowire arrays for integrated nanosystems, *Nano Lett.*, vol. 3, no. 9, pp. 1255-1259, 2003.
- 597.Y. Huang, X. Duan, Q. Wei, and C. M. Lieber, Directed assembly of one-dimensional nanostructures into functional networks, *Science*, vol. 291, pp. 630-633, 2001.
- 598.V. A. Shchukin, N. N. Ledentsov, and D. Bimberg, *Epitaxy of nanostructures*, Springer, 2003.
- 599.G.B. Stringfellow, *Organometallic vapor-phase epitaxy: Theory and practice*, 2nd Edition, Academic Press, 1999.
- 600.T. J. Mountziaris, K. F. Jensen, Gas-phase and surface reaction mechanisms in MOCVD of GaAs with trimethyl-gallium and arsine, *J. Electrochem. Soc.*, vol. 138, no. 8, pp. 2426-2439, Aug. 1991.
- 601.K. Reuter, M. Scheffler, First-principles kinetic Monte Carlo simulations for heterogeneous catalysis: Application to the CO oxidation at RuO₂(110), *Phys. Rev. B*, 73, 045433, 2006.
- 602.H. Moffat, K. F. Jensen, Complex flow phenomena in MOCVD reactors I. horizontal reactors, *J. Cryst. Growth*, 77, 108-119, 1986.

- 603.J. Ouazzani, F. Rosenberger, Three-dimensional modelling of horizontal chemical vapor deposition I. MOCVD at atmospheric pressure, *J. Cryst. Growth*, 100, 545-576, 1990.
- 604.D. I. Fotiadis, M. Boekholt, K. F. Jensen, and W. Richter, Flow and heat transfer in CVD reactors: comparison of Raman temperature measurements and finite element model predictions, *J. Cryst. Growth*, 100, 577-599, 1990.
- 605.D. I. Fotiadis, K. F. Jensen, Thermophoresis of solid particles in horizontal chemical vapor deposition reactors, *J. Cryst. Growth*, 102, 743-761, 1990.
- 606.K. F. Jensen, D. I. Fotiadis, T. J. Mountziaris, Detailed models of the MOVPE process, *J. Cryst. Growth*, 107, 1-11, 1991.
- 607.L. R. Black, I. O. Clark, B. A. Fox, and W. A. Jesser, MOCVD of GaAs in a horizontal reactor: modeling and growth, *J. Cryst. Growth*, 109, 241-245, 1991.
- 608.M. Dauelsberg, C. Martin, H. Protzmann, A. R. Boyd, E. J. Thrush, J. Kappeler, M. Heuken, R. A. Talalaev, E. V. Yakovlev, and A. V. Kondratyev, Modeling and process design of III-nitride MOVPE at near-atmospheric pressure in close coupled showerhead and planetary reactors, *J. Cryst. Growth*, 298, 418-424, 2007.
- 609.Y. -C. Chuang, C. -T. Chen, Mathematical modeling and optimal design of an MOCVD reactor for GaAs film growth, *J. Taiwan Instit. Chem. Engin.*, 45, 254-267, 2014.
- 610.L. Xu, Q. Huang, Growth process modeling of III-V nanowire synthesis via selective area metal-organic chemical vapor deposition, *IEEE Trans. Nanotechnol.*, vol. 13, no. 6, Nov. 2014.
- 611.C. Theodoropoulos, N. K. Ingle, and T. J. Mountziaris, Computational studies of the transient behavior of horizontal MOVPE reactors, *J. Cryst. Growth*, 170, 72-76, 1997.
- 612.R. A. Talalaev, E. V. Yakovlev, S. Yu. Karpov, and Yu. N. Makarov, On low temperature kinetic effects in metal-organic vapor phase epitaxy of III-V compounds, *J. Cryst. Growth*, 230, 232-238, 2001.
- 613.I. Im, H. J. Oh, M. Sugiyama, Y. Nakano, and Y. Shimogaki, Fundamental kinetics determining growth rate profiles of InP and GaAs in MOCVD with horizontal reactor, *J. Cryst. Growth*, 261, 214-224, 2004.
- 614.R. Onitsuka, M. Sugiyama, Y. Shimogaki, Y. Nakano, Reactor-scale profile of group-V composition of InGaAsP studied by fluid dynamics simulation and *in situ* analysis of surface kinetics, *J. Cryst. Growth*, 310, 3042-3048, 2008.
- 615.D. I. Fotiadis, A. M. Kremer, D. R. McKenna, and K. F. Jensen, Complex flow phenomena in vertical MOCVD reactors: effects on deposition uniformity and interface abruptness, *J. Cryst. Growth*, 85, 154-164, 1987.
- 616.D. I. Fotiadis, S. Kieda, and K. F. Jensen, Transport phenomena in vertical reactors for metalorganic vapor phase epitaxy I. effects of heat transfer characteristics, reactor geometry, and operating conditions, *J. Cryst. Growth*, 102, 441-470, 1990.
- 617.C. Theodoropoulos, T. J. Mountziaris, H. K. Moffat, and J. Han, Design of gas inlets for the growth of gallium nitride by metalorganic vapor phase epitaxy, *J. Cryst. Growth*, 217, 65-81, 2000.
- 618.R. P. Pawlowski, C. Theodoropoulos, A. G. Salinger, T. J. Mountziaris, H. K. Moffat, J. N. Shadid, and E. J. Thrush, Fundamental models of the metalorganic vapor-phase epitaxy of gallium nitride and their use in reactor design, *J. Cryst. Growth*, 221, 622-628, 2000.

- 619.L. Kadinski, V. Merai, A. Parekh, J. Ramer, E. A. Armour, R. Stall, A. Gurary, A. Galyukov, and Yu. Makarov, Computational analysis of GaN/InGaN deposition in MOCVD vertical rotating disk reactors, *J. Cryst. Growth*, 261, 175-181, 2004.
- 620.B. Mitrovic, A. Gurary, and W. Quinn, Process conditions optimization for the maximum deposition rate and uniformity in vertical rotating disc MOCVD reactors based on CFD modeling, *J. Cryst. Growth*, 303, 323-329, 2007.
- 621.R. A. Granger, *Fluid mechanics*, Dover edition, Dover Pub. Inc., 1995.
- 622.A. Ern, V. Giovangigli, and M. D. Smooke, Numerical study of a three-dimensional chemical vapor deposition reactor with detailed chemistry, *J. Comput. Phys.*, 126, 21-39, 1996.
- 623.L. J. Giling, Gas flow patterns in horizontal, *J. Electrochem. Soc.*, 129, 634, 1982.
- 624.O. C. Zienkiewicz, R. L. Taylor, *The finite element method*, Vol. 1, The basis, 5th edition, Butterworth Heinemann, 2000.
- 625.O. C. Zienkiewicz, R. L. Taylor, *The finite element method*, Vol. 3, Fluid dynamics, 5th edition, Butterworth Heinemann, 2000.
- 626.D. E. Rosner, *Transport processes in chemically reacting flow systems*, Dover edition, Dover Pub. Inc., 2000.
- 627.A. G. Salinger, J. N. Shadid, S. A. Hutchinson, G. L. Hennigan, K. D. Devin, and H. K. Moffat, Massively parallel computation of 3D flow and reactions in chemical vapor deposition reactors, SAND97-3092, Dec. 1997.
- 628.J. N. Shadid, A. G. Salinger, R. P. Pawlowski, P. T. Lin, G. L. Hennigan, R. S. Tuminaro, and R. B. Lehoucq, Large-scale stabilized FE computational analysis of nonlinear steady-state transport/reaction systems, *Comput. Methods Appl. Mech. Engrg.*, 195, 1846-1871, 2006.
- 629.J. N. Shadid, H. K. Moffat, S. A. Hutchinson, G. L. Hennigan, K. D. Devine, and A. G. Salinger, MPSalsa, A finite element computer program for reacting flow problems, Part 1-Theoretical development, SAND95-2752, May 1996; A. Salinger, K. Devine, G. Hennigan, H. Moffat, S. Hutchinson, and J. Shadid, MPSalsa, A finite element computer program for reacting flow problems, Part 2-User's guide, SAND96-2331, Oct. 1996.
- 630.S. Lanteri, Parallel solutions of compressible flows using overlapping and non-overlapping mesh partitioning strategies, *Parallel Comp.*, 22, 943-968, 1996.
- 631.M.E. Coltrin, F.J. Kee, G.H. Evans, E. Meeks, F.M. Rupley, J.F. Grcar, Sandia National Laboratories Technical Report, SAND87-8248, 1987.
- 632.R. J. Kee, G. Dixon-Lewis, J. Warnatz, M. E. Coltrin, J. A. Miller, and H. K. Moffat, A FORTRAN computer code package for the evaluation of gas-phase, multicomponent transport properties, SAND86-8246B, Mar. 1998.
- 633.Transport: A software package for the evaluation of gas-phase, multicomponent, transport properties, CHEMKIN, Sep. 2000.
- 634.R. J. Kee, G. Dixon-Lewis, J. Warnatz, M. E. Coltrin, and J. A. Miller, A FORTRAN computer package for the evaluation of gas-phase multicomponent transport properties, SAND86-8246, 1986.
- 635.J. R. Arthur Jr. Interaction of Ga and As₂ molecular beams with GaAs surfaces, *J. Appl. Phys.*, 39, 4032, 1968.
- 636.A. Y. Cho, Film deposition by molecular-beam techniques, *J. Vac. Sci. Tech.*, 8, S31, 1971.
- 637.A. Y. Cho, GaAs epitaxy by a molecular beam method: Observations of surface structure on the (001) face, *J. Appl. Phys.*, 42, 2074, 1971.

- 638.A. Y. Cho, J. R. Arthur, Molecular beam epitaxy, *Prog. Solid-State Chem.*, vol. 10, part 3, pp. 157-191, 1975.
- 639.J. Ristic, E. Calleja, S. Rernandez-Garrido, L. Cerutti, A. Trampert, U. Jahn, and K. H. Ploog, On the mechanisms of spontaneous growth of III-nitride nanocolumns by plasma-assisted molecular beam epitaxy, *J. Crys. Growth*, 310, 4035-4045, 2008.
- 640.N. Al-Sarraf, J. T. Stuckless, and D. A. King, Direct measurement of potassium-promoted change in heat of adsorption of CO on Ni{100}, *Nature*, vol. 360, pp. 243-245, Nov. 1992.
- 641.J. T. Stuckless, N. Al-Sarraf, C. Warnaby, and D. A. King, Calorimetric heats of adsorption for CO on nickel single crystal surfaces, *J. Chem. Phys.*, 99, 2202, 1993.
- 642.D. A. King, Thermal desorption from metal surfaces: A review, *Surf. Sci.*, 47, 384-402, 1975.
- 643.P. A. Redhead, Thermal desorption of gases, *Vacuum*, 12, pp. 203-211, 1962.
- 644.E. Bauer, F. Bonczek, H. Poppa, and G. Todd, Thermal desorption of metals from tungsten single crystal surfaces, *Surf. Sci.*, 53, 87-109, 1975.
- 645.S.C. Lee, L. R. Dawson, S. R. J. Brueck, and A. Stintz, Heteroepitaxial selective growth of $\text{In}_x\text{Ga}_{1-x}\text{As}$ on SiO_2 -patterned GaAs(001) by molecular beam epitaxy, *J. Appl. Phys.*, 96, 4856, 2004.
- 646.M. Hei, E. Riedlberger, D. Spirkoska, M. Bichler, G. Abstreiter, A. F. i Morral, Growth mechanisms and optical properties of GaAs-based semiconductor microstructures by selective area epitaxy, *J. Crys. Growth*, 310, 1049-1056, 2008.
- 647.T. Martensson, M. Borgstrom, W. Seifert, B. J. Ohlsson, and L. Samuelson, Fabrication of individually seeded nanowire arrays by vapour-liquid-solid growth, *Nanotechnol.*, 14, 1255-1258, 2003.
- 648.L. E. Jensen, M. T. Bjork, S. Jeppesen, A. I. Persson, B. J. Ohlsson, and L. Samuelson, Role of surface diffusion in chemical beam epitaxy of InAs nanowires, *Nano Lett.*, vol. 4, no. 10, 1961-1964, 2004.
- 649.T. Martensson, P. Carlberg, M. Borgstrom, L. Montelius, W. Seifert, and L. Samuelson, Nanowire arrays defined by nanoimprint lithography, *Nano Lett.*, vol. 4, no. 4, 699-702, 2004.
- 650.H. Schiff, Nanoimprint lithography: An old story in modern times? A review, *J. Vacu. Sci. Tech. B*, 26, 458, 2008.
- 651.G. V. Jayanthi, S. C. Zhang, and G. L. Messing, Modeling of solid particle formation during solution aerosol thermolysis, The evaporation stage, *Aerosol Sci. Tech.*, 19, 478-490, 1993.
- 652.L. Nanai, I. Hevesi, F. V. Bunkin, B. S. Lukyanchuk, M. R. Brook, G. A. Shafeev, D. A. Jelski, Z. C. Wu, and T. F. George, Laser-induced metal deposition on semiconductors from liquid electrolytes, *Appl. Phys. Lett.*, 54, 736, 1989.
- 653.H. G. Scheibel, J. Porstendorfer, Generation of monodisperse Ag- and NaCl-aerosols with particle diameters between 2 and 300 nm, *J. Aerosol Sci.*, vol. 14, no. 2, pp. 113-126, 1983.
- 654.S. Link, Z. L. Wang, and M. A. El-Sayed, Alloy formation of gold-silver nanoparticles and the dependence of the plasmon absorption on their composition, *J. Phys. Chem. B*, 103, 3529-3533, 1999.
- 655.M. H. Magnusson, B. J. Ohlsson, M. T. Bjork, K. A. Dick, M. T. Borgstrom, K. Deppert, and L. Samuelson, Semiconductor nanostructures enabled by aerosol technology, *Front. Phys.*, 9, 3, 398-418, 2014.

- 656.B. O. Meuller, M. E. Messing, D. L. J. Engberg, A. M. Jansson, L. I. M. Johansson, S. M. Norlen, N. Tureson, K. Deppert, Review of spark discharge generators for production of nanoparticle aerosols, *Aerosol Sci. Tech.*, 46, 11, 1256-1270, 2012.
- 657.D. V. Ralapin, A. L. Rogach, M. Haase, and H. Weller, Evolution of an ensemble of nanoparticles in a colloidal solution: theoretical study, *J. Phys. Chem. B*, 105, 12278-12285, 2001.
- 658.A. L. Rogach, D. V. Talapin, E. V. Shevchenko, A. Kornowski, M. Haase, and H. Weller, Organization of matter on different size scales: monodisperse nanocrystals and their superstructures, *Adv. Funct. Mater.*, 12, no. 10, 653, Oct. 2002.
- 659.I. M. Lifshitz, V. V. Slyozov, The kinetics of precipitation from supersaturated solid solutions, *J. Phys. Chem. Solids*, vol. 19, no. 1/2, 35, 1961.
- 660.M. Hillert, O. Hunderi, N. Ryum, T. O. Sætre, A comment on the Lifshitz-Slyozov-Wagner (L-S-W) theory of particle coarsening, *Scripta Metall.*, vol. 23, 11, pp. 1979-1981, Nov. 1989.
- 661.T. H. Tsang, J. R. Brock, On Ostwald ripening, *Aerosol Sci. Tech.*, 3, 3, 283-292, 1984.
- 662.G. W. Greenwood, The growth of dispersed precipitates in solutions, *ACTA Metall.*, vol. 4, p. 243, May 1956.
- 663.E. O. Knutson, K. T. Whitby, Aerosol classification by electric mobility: apparatus, theory, and applications, *Aerosol Sci.*, vol. 6, pp. 443-451, 1975.
- 664.P. Wynblatt, N. A. Gjostein, Particle growth in model supported metal catalysts—I. Theory, *ACTA Metall.*, vol. 24, pp. 1165-1174, 1976.
- 665.K. Deppert, M. H. Magnusson, L. Samuelson, J. -O. Malm, C. Svensson, and J. -O. Bovin, Size-selected nanocrystals of III-V semiconductor materials by the aerotaxy method, *J. Aerosol Sci.*, vol. 29, no. 5/6, pp. 737-748, 1998.
- 666.F. J. Romay, S. S. Takagaki, D. Y. H. Pui, and B. Y. H. Liu, Thermophoretic deposition of aerosol particles in turbulent pipe flow, *J. Aerosol Sci.*, vol. 29, no. 8, pp. 943-959, 1998.
- 667.B. Y. H. Liu, D. Y. H. Pui, Electrical neutralization of aerosols, *Aerosol Sci.*, vol. 5, pp. 465-472, 1974.
- 668.B. Y. H. Liu, D. Y. H. Pui, Equilibrium bipolar charge distribution of aerosols, *J. Coll. Interface Sci.*, vol. 49, no. 2, Nov. 1974.
- 669.T. J. Krinke, H. Fissan, K. Deppert, M. H. Magnusson, and L. Samuelson, Positioning of nanometer-sized particles on flat surfaces by direct deposition from the gas phase, *Appl. Phys. Lett.*, 78, 3708, 2001.
- 670.W. W. Mullins, R. F. Sekerka, Morphological stability of a particle growing by diffusion or heat flow, *J. Appl. Phys.*, 34, 323, 1963.
- 671.W. D. Kaplan, D. Chatain, P. Wynblatt, W. C. Carter, A review of wetting versus adsorption, complexions, and related phenomena: the rosetta stone of wetting, *J. Mater. Sci.*, 48, 5681-5717, 2013.
- 672.H. Yonezu, Control of structural defects in group III-V-N alloys grown on Si, *Semicond. Sci. Technol.*, 17, pp. 762-768, 2002.
- 673.D. W. Hoffman, J. W. Cahn, A vector thermodynamics for anisotropic surfaces I. Fundamentals and application to plane surface junctions, *Surf. Sci.*, 31, 368-388, 1972.
- 674.J. W. Cahn, D. W. Hoffman, A vector thermodynamics for anisotropic surfaces II. Curved and faceted surfaces, *ACTA Metall.*, vol. 22, 1205, Oct. 1974.

- 675.J. E. Taylor, J. W. Cahn, and C. A. Handwerker, Overview no. 98 I. Geometric models of crystal growth, *ACTA Metall. Mater.*, vol. 40, no. 7, pp. 1443-1474, 1992.
- 676.J. E. Taylor, Overview no. 98, II. Mean curvature and weighted mean curvature, *ACTA Metall. Mater.*, vol. 40, no. 7, pp. 1475-1485, 1992.
- 677.T. Akiama, K. Nakamura, and T. Ito, Structural stability and electronic structures of InP nanowires: Role of surface dangling bonds on nanowire facets, *Phys. Rev. B*, 73, 235308, 2006.
- 678.M. Galicka, M. Bukala, R. Buczko, and P. Kacman, Modelling the structure of GaAs and InAs nanowires, *J. Phys.: Condens. Matter*, 20, 454226, 2008.
- 679.M. C. Plante, R. R. LaPierre, Control of GaAs nanowire morphology and crystal structure, *Nanotechnol.*, 19, 495603, 2008.
- 680.N. Skold, J. B. Wagner, G. Karlsson, T. Hernan, W. Seifert, M. -E. Pistol, and L. Samuelson, Phase segregation in AlInP shells on GaAs nanowires, *Nano Lett.*, vol. 6, no. 12, 2743-2747, 2006.
- 681.H. Shtrikman, R. Popovitz-Biro, A. Kretinin, L. Houben, M. Heiblum, M. Bukala, M. Galicka, R. Buczko, and P. Kacman, Method for suppression of stacking faults in wurtzite III-V nanowires, *Nano Lett.*, vol. 9, no. 4, 1506-1510, 2009.
- 682.J. Johansson, J. Bolinsson, M. Ek, P. Caroff, and K. A. Dick, Combinatorial approaches to understanding polytypism in III-V nanowires, *ACS Nano*, vol. 6, no. 7, pp. 6142-6149, 2012.
- 683.D. L. Dheeraj, G. Patriarche, H. Zhou, T. B. Hoang, A. F. Moses, S. Gronberg, A. T. J. van Helvoort, B. -O. Fimland, and H. Weman, Growth and characterization of wurtzite GaAs nanowires with defect-free zinc blende GaAsSb inserts, *Nano Lett.*, vol. 8, no. 12, 4459-4463, 2008.
- 684.D. L. Dheeraj, G. Patriarche, L. Largeau, H. L. Zhou, A. T. J. van Helvoort, F. Glas, J. C. Harmand, B. O. Fimland, and H. Weman, Zinc blende GaAsSb nanowires grown by molecular beam epitaxy, *Nanotechnol.*, 19, 275605, 2008.
- 685.A. Belabbes, C. Panse, J. Furthmuller, and F. Bechstedt, Electronic bands of III-V semiconductor polytypes and their alignment, *Phys. Rev. B*, 86, 075208, 2012.
- 686.K. L. Kavanagh, Misfit dislocations in nanowires heterostructures, *Semicond. Sci. Technol.*, 25, 024006, 2010.
- 687.R. F. Davis, Substrates and epitaxial deposition processes for group III-nitride thin films and power device heterostructures, *MRS Bulletin*, vol. 40, pp. 406-411, May 2015.
- 688.S. D. Hersee, D. Zubia, X. Sun, R. Bommena, M. Fairchild, S. Zhang, D. Burckel, A. Frauenglass, and S. R. J. Brueck, Nanoheteroepitaxy for the integration of highly mismatched semiconductor materials, *IEEE J. Quant. Electron.*, vol. 38, no. 8, Aug. 2002.
- 689.Y. S. Touloukian, R. K. Kirby, E. R. Taylor, and T. Y. R. Lee, Thermophysical properties of matter-The TPRC Data Series, vol. 13, Thermal Expansion-Nonmetallic Solids, Jan. 1977.
- 690.A. A. Maradudin, Thermal expansion and phonon frequency shifts, *Phys. Stat. Sol.*, 2, 1493, 1962.
- 691.Y. Zhang, M. Aagesen, J. V. Holm, H. I. Jorgensen, J. Wu, and H. Liu, Self-catalyzed GaAsP nanowires grown on silicon substrates by solid-source molecular beam epitaxy, *Nano Lett.*, 13, pp. 3897-3902, 2013.
- 692.Z. Wang, B. Tian, M. Paladugu, M. Pantouvaki, N. Le Thomas, C. Merckling, W. Guo, J. Dekoster, J. Van Campenhout, P. Absil, and D. Van Thourhout, Polytypic

- InP nanolaser monolithically integrated on (001) silicon, *Nano Lett.*, 13, pp. 5063-5069, 2013.
- 693.S. Conesa-Boj, D. Kriegner, X. Han, S. Plissard, X. Wallart, J. Stangl, A. F. i Morral, and P. Caroff, Gold-free ternary III-V antimonide nanowire arrays on silicon: Twin-free down to the first binary, *Nano Lett.*, 14, pp. 326-332, 2014.
 - 694.J. V. Holm, H. I. Jorgensen, P. Krogstrup, J. Nygard, H. Liu, and M. Aagesen, Surface-passivated GaAsP single-nanowire solar cells exceeding 10% efficiency grown on silicon, *Nature Commun.*, 4, 1498, Feb. 2013.
 - 695.E. Dimakis, U. Jahn, M. Ramsteiner, A. Tahraoui, J. Grandal, X. Kong, O. Marquardt, A. Trampert, H. Riechert, and L. Geelhaar, Coaxial multishell (In,Ga)As/GaAs nanowires for near-infrared emission on Si substrates, *Nano Lett.*, 14, pp. 2604-2609, 2014.
 - 696.J. R. Lang, J. Faucher, S. Tomasulo, K. N. Yaung, and M. L. Lee, Comparison of GaAsP solar cells on GaP and GaP/Si, *Appl. Phys. Lett.*, 103, 092102, 2013.
 - 697.K. Tomioka, F. Izhizaka, and T. Fukui, Selective-area growth of InAs nanowires on Ge and vertical transistor application, *Nano Lett.*, 15, pp. 7253-7257, 2015.
 - 698.S. Hearne, E. Chason, J. Han, J. A. Floro, J. Figiel, J. Hunter, H. Amano, and I. S. T. Tsong, Stress evolution during metalorganic chemical vapor deposition of GaN, *Appl. Phys. Lett.*, vol. 74, no. 3, Jan. 1999.
 - 699.W. Seifert, M. Borgstrom, K. Deppert, K. A. Dick, J. Johansson, M. W. Larsson, T. Martensson, N. Skold, C. P. T. Svensson, B. A. Wacaser, L. R. Wallenberg, and L. Samuelson, Growth of one-dimensional nanostructures in MOVPE, *J. Cryst. Growth*, 272, 211-220, 2004.
 - 700.Z. Li, C. Moller, V. Migunov, M. Spasova, M. Farie, A. Lysov, C. Gutsche, I. Regolin, W. Prost, F. Tegude, and P. Ercius, Planar-defect characteristics and cross-sections of <001>, <111>, and <112> InAs nanowires, *J. Appl. Phys.*, 109, 114320, 2011.
 - 701.S. Murakami, H. Funayama, K. Shimomura, and T. Waho, Au-assisted growth of InAs nanowires on GaAs (111)B, GaAs (100), InP (111)B, InP (100) by MOVPE, *Phys. Status Solidi C*, 10, no. 5, pp. 761-764, 2013.
 - 702.U. Krishnamachari, M. Borgstrom, B. J. Ohlsson, N. Panev, L. Samuelson, W. Seifert, M. W. Larsson, and L. R. Wallenberg, Defect-free InP nanowires grown in [001] direction on InP (001), *Appl. Phys. Lett.*, 85, 2077, 2004.
 - 703.H. A. Fonseka, P. Caroff, J. Wong-Leung, A. S. Ameruddin, H. H. Tan, and C. Jagadish, Nanowires grown on InP (100): Growth directions, facets, crystal structures, and relative yield control, *ACS Nano*, vol. 8, no. 7, 6945-6954, 2014.
 - 704.J. Wang, S. Plissard, M. Hocevar, T. T. T. Vu, T. Zehender, G. G. W. Immink, M. A. Verheijen, J. Haverkort, and E. P. A. M. Bakkers, Position-controlled [100] InP nanowire arrays, *Appl. Phys. Lett.*, 100, 053107, 2012.
 - 705.S. A. Fortuna, J. Wen, I. S. Chun, and X. Li, Planar GaAs nanowires on GaAs (100) substrates: self-aligned, nearly twin-defect free, and transfer-printable, *Nano Lett.*, vol. 8, no. 12, 4421-4427, 2008.
 - 706.T. Xu, K. A. Dick, S. Plissard, T. H. Nguyen, Y. Makoudi, M. Berthe, J. -P. Nys, X. Wallart, B. Grandidier, and P. Caroff, Faceting, composition and crystal phase evolution in III-V antimonide nanowire heterostructures revealed by combining microscopy techniques, *Nanotechnol.*, 23, 095702, 2012.
 - 707.Y. Li, M. Niewczas, Strain relaxation in (100) and (311) GaP/GaAs thin films, *J. Appl. Phys.*, 101, 064910, 2007.

- 708.A. R. Lubinsky, C. B. Duke, B. W. Lee, and P. Mark, Semiconductor surface reconstruction: The rippled geometry of GaAs (110), *Phys. Rev. Lett.*, vol. 36, no. 17, pp. 1058-1061, Apr. 1976.
- 709.S. Y. Tong, A. R. Lubinsky, B. J. Mrstik, and M. A. Van Hove, Surface bond angle and bond lengths of rearranged As and Ga atoms on GaAs (110), *Phys. Rev. B*, vol. 17, no. 8, pp. 3303-3309, Apr. 1978.
- 710.D. J. Chadi, (110) surface atomic structures of covalent and ionic semiconductors, *Phys. Rev. B*, vol. 19, no. 4, pp. 2074-2082, Feb. 1979.
- 711.A. Kahn, E. So, P. Mark, C. B. Duke, and R. J. Meyer, Surface and near-surface atomic structure of GaAs (110), *J. Vac. Sci. Technol.*, 15, 1223, 1978.
- 712.J. E. Jaffe, R. Pandery, and P. Zapol, Ab initio prediction of GaN ($10\bar{1}0$) and (110) anomalous surface relaxation, *Phys. Rev. B*, vol. 53, no. 8, Feb. 1996-II.
- 713.M. -H. Tsai, J. D. Dow, R. -P. Wang, and R. V. Kasowski, Relaxation of zinc-blende (110) surfaces, *Phys. Rev. B*, vol. 40, no. 14, Nov. 1989-I.
- 714.J. L. A. Alves, J. Hebenstreit, and M. Scheffler, Calculated atomic structures and electronic properties of GaP, InP, GaAs, and InAs (110) surfaces, *Phys. Rev. B*, vol. 44, no. 12, Sep. 1991-II.
- 715.U. Grossner, J. Furthmuller, and F. Bechstedt, Bond-rotation versus bond-contraction relaxation of (110) surfaces of group-III nitrides, *Phys. Rev. B*, vol. 58, no. 4, Jul. 1998-II.
- 716.S. Y. Tong, W. N. Mei, and G. Xu, The geometric structures of the GaAs (111) and (110) surfaces, *J. Vac. Sci. Technol. B*, 2, 393, 1984.
- 717.F. J. Himpsel, F. R. McFeely, A. Taleb-Ibrahimi, J. A. Tarmoff, and G. Hollinger, Microscopic structure of the SiO₂/Si interface, *Phys. Rev. B*, vol. 38. no. 9, Sep. 1988-II.
- 718.T. Hattori, T. Aiba, E. Iijima, Y. Okube, H. Nohira, N. Tate, M. Katayama, Initial stage of oxidation of hydrogen-terminated silicon surfaces, *Appl. Surf. Sci.*, 104/105, 323-328, 1996.
- 719.J. Johansson, L. S. Karlsson, K. A. Dick, J. Bolinsson, B. A. Wacaser, K. Deppert, and L. Samuelson, Effects of supersaturation on the crystal structure of gold seeded III-V nanowires, *Crys. Growth Design*, vol. 9, no. 2, 766-773, 2009.
- 720.R. E. Algra, M. A. Verheijen, L. -F. Feiner, G. G. W. Immink, W. J. P. van Enckevort, E. Vlieg, and E. P. A. M. Bakkers, The role of surface energies and chemical potential during nanowire growth, *Nano Lett.*, 11, 1259-1264, 2011.
- 721.L. S. Karlsson, K. A. Dick, J. B. Wagner, J. Malm, K. Deppert, L. Samuelson, and L. R. Wallenberg, Understanding the 3D structure of GaAs <111>V nanowires, *Nanotechnol.*, 18, 485717, 2007.
- 722.H. J. Joyce, Q. Gao, H. H. Tan, C. Jagadish, Y. Kim, M. A. Fickenscher, S. Perera, T. B. Hoang, L. M. Smith, H. E. Jackson, J. M. Yarrison-Rice, X. Zhang, and J. Zou, Unexpected benefits of rapid growth rate for III-V nanowires, *Nano Lett.*, vol. 9, no. 2, 695-701, 2009.
- 723.H. J. Joyce, Q. Gao, H. H. Tan, C. Jagadish, Y. Kim, M. A. Fickenscher, S. Perera, T. B. Hoang, L. M. Smith, H. E. Jackson, J. M. Yarrison-Rice, X. Zhang, and J. Zou, High purity GaAs nanowires free of planar defects: Growth and characterization, *Adv. Funct. Mater.*, 18, 3794-3800, 2008.

724. B. A. Wacaser, K. Deppert, L. S. Karlsson, L. Samuelson, and W. Seifert, Growth and characterization of defect free GaAs nanowires, *J. Crys. Growth*, 287, 504-508, 2006
725. S. O. Mariager, C. B. Sorensen, M. Aagesen, J. Nygard, R. Feidenhans'l, and P. R. Willmott, Facet structure of GaAs nanowires grown by molecular beam epitaxy, *Appl. Phys. Lett.*, 91, 083106, 2007.
726. M. A. Verheijen, G. Immink, T. de Smet, M. T. Borgstrom, and E. P. A. M. Bakkers, Growth kinetics of heterostructured GaP-GaAs nanowires, *J. Am. Chem. Soc.*, 128, 1353-1359, 2006.
727. M. A. Verheijen, R. E. Algra, M. T. Borgstrom, G. Immink, E. Sourty, W. J. P. van Enckevort, E. Vlieg, and E. P. A. M. Bakkers, Three-dimensional morphology of GaP-GaAs nanowires revealed by transmission electron microscopy tomography, *Nano Lett.*, vol. 7, no. 10, 3051-3055, 2007.
728. N. Jiang, J. Wong-Leung, Q. Gao, H. H. Tan, and C. Jagadish, Sidewall evolution in VLS grown GaAs nanowires, *Optoelectr. Microelectr. Mater. Dev.*, 14920641, pp. 87-89, Dec. 2014.
729. D. B. Migas, A. B. Filonov, D. A. Yatsyna, D. Rusli, and C. Soci, Role of edge facets on stability and electronic properties of III-V nanowires, *Nano Convergence*, 2:14, 2015.
730. C. Thelander, P. Caroff, S. Plissard, A. W. Dey, and K. A. Dick, Effects of crystal phase mixing on the electrical properties of InAs nanowires, *Nano Lett.*, 11, pp. 2424-2429, 2011.
731. L. Largeau, D. L. Dheeraj, M. Tchernycheva, G. E. Cirlin, and J. C. Harmand, Facet and in-plane crystallographic orientations of GaN nanowires grown on Si (111), *Nanotechnol.*, 19, 155704, 2008.
732. D. Tsivion, M. Schvartzman, R. Popovitz-Biro, P. von Huth, E. Joselevich, Guided growth of millimeter-long horizontal nanowires with controlled orientations, *Science*, vol. 333, pp. 1003-1007, Aug. 2011.
733. F. Qian, M. Brewster, S. K. Lim, Y. Ling, C. Greene, O. Laboutin, J. W. Johnson, S. Gradecak, Y. Cao, and Y. Li, Controlled synthesis of AlN/GaN multiple quantum well nanowire structures and their optical properties, *Nano Lett.*, 12, 3344-3350, 2012.
734. S. K. Lim, S. Crawford, G. Haberfehlner, S. Gradecak, Controlled modulation of diameter and composition along individual III-V nitride nanowires, *Nano Lett.*, 13, 331-336, 2013.
735. D. Spirkoska, J. Arbiol, A. Gustafsson, S. Conesa-Boj, F. Glas, I. Zardo, M. Heigoldt, M. H. Gass, A. L. Bleloch, S. Estrade, M. Kaniber, J. Rossler, F. Peiro, J. R. Morante, G. Abstreiter, L. Samuelson, and A. F. i Morral, Structural and optical properties of high quality zinc-blende/wurzite GaAs nanowire heterostructures, *Phys. Rev. B*, 80, 245325, 2009.
736. H. Eisele, P. Ebert, Non-polar group-III nitride semiconductor surfaces, *Phys. Status Solidi RRL*, 6, no. 9-10, 359-369, 2012.
737. M. Bertelli, P. Loptien, M. Wenderoth, A. Rizzi, R. G. Ulbrich, M. C. Righi, A. Ferretti, L. Martin-Samos, C. M. Bertoni, and A. Catellani, Atomic and electronic structure of the nonpolar GaN ($\bar{1}100$) surface, *Phys. Rev. B*, 80, 115324, 2009.
738. J. E. Northrup, J. Neugebauer, Theory of GaN ($10\bar{1}0$) and ($1\bar{1}20$) surfaces, *Phys. Rev. B*, vol. 53, no. 16, Apr. 1996-II.

- 739.J. E. Jaffe, R. Pandey, and P. Zapol, Ab initio prediction of GaN ($10\bar{1}0$) and (110) anomalous surface relaxation, Phys. Rev. B, vol. 53, no. 8, Feb. 1996-II.
- 740.A. Filippetti, V. Fiorentini, G. Cappellini, and A. Bosin, Anomalous relaxations and chemical trends at III-V semiconductor nitride nonpolar surfaces, Phys. Rev. B, vol. 59, no. 12, Mar. 1999-II.
- 741.C. B. Duke, Semiconductor surface reconstruction: The structural chemistry of two-dimensional surface compounds, Chem. Rev., 96, 1237-1259, 1996.
- 742.J. P. LaFemina, Total-energy calculations of semiconductor surface reconstructions, Surf. Sci. Rep., 16, pp. 133-260, 1992.
- 743.A. Kahn, Thirty years of atomic and electronic structure determination of surfaces of tetrahedrally coordinated compound semiconductors, Surf. Sci., 299/300, pp. 469-486, 1994.
- 744.J. Neugebauer, Ab initio analysis of surface structure and adatom kinetics of group-III nitrides, Phys. Stat. Sol. (b), 227, no. 1, pp. 93-114, 2001.
- 745.Ph. Ebert, Nano-scale properties of defects in compound semiconductor surfaces, Surf. Sci. Rep., 33, 121-303, 1999.
- 746.W. Monch, Semiconductor surfaces and interfaces, 3rd edition, Springer, 2001.
- 747.P. K. Larsen, J. F. van der Veen, A. Mazur, J. Pollmann, J. H. Neave, and B. A. Joyce, Surface electronic structure of GaAs (001)-(2×4): Angle-resolved photoemission and tight-binding calculations, Phys. Rev. B, vol. 26, no. 6, Sep. 1982.
- 748.D. K. Biegelsen, R. D. Bringans, J. E. Northrup, and L. -E. Swartz, Surface reconstructions of GaAs(100) observed by scanning tunneling microscopy, Phys. Rev. B, vol. 41, no. 9, Mar. 1990-II.
- 749.E. J. Heller, M. G. Lagally, *In situ* scanning tunneling microscopy observation of surface morphology of GaAs (001) grown by molecular beam epitaxy, Appl. Phys. Lett., 60, 2675, 1992.
- 750.H. Xu, T. Hashizume, and T. Sakurai, GaAs (100) (2×4) surface study by molecular beam epitaxy and field-ion-scanning-tunneling-microscopy, Jpn. J. Appl. Phys., vol. 32, pp. 1511-1514, 1993.
- 751.Q. Xue, T. Hashizume, J. M. Zhou, T. Sakata, T. Ohno, and T. Sakurai, Structures of the Ga-rich 4×2 and 4×6 reconstructions of the GaAs (001) surface, Phys. Rev. Lett., vol. 74, no. 16, Apr. 1995.
- 752.A. R. Avery, D. M. Holmes, J. Sudijono, T. S. Jones, and G. A. Joyce, The As-terminated reconstructions formed by GaAs (001): a scanning tunnelling microscopy study of the (2×4) and c(4×4) surfaces, Surf. Sci., 323, 91-101, 1995.
- 753.W. G. Schmidt, F. Bechstedt, Atomic structures of GaAs (100)-(2×4) reconstructions, Surf. Sci., 360, L473-L477, 1996.
- 754.N. Moll, A. Kley, E. Pehlke, and M. Scheffler, GaAs equilibrium crystal shape from first principles, Phys. Rev. B, vol. 54, no. 12, Sep. 1996-II.
- 755.H. H. Farrell, C. J. Palmstrom, Reflection high energy electron diffraction characteristic absences in GaAs (100) (2×4)-As: A tool for determining the surface stoichiometry, J. Vac. Sci. Technol. B, 8, 903, 1990.
- 756.W. Ranke, K. Jacobi, Structure and reactivity of GaAs surfaces, Prog. Surf. Sci., vol. 10, pp. 1-52, 1981.
- 757.C. D. MacPherson, R. A. Wolkow, C. E. J. Mitchell, and A. B. McLean, Scanning tunneling microscopy study of InP (100)-(2×4): An exception to the dimer model, Phys. Rev. Lett., vol. 77, no. 4, Jul. 1996.

- 758.K. B. Ozanyan, P. J. Parbrook, M. Hopkinson, C. R. Whitehouse, Z. Sobiesierski, and D. I. Westwood, *In situ* monitoring of the surface reconstructions on InP (001) prepared by molecular beam epitaxy, *J. Appl. Phys.*, 82, 474, 1997.
- 759.V. P. LaBella, Z. Ding, D. W. Bullock, C. Emery, and P. M. Thibado, Reflection high-energy electron diffraction and scanning tunneling microscopy study of InP (001) surface reconstructions, *J. Vac. Sci. Technol. A*, 18, 1492, 2000.
- 760.W. G. Schmidt, N. Esser, A. M. Frisch, P. Vogt, J. Bernholc, F. Bechstedt, M. Zorn, Th. Hannappel, S. Visbeck, F. Willig, and W. Richter, Understanding reflectance anisotropy: Surface-state signatures and bulk-related features in the optical spectrum of InP (001) (2×4), *Phys. Rev. B*, vol. 61, no. 24, Jun. 2000-II.
- 761.D. Fuster, M. U. Gonzalez, Y. Gonzalez, and L. Gonzalez, *In situ* measurements of InAs and InP (001) surface stress changes induced by surface reconstruction transitions, *Surf. Sci.*, 600, 23-32, 2006.
- 762.K. B. Ozanyan, P. J. Parbrook, M. Hopkinson, C. R. Whitehouse, Static and growing InP and InAs surfaces: reflection-anisotropy spectroscopy under the conditions of solid-source MBE, *Thin Solid Films*, 364, 6-11, 2000.
- 763.H. Yamaguchi, Y. Horikoshi, First-order surface-structure transition on the (001) InAs surface studied with improved high-energy electron reflectivity measurements, *Phys. Rev. B*, vol. 45, no. 3, Jan. 1992-I.
- 764.M. Noguchi, K. Hirakawa, and T. Ikoma, Intrinsic electron accumulation layers on reconstructed clean InAs (100) surfaces, *Phys. Rev. Lett.*, vol. 66, no. 17, Apr. 1991.
- 765.M. Zorn, B. Junno, T. Trepk, S. Bose, L. Samuelson, J. –T. Zettler, and W. Richter, Optical response of reconstructed GaP (001) surfaces, *Phys. Rev. B*, vol. 60, no. 16, Oct. 1999-II.
- 766.A. M. Frisch, W. G. Schmidt, J. Bernholc, M. Pristovsek, N. Esser, and W. Richter, (2×4) GaP (001) surface: Atomic structure and optical anisotropy, *Phys. Rev. B*, vol. 60, no. 4, Jul. 1999-II.
- 767.J. M. Millunchick, A. Riposan, B. J. Dall, C. Pearson, and B. G. Orr, Surface reconstructions of InGaAs alloys, *Surf. Sci.*, 550, 1-7, 2004.
- 768.U. Seidel, T. Hannappel, MOVPE preparation of InGaAs (100) surface reconstructions employing transient in-situ RDS, *J. Crys. Growth*, 310, 2334-2338, 2008.
- 769.D. J. Chadi, Atomic structure of GaAs (100)-(2×1) and (2×4) reconstructed surfaces, *J. Vac. Sci. Technol. A*, 5, 834, 1987.
- 770.L. Daweritz, R. Hey, Reconstruction and defect structure of vicinal GaAs (001) and AlGaAs (001) surfaces during MBE growth, *Surf. Sci.*, 236, 15-22, 1990.
- 771.C. F. McConville, T. S. Jones, F. M. Leibsle, S. M. Driver, T. C. Q. Noakes, M. O. Schweitzer, and N. V. Richardson, Surface reconstructions of InSb (100) observed by scanning tunneling microscopy, *Phys. Rev. B*, vol. 50, no. 20, Nov. 1994-II.
- 772.T. Mori, T. Hanada, T. Morimura, K. Shin, H. Makino, and T. Yao, Surface structure of InGaAs/InP (001) ordered alloy during and after growth, *Appl. Surf. Sci.*, 237, pp.230-234, 2004.
- 773.W. Barvosa-Carter, A. S. Bracker, J. C. Culbertson, B. Z. Nosho, B. V. Shanabrook, L. J. Whitman, H. Kim, N. A. Modine, and E. Kaxiras, Structure of III-Sb (001) growth surfaces: The role of heterodimers, *Phys. Rev. Lett.*, vol. 84, no. 20, May 2000.
- 774.C. F. McConville, T. S. Jones, F. M. Leibsle, N. V. Richardson, Direct observation of Sb dimers on InSb (100)-c(4×4), *Surf. Sci. Lett.*, 303, pp. L373-L378, 1994.

- 775.M. O. Schweitzer, F. M. Leibsle, T. S. Jones, C. F. McConville, and N. V. Richardson, An STM study of the InSb (100)-c(8×2) surface, *Surf. Sci.*, 280, pp. 63-70, 1993.
- 776.D. J. Chadi, C. Tanner, and J. Ihm, Theoretical study of the atomic and electronic structure of the c-4×4 reconstructed GaAs (100) surface, *Surf. Sci.*, 120, L425-L430, 1982.
- 777.P. K. Larsen, J. H. Neave, J. F. Van der Veen, P. J. Dobson, and B. A. Joyce, GaAs (001)-c(4×4): A chemisorbed structure, *Phys. Rev. B*, vol. 27, no. 8, Apr. 1983.
- 778.O. Brandt, H. Yang, B. Jenichen, Y. Suzuki, L. Daweritz, and K. H. Ploog, Surface reconstructions of zinc-blende GaN/GaAs(001) in plasma-assisted molecular-beam epitaxy, *Phys. Rev. B*, vol. 52, no. 4, Jul. 1995-II.
- 779.O. Brandt, H. Yang, and K. H. Ploog, Surface kinetics of zinc-blende (001) GaN, *Phys. Rev. B*, vol. 54, no. 7, Aug. 1996-I.
- 780.J. Neugebauer, T. Zywietz, M. Scheffler, J. E. Northrup, and C. G. Van de Walle, Clean and As-covered zinc-blende GaN (001) surfaces: novel surface structures and surfactant behavior, *Phys. Rev. Lett.*, vol. 80, no. 14, pp. 3097-3100, Apr. 1998.
- 781.G. Feuillet, H. Hamaguchi, K. Ohta, P. Hacke, H. Okumura, and S. Yoshida, Arsenic mediated reconstructions on cubic (001) GaN, *Appl. Phys. Lett.*, 70, 1025, 1997.
- 782.J. V. Knutsson, S. Lehmann, M. Hjort, P. Reinke, E. Lundgren, K. A. Dick, R. Timm, and A. Mikkelsen, Atomic scale surface structure and morphology of InAs nanowire crystal superlattices: The effect of epitaxial overgrowth, *ACS, Appl. Mater. Interfaces*, 7, pp. 5748-5755, 2015.
- 783.D. J. Chadi, Vacancy-induced 2×2 reconstruction of the Ga (111) surface of GaAs, *Phys. Rev. Lett.*, vol. 52, no. 21, May 1984.
- 784.S. Y. Tong, G. Xu, and W. N. Mei, Vacancy-buckling model for the (2×2) GaAs (111) surface, *Phys. Rev. Lett.*, vol. 52, no. 19, May 1984.
- 785.D. J. Chadi, Atomic and electronic structures of (111), (211), and (311) surfaces of GaAs, *J. Vac. Sci. Technol. B*, 3, 1167, 1985.
- 786.E. Kaxiras, Y. Bar-Yam, J. D. Joannopoulos, K. C. Pandey, (2×2) reconstructions of the {111} polar surfaces of GaAs, *Phys. Rev. B*, vol. 33, no. 6, Mar. 1986.
- 787.D. J. Chadi, Atomic structure of polar (111) surfaces of GaAs and ZnSe, *J. Vac. Sci. Technol. A*, 4, 944, 1986.
- 788.E. Kaxiras, Y. Bar-Yam, J. D. Joannopoulos, K. C. Pandey, Ab initio theory of polar semiconductor surfaces. I. Methodology and the (2×2) reconstructions of GaAs (111), *Phys. Rev. B*, vol. 35, no. 18, Jun. 1987-II.
- 789.K. W. Haberern, M. D. Pashley, GaAs (111)A-(2×2) reconstruction studied by scanning tunneling microscopy, *Phys. Rev. B*, vol. 41, no. 5, Feb. 1990-I.
- 790.B. Murphy, P. Moriarty, L. Roberts, T. Cafolla, G. Hughes, L. Koenders, P. Bailey, Chemical and structural studies of the interactions of molecular sulfur with the GaAs (111)A and GaAs (111)B surfaces, *Surf. Sci.*, 317, pp. 73-83, 1994.
- 791.A. Ohtake, M. Ozeki, and J. Nakamura, Strain relaxation in InAs/GaAs (111)A heteroepitaxy, *Phys. Rev. Lett.*, vol. 84, no. 20, May, 2000.
- 792.G. Xu, W. Y. Hu, M. W. Puga, S. Y. Tong, J. L. Yeh, S. R. Wang, and B. W. Lee, Atomic geometry of the 2×2 GaP (111) surface, *Phys. Rev. B*, vol. 32, no. 12, Dec. 1985.

- 793.R. Feidenhans'l, M. Nielsen, F. Grey, R. L. Johnson, and I. K. Robinson, X-ray determination of the GaSb (111) 2×2 surface structure, *Surf. Sci.*, 186, pp. 499-510, 1987.
- 794.A. Belzner, E. Ritter, and H. Schulz, Disorder in the reconstructed (111) 2×2 surfaces of InSb and GaSb, *Surf. Sci.*, 209, pp. 379-386, 1989; I. K. Robinson, J. Bohr, R. Feidenhans'l, M. Nielsen, F. Grey and R. L. Johnson, Reexamination of the InSb (111) and GaSb (111) structures: Comment on 'Disorder in the reconstructed (111) 2×2 surfaces of InSb and GaSb' by A. Belzner, E. Ritter, and H. Schulz, *Surf. Sci.*, 217, pp. L435-L440, 1989.
- 795.J. Bohr, R. Feidenhans'l, M. Nielsen, M. Toney, R. L. Johnson, and I. K. Robinson, Model-independent structure determination of the InSb (111) 2×2 surface with use of synchrotron X-ray diffraction, *Phys. Rev. Lett.*, vol. 54, no. 12, Mar. 1985.
- 796.E. Kaxiras, K. C. Pandey, Y. Bar-Yam, and J. D. Joannopoulos, Role of chemical potentials in surface reconstruction: A new model and phase transition on GaAs (111) 2×2 , *Phys. Rev. Lett.*, vol. 56, no. 26, Jun. 1986.
- 797.D. K. Biegelsen, R. D. Bringans, J. E. Northrup, and L. -E. Swartz, Reconstructions of GaAs ($\bar{1}\bar{1}\bar{1}$) surfaces observed by scanning tunneling microscopy, *Phys. Rev. Lett.*, vol. 65, no. 4, Jul. 1990.
- 798.J. M. C. Thornton, D. A. Woolf, and P. Weightman, Reconstructions of the GaAs (111)B surface, *Appl. Surf. Sci.*, 123/124, 115-119, 1998.
- 799.J. M. C. Thornton, D. A. Woolf, and P. Weightman, Surface reconstructions and phase transitions on the GaAs (111)B surface, *Surf. Sci.*, 380, 548-555, 1997.
- 800.H. H. Farrell, J. Lu, B. D. Schultz, A. B. Denison, and C. J. Palmstrom, GaAs (111)B ($\sqrt{19}\times\sqrt{19}$) $R23.4^\circ$ surface reconstruction, *J. Vac. Sci. Technol. B*, 19, 1597, 2001.
- 801.C. B. M. Andersson, U. O. Karlsson, M. C. Hakansson, L. O. Olsson, L. Ilver, J. Kanski, and P. -O. Nilsson, Surface atomic structure of InAs ($\bar{1}\bar{1}\bar{1}$) 2×2 and InSb ($\bar{1}\bar{1}\bar{1}$) 2×2 studied by core level spectroscopy, *Surf. Sci.*, 347, 199-206, 1996.
- 802.P. Hacke, G. Feuillet, H. Okumura, and S. Yoshida, Monitoring surface stoichiometry with the (2×2) reconstruction during growth of hexagonal-phase GaN by molecular beam epitaxy, *Appl. Phys. Lett.*, 69, 2507, 1996.
- 803.M. M. Sung, J. Ahn, V. Bykov, J. W. Rabalais, D. D. Koleske, and A. E. Wickenden, Composition and structure of the GaN $\{000\bar{1}\}$ -(1×1) surface, *Phys. Rev. B*, vol. 54, no. 20, Nov. 1996-II.
- 804.J. Fritsch, O. F. Sankey, K. E. Schmidt, and J. B. Page, Ab initio calculation of the stoichiometry and structure of the (0001) surfaces of GaN and AlN, *Phys. Rev. B*, vol. 57, no. 24, Jun. 1998-II.
- 805.A. R. Smith, R. M. Feenstra, D. W. Greve, M. S. Shin, M. Skowronski, J. Neugebauer, and J. E. Northrup, Reconstructions of GaN (0001) and ($000\bar{1}$) surfaces: Ga-rich metallic structures, *J. Vac. Sci. Technol. B*, 16, 2242, 1998.
- 806.A. R. Smith, R. M. Feenstra, D. W. Greve, J. Neugebauer, and J. E. Northrup, Scanning tunneling microscopy of the GaN ($000\bar{1}$) surface, *Appl. Phys. A*, 66, S947-S951, 1998.
- 807.Q. -K. Xue, Q. Z. Xue, R. Z. Bakhtizin, Y. Hasegawa, I. S. T. Tsong, T. Sakurai, and T. Ohno, Structures of GaN (0001)-(2×2), -(4×4), and -(5×5) surface reconstructions, *Phys. Rev. Lett.*, vol. 82, no. 15, Apr. 1999.

808. A. R. Smith, R. M. Feenstra, D. W. Greve, M. -S. Shin, M. Skowronski, J. Neugebauer, and J. E. Northrup, GaN (0001) surface structures studied using scanning tunneling microscopy and first-principles total energy calculations, *Surf. Sci.*, 423, 70-84, 1999.
809. H. P. D. Schenk, G. D. Kipshidze, U. Kaiser, A. Fissel, J. Kraußlich, J. Schulze, and W. Richter, Investigation of two-dimensional growth of AlN (0001) on Si (111) by plasma-assisted molecular beam epitaxy, *J. Crys. Growth*, 200, 45-54, 1999.
810. V. Ramachandran, C. D. Lee, R. M. Feenstra, A. R. Smith, J. E. Northrup, and D. W. Greve, Structure of clean and arsenic-covered GaN (0001) surfaces, *J. Crys. Growth*, 209, 355-363, 2000.
811. J. E. Northrup, J. Neugebauer, R. M. Feenstra, and A. R. Smith, Structure of GaN (0001): The laterally contracted Ga bilayer model, *Phys. Rev. B*, vol. 61, no. 15, Apr. 2000-I.
812. S. Vezian, F. Semond, J. Massies, D. W. Bullock, Z. Ding, and P. M. Thibado, Origins of GaN (0001) surface reconstructions, *Surf. Sci.*, 541, 242-251, 2003.
813. C. K. Gan, D. J. Srolovitz, First-principles study of wurtzite InN (0001) and ($000\bar{1}$) surfaces, *Phys. Rev. B*, 74, 115319, 2006.
814. A. Jenichen, C. Engler, and B. Rauschenbach, Comparison of wurtzite and zinc-blende GaAs surfaces as possible nanowire side walls: DFT stability calculations, *Surf. Sci.*, 613, 74-79, 2013.
815. A. Jenichen, C. Engler, Reconstructions and surface facets of the GaAs (112)A and (112)B surfaces: First-principles DFT supercell calculations, *Surf. Sci.*, 608, 204-211, 2013.
816. M. Hjort, S. Lehmann, J. Knutsson, R. Timm, D. Jacobsson, E. Lundgren, K. A. Dick, and A. Mikkelsen, Direct imaging of atomic scale structure and electronic properties of GaAs wurtzite and zinc blende nanowire surfaces, *Nano Lett.*, 13, pp. 4492-4498, 2013.
817. E. Hilner, U. Hakanson, L. E. Froberg, M. Karlsson, P. Kratzer, E. Lundgren, L. Samuelson, and A. Mikkelsen, Direct atomic scale imaging of III-V nanowire surfaces, *Nano Lett.*, vol. 8, no. 11, 3978-3982, 2008.
818. C. B. Duke, A. Paton, A. Kahn, and C. R. Bonapace, Dynamical analysis of low-energy electron-diffraction intensities from InAs (110), *Phys. Rev. B*, vol. 27, no. 10, May 1983.
819. Ph. Ebert, G. Cox, U. Poppe, and K. Urban, The electronic structure of the InP (110) surface studied by scanning tunneling microscopy and spectroscopy, *Surf. Sci.*, 271, 587-595, 1992.
820. Ph. Ebert, G. Cox, U. Poppe, and K. Urban, A STM study of the InP (110) surface, *Ultramicroscopy*, 42-44, pp. 871-877, 1992.
821. X. M. Chen, K. F. Canter, C. B. Duke, A. Paton, D. L. Lessor, and W. K. Ford, Low-energy positron diffraction from the (110) surfaces of GaAs and InP, *Phys. Rev. B*, vol. 48, no. 4, Jul. 1993-II.
822. S. Gota, R. Gunnella, Z. -Y. Wu, G. Jezequel, C. R. Natoli, D. Sebilliau, E. L. Bullock, F. Proix, C. Guillot, and A. Quémenerais, Chemical-shift low-energy photoelectron diffraction: A determination of the InP (110) clean surface structural relaxation, *Phys. Rev. Lett.*, vol. 71, no. 20, Nov. 1993.
823. S. Cahangirov, S. Ciraci, First-principles study of GaAs nanowires, *Phys. Rev. B*, 79, 165118, 2009.

- 824.S. B. Zhang, S. -H. Wei, and A. Zunger, A phenomenological model for systematization and prediction of doping limits in II-VI and I-III-VI₂ compounds, *J. Appl. Phys.*, 83, 3192, 1998.
- 825.V. Ramachandran, R. M. Feenstra, W. L. Sarney, L. Salamanca-Riba, J. E. Northrup, L. T. Romano, and D. W. Greve, Inversion of wurtzite GaN (0001) by exposure to magnesium, *Appl. Phys. Lett.*, 75, 808, 1999.
- 826.E. Cimpoeasu, E. Stern, R. Klie, R. A. Munden, G. Cheng, and M. A. Reed, The effect of Mg doping on GaN nanowires, *Nanotechnol.*, 17, pp.5735-5739, 2006.
- 827.R. E. Algra, M. A. Verheijen, M. T. Borgstrom, L. -F. Feiner, G. Immink, W. J. P. van Enckevort, E. Vlieg, and E. P. A. M. Bakkers, Twinning superlattices in indium phosphide nanowires, *Nature*, vol. 456, pp. 369-372, Nov. 2008.
- 828.J. Wallentin, M. Ek, L. R. Wallenberg, L. Samuelson, K. Deppert, and M. T. Borgstrom, Changes in contact angle of seed particle correlated with increased zincblende formation in doped InP nanowires, *Nano Lett.*, 10, pp. 4807-4812, 2010.
- 829.J. E. Northrup, Hydrogen and magnesium incorporation on c-plane and m-plane GaN surfaces, *Phys. Rev. B*, 77, 045313, 2008.
- 830.M. T. Borgstrom, E. Norberg, P. Wickert, H. A. Nilsson, J. Tragardh, K. A. Dick, G. Statkute, P. Ramvall, K. Deppert, and L. Samuelson, Precursor evaluation for *in situ* InP nanowire doping, *Nanotechnol.*, 19, 445602, 2008.
- 831.L. Rigutti, A. D. L. Bugallo, M. Tchernycheva, G. Jacopin, F. H. Julien, G. Cirlin, G. Patriarche, D. Lucot, L. Travers, and J. -C. Harmand, Si incorporation in InP nanowires grown by Au-assisted molecular beam epitaxy, *J. Nanomater.*, vol. 2009, no. 27, Jan. 2009.
- 832.J. Arbiol, S. Estrade, J. D. Prades, A. Cirera, F. Furtmayr, C. Stark, A. Laufer, M. Stutzmann, M. Eickhoff, M. H. Gass, A. L. Bleloch, F. Peiro, and J. R. Morante, Triple-twin domains in Mg doped GaN wurtzite nanowires: structural and electronic properties of this zinc-blende-like stacking, *Nanotechnol.*, 20, 145704, 2009.
- 833.C. Thelander, K. A. Dick, M. T. Borgstrom, L. E. Froberg, P. Caroff, H. A. Nilsson, and L. Samuelson, The electrical and structural properties of n-type InAs nanowires grown from metal-organic precursors, *Nanotechnol.*, 21, 205703, 2010.
- 834.T. Stoica, R. Calarco, Doping of III-nitride nanowires grown by molecular beam epitaxy, *IEEE J. Selec. Topic Quantum Elec.*, vol. 17, no. 4, Jul./Aug. 2011.
- 835.J. Wallentin, M. T. Borgstrom, Doping of semiconductor nanowires, *J. Mater. Res.*, vol. 26, no. 17, pp. 2142-2156, Sep. 2011.
- 836.H. Ghoneim, P. Mensch, H. Schmid, C. D. Bessire, R. Rhyner, A. Schenk, C. Rettner, S. Karg, K. E. Moselund, H. Riel, and M. T. Bjork, *In situ* doping of catalyst-free InAs nanowires, *Nanotechnol.*, 23, 505708, 2012.
- 837.C. Rolland, P. Caroff, C. Coinon, X. Wallart, and R. Leturcq, Inhomogeneous Si-doping of gold-seeded InAs nanowires grown by molecular beam epitaxy, *Appl. Phys. Lett.*, 102, 223105, 2013.
- 838.W. Walukiewicz, Doping-induced suppression of dislocation formation in semiconductors, *Phys. Rev. B*, vol. 39, no. 12, Apr. 1989-II.
- 839.W. Walukiewicz, Amphoteric native defects in semiconductors, *Appl. Phys. Lett.*, 54, 2094, 1989.
- 840.W. Walukiewicz, Application of the amphoteric native defect model to diffusion and activation of shallow impurities in III-V semiconductors, *Mat. Res. Soc. Symp. Proc.*, vol. 300, pp. 421-432, 1993.

- 841.W. Walukiewicz, Defect formation and diffusion in heavily doped semiconductors, *Phys. Rev. B*, vol. 50, no. 8, Aug. 1994-II.
- 842.J. A. Chisholm, P. D. Bristowe, Ab initio study of the effect of doping on stacking faults in GaN, *J. Crys. Growth*, 230, pp. 432-437, 2001.
- 843.C. Tessarek, M. Heilmann, E. Butzen, A. Haab, H. Hardtdegen, C. Dieker, E. Spiecker, and S. Christiansen, The role of Si during the growth of GaN micro- and nanorods, *Crys. Growth Des.*, 14, pp. 1486-1492, 2014.
- 844.A. P. Alivisatos, Semiconductor clusters, nanocrystals, and quantum dots, *Science*, vol. 271, no. 5251, pp. 933-937, Feb. 1996.
- 845.D. R. Khanal, J. W. L. Yim, W. Walukiewicz, and J. Wu, Effects of quantum confinement on the doping limit of semiconductor nanowires, *Nano Lett.*, vol. 7, no. 5, pp. 1186-1190, 2007.
- 846.J. H. Davis, *The physics of low-dimensional semiconductors: An introduction*, Cambridge Univ. Press, 1998.
- 847.A. I. Ekimov, I. A. Kudryavtsev, M. G. Ivanov, and Al. L. Efros, Spectra and decay kinetics of radiative recombination in CdS microcrystals, *J. Lumin.*, 46, pp. 83-95, 1990.
- 848.W. Walukiewicz, Mechanism of Schottky barrier formation: The role of amphoteric native defects, *J. Vac. Sci. Technol. B*, 5, 1062, 1987.
- 849.W. Walukiewicz, Intrinsic limitations to the doping of wide-gap semiconductors, *Physica B*, 302-303, pp. 123-134, 2001.
- 850.S. B. Zhang, S. -H. Wei, and A. Zunger, Microscopic origin of the phenomenological equilibrium “doping limit rule” in n-type III-V semiconductors, *Phys. Rev. Lett.*, vol. 84, no. 6, Feb. 2000.
- 851.S. B. Zhang, The microscopic origin of the doping limits in semiconductors and wide-gap materials and recent developments in overcoming these limits: a review, *J. Phys.: Condens. Matter*, 14, pp. R881-R903, 2002.
- 852.A. Zunger, Practical doping principles, *Appl. Phys. Lett.*, 83, 57, 2003.
- 853.S. B. Zhang, S. -H. Wei, Nitrogen solubility and induced defect complexes in epitaxial GaAs:N, *Phys. Rev. Lett.*, vol. 86, no. 9, Feb. 2001.
- 854.J. Li, S. -H. Wei, and L. -W. Wang, Stability of the DX⁻ center in GaAs quantum dots, *Phys. Rev. Lett.*, 94, 185501, 2005.
- 855.D. T. J. Hurle, A thermodynamic analysis of native point defect and dopant solubilities in zinc-blende III-V semiconductors, *J. Appl. Phys.*, 107, 121301, 2010.
- 856.J. Tersoff, Enhanced solubility of impurities and enhanced diffusion near crystal surfaces, *Phys. Rev. Lett.*, vol. 74, no. 25, Jun. 1995.
- 857.J. Tersoff, Kinetic surface segregation and the evolution of nanostructures, *Appl. Phys. Lett.*, 83, 353, 2003.
- 858.H. Abu-Farsakh, J. Neugebauer, Enhancing nitrogen solubility in GaAs and InAs by surface kinetics: An ab initio study, *Phys. Rev. B*, 79, 155311, 2009.
- 859.M. Hilse, M. Ramsteiner, S. Breuer, L. Geelhaar, and H. Riechert, Incorporation of the dopants Si and Be into GaAs nanowires, *Appl. Phys. Lett.*, 96, 193104, 2010.
- 860.C. Gutsche, A. Lysov, I. Regolin, K. Blekker, W. Prost, F. -J. Tegude, n-type doping of vapor-liquid-solid grown GaAs nanowires, *Nanoscale Res. Lett.*, 6:65, 2011.
- 861.O. Salehzadeh, K. L. Kavanagh, and S. P. Watkins, Controlled axial and radial Te-doping of GaAs nanowires, *J. Appl. Phys.*, 112, 054324, 2012.

- 862.J. L. Boland, S. Conesa-Boj, P. Parkinson, G. Tutuncuoglu, F. Matteini, D. Ruffer, A. Casadei, F. Amaduzzi, F. Jabeen, C. L. Davies, H. J. Joyce, L. M. Herz, A. F. i Morral, and M. B. Johnston, Modulation doping of GaAs/AlGaAs core-shell nanowires with effective defect passivation and high electron mobility, *Nano Lett.*, 15, pp. 1336-1342, 2015.
- 863.Y. Huang, X. Duan, Y. Cui, and C. M. Lieber, Gallium nitride nanowire nanodevices, *Nano Lett.*, vol. 2, no. 2, pp. 101-104, 2002.
- 864.Z. Chen, L. Cheng, G. Q. Lu, and J. Zou, Sulfur-doped gallium phosphide nanowires and their optoelectronic properties, *Nanotechnol.*, 21, 375701, 2010.
- 865.S. Zhao, S. Fatholouloumi, K. H. Bevan, D. P. Liu, M. G. Kibria, Q. Li, G. T. Wang, H. Guo, and Z. Mi, Tuning the surface charge properties of epitaxial InN nanowires, *Nano Lett.*, 12, pp. 2877-2882, 2012.
- 866.C. Gutsche, I. Regolin, K. Blekker, A. Lysov, W. Prost, and F. J. Tegude, Controllable p-type doping of GaAs nanowires during vapor-liquid-solid growth, *J. Appl. Phys.*, 105, 024305, 2009.
- 867.O. Salehzadeh, X. Zhang, B. D. Gates, K. L. Kavanagh, and S. P. Watkins, p-type doping of GaAs nanowires using carbon, *J. Appl. Phys.*, 112, 094323, 2012.
- 868.H. W. Seo, S. Y. Bae, J. Park, M. Kang, S. Kim, Nitrogen-doped gallium phosphide nanowires, *Chem. Phys. Lett.*, 378, pp. 420-424, 2003.
- 869.W. -H. Chu, H. -W. Chiang, C. -P. Liu, Y. -F. Lai, K. -Y. Hsu, and H. -C. Chung, Defect-induced negative differential resistance of GaN nanowires measured by conductive atomic force microscopy, *Appl. Phys. Lett.*, 94, 182101, 2009.
- 870.B. S. Sorensen, M. Aagesen, C. B. Sorensen, P. E. Lindelof, K. L. Martinez, and J. Nygard, Ambipolar transistor behavior in p-doped InAs nanowires grown by molecular beam epitaxy, *Appl. Phys. Lett.*, 92, 012119, 2008.
- 871.H. -Y. Li, O. Wunnicke, M. T. Borgstrom, W. G. G. Immink, M. H. M. van Weert, M. A. Verheijen, and E. P. A. M. Bakkers, Remote p-doping of InAs nanowires, *Nano Lett.*, vol. 7, no. 5, pp. 1144-1148, 2007.
- 872.J. Dabrowski, M. Scheffler, Theory of defect metastabilities in III-V compounds, *Physica Scripta.*, vol. T45, pp. 151-153, 1992.
- 873.D. T. J. Hurle, A comprehensive thermodynamic analysis of native point defect and dopant solubilities in gallium arsenide, *J. Appl. Phys.*, 85, 6957, 1999.
- 874.H. Komsa, A. Pasquarello, Intrinsic defects in GaAs and InGaAs through hybrid functional calculations, *Physica B*, 407, pp. 2833-2837, 2012.
- 875.S. B. Zhang, J. E. Northrup, Chemical potential dependence of defect formation energies in GaAs: Application to Ga self-diffusion, *Phys. Rev. Lett.*, vol. 67, no. 17, Oct. 1991.
- 876.M. Jaros, S. Brand, Localized defects in III_V semiconductors, *Phys. Rev. B*, vol. 14, no. 10, Nov. 1976.
- 877.G. A. Baraff, M. Schluter, Electronic structure, total energies, and abundances of the elementary point defects in GaAs, *Phys. Rev. Lett.*, vol. 55, no. 12, Sep. 1985.
- 878.W. A. Oates, H. Wenzl, Temperature-chemical potential diagrams for the representation of defect and phase equilibria in compound semiconductors-application to gallium arsenide, *J. Phys. Chem. Solids*, vol. 49, no. 11, pp. 1363-1371, 1988.
- 879.Y. H. Park, R. Ha, R. Park, S. W. Kim, D. Seo, and H. Choi, Magnertic $\text{In}_x\text{Ga}_{1-x}\text{N}$ nanowires at room temperature using Cu dopant and annealing, *Nanoscale Res. Lett.*, 10:3, 2015.

- 880.J. L. Lyons, A. Janotti, and C. G. Van de Walle, Effects of hole localization on limiting p-type conductivity in oxide and nitride semiconductors, *J. Appl. Phys.*, 115, 012014, 2014.
- 881.J. Chevallier, W. C. Dautremont-Smith, C. W. Tu, and S. J. Pearton, Donor neutralization in GaAs (Si) by atomic hydrogen, *Appl. Phys. Lett.*, 47, 108, 1985.
- 882.N. M. Johnson, R. D. Burnham, R. A. Street, and R. L. Thornton, Hydrogen passivation of shallow-acceptor impurities in p-type GaAs, *Phys. Rev. B*, vol. 33, no. 2, Jan. 1986.
- 883.W. Ulrici, Hydrogen-impurity complexes in III-V semiconductors, *Rep. Prog. Phys.*, 67, pp. 2233-2286, 2004.
- 884.J. E. Northrup, S. B. Zhang, Dopant and defect energetics: Si in GaAs, *Phys. Rev. B*, vol. 47, no. 11, Mar. 1993-I.
- 885.H. Wenzl, K. Mika, and D. Henkel, Phase relations and point defect equilibria in GaAs crystal growth, *J. Crys. Growth*, 100, pp. 377-394, 1990.
- 886.R. W. Haisty, E. W. Mehal, and R. Stratton, Preparation and characterization of high resistivity GaAs, *J. Phys. Chem. Solids*, vol. 23, pp. 829-836, 1962.
- 887.C. -Y. Song, B. Pajot, and C. Porte, Piezospectroscopic study of interstitial oxygen in gallium arsenide, *Phys. Rev. B*, vol. 41, no. 17, Jun. 1990-I.
- 888.S. J. Pearton, J. W. Corbett, and T. S. Shi, Hydrogen in crystalline semiconductors, *Appl. Phys. A*, 43, pp. 153-195, 1987.
- 889.J. Lagowski, M. Kaminska, J. M. Parsey Jr., H. C. Gatos, and M. Lichtensteiger, Passivation of the dominant deep level (EL2) in GaAs by hydrogen, *Appl. Phys. Lett.*, 41, 1078, 1982.
- 890.<http://kinetics.nist.gov/janaf/html/H-050.html>
- 891.D. J. Chadi, K. J. Chang, Energetics of DX-center formation in GaAs and $\text{Al}_x\text{Ga}_{1-x}\text{As}$ alloys, *Phys. Rev. B*, vol. 39, no. 14, May 1989-I.
- 892.M. E. Weiner, A. S. Jordan, Analysis of doping anomalies in GaAs by means of a silicon-oxygen complex model, *J. Appl. Phys.*, 43, 1767, 1972.
- 893.C. G. Van de Walle, J. Neugebauer, First-principles calculations for defects and impurities: applications to III-nitrides, *J. Appl. Phys.*, 95, 3851, 2004.
- 894.S. Limpijumnong, C. G. Van de Walle, Diffusivity of native defects in GaN, *Phys. Rev. B*, 69, 035207, 2004.
- 895.T. Richter, H. L. R. Meijers, R. Calarco, and M. Marso, Doping concentration of GaN nanowires determined by opto-electrical measurements, *Nano Lett.*, vol. 8, no. 9, pp. 3056-3059, 2008.
- 896.R. B. Simon, J. Anaya, and M. Kuball, Thermal conductivity of bulk GaN-Effects of oxygen, magnesium doping, and strain field compensation, *Appl. Phys. Lett.*, 105, 202105, 2014.
- 897.T. Mattila, R. M. Nieminen, Point-defect complexes and broadband luminescence in GaN and AlN, *Phys. Rev. B*, vol. 55, no. 15, Apr. 1997-I.
- 898.C. G. Van de Walle, S. Limpijumnong, and J. Neugebauer, First-principles studies of beryllium doping of GaN, *Phys. Rev. B*, vol. 63, 245205, 2001.
- 899.W. Gotz, R. S. Kern, C. H. Chen, H. Liu, D. A. Steigerwald, and R. M. Fletcher, Hall-effect characterization of III-V nitride semiconductors for high efficiency light emitting diodes, *Mater. Sci. Eng.*, B59, pp. 211-217, 1999.
- 900.M. A. Reshchikov, H. Morkoc, Luminescence properties of defects in GaN, *J. Appl. Phys.*, 97, 061301, 2005.

- 901.B. -C. Chung, M. Gershenson, The influence of oxygen on the electrical and optical properties of GaN crystals grown by metalorganic vapor phase epitaxy, *J. Appl. Phys.*, 72, 651, 1992.
- 902.C. Wetzel, T. Suski, J. W. Ager III, E. R. Weber, E. E. Haller, S. Fischer, B. K. Meyer, R. J. Molnar, and P. Perlin, Pressure induced deep gap state of oxygen in GaN, *Phys. Rev. Lett.*, vol. 78, no. 20, May 1997.
- 903.G. A. Slack, L. J. Schowalter, D. Morelli, and J. A. Freitas Jr., Some effects of oxygen impurities on AlN and GaN, *J. Crys. Growth*, 246, pp. 287-298, 2002.
- 904.J. L. Lyons, A. Janotti, and C. G. Van de Walle, Carbon impurities and the yellow luminescence in GaN, *Appl. Phys. Lett.*, 97, 152108, 2010.
- 905.J. L. Lyons, A. Janotti, and C. G. Van de Walle, Effects of carbon on the electrical and optical properties of InN, GaN, and AlN, *Phys. Rev. B*, 89, 035204, 2014.
- 906.A. Y. Polyakov, N. B. Smimov, S. J. Pearton, F. Ren, B. Theys, F. Jomard, Z. Teukam, V. A. Dmitriev, A. E. Nikolaev, A. S. Usikov, and I. P. Nikitina, Fermi level dependence of hydrogen diffusivity in GaN, *Appl. Phys. Lett.*, 79, 1834, 2001.
- 907.C. H. Seager, S. M. Myers, A. F. Wright, D. D. Koleske, and A. A. Allerman, Drift, diffusion, and trapping of hydrogen in p-type GaN, *J. Appl. Phys.*, 92, 7246, 2002.
- 908.A. F. Wright, C. H. Seager, S. M. Myers, D. D. Koleske, and A. A. Allerman, Hydrogen configurations, formation energies, and migration barriers in GaN, *J. Appl. Phys.*, 94, 2311, 2003.
- 909.C. G. Van de Walle, J. Neugebauer, Hydrogen in semiconductors, *Annu. Rev. Mater. Res.*, 36: 179-98, 2006
- 910.C. G. Van de Walle, C. Stampfl, J. Neugebauer, M. D. McCluskey, and N. M. Johnson, Doping of AlGa_N alloys, *MRS Internet J. Nitride Semicond. Res.* 4s1, G10.4, 1999.
- 911.J. Neugebauer, C. G. Van de Walle, Gallium vacancies and yellow luminescence in GaN, *Appl. Phys. Lett.*, 69, 503, 1996.
- 912.J. Neugebauer, C. G. Van de Walle, Role of hydrogen in doping of GaN, *Appl. Phys. Lett.*, 68, 1829, 1996.
- 913.A. Sedhain, J. Li, J. Y. Lin, and H. X. Jiang, Nature of deep center emissions in GaN, *Appl. Phys. Lett.*, 96, 151902, 2010.
- 914.R. Armitage, W. Hong, Q. Yang, H. Feick, J. Gebauer, E. R. Weber, S. Hautakangas, and K. Saarinen, Contributions from gallium vacancies and carbon-related defects to the “yellow luminescence” in GaN, *Appl. Phys. Lett.*, 82, 3457, 2003.
- 915.D. O. Demchenko, I. C. Diallo, and M. A. Reshchikov, Yellow luminescence of gallium nitride generated by carbon defect complexes, *Phys. Rev. Lett.*, 110, 087404, 2013.
- 916.Z. M. Fang, K. Y. Ma, R. M. Cohen, and G. B. Stringfellow, Effect of growth temperature on photoluminescence of InAs grown by organometallic vapor phase epitaxy, *Appl. Phys. Lett.*, 59, 1446, 1991.
- 917.H. C. Casey Jr., A. Y. Cho, and E. H. Nicollian, Use of oxygen-doped Al_xGa_{1-x}As for the insulating layer in MIS structures, *Appl. Phys. Lett.*, 32, 678, 1978.
- 918.J. P. Donnelly, G. A. Ferrante, The electrical characteristics of InP implanted with the column IV elements, *Solid States Electron.*, vol. 23, pp. 1151-1154, 1980.
- 919.W. Ulrici, B. Clerjaud, A carbon-nitrogen complex in gallium phosphide, *Phys. Rev. B*, 72, 045203, 2005.

- 920.A. Laakso, J. Oila, A. Kemppinen, K. Saarinen, W. Egger, L. Liskay, P. Sperr, H. Lu, and W. J. Schaff, Vacancy defects in epitaxial InN: identification and electrical properties, *J. Crys. Growth*, 269, pp. 41-49, 2004.
- 921.C. G. Van de Walle, J. L. Lyons, and A. Janotti, Controlling the conductivity of InN, *Phys. Status Solidi A*, 207, no. 5, pp. 1024-1036, 2010.
- 922.A. Janotti, C. G. Van de Walle, Sources of unintentional conductivity in InN, *Appl. Phys. Lett.*, 92, 032104, 2008.
- 923.B. Clerjaud, Transition-metal impurities in III-V compounds, *J. Phys. C: Solid State Phys.*, 18, pp. 3615-3661, 1985.
- 924.W. Monch, *Electronic properties of semiconductor interfaces*, Springer, 2004.
- 925.A. Zunger, Theory of 3d transition atom impurities in semiconductors, *Ann. Rev. Mater. Sci.*, 15, pp. 411-453, 1985.
- 926.B. Clerjaud, D. Cote, and C. Naud, Evidence for complexes of hydrogen with deep-level defects in bulk III-V materials, *Phys. Rev. Lett.*, vol. 58, no. 17, Apr. 1987.
- 927.L. -A. Ledebø, B. K. Ridley, On the position of energy levels related to transition-metal impurities in III-V semiconductors, *J. Phys. C: Solid State Phys.*, 15, pp. L961-L964, 1982.
- 928.J. M. Langer, H. Heinrich, Deep-level impurities: A possible guide to prediction of band-edge discontinuities in semiconductor heterojunctions, *Phys. Rev. Lett.*, vol. 55, no. 13, Sep. 1985.
- 929.M. van Schilfgaarde, O. N. Mryasov, Anomalous exchange interactions in III-V dilute magnetic semiconductors, *Phys. Rev. B*, vol. 63, 233205, 2001.
- 930.L. A. Hemstreet, J. O. Dimmock, Electronic states of a substitutional chromium impurity in GaAs, *Phys. Rev. B*, vol. 20, no. 4, Aug. 1979.
- 931.N. Kullendorff, L. Jansson, and L.-A. Ledebø, Copper-related deep level defects in III-V semiconductors, *J. Appl. Phys.*, 54, 3203, 1983.
- 932.C. G. Van de Walle, Band lineups and deformation potentials in the model-solid theory, *Phys. Rev. B*, vol. 39, no. 3, Jan. 1989-II.
- 933.C. E. Dreyer, A. Janotti, and C. G. Van de Walle, Effects of strain on the electron effective mass in GaN and AlN, *Appl. Phys. Lett.*, 102, 142105, 2013.
- 934.H. Kroemer, Polar-on-nonpolar epitaxy, *J. Crys. Growth*, 81, pp. 193-204, 1987.
- 935.O. Ambacher, Growth and applications of group III-nitrides, *J. Phys. D: Appl. Phys.*, 31, 2653-2710, 1998.
- 936.D. M. Ceperley, B. J. Alder, Ground state of the electron gas by a Stochastic method, *Phys. Rev. Lett.*, vol. 45, no. 7, Aug. 1980.
- 937.J. P. Perdew, A. Zunger, Self-interaction correction to density-functional approximations for many-electron systems, *Phys. Rev. B*, vol. 23, no. 10, May 1981.
- 938.J. P. Perdew, K. Burke, M. Ernzerhof, Generalized gradient approximation made simple, *Phys. Rev. Lett.*, vol. 77, no. 18, Oct. 1996.
- 939.C. Stampfl, C. G. Van de Walle, Density-functional calculations for III-V nitrides using the local-density approximation and the generalized gradient approximation, *Phys. Rev. B*, vol. 59, no. 8, Feb. 1999-II.
- 940.D. Segev, C. G. Van de Walle, Origins of Fermi-level pinning on GaN and InN polar and nonpolar surfaces, *Europhys. Lett.*, 76(2), pp 305-311, 2006.
- 941.P. Hohenberg, W. Kohn, Inhomogeneous electron gas, *Phys. Rev.*, vol. 136, no. 3B, Nov. 1964.
- 942.W. Kohn, L. J. Sham, Self-consistent equations including exchange and correlation effects, *Phys. Rev.*, vol. 140, no. 4A, Nov. 1965.

- 943.P. E. Blochl, Projector augmented-wave method, Phys. Rev. B, vol. 50, no. 24, Dec. 1994-II.
- 944.M. Rohlfing, P. Kruger, and J. Pollmann, Quasiparticle band-structure calculations for C, Si, Ge, GaAs, and SiC using Gaussian-orbital basis sets, Phys. Rev. B, vol. 48, no. 24, Dec. 1993-II.
- 945.H. J. F. Jansen, A. J. Freeman, Total-energy full-potential linearized augmented-plane-wave method for bulk solids: Electronic and structural properties of tungsten, Phys. Rev. B, vol. 30, no. 2, Jul. 1984.
- 946.C. Hartwigsen, S. Goedecker, and J. Hutter, Relativistic separable dual-space Gaussian pseudopotentials from H to Rn, Phys. Rev. B, vol. 58, no. 7, Aug. 1998-I.
- 947.W. E. Pickett, Pseudopotential methods in condensed matter applications, Comp. Phys. Rep., 9, pp. 115-198, 1989.
- 948.P. Rinke, M. Scheffler, A. Qteish, M. Winkelnkemper, D. Bimberg, and J. Neugebauer, Band gap and band parameters of InN and GaN from quasiparticle energy calculations based on exact-exchange density-functional theory, Appl. Phys. Lett., 89, 161919, 2006.
- 949.A. De, C. E. Pryor, Predicted band structure of III-V semiconductors in the wurtzite phase, Phys. Rev. B, 81, 155210, 2010.
- 950.S. K. Pugh, D. J. Dugdale, S. Brand, and R. A. Abram, Band-gap and k.p. parameters for GaAlN and GaInN alloys, J. Appl. Phys., 86, 3768, 1999.
- 951.D. Fritsch, H. Schmidt, and M. Grundmann, Band-structure pseudopotential calculation of zinc-blende and wurtzite AlN, GaN, and InN, Phys. Rev. B, 67, 235205, 2003.
- 952.J. P. Perdew, Y. Wang, Accurate and simple analytic representation of the electron-gas correlation energy, Phys. Rev. B, vol. 45, no. 23, Jun. 1992-I.
- 953.A. D. Becke, A new mixing of Hartree-Fock and local density-functional theories, J. Chem. Phys., 98, 1372, 1993.
- 954.M. D. Segall, P. J. D. Lindan, M. J. Probert, C. J. Pickard, P. J. Hasnip, S. J. Clark, and M. C. Payne, First-principles simulation: ideas, illustrations and the CASTEP code, J. Phys.: Condens. Matter, 14, pp. 2717-2744, 2002.
- 955.F. Nogueira, A. Castro, and M. A. L. Marques, A tutorial on density functional theory, Lecture notes in physics, 620, 218256, 2003.
- 956.Z. -K. Liu, First-principles calculations and CALPHAD modeling of thermodynamics, J. Phase Equil. Diff., vol. 30, no. 5, pp. 517-534, 2009.
- 957.P. E. A. Turchi, I. A. Abrikosov, B. Burton, S. G. Fries, G. Grimvall, L. Kaufman, P. Korzhavyi, V. R. Manga, M. Ohno, A. Pisch, A. Scott, and W. Zhang, Interface between quantum-mechanical-based approaches, experiments, and CALPHAD methodology, Comp. Coupling Phase Diagrams Thermochem., 31, pp. 4-27, 2007.
- 958.D. S. Sholl, J. A. Steckel, Density functional theory: A practical introduction, Wiley, 2009.
- 959.A. Janotti, C. G. Van de Walle, Native point defects in ZnO, Phys. Rev. B, 76, 165202, 2007.
- 960.V. I. Anisimov, I. V. Solovyev, M. A. Korotin, M. T. Czyzyk, and G.A. Sawatzky, Density-functional theory and NiO photoemission spectra, Phys. Rev. B, vol. 48, no. 23, Dec. 1993-I.
- 961.A. I. Lichtenstein, M. I. Katsnelson, Ab initio calculations of quasiparticle band structure in correlated systems: LDA ++ approach, Phys. Rev. B, vol. 57, no. 12, Mar. 1998-II.

- 962.L. J. Sham, M. Schluter, Density functional theory of the energy gap, Phys. Rev. Lett., vol. 51, no. 20, Nov. 1983.
- 963.J. P. Perdew, M. Levy, Physical content of the exact Kohn-Sham orbital energies: Band gaps and derivative discontinuities, Phys. Rev. Lett., vol. 51, no. 20, Nov. 1983.
- 964.J. P. Perdew, J. A. Chevary, S. H. Vosko, K. A. Jackson, M. R. Pederson, D. J. Singh, and C. Fiolhais, Atoms, molecules, solids, and surfaces: Applications of the generalized gradient approximation for exchange and correlation, Phys. Rev. B, vol. 46, no. 11, Sep. 1992-I.
- 965.D. C. Langreth, J. P. Perdew, Theory of nonuniform electronic systems. I. Analysis of the gradient approximation and a generalization that works, Phys. Rev. B, vol. 21, no. 12, Jun. 1980.
- 966.D. C. Langreth, M. J. Mehl, Beyond the local-density approximation in calculations of ground-state electronic properties, Phys. Rev. B, vol. 28, no. 4, Aug. 1983.
- 967.J. Heyd, G. E. Scuseria, and M. Emzerhof, Hybrid functions based on a screened Coulomb potential, J. Chem. Phys., 118, 8207, 2003.
- 968.A. D. Becke, Density-functional thermochemistry. III. The role of exact exchange, J. Chem. Phys., 98, 5648, 1993.
- 969.J. P. Perdew, M. Emzerhof, and K. Burke, Rationale for mixing exact exchange with density functional approximations, J. Chem. Phys., 105, 9982, 1996.
- 970.G. Pacchioni, F. Frigoli, and D. Ricci, Theoretical description of hole localization in a quartz Al center: The importance of exact electron exchange, Phys. Rev. B, vol. 63, 054102, 2000.
- 971.G. Kresse, D. Joubert, From ultrasoft pseudopotentials to the projector augmented-wave method, Phys. Rev. B, vol. 59, no. 3, Jan. 1999-I.
- 972.G. Kresse, J. Furthmüller, Efficient iterative schemes for ab initio total-energy calculations using a plane-wave basis set, Phys. Rev. B, vol. 54, no. 16, Oct. 1996-II.
- 973.A. Alkauskas, P. Broqvist, and A. Pasquarello, Defect energy levels in density functional calculations: Alignment and band gap problem, Phys. Rev. Lett., 101, 046405, 2008.
- 974.A. Alkauskas, P. Broqvist, and A. Pasquarello, Defect levels through hybrid density functionals: Insights and applications, Phys. Status Solidi B, 248, no. 4, pp. 775-789, 2011.
- 975.R. M. Martin, Electronic structure: Basic theory and practical methods, Cambridge, 2004.
- 976.E. O. Kane, Band structure of indium antimonide, J. Phys. Chem. Solids, vol. 1, pp. 249-261, 1957.
- 977.M. -E. Pistol, C. E. Pryor, Band structure of core-shell semiconductor nanowires, Phys. Rev. B, 78, 115319, 2008.
- 978.C. R. Pidgeon, R. N. Brown, Interband magneto-absorption and Faraday rotation in InSb, Phys. Rev., vol. 146, no. 2, Jun. 1966.
- 979.T. B. Bahder, Eight-band k - p model of strained zinc-blende crystals, Phys. Rev. B, vol. 41, no. 17, Jun. 1990-I.
- 980.I. Saidi, S. B. Radhia, and K. Boujdaria Band parameters of GaAs, InAs, InP, and InSb in the 40-band k - p model, J. Appl. Phys., 107, 043701, 2010.
- 981.J. M. Luttinger, W. Kohn, Motion of electrons and holes in perturbed periodic fields, Phys. Rev., vol. 97, no. 4, Feb. 1955.
- 982.J. M. Luttinger, Quantum theory of cyclotron resonance in semiconductors: General theory, Phys. Rev., vol. 102, no. 4, May 1956.

- 983.M. Suzuki, T. Uenoyama, First-principles calculations of effective-mass parameters of AlN and GaN, Phys. Rev. B, vol. 52, no. 11, Sep. 1995-I; M. Suzuki, T. Uenoyama, and A. Yanase, Erratum: First-principles calculations of effective-mass parameters of AlN and GaN, Phys. Rev. B, vol. 58, no. 15, Oct. 1998-I.
- 984.K. Kim, W. R. L. Lambrecht, B. Segall, and M. van Schilfgaarde, Effective masses and valence-band splittings in GaN and AlN, Phys. Rev. B, vol. 56, no. 12, Sep. 1997-II.
- 985.Y. C. Yeo, T. C. Chong, and M. F. Li, Electronic band structures and effective-mass parameters of wurtzite GaN and InN, J. Appl. Phys., 83, 1429, 1998.
- 986.I. Vurgaftman, J. R. Meyer, and L. R. Ram-Mohan, Band parameters for III-V compound semiconductors and their alloys, J. Appl. Phys., 89, 5815, 2001.
- 987.S. L. Chuang, C. S. Chang, k·p method for strained wurtzite semiconductors, Phys. Rev. B, vol. 54, no. 4, Jul. 1996-II.
- 988.S. -H. Park, S. -L. Chuang, Crystal-orientation effects on the piezoelectric field and electronic properties of strained wurtzite semiconductors, Phys. Rev. B, vol. 59, no. 7, Feb. 1999-I.
- 989.M. Murayama, T. Nakayama, Chemical trend of band offsets at wurtzite/zinc-blende heterocrystalline semiconductor interfaces, Phys. Rev. B, vol. 49, no. 7, Feb. 1994-I.
- 990.A. Kobayashi, O. F. Sankey, S. M. Volz, and J. D. Dow, Semiempirical tight-binding band structures of wurtzite semiconductors: AlN, CdS, CdSe, ZnS, and ZnO, Phys. Rev. B, vol. 28, no. 2, Jul. 1983.
- 991.P. Y. Yu, M. Cardona, Fundamentals of semiconductors: Physics and materials properties, 4th edition, Springer, 2010.
- 992.T. Dietl, H. Ohno, and F. Matsukura, Hole mediated ferromagnetism in tetrahedrally coordinated semiconductors, Phys. Rev. B, vol. 63, 195205, 2001.
- 993.J. P. Loehr, Improved effective-bond-orbital model for superlattices, Phys. Rev. B, vol. 50, no. 8, Aug. 1994-II.
- 994.C. Freysoldt, B. Grabowski, T. Hickel, J. Neugebauer, G. Kresse, A. Janotti, and C. G. Van de Walle, First-principles calculations for point defects in solids, Rev. Mod. Phys., vol. 86, no. 1, pp. 253-305, Jan.-Mar. 2014.
- 995.C. G. Van de Walle, R. M. Martin, Theoretical calculations of semiconductor heterojunction discontinuities, J. Vac. Sci. Technol. B, 4, 1055, 1986.
- 996.M. Cardona, N. E. Christensen, Acoustic deformation potentials and heterostructure band offsets in semiconductors, Phys. Rev. B, vol. 35, no. 12, Apr. 1987-II.
- 997.W. E. Pickett, S. G. Louie, and M. L. Cohen, Self-consistent calculations of interface states and electronic structure of the (110) interfaces of Ge-GaAs and AlAs-GaAs, Phys. Rev. B, vol. 17, no. 2, Jan. 1978.
- 998.W. R. L. Lambrecht, B. Segall, O. K. Andersen, Self-consistent dipole theory of heterojunction band offsets, Phys. Rev. B, vol. 41, no. 5, Feb. 1990-I.
- 999.T. Akiyama, T. Yamashita, K. Nakamura, and T. Ito, Band alignment tuning in twin-plane superlattices of semiconductor nanowires, Nano Lett., 10, pp. 4614-4618, 2010.
- 1000.Z. Zanolli, F. Fuchs, J. Furthmüller, U. von Barth, and F. Bechstedt, Model GW band structure of InAs and GaAs in the wurtzite phase, Phys. Rev. B, 75, 245121, 2007.
- 1001.N. Vainorius, D. Jacobsson, S. Lehmann, A. Gustafsson, K. A. Dick, L. Samuelson, and M. -E. Pistol, Observation of type-II recombination in single wurtzite/zinc-blende GaAs heterojunction nanowires, Phys. Rev. B, 89, 165423, 2014.

- 1002.J. Bao, D. C. Bell, and F. Capasso, Optical properties of rotationally twinned InP nanowire heterostructures, *Nano Lett.*, vol. 8, no. 3, pp. 836-841, 2008.
- 1003.K. Pemasiri, M. Montazeri, R. Gass, L. M. Smith, H. E. Jackson, J. Yarrison-Rice, S. Paiman, Q. Gao, H. H. Tan, C. Jagadish, X. Zhang, and J. Zou, Carrier dynamics and quantum confinement in type II ZB-WZ InP nanowire homostructures, *Nano Lett.*, vol. 9, no. 2, pp. 648-654, 2009.
- 1004.M. D. Schroer, J. R. Petta, Correlating the nanostructure and electronic properties of InAs nanowires, *Nano Lett.*, 10, pp. 1618-1622, 2010.
- 1005.M. Hjort, S. Lehmann, J. Knutsson, A. A. Zakharov, Y. A. Du, S. Sakong, R. Timm, G. Nylund, E. Lundgren, P. Kratzer, K. A. Dick, and A. Mikkelsen, Electronic and structural differences between wurtzite and zinc blende InAs nanowire surfaces: experiment and theory, *ACS Nano*, vol. 8, no. 12, pp. 12346-12355, 2014.
- 1006.J. Tersoff, Theory of semiconductor heterojunctions: The role of quantum dipoles, *Phys. Rev. B*, vol. 30, no. 8, Oct. 1984.
- 1007.C. Tejedor, F. Flores, A simple approach to heterojunctions, *J. Phys. C: Solid State Phys.*, vol. 11, no. 1, 1978.
- 1008.Y. P. Varshni, Temperature dependence of the energy gap in semiconductors, *Physica*, 34, pp. 149-154, 1967.
- 1009.K. P. O'Donnell, X. Chen, Temperature dependence of semiconductor band gaps, *Appl. Phys. Lett.*, 58, 24, Jun. 1991.
- 1010.F. Gygi, A. Baldereschi, Quasiparticle energies in semiconductors: Self-energy correction to the local-density approximation, *Phys. Rev. Lett.*, vol. 62, no. 18, May 1989.
- 1011.X. Zhao, C. M. Wei, L. Yang, and M. Y. Chou, Quantum confinement and electronic properties of silicon nanowires, *Phys. Rev. Lett.*, vol. 92, no. 23, Jun. 2004.
- 1012.Y. M. Niquet, A. Lherbier, N. H. Quang, M. V. Fernandez-Serra, and C. Delerue, Electronic structure of semiconductor nanowires, *Phys. Rev. B*, 73, 165319, 2006.
- 1013.L. Hedin, B. I. Lundqvist, and S. Lundqvist, Local exchange-correlation potentials, *Solid State Commun.*, vol. 9, pp. 537-541, 1971.
- 1014.M. Rohlffing, N. -P. Wang, P. Kruger, and J. Pollmann, Image states and excitons at insulator surfaces with negative electron affinity, *Phys. Rev. Lett.*, vol. 91, no. 25, Dec. 2003.
- 1015.F. Aryasetiawan, O. Gunnarsson, The GW method, *Rep. Prog. Phys.*, 61, pp. 237-312, 1998.
- 1016.C. Li, M. Bescond, and M. Lannoo, GW investigation of interface-induced correlation effects on transport properties in realistic nanoscale structures, *Phys. Rev. B*, 80, 195318, 2009.
- 1017.M. S. Hybertsen, S. G. Louie, Electron correlation in semiconductors and insulators: Band gaps and quasiparticle energies, *Phys. Rev. B*, vol. 34, no. 8, Oct. 1986.
- 1018.P. A. Sterne, J. C. Inkson, Exchange-correlation potential in semiconductors and insulators, *J. Phys. C: Solid State Phys.*, 17, pp. 1497-1510, 1984.
- 1019.T. Cheiwchanchamnangij, W. R. L. Lambrecht, Band structure parameters of wurtzite and zinc-blende GaAs under strain in the GW approximation, *Phys. Rev. B*, 84, 035203, 2011.
- 1020.M. M. Waldrop, The chips are down for Moore's law, *Nature*, vol. 530, pp. 144-147, Feb. 2016.

- 1021.K. K. Bhuiwarka, J. Schulze and I. Eisele, Performance enhancement of vertical tunnel field-effect transistor with SiGe in the δp^+ layer, Jpn. J. Appl. Phys., vol. 43, p. 4073-4078, Jul. 2004.
- 1022.H. Kroemer, Quantum Mechanics for Engineering, Materials Science, and Applied Physics, 1st edition, Prentice Hall, 1994.
1023. J. Appenzeller, J. Knoch, M. T. Bjork, H. Riel, H. Schmid, and W. Riess, Toward Nanowire Electronics, IEEE Trans. Elec. Dev., vol. 55, no. 11, Nov. 2008.
- 1024.K. Tomioka, T. Fukui, Vertical tunnel FETs using III-V nanowire/Si heterojunctions, ECS Trans., vol. 61, 3, pp. 81-89, 2014.
- 1025.K. Tomioka, T. Fukui, and J. Motohisa, Surrounding-gate tunnel FET using InAs/Si heterojunction, ECS Trans., vol. 69, 10, pp. 109-118, 2015.
- 1026.M. Reiche, M. Kittler, H. Ubensee, M. Krause, and E. Pippel, Trap-assisted tunneling on extended defects in tunnel field-effect transistors, Jpn. J. Appl. Phys., 53, 04EC03, 2014.
- 1027.R. M. Iutzi, E. A. Fitzgerald, Microstructure and conductance-slope of InAs/GaSb tunnel diodes, J. Appl. Phys., 115, 234503, 2014.
- 1028.G. Zhou, Y. Lu, R. Li, W. Hwang, Q. Zhang, Q. Liu, T. Vasen, C. Chen, H. Zhu, J. Kuo, S. Koswatta, T. Kosel, M. Wistey, P. Fay, A. Seabaugh, and H. Xing, Self-aligned $\text{In}_{0.53}\text{Ga}_{0.47}\text{As}/\text{InAs}/\text{InP}$ vertical tunnel FETs, Proc. Int. Conf. Compound Semicond. Manuf. Technol., pp. 339-342, May 2011.
- 1029.G. Zhou, Y. Lu, R. Li, Q. Zhang, Q. Liu, T. Vasen, H. Zhu, J. Kuo, T. Kosel, M. Wistey, P. Fay, A. Seabaugh, and H. Xing, InGaAs/InP tunnel FETs with a subthreshold swing of 93 mV/dec and $I_{\text{on}}/I_{\text{off}}$ ratio near 10^6 , IEEE Electron Dev. Lett., vol. 33, no. 6, Jun. 2012.
- 1030.B. Ganjipour, J. Wallentin, M. T. Borgstrom, L. Samuelson, and C. Thelander, Tunnel field-effect transistors based on InP-GaAs heterostructure nanowires, ACS Nano, vol. 6, no. 4, pp. 3109-3113, 2012.
- 1031.B. Rajamohanam, D. Mohata, Y. Zhu, M. Hudait, Z. Jiang, M. Hollander, G. Klimeck, and S. Datta, Design, fabrication, and analysis of p-channel arsenide/antimonide hetero-junction tunnel transistors, J. Appl. Phys., 115, 044502, 2014.
- 1032.C. Sun, M. T. Wade, Y. Lee, J. S. Orcutt, L. Alloatti, M. S. Georgas, A. S. Waterman, J. M. Shainline, R. R. Avizienis, S. Lin, B. R. Moss, R. Kumar, F. Pavanello, A. H. Atabaki, H. M. Cook, A. J. Ou, J. C. Leu, Y. Chen, K. Asanovic, R. J. Ram, M. A. Popovic, and V. M. Stojanovic, Single-chip microprocessor that communicates directly using light, Nature, vol. 528, pp. 534-538, Dec. 2015.
- 1033.S. Mokkapati, C. Jagadish, III-V compound SC for optoelectronic devices, Materialstoday, vol. 12, no. 4, pp. 22-32, Apr. 2009.
- 1034.L. A. Coldren, S. W. Corzine, and M. L. Masanovic, Diode lasers and photonic integrated circuits, 2nd Edition, Wiley, 2012.
- 1035.D. Saxena, S. Mokkapati, P. Parkinson, N. Jiang, Q. Gao, H. H. Tan, and C. Jagadish, Optically pumped room-temperature GaAs nanowire lasers, Nature photonics, vol. 7, pp. 963-968, Dec. 2013.
- 1036.D. L. Huffaker, D. G. Deppe, Electroluminescence efficiency of 1.3 μm wavelength InGaAs/GaAs quantum dots, Appl. Phys. Lett., 73, 520, 1998.

- 1037.M. Yamada, T. Anan, K. Tokutome, A. Kamei, K. Nishi, and S. Sugou, Low-threshold operation of 1.3- μm GaAsSb quantum-well lasers directly grown on GaAs substrates, *IEEE Photon. Technol. Lett.*, vol. 12, no. 7, Jul. 2000.
- 1038.E. Stark, T. Frost, S. Jahangir, S. Deshpande, and P. Bhattacharya, A monolithic electrically injected InGaN/GaN disk-in-nanowire ($\lambda=533\text{nm}$) laser on (001) silicon, *IEEE Photon. Conf.*, pp. 591-592, Oct. 2014.
- 1039.A. B. Greytak, C. J. Barrelet, Y. Li, and C. M. Lieber, Semiconductor nanowire laser and nanowire waveguide electro-optic modulators, *Appl. Phys. Lett.*, 87, 151103, 2005.
- 1040.H. Choi, J. C. Johnson, R. He, S. Lee, F. Kim, P. Pauzauskie, J. Goldberger, R. J. Saykally, and P. Yang, Self-organized GaN quantum wire UV lasers, *J. Phys. Chem. B*, 107, pp. 8721-8725, 2003.
- 1041.K. H. Li, X. Liu, Q. Wang, S. Zhao, and Z. Mi, Ultralow-threshold electrically injected AlGaIn nanowire ultraviolet lasers on Si operating at low temperature, *Nature Nanotechnology*, vol. 10, pp. 140-144, Feb. 2015.
- 1042.F. Qian, Y. Li, S. Gradecak, H. Park, Y. Dong, Y. Ding, Z. L. Wang, and C. M. Lieber, Multi-quantum-well nanowire heterostructures for wavelength-controlled lasers, *Nature Materials*, vol. 7, pp. 701-706, Sep. 2008.
- 1043.C. Chang, C. Chi, M. Yao, N. Huang, C. Chen, J. Theiss, A. W. Bushmaker, S. LaLumondiere, T. Yeh, M. L. Povinelli, C. Zhou, P. D. Dapkus, and S. B. Cronin, Electrical and optical characterization of surface passivation in GaAs nanowires, *Nano Lett.*, 12, pp. 4484-4489, 2012.
- 1044.Y. Zhang, M. Loncar, Ultra-high quality factor optical resonators based on semiconductor nanowires, *Optics Express*, vol. 16, no. 22, pp. 17400-17409, Oct. 2008.
- 1045.S. E. Venegas-Andraca, Quantum walks: A comprehensive review, *Quantum Inf. Process.*, 11, 5, pp. 1015-1106, 2012.
- 1046.A. M. Childs, Universal Computation by Quantum Walk, *Phys. Rev. Lett.*, 102, 180501, 2009.
- 1047.D. Aharonov, W. van Dam, J. Kempe, S. Lloyd, and O. Regev, Adiabatic quantum computation is equivalent to standard quantum computation, *SIAM Rev.*, vol. 50, no. 4, pp. 755-787, 2008.
- 1048.J. Kempe, A. Kitaev, and O. Regev, The complexity of the local Hamiltonian problem, *SIAM J. Comput.*, vol. 35, no. 5, pp. 1070-1097, 2006.
- 1049.F. Verstraete, M. M. Wolf, and J. I. Cirac, Quantum computation and quantum-state engineering driven by dissipation, *Nature Physics*, vol. 5, pp. 633-636, Sep. 2009.
- 1050.T. D. Ladd, F. Jelezko, R. Laflamme, Y. Nakamura, C. Monroe, and J. L. O'Brien, Quantum computers, *Nature*, vol. 464, pp. 45-53, Mar. 2010.
- 1051.A. Montanaro, Quantum algorithms: an overview, *Nature Partner J. Quantum Inf.*, 2, 15023, 2016.
- 1052.<http://math.nist.gov/quantum/zoo/>
- 1053.I. Buluta, S. Ashhab, and F. Nori, Natural and artificial atoms for quantum computation, *Rep. Prog. Phys.*, 74, 104401, 2011.
- 1054.B. Schumacher, Quantum coding, *Phys. Rev. A*, vol. 51, no. 4, Apr. 1995.
- 1055.D. P. DiVincenzo, The physical implementation of quantum computation, *Fortschr. Phys.*, 48, 9-11, pp. 771-783, 2000.

- 1056.P. Michler, A. Kiraz, C. Becher, W. V. Schoenfeld, P. M. Petroff, L. Zhang, E. Hu, and A. Imamoglu, A quantum dot single-photon turnstile device, *Science*, vol. 290, pp. 2282-2285, Dec. 2000.
- 1057.B. Darquie, M. P. A. Jones, J. Dingjan, J. Beugnon, S. Bergamini, Y. Sortais, G. Messin, A. Browaeys, and P. Grangier, Controlled single-photon emission from a single trapped two-level atom, *Science*, vol. 309, pp. 454-456, Jul. 2005.
- 1058.A. J. Shields, Semiconductor quantum light sources, *Nature Photonics*, vol. 1, pp. 215-223, Apr. 2007.
- 1059.E. Knill, R. Laflamme, and G. J. Milburn, A scheme for efficient quantum computation with linear optics, *Nature*, vol. 409, pp. 46-52, Jan. 2001.
- 1060.N. Panev, A. I. Persson, N. Skold and L. Samuelson, Sharp exciton emission from single InAs quantum dots in GaAs NW, *Appl. Phys. Lett.*, 83, 2238, 2003.
- 1061.M. T. Borgstrom, V. Zwiller, E. Muller, and A. Imamoglu, Optically bright quantum dots in single nanowire, *Nano Lett.*, vol. 5, no. 7, pp. 1439-1443, 2005.
- 1062.I. Friedler, C. Sauvan, J. P. Hugonin, P. Lalanne, J. Claudon, and J. M. Gerard, Solid-state single photon sources: the nanowire antenna, *Optics Express*, vol. 17, no. 4, pp. 2095-2110, Feb. 2009.
- 1063.J. Heinrich, A. Huggenberger, T. Heindel, S. Reitzenstein, S. Hofling, L. Worschech, and A. Forchel, Single photon emission from positioned GaAs/AlGaAs photonic nanowires, *Appl. Phys. Lett.*, 96, 211117, 2010.
- 1064.J. Claudon, J. Bleuse, N. S. Malik, M. Bazin, P. Jaffrennou, N. Gregersen, C. Sauvan, P. Lalanne, and J. -M. Gerard, A highly efficient single-photon source based on a quantum dot in a photonic nanowire, *Nature Photonics*, vol. 4, pp. 174-177, Mar. 2010.
- 1065.J. Bleuse, J. Claudon, M. Creasey, N. S. Malik, and J. -M. Gerard, Inhibition, enhancement, and control of spontaneous emission in photonic nanowires, *Phys. Rev. Lett.*, 106, 103601, Mar. 2011.
- 1066.M. E. Reimer, G. Bulgarini, N. Akopian, M. Hocevar, M. B. Bavinck, M. A. Verheijen, E. P. A. M. Bakkers, L. P. Kouwenhoven, and V. Zwiller, Bright single-photon sources in bottom-up tailored nanowires, *Nature Commun.*, 3, 737, Mar. 2012.
- 1067.M. N. Makhonin, A. P. Foster, A. B. Krysa, P. W. Fry, D. G. Davies, T. Grange, T. Walther, M. S. Skolnick, and L. R. Wilson, Homogeneous array of nanowire-embedded quantum light emitters, *Nano Lett.*, 13, pp. 861-865, 2013.
- 1068.M. Heiss, Y. Fontana, A. Gustafsson, G. Wust, C. Magen, D. D. O'Regan, J. W. Luo, B. Ketterer, S. Conesa-Boj, A. V. Kuhlmann, J. Houel, E. Russo-Averchi, J. R. Morante, M. Cantoni, N. Marzari, J. Arbiol, A. Zunger, R. J. Warburton, and A. F. i Morral, Self-assembled quantum dots in a nanowire system for quantum photonics, *Nature Mater.*, vol. 12, pp. 439-444, May 2013.
- 1069.R. Hanson, L. P. Kouwenhoven, J. R. Petta, S. Tarucha, and L. M. K. Vandersypen, Spins in few-electron quantum dots, *Rev. Mod. Physics*, vol. 79, pp.1217-1265, Oct.-Dec. 2007.
- 1070.L. P. Kouwenhoven, D. G. Austing, and S. Tarucha, Few-electron quantum dots, *Rep. Prog. Phys.*, 64, pp. 701-736, 2001.
- 1071.W. G. van der Wiel, S. De Franceschi, J. M. Elzerman, T. Fujisawa, S. Tarucha, and L. P. Kouwenhoven, Electron transport through double quantum dots, *Rev. Mod. Physics*, vol. 75, pp. 1-22, Jan. 2003.

- 1072.C. Flindt, A. S. Sorensen, and K. Flensberg, Spin-orbit mediated control of spin qubits, *Phys. Rev. Lett.*, 97, 240501, 2006.
- 1073.S. Nadj-Perge, S. M. Frolov, E. P. A. M. Bakkers, and L. P. Kouwenhoven, Spin-orbit qubit in a semiconductor nanowire, *Nature*, vol. 468, pp. 1084-1087, Dec. 2010.
- 1074.K. D. Petersson, L. W. McFaul, M. D. Schroer, M. Jung, J. M. Taylor, A. A. Houck, and J. R. Petta, Circuit quantum electrodynamics with a spin qubit, *Nature*, vol. 490, pp. 380-383, Oct. 2012.
- 1075.T. W. Larsen, K. D. Petersson, F. Kuemmeth, T. S. Jespersen, P. Krogstrup, J. Nygard, and C. M. Marcus, Semiconductor-nanowire-based superconducting qubit, *Phys. Rev. Lett.*, 115, 127001, 2015.
- 1076.J. V. Holm, H. I. Jorgensen, P. Krogstrup, J. Nygard, H. Liu, and M. Aagesen, Surface-passivated GaAsP single-nanowire solar cells exceeding 10% efficiency grown on silicon, *Nature Commun.*, 4, 1498, pp. 1-5, Feb. 2013.
- 1077.L. Yu, F. Fortuna, B. O'Donnell, T. Jeon, M. Foldyna, G. Picardi, and P. R. i Cabarrocas, Bismuth-catalyzed and doped silicon nanowires for one-pump-down fabrication of radial junction solar cells, *Nano Lett.*, 12, pp. 4153-4158, 2012.
- 1078.K. S. Leschkies, R. Divakar, J. Basu, E. Enache-Pommer, J. E. Boercker, C. B. Carter, U. R. Kortshagen, D. J. Norris, and E. S. Aydil, Photosensitization of ZnO nanowires with CdSe quantum dots for photovoltaic devices, *Nano Lett.*, vol. 7, no. 6, pp. 1793-1798, 2007.
- 1079.M. A. Green, K. Emery, Y. Hihikawa, W. Warta, and E. D. Dunlop, Solar cell efficiency tables (version 44), *Prog. Photovolt: Res. Appl.*, 22, pp. 701-710, 2014.
- 1080.E. C. Garnett, M. L. Brongersma, Y. Cui, and M. D. McGehee, Nanowire solar cells, *Annu. Rev. Mater. Res.*, 41, pp. 269-295, 2011.
- 1081.J. Simon, K. L. Schulte, D. L. Young, N. M. Haegel, and A. J. Ptak, GaAs solar cells grown by hydride vapor-phase epitaxy and the development of GaInP cladding layers, *IEEE J. Photovolt.*, vol. 6, no. 1, Jan. 2016.
- 1082.M. D. Kelzenberg, S. W. Boettcher, J. A. Petykiewicz, D. B. Turner-Evans, M. C. Putnam, E. L. Warren, J. M. Spurgeon, R. M. Briggs, N. S. Lewis, and H. A. Atwater, Enhanced absorption and carrier collection in Si wire arrays for photovoltaic applications, *Nature Materials*, vol. 9, pp. 239-244, Mar. 2010.
- 1083.Z. Fan, H. Razavi, J. Do, A. Moriwaki, O. Ergen, Y. Chueh, P. W. Leu, J. C. Ho, T. Takahashi, L. A. Reichertz, S. Neale, K. Yu, M. Wu, J. W. Ager, and A. Javey, Three-dimensional nanopillar-array photovoltaics on low-cost and flexible substrates, *Nature Mater.*, vol. 8, pp. 648-653, Aug. 2009.